Contribution to the understanding of the mechanisms involved upon cycling at high voltage of doped LiCoO2

Fatima-Ezzahra Er-Rami

université de BORDEAUX

THÈSE PRÉSENTÉE

POUR OBTENIR LE GRADE DE

DOCTEUR DE L'UNIVERSITÉ DE BORDEAUX

ÉCOLE DOCTORALE DES SCIENCES CHIMIQUES

SPÉCIALITÉ: PHYSICO-CHIMIE DE LA MATIERE CONDENSEE

Par Fatima-Ezzahra ER-RAMI

Contribution to the understanding of the mechanisms involved upon cycling at high voltage of doped $LiCoO_2$

Sous la direction de: Dany CARLIER-LARREGARAY
co-directeur: Claude DELMAS

Soutenue le 24 mars 2022

Membres du jury:

M. AYMONIER, Cyril	Directeur de recherche, ICMCB	Président
M. STIEVANO, Lorenzo	Professeur, ICGM	Rapporteur
Mme. PRALONG, Valérie	Directrice de recherche, CRISMAT	Rapporteur
Mme. SALAGER, Elodie	Chargée de recherche, CEMTHI	Examinatrice
M. AUVERGNIOT, Jérémie	Docteur, Umicore	Examinateur
Mme. CARLIER-LARREGARAY, Dany	Professeur, ICMCB	Directrice de thèse
M. DELMAS, Claude	Directeur de recherche, ICMCB	Co-directeur

À mes parents…

Acknowledgements

First of all, I want to take a moment to thank my two supervisors, Dany and Claude, for having taken me on as a PhD student. Thanks for always being the inspiring and encouraging sources during the whole Ph.D project. I really appreciate the several opportunities that you have given to me, including the numerous conferences, scientific trainings. Through these occasions, you have helped me to have a complete confidence in myself and allowed a total integration into the research society. Thanks a lot for all your personal and scientific advice, which kept me always on the right track.

I would also like to express my gratitude to all the members of my jury. I would like to start thanking the two reviewers, Prof. Lorenzo STIEVANO (ICGM) and Dr. Valérie PRALONG (CRISMAT), for having accepted to evaluate this thesis. My sincere acknowledgement is also extended to Dr. Elodie SALAGER (CEMTHI), Dr. Cyril AYMONIER (ICMCB) and Dr. Jérémie AUVERGNIOT (Umicore) for having taken part in the defense committee and for the great discussion during the defense.

This project was funded by UMICORE company. I want to thank Maxime BLANGERO, Pierre-Etienne CABELGUEN and Kyongse SONG for the fruitful discussion.

During these three years, I have been led to collaborate with several people whom I would also like to thank: François Fauth (ALBA, Spain) for the synchrotron XRD, François Weill for TEM, Paula for NMR and Mathieu for NMR and EPR. Cathy, Manu and Jérome are acknowledged for their support with the daily experiment. Lastly, I want to thank Eric for the XRD acquisition. I also want to thank: Mario MAGLIONE, Laurence CROGUENNEC, Marie GUIGNARD, Liliane

GUERLOU-DEMOURGUES, Jacob OLCHOWKA and all the permanents members of group 2.

My daily life and labwork would have not been that great without the presence of my labmates: Sunkyu, Jon, Ronan, Adrien, Yohan, Annie-Kim, Edgar, Valentin, Romain, Rafael, Quentin, Vadim Eva, Marie, Giles, Louise and many other people that the list is so long that I cannot all list here. Many thanks for all your support, for the great sense of humor, for the time spending together.

Finally, I want to thank my family: my parents (Aicha and Abderhaman), my sisters (Ouma and Koki) my aunts, my grandmother and all my friends (Nouha, Simo, Ayman, Ayoub…) for having been an unlimited support during my entire life and particularly in these last years.

Titre: Contribution à la compréhension des mécanismes mis en jeu lors du cyclage à haute tension du $LiCoO_2$ dopé

Résumé

Encore aujourd'hui, l'oxyde lamellaire O3-$LiCoO_2$ est l'un des matériaux d'électrode positive les plus répandus dans les batteries lithium-ion du commerce, grâce à sa densité d'énergie volumétrique plus élevée qui pourrait encore être améliorée en chargeant à plus haute tension. Cependant, $LiCoO_2$ présente une mauvaise tenue en cyclage au-dessus de 4.3 V par rapport à Li^+/Li. Les causes principales de ce phénomène sont : i) les instabilités de structure, ii) la dégradation de l'électrolyte et iii) la dissolution du cobalt. Deux stratégies principales ont été identifiées pour surmonter ces problèmes : les revêtements et le dopage du matériau. Les ions aluminium Al^{3+} ou magnésium Mg^{2+} ont été parmi les premiers envisagés. Un rayon similaire pour Al^{3+} comparé à Co^{3+} (0.535 Å vs. 0.545 Å) facilite la substitution de ce dernier tout en maintenant la structure. Au contraire, comme les ions Mg^{2+} sont beaucoup plus gros (0.720 Å), ils déforment fortement le réseau localement, impliquent également un changement de l'état d'oxydation des ions Co adjacents et peuvent migrer pendant le cyclage. Pour une application pratique, la quantité de dopant doit être faible. On s'intéresse ici aux matériaux dopés à 2 ou 4%. Comme $LiCoO_2$ peut également être préparé avec un excès de lithium, nous avons synthétisé plusieurs matériaux en faisant varier le rapport Li/M. Nous avons caractérisé les échantillons par DRX et RMN pour étudier la structure à différentes échelles et discuter de l'homogénéité du dopage. Les mécanismes impliqués dans le processus de désintercalation du Li, en particulier à haute tension, ont été étudiés par DRX et RMN.

Mots clés: Batterie Li-ion, Electrode positive, $LiCoO_2$, Haut potentiel, Dopage par Al et Mg

Title: Contribution to the understanding of the mechanisms involved upon cycling at high voltage of doped $LiCoO_2$

Abstract

Still today, lamellar oxide O3-$LiCoO_2$ is one of the most common positive electrode material in commercial lithium-ion batteries, thanks to its high volumetric energy density which can be further improved by charging at high voltages. However, bare $LiCoO_2$ exhibits very poor cycling performances above 4.3 V vs. Li^+/Li. It is believed that the main causes for this are i) structural instabilities, ii) electrolyte degradation and iii) cobalt dissolution. Two main strategies have been identified to overcome these issues: coatings and doping of the material. Aluminum Al^{3+} or magnesium Mg^{2+} ions as dopants were among the first considered. A similar radius for Al^{3+} compared to Co^{3+} (0.535 Å vs. 0.545 Å) facilitates the substitution of the latter while maintaining the structure. On the opposite, as Mg^{2+} ions are much larger (0.720 Å), they strongly distort locally the lattice, and also involve a change in the oxidation state of the adjacent Co ions and may migrate during cycling. For practical application, the amount of the dopant has to be low. We focus here on 2 or 4% doped materials. As $LiCoO_2$ can also be prepared with lithium excess, we synthetized several materials varying the Li/M ratio. We characterized the samples by XRD and NMR to study the structure at different scales and discuss the homogeneity of the doping. The mechanisms involved in the Li deintercalation process, especially at high voltage was studied by XRD and NMR.

Keywords: Li-ion battery, Positive electrode, $LiCoO_2$, High voltage, Al and Mg doping

---

Institut de Chimie de la Matière Condensée de Bordeaux

ICMCB/CNRS – UPR 9048

87, Avenue du Docteur Schweitzer, 33608 Pessac Cedex

Résumé étendu

Les batteries sont des dispositifs de stockage électrochimiques permettant de stocker de manière réversible de l'énergie sous forme d'énergie chimique et de l'utiliser quand on en a besoin. Encore aujourd'hui les batteries Li-ion se développent comme un moyen essentiel pour stocker l'énergie. La technologie Li-ion, dont le prix Nobel de chimie a été décerné aux trois inventeurs (John Goodenough, Stanley Whittingham et Akira Yoshino) le 9 octobre 2019, a été commercialisée pour la première fois par Sony en 1991,[1] au travers d'une batterie composée d'une électrode négative en carbone, d'une électrode positive en oxyde de lithium-cobalt ($LiCoO_2$) et d'un électrolyte liquide organique. L'oxyde lamellaire O3-$LiCoO_2$ est l'un des matériaux d'électrode positive les plus répandus dans les batteries lithium-ion, grâce à sa densité d'énergie volumétrique plus élevée qui pourrait encore être améliorée en chargeant à plus haute tension.[2] $LiCoO_2$ synthétisé à haute température présente la structure de type α-$NaFeO_2$ (groupe d'espace R-3m avec $a_{hex.}$ = 2.816 Å ; $c_{hex.}$ = 14.052 Å) avec un empilement de type O3 d'après la nomenclature développer par Delmas.[3] Où O indique que le lithium est un site octaédrique et 3 couches de CoO_2 sont nécessaires pour former la cellule unitaire hexagonale. Des efforts considérables ont été déployés pour comprendre les changements structurels se produisant au cours du cyclage électrochimique par la diffraction des rayons X et les premiers principes de calcul.[4–6] Lorsque le Li est désintercalé à partir de $LiCoO_2$, le matériau subit une série de transitions de phase; la première se produit autour de ~3.9V par rapport au couple Li^+/Li caractéristique à un plateau de potentiel ($0.75 \leq x \leq 0.94$ in Li_xCoO_2). Il correspond à une région biphasée induite par une transition isolant-métal où une phase rhomboédrique nouvellement apparue (appelée $O3_2$) coexiste avec le $LiCoO_2$ ($O3_1$).[8] Plus récemment, le domaine de composition du plateau a été revisité pour un "vrai" $LiCoO_2$ stœchiométrique : seulement lorsqu'absolument aucun défaut structurel n'est présent, le domaine biphasé commence tout à fait au début de la désintercalation du Li.[9] Ensuite, lorsque ~ 0.5 de Li est désintercalé, le système subit une transition de l'O3 rhomboédrique à l'O'3 monoclinique en raison d'un ordre lithium/lacune dans l'espace interfeuillet.[6,7,10] Lorsque la cellule est cyclée jusqu'à 4.35 V par rapport au couple Li^+/Li, la réaction de désintercalation est hautement réversible, donnant naissance à des batteries avec une excellente cyclabilité avec une capacité spécifique de 174 mAh/g. Afin d'obtenir une capacité plus élevée et d'augmenter la densité d'énergie, une tension

de cyclage supérieure à 4.35 V par rapport au couple Li^+/Li est nécessaire. Cependant, travailler à haut potentiel entraîne une détérioration des performances de cyclage, causée par des instabilités structurelles, l'oxydation des électrolytes et la dissolution de Co.[13–18] Plus précisément, pour des potentiel de charge supérieures à 4.5 V, $LiCoO_2$ présente des transformations de phase néfastes : O3 vers H1-3 et H1-3 vers O1 impliquant des glissements de feuillet. Par conséquent, une déformation interne s'accumule, entraînant la formation de fissures et la pulvérisation de particules. Plusieurs stratégies ont été étudiées pour améliorer la stabilité en cyclage de $LiCoO_2$. Parmi celles-ci, les substitutions de métaux pour le cobalt (Al, Mg, Ti…) se sont révélés être une méthode prometteuse et efficace pour améliorer les performances électrochimiques de $LiCoO_2$ à haute tension. Les ions aluminium Al^{3+} ou magnésium Mg^{2+} comme dopants ont été parmi les premiers envisagés. En 1998, Ceder et al.[29] ont identifié l'aluminium comme un dopant potentiellement attractif : ils ont observé que la substitution de Co par Al conduit à potentiel moyen de cellule de Li plus élevée mais souffre d'une capacité inférieure à la première charge jusqu'à 4.4 V par rapport au couple Li^+/Li. Les rayons ioniques Al^{3+} et LS-Co^{3+} similaires (0.535 Å contre 0.545 Å) facilitent la substitution tout en maintenant la structure en couches. Selon le rayon ionique des ions Mg^{2+} (0.72 Å) par rapport à Li^+ (0.76 Å) et Co^{3+} (0.545 Å), plusieurs hypothèses structurales ont été faites dans la littérature.

Dans ces travaux antérieurs, les auteurs supposent que l'élément dopant est distribué et substitué de manière homogène dans les sites de Co. L'effet du dopage à l'aluminium ou au magnésium avec des faibles quantités (telles que 2% et 4%) n'a pas encore été beaucoup étudié, en particulier dans la région des hautes tensions. La détection du dopant pour une très faible teneur en Al ou Mg serait difficile en raison de la faible résolution des techniques de caractérisation conventionnelles par rapport au cas de quantités plus importantes du dopant. Les objectifs de cette thèse sont d'étudier l'effet de la variation du rapport Li/M pour les matériaux $LiCoO_2$ dopés à l'Al ou au Mg : en caractérisant finement à la fois la répartition Al ou Mg et les mécanismes de désintercalation dans un échantillon $LiCoO_2$ dopé à l'Al ou au Mg à faible concentration de dopage pour des applications industrielles (2 ou 4 %).

Le contenu de ce travail de thèse s'articule principalement autour de 2 parties : La partie A est dédiée à la compréhension de l'effet réel du dopage par Al avec des stoichiometries

Li/M(M=Co+Al) bien contrôlées dans l'amélioration des propriétés électrochimiques et composée de deux chapitres. Dans la partie B, nous avons réalisé une étude approfondie des propriétés structurales et électrochimiques des phases $LiCoO_2$ dopées à 2% du Mg en fonction du rapport Li/M nominal introduit lors de la préparation des échantillons.

Comprendre le rôle du dopage d'Al en fonction du rapport Li/M (M=Co+Al) dans l'amélioration des propriétés électrochimiques

Dans une première partie, l'étude est consacrée à comprendre l'effet réel d'un dopage à 2% d'Al avec des stoichiometries Li/M(M=Co+Al) bien contrôlées. Par conséquent, des matériaux "$Li_xCo_{0.98}Al_{0.02}O_2$" (x = 0.98, 1.00 et 1.02) ont été synthétisés et caractérisés à différentes échelles afin de mettre en évidence l'homogénéité de la distribution de l'aluminium dans ces matériaux.

Une série des matériaux $LiCoO_2$ dopés à 2 % d'Al a été synthétisée par une voie solide au centre de R&D d'Umicore. Les précurseurs Li_2CO_3 et Co_3O_4 ont été initialement mélangés avec Al_2O_3 et traités thermiquement à 1050°C pendant 12h pour former les poudres de $LiCoO_2$ dopées avec Li/M et Li/M =0.98, 1.00 ou 1.02. Par la suite, un broyage et un recuit à 800 °C pendant 5 heures ont été effectués afin d'assurer une bonne homogénéité des matériaux. La compréhension de la distribution d'Al au sein de ces poudres de $LiCoO_2$ dopées à l'Al a été obtenue grâce à l'utilisation combinée de la diffraction des rayons X (DRX) synchrotron avec la résonance magnétique nucléaire (RMN) d'^{27}Al et de ^{59}Co. De plus, la RMN du ^{7}Li s'est révélée être une technique clé lorsqu'il s'agit de discuter de la stœchiométrie de Li appropriée, et la présence d'un excès de Li dans la structure pour former des phases surlithiées ne peut être certifiée que par leurs spectres RMN, car la différence est dans l'échelle locale et ne peut pas être détecté par XRD.

Des analyses par microscopie électronique à balayage ont permis de montrer que les poudres présentent des particules de forme sphérique et la taille des particules augmente avec le rapport nominal Li/M en raison du rôle de flux joué par Li_2CO_3. Les divers matériaux de départ cristallisent dans le système trigonal (R-3m) caractéristique de la structure lamellaire de $LiCoO_2$

haute température. Des matériaux monophasés sont obtenus sauf dans le cas de la composition Li/M= 0.98 où quantité de Co_3O_4 est visible sur le diffractogramme X. Des informations concernant l'homogénéité du dopage peuvent être tiré à partir de la DRX synchrotron. En effet, si une composition de gradient d'Al existe dans l'échantillon, cela conduit à une distribution des paramètres de maille entraînant un certain élargissement asymétrique. Parmi les différents matériaux dopés à l'Al, celui préparé avec un rapport Li/M =0.98 présente une certaine asymétrie vers des angles plus petits pour le pic (018), et vers des angles plus élevés pour celui (110). Ceci suggère que ce composé présente une distribution inhomogène d'Al avec des domaines contenant plus de 2% d'Al et des domaines contenant moins de 2% avec un gradient de composition. Les autres échantillons dopés présentent des raies de diffraction symétriques indiquant une bonne homogénéité de répartition des cations Al/Co.

La combinaison des mesures magnétiques, DRX synchrotron et RMN MAS de ^{7}Li, ^{27}Al et ^{59}Co, conduit aux conclusions suivantes :

- L'échantillon préparé avec Li/M = 0.98 est biphasé : il est constitué d'un matériau dopé à l'Al non homogène avec une teneur moyenne en Al légèrement supérieure à 2 % ($LiCo_{0.98-\varepsilon}Al_{0.02+\varepsilon}O_2$) et Co_3O_4.
- L'échantillon préparé avec Li/M=1.00 est le matériau dopé à l'Al le plus homogène de la série correspondant à une seule phase $LiCo_{0.98}Al_{0.02}O_2$ avec uniquement des ions LS-Co^{3+}.
- L'échantillon préparé avec Li/M=1.02 consiste à une phase $Li_{\sim 1.02}[Co_{\sim 0.98}Al_{\sim 0.02}]_{\sim 0.98}O_{\sim 1.98}$ avec une quantité ε de domaines de type α-$LiAlO_2$ que l'on pense être situés à la surface des particules, cela a légèrement abaissé la quantité d'excès de Li et d'Al dans le matériau dopé. Le matériau $Li_{\sim 1.02}[Co_{\sim 0.98}Al_{\sim 0.02}]_{\sim 0.98}O_{\sim 1.98}$ présente une répartition assez homogène d'Al, bien qu'autour des ions Li en excès dans le feuillet de métal de transition, il semble plus favorable d'avoir soit deux ions Co^{3+} en spin intermédiaire (IS-Co^{3+}) soit deux ions Al^{3+} en pyramides à base carrée (et non un IS-Co^{3+} et un Al^{3+}).

Les tests électrochimiques ont clairement montré que le rapport Li/M initial influence les propriétés électrochimiques même avec la même quantité d'aluminium, et il a été démontré à partir de ces résultats que la contribution possible de l'excès de Li conduit à l'augmentation des pertes de capacité. Cependant, de bonnes rétentions de capacité ont été obtenues pour des échantillons avec Li/M ≤1.00 jusqu'à 4.6V.

Le deuxième chapitre de cette partie a été consacrée à l'étude détaillée de $LiCoO_2$ dopé à 4 % d'Al. Nous avons choisi d'étudier un matériau avec une plus grande quantité de dopant (4% d'Al) pour mieux visualiser l'effet du dopant dans les différents phénomènes à bas et haut potentiel. $LiCo_{0.96}Al_{0.04}O_2$ a été synthétisé par voie solide à partir d'un mélange des précurseurs Al_2O_3, Co_3O_4 et Li_2CO_3. La synthèse consiste d'abord à préparer un matériau avec excès de Li et ensuite procédé au réajustement du Li par ajout de Co_3O_4. Les études ^{27}Al MAS RMN et DRX ont révélé que le dopage en Al dans ce matériau est homogène tandis que la RMN ^{7}Li MAS indique que sa stœchiométrie (Li/M=1.00) est idéale. Notre étude de cyclage électrochimique dans les cellules Li révèle que même une faible quantité substituée de Co par Al (4 %) a un effet profond sur les performances électrochimiques et donne une meilleure stabilité de cyclage dans la plage de tension de 3 à 4.6 V.

Afin d'avoir un aperçu général des mécanismes impliqués lors de la désintercalation du Li, des études par DRX et RMN ont été réalisées sur des échantillons désintercalés soit en fixant le teneur en Li soit en fixant le potentiel de coupure. Les études DRX et RMN MAS de ^{7}Li ont révélé que jusqu'à 4.5 V par rapport au couple Li^+/Li, l'évolution structurelle globale des phases $LiCo_{0.96}Al_{0.04}O_2$ et $LiCoO_2$ stœchiométrique (st $LiCoO_2$) est similaire, bien que i) la transition isolant-métal ne se produise pas dans la même gamme de composition et ii) la distorsion monoclinique à x = 0.5 est supprimé par le dopage à l'Al. À des tensions plus élevées (> 4.6 V par rapport au couple Li^+/ Li), des différences structurelles notables ont été mises en évidence dans les matériaux désintercalés $Li_xCo_{0.96}Al_{0.04}O_2$ et Li_xCoO_2 et peuvent être responsables de la stabilité de cyclage améliorée de $LiCoO_2$ dopé à l'Al. L'étude par DRX a montré que les phases désintercalés préparées pour x < 0.2 à partir de st-$LiCoO_2$, soit en fixant de la teneur en Li, soit par une méthode flottante, présentent la coexistence de plusieurs phases (O3, H1-3, O1 et des phases à intermédiaires espace interfeuillé) avec des défauts d'empilement. Tandis que les échantillons désintercalés

préparés à partir de $LiCo_{0.96}Al_{0.04}O_2$ sont plus cristallins, et la formation de phases avec un espace intermédiaire entre les feuillées n'est pas observée. De plus, à 4.6V, la phase O1 n'est pas observée pour l'échantillon dopé à l'Al.

Plus intéressant, la RMN ^{7}Li MAS a révèlé des environnements locaux de Li très différents dans les phases à haut potentiel. Contrairement à Li_xCoO_2, pour les phases dopées à l'Al, des signaux attribués à Li dans des environnements de type spinelle et dans une couche CEI (Cathode Electrolyte Interphase) diamagnétique sont observés en plus du signal correspondant à Li dans l'espace interfeuillé des structures O3/H1-3. Ces observations ne dépendent pas de la préparation des matériaux (en fixant la teneur en Li ou le potentiel flottant). La phase spinelle est toujours détectée après quelques cycles en phase $LiCo_{0.96}Al_{0.04}O_2$ déchargée et l'étude par microscopie électronique à transmission a révélé qu'elle se situe à la surface des particules. Étant donné que seuls des signaux de Li dans l'espace interfeuillé de la structure O3 ou H1-3 ont été observés pour Li_xCoO_2, nous pensons que le CEI formé sur ce matériau a une nature différente et est instable (soit dissous après le désassemblage de la cellule, soit par le lavage des électrodes étape préalable aux mesures). La réactivité différente de la surface de $LiCoO_2$ et $LiCoO_2$ dopé à l'Al a déjà été rapportée dans la littérature : le caractère basique de la surface $LiCo_{1-x}Al_xO_2$ rend ces matériaux moins réactifs que $LiCoO_2$ vis-à-vis des espèces acides (telles que HF) qui sont présents dans les électrolytes à base de $LiPF_6$. La forte polarisation observée au début de la décharge de 5V dans le système st-$LiCoO_2$ pourrait donc résulter i) du caractère de haute résistivité de ce CEI à haute tension qui peut se dissoudre ensuite tout en déchargeant comme instable ; ii) la formation de la phase H1-3 ou O1 à la surface des particules avec un faible espace entre les feuillets qui peut également empêcher une bonne diffusivité des ions Li^+ vers les particules.

Sur la base de notre étude, nous pensons que le dopage par Al améliore les performances de cyclage du $LiCoO_2$ jusqu'à 4.6 V, principalement en modifiant l'évolution de la surface des particules lors du cyclage à haute tension. Même lors de la première charge, il conduit à la formation d'une reconstruction de surface avec formation d'une phase de type spinelle lithiée qui doit avoir une bonne conductivité ionique. Dans le cas de $LiCoO_2$, où la formation d'une phase spinelle a également été signalée, n'est pas lithiée car non détectée par RMN MAS de ^{7}Li ou formée uniquement lors d'un cycle prolongé. La phase spinelle lithiée formée sur le composé dopé à l'Al,

peut alors réagir différemment avec l'électrolyte pour former une couche CEI stable, dont la composition est différente de celle formée sur Li_xCoO_2. La formation de la phase spinelle contenant du Li et un CEI stable à la surface des particules expliquent probablement aussi la forte réduction de la dissolution du Co observée à haut potentiel.

Comparaison du rôle du dopant dans les différents matériaux $LiCoO_2$ dopés au Mg en fonction du rapport Li/M (M=Co+Mg)

Cette partie est consacrée à la compréhension de l'effet du dopage au Mg sur des échantillons avec des stoichiometries Li/M (M=Co+Mg) bien contrôlées. Selon le rayon ionique des ions Mg^{2+} plusieurs hypothèses quant à localisation du magnésium dans la structure peuvent être envisagées. Si le Mg^{2+} substitut le Co^{3+}, cela devrait conduire à la formation d'ions Co^{4+} pour la compensation de charge ou éventuellement à IS-Co^{3+} si des lacunes d'oxygène se forment comme cela a été montré par Levasseur et al.[11] Ç'était rapporté que cette substitution augment la conductivité électronique.[12] Si les ions Mg^{2+} substituent à la fois les ions Li^+ et Co^{3+}, cela conduit que le Co reste 3+ et aucune lacune d'oxygène n'est nécessaire pour la compensation de charge. En fin, la substitution du Mg^{2+} au Li^+ dans la couche de lithium devrait conduire à la formation d'ions Co^{2+}.

Dans un premier temps, des matériaux $LiCoO_2$ dopés à 2% du Mg préparés par réaction à l'état solide avec différents rapports Li/M (0.96, 0.98 et 1.00) ont été étudiés. Notre étude permet de séparer les effets relatifs du dopage au Li et des différentes stoichiometries dans le lithium en se basant sur la combinaison de techniques de caractérisation telles que l'ICP, la DRX synchrotron, MEB, les mesures magnétiques et la RMN MAS de ^{7}Li et ^{59}Co. Ces matériaux ont été synthétisé en suivant le même protocole expérimental utilisé pour la préparation des matériaux dopés à 2% d'Al. Les divers matériaux de départ cristallisent dans le système trigonal (R-3m) caractéristique de la structure lamellaire de $LiCoO_2$ synthétisé à haute température. Seule le matériau avec Li/M=1.00 est pur, alors que les échantillons préparés avec Li/M≤0.98 sont monophasé où quantité de MgO est visible sur les diffractogrammes X. Aucune asymétrie prononcée n'a été observée

agissant, par conséquent, comme une première preuve de la bonne homogénéité de la distribution de Mg dans les phases O3.

Les résultats de la RMN MAS de ^{7}Li des matériaux dopés Mg avec différents Li/M ont montré que :

- L'échantillon avec Li/M = 0.96 présente un signal étroit proche de 0 ppm similaire au st-$LiCoO_2$. Comme aucun élargissement du signal n'a été détecté, cela tend à montrer qu'aucune ou une très faible quantité de Mg n'est incorporée dans la structure.
- Pour l'échantillon avec Li/M=0.98, en plus du signal à 0 ppm, de petits signaux supplémentaires sont observés à 2.4, -3.9 et 60 ppm. On peut considérer que ce matériau est diamagnétique en première approximation avec une quantité négligeable d'ions paramagnétiques conduisant à ces signaux décalés par contact de Fermi.
- Pour la phase dopée Li/M=1.00, le spectre RMN a montré, qu'en plus du signal diamagnétique à 0 ppm, plusieurs nouveaux signaux à 289, 60, 5.7, 2.4, -3.9, -8.4, -18 et -24.7 ppm. Ces caractéristiques prouvent clairement que le matériau est paramagnétique. Il est à noter que certains de ces signaux décalés sont différents de ceux observés dans le $LiCoO_2$ surlithié. Ils sont également différents de ceux observés dans la littérature pour les phases dopées au Mg. Selon la forte différence avec les spectres RMN MAS de'^{7}Li de la phase surlithiée, nous pensons cependant que la configuration électronique locale dans l'échantillon dopé au Mg avec Li/M =1.00 est différente. Tous les signaux observés pourraient résulter de la formation d'ions Co^{4+}, bien qu'une attribution complète des signaux n'ait pas pu être proposée ici. La présence d'ions Co^{4+} dans l'échantillon dopé au Mg avec Li/M =1.00 expliquerait la forte augmentation de la conductivité observée pour de tels matériaux dans la littérature.

Sur la base de nos études DRX synchrotron, RMN MAS de l'^{7}Li, ^{59}Co et des propriétés magnétiques, nous avons conclu que : le matériau avec Li/M=0.96 consiste en un mélange de deux

phases : $LiCoO_2$ dopé ε au Mg et MgO contenant des ions Co. Le matériau avec Li/M=0.98 est un $LiCoO_2$ dopé au Mg avec principalement des ions LS-Co^{3+} avec une coexistence de Mg dans les couches de Li et de Co : $[Li_{0.99}Mg_{0.01}]_{Li}$ $[Co^{3+}{}_{0.99}\ Mg_{0.01}]CoO_2$ et des traces de MgO. Enfin, l'échantillon préparé avec Li/M=1.00 est une seule phase dopée au Mg dont la formule peut s'écrire comme suit $[Li_{1.00}]_{Li}[Co^{3+}{}_{0.96}Co^{4+}{}_{0.02}Mg_{0.02}]_{Co}O_2$.

La mise en évidence de l'effet du dopage au Mg pour une très faible teneur en Mg (2%) dans $LiCoO_2$ est plus difficile que dans le cas de plus grandes quantités de Mg. On pourrait supposer que les effets rapportés pour le dopage au Mg concernant ses propriétés électrochimiques, sont fortement dépendants de la distribution de Mg au sein de $LiCoO_2$ liée au rapport Li/M. Une série de $LiCoO_2$ dopé à 2% Mg avec un rapport Li/M bien contrôlé ont été étudiées à partir de tests électrochimiques. Il a été confirmé que même avec la même quantité de dopage, le rapport Li/M influence les propriétés électrochimiques. Le matériau préparé avec Li/M = 1.00 présente la polarisation et les pertes de capacité irréversibles les plus élevés ; cet effet a déjà été observé pour le matériau non dopé avec un Li/Co initial plus grand dans une étude précédente. Nous avons également montré que le rapport initiale Li/M impacte les changements structurels associés à l'intercalation du Li (plateau de potentiel, transition O3-H1-3). Alors qu'aucun rôle bénéfique du dopage au Mg sur la rétention de capacité n'a été observé sauf pour le matériau préparé avec Li/M=0.96 qui contient du MgO en surface.

Afin de mieux comprendre le rôle du dopage au Mg sur les mécanismes mis en jeu lors du cyclage, plusieurs phases du matériau avec Li/M=0.98 et 1.00 ont été préparées par désintercalation électrochimique et étudiées par DRX et RMN MAS de ^7Li. Ces deux matériaux ont été choisis car nous avons montré la substitution réussie du Mg pour Li/M≥0.98. Sur la base de la RMN MAS, il a été clairement observé l'apparition des environnements similaires que ceux détecté dans le cas du matériau dopé à 4% d'Al. Des signaux attribués au Li dans des environnements de type spinelle et dans la couche CEI diamagnétique sont observés en plus de celui de Li dans l'espace interfeuillet de la structure O3 ou H1-3. La comparaison des matériaux Li/M=0.98 et Li/M=1.00 a mis en évidence le rôle du rapport Li/M sur le cyclage. Le fait de maintenir le voltage à haut potentiel a montré un comportement prononcé pour Li/M=0.98. En effet, après cyclage, les environnements de type spinelle sont maintenus. Toutes ces caractéristiques peuvent jouer un rôle favorable dans

le comportement électrochimique à haut potentiel. Des travaux supplémentaires seront nécessaires pour le confirmer. Aussi, l'étude du matériau Li/M = 0.96 électrochimiquement désintercalé qui n'a pu être faite dans le cadre de cette thèse, serait intéressante pour comprendre le rôle de MgO à la surface des particules sur la formation de la SEI.

(1) Mizushima, K.; Jones, P. C.; Wiseman, P. J.; Goodenough, J. B. Li_xCoO_2 (0. *Mater. Res. Bull.* **1980**, *15* (6), 783–789. https://doi.org/10.1016/0025-5408(80)90012-4.

(2) Wang, L.; Chen, B.; Ma, J.; Cui, G.; Chen, L. Reviving Lithium Cobalt Oxide-Based Lithium Secondary Batteries-toward a Higher Energy Density. *Chem. Soc. Rev.* **2018**, *47* (17), 6505–6602. https://doi.org/10.1039/C8CS00322J.

(3) Delmas, C.; Fouassier, C.; Hagenmuller, P. Structural Classification and Properties of the Layered Oxides. *Phys. BC* **1980**, *99* (1), 81–85. https://doi.org/10.1016/0378-4363(80)90214-4.

(4) Ven, A. V. der; Aydinol, M. K.; Ceder, G. First-Principles Evidence for Stage Ordering in $LiCoO_2$. *J. Electrochem. Soc.* **1998**, *145* (6), 2149. https://doi.org/10.1149/1.1838610.

(5) Van der Ven, A.; Aydinol, M. K.; Ceder, G.; Kresse, G.; Hafner, J. First-Principles Investigation of Phase Stability in $LiCoO_2$. *Phys. Rev. B* **1998**, *58* (6), 2975–2987. https://doi.org/10.1103/PhysRevB.58.2975.

(6) Reimers, J. N.; Dahn, J. R. Electrochemical and in Situ X-Ray Diffraction Studies of Lithium Intercalation in Li_xCoO_2. *J. Electrochem. Soc.* **1992**, *139* (8), 2091–2097.

(7) Ohzuku, T.; Ueda, A. Solid-State Redox Reactions of $LiCoO_2$ (R3m) for 4 Volt Secondary Lithium Cells. *J. Electrochem. Soc.* **1994**, *141* (11), 2972–2977.

(8) Ménétrier, M.; Saadoune, I.; Levasseur, S.; Delmas, C. The Insulator-Metal Transition upon Lithium Deintercalation from $LiCoO_2$: Electronic Properties and ^7Li NMR Study. *J. Mater. Chem.* **1999**, *9* (5), 1135–1140.

(9) Ménétrier, M.; Carlier, D.; Blangero, M.; Delmas, C. On "Really" Stoichiometric $LiCoO_2$. *Electrochem. Solid-State Lett.* **2008**, *11* (11), A179. https://doi.org/10.1149/1.2968953.

(10) Shao-Horn, Y.; Levasseur, S.; Weill, F.; Delmas, C. Probing Lithium and Vacancy Ordering in O3 Layered Li_xCoO_2 ($x \approx 0.5$). *J. Electrochem. Soc.* **2003**, *150* (3), A366. https://doi.org/10.1149/1.1553787.

(11) Levasseur, S.; Ménétrier, M.; Delmas, C. On the $Li_xCo_{1-y}Mg_yO_2$ System upon Deintercalation: Electrochemical, Electronic Properties and ^7Li MAS NMR Studies. *J. Power Sources* **2002**, *112* (2), 419–427. https://doi.org/10.1016/S0378-7753(02)00456-1.

(12) Tukamoto, H.; West, A. R. Electronic Conductivity of $LiCoO_2$ and Its Enhancement by Magnesium Doping. *J. Electrochem. Soc.* **1997**, *144* (9), 3164–3168.

Table of contents

General introduction 16

References 18

Generalities 23

1. Lithium ion batteries 23
 1.1. The working principle of a Li ion battery 26
2. $LiCoO_2$ as a positive electrode for Lithium-ion batteries 31
 2.1. Description of $LiCoO_2$ structure 31
 2.2. Phases transitions upon lithium deintercalation of $LiCoO_2$ 32
 2.3. Capacity and voltage fading of $LiCoO_2$ occurring during high voltage cycling 34
  2.3.1. Delithiation induced phase transitions 36
  2.3.2. Interfacial degradation at electrode/electrolyte surface 42
3. Overstoichiometric $LiCoO_2$ 44
4. Nuclear magnetic resonance 47
 4.1. Electronic structure 48
 4.2. Hyperfine interactions 50
  4.2.1. Fermi Contact interaction 51
  4.2.2. Knight shift 52
  4.2.3. Dipolar interaction 53
  4.2.4. Quadrupolar interaction 54
References 57

A. Understanding the role of Al doping as a function of the ratio Li/M (M=Co+Al) in the improvement of the electrochemical properties 65

A.1. Introduction 65
A.2. Experimental details and technical background 66

A.3. Study of the 2% Al doped $LiCoO_2$ materials as a function of the Li/M ratio (M=Co+Al) 69
A.3.1. Preparation of Al doped $LiCoO_2$ samples from solid state reaction 69
A.3.2. Structural characterization of the starting materials 70
a) ^{7}Li MAS NMR 75
b) ^{27}Al MAS NMR 77
c) ^{59}Co MAS NMR 82
A.3.3. Influence of Li/M ratio on the electrochemical performance 85
A.3.4. Conclusion on the 2% Al doped $LiCoO_2$ with various Li/M ratio 88
A.4. Understanding the role of Al doping of $LiCoO_2$ on the mechanisms upon cycling up to 4.8V vs. Li^+/Li 90
A.4.1. Preparation of the 4% Al-doped $LiCoO_2$ 90
A.4.2. Structural properties of pristine st-$LiCoO_2$ and $LiCo_{0.96}Al_{0.04}O_2$ materials 91
A.4.3. Electrochemical properties and general overview 95
A.4.4. Detailed study in the low and high voltage regions 103
a) Sample prepared by fixing the Li amount 105
b) Samples prepared with floating voltages 107
c) Structural characterization after cycling at high voltage (3-cycles) 110
A.4.5. Discussion and Conclusion 115
References 117

B. Comparison of the dopant role in the different Mg doped $LiCoO_2$ material as a function of the ratio Li/M (M=Co+Mg) 125

B.1. General introduction 125
B.2. Structural characterization of the starting materials 126
B.2.1. Introduction 126
B.2.2. Syntheses of Mg doped $LiCoO_2$ 127
B.2.3. Study of the morphology 128
B.2.4. Study of the average structure by XRD 129
B.2.5. Study of the local structure by ^{7}Li and ^{59}Co MAS NMR 133
B.2.6. Study of magnetic properties 138

B.2.7. General discussion 140
B.2.8. Conclusion on chapter B.2 145
B.3. Evaluation of the electrochemical performances for the 2%Mg doped materials 147
B.3.1. Cycling experiments with various upper cutoff voltages 148
B.3.2. GITT in the low voltage region 151
B.4. Study of the mechanisms occurring during Li deintercalation for the 2% Mg doped $LiCoO_2$ samples with $Li/M \geq 0.98$ up to 4.8 V vs Li^+/Li 155
B.4.1. Study of the average structure by XRD 157
B.4.2. Study of the local structure by ^7Li MAS NMR 159
B.4.3. Structural characterization after cycling at high voltage for Li/M=0.98 162
B.5. Conclusion for chapter B.3 and B.4 166
References 167

General conclusion 170

General introduction

O3-$LiCoO_2$ was first proposed as positive electrode material for lithium-ion batteries (LIBs) by Goodenough et al. in1980.[1] It is still widely used positive electrode material in commercialized LIBs due to relatively easy synthesis, a relatively large theoretical specific capacity as high as 274 mAh/g and electrode density close to 4.0 g/cm^3 resulting in high practicable energy density and excellent cycle stability.[2] Layered $LiCoO_2$ synthesized at high temperature exhibits the α-$NaFeO_2$ type structure (R-3m space group with $a_{hex.}$ = 2.816 Å; $c_{hex.}$= 14.052 Å) with an O3 stacking.[3,4] Considerable efforts have been carried out to understand the structural changes occurring during electrochemical cycling by X-Ray diffraction and first principles calculations many years ago.[3,5,6] When the cell is cycled up to 4.2 V vs Li^+/Li, the deintercalation reaction is highly reversible, giving rise to batteries with excellent cyclability with a specific capacity of 137 mAh/g vs Li^+/Li. In order to achieve a higher capacity and increase the energy density, cycling voltage above 4.3 V vs Li^+/Li is required. However, working at high voltage leads to a deterioration of the cycling performances,[7] caused by structural instabilities, electrolyte oxidation and Co dissolution.[8–13] Several strategies were investigated to improve the cycling stability of $LiCoO_2$.[14–16] Among these, metal substitutions for cobalt (Al, Mg, Ti…) have been demonstrated to be a promising and effective method to enhance the electrochemical performances of $LiCoO_2$ at high voltage.[2,17–20] Aluminum Al^{3+} or magnesium Mg^{2+} ions as dopants were among the first considered. In these previous works, the authors speculate that dopant element is homogeneously distributed and substituted Co sites. The aims of this PhD is to study the effect of varying the Li/M ratio for Al or Mg doped $LiCoO_2$ materials: with characterizing both the Al or Mg repartition and the deintercalation mechanisms in an Al or Mg doped-$LiCoO_2$ sample with a low concentration doping at a level of industrial relevance (2 or 4%).

The content of this PhD work mainly focuses on 2 parts:

-The Part A is dedicated to understand the real effect of Al doping with well controlled Li/M(M=Co+Al) stoichiometries in the improvement of the electrochemical properties and composed of two chapters. First a study was conducted on the effects of 2% Al combining

synchrotron XRD and ^{7}Li, ^{59}Co, and ^{27}Al MAS NMR to probe different scales in order to evidence the homogeneity of aluminum distribution in the prepared materials with different Li/M ratio. Then, in the second chapter we investigated the role of Al in the most homogeneously doped $LiCo_{0.96}Al_{0.04}O_2$ material on the mechanisms involved during cycling at high voltage.

-In Part B, we carried out an in-depth study of the structural and electrochemical properties of the 2% Mg doped $LiCoO_2$ phases as a function of the nominal Li/M ratio introduced during the preparation. This part is composed of 3 chapters: in the first one, our efforts were dedicated to accurately explore the effect of Mg^{2+} distribution on the average and local structure and electronic structure. The second chapter focuses on the understanding of the role of Mg as a dopant on the electrochemical performances. In the last chapter, we were particularly interested in the influence of the initial Li/M ratio of the Mg doped materials on the phase transitions occurring at high voltage. Therefore, an ex situ X-ray diffraction and ^{7}Li MAS NMR characterizations were conducted on de-intercalated phases in order to study in more detail the structural and electronic changes occurring during cycling.

-The main results, some open questions and perspectives will be given in the conclusion.

References

(1) Mizushima, K.; Jones, P. C.; Wiseman, P. J.; Goodenough, J. B. Li_xCoO_2 (0. *Mater. Res. Bull.* **1980**, *15* (6), 783–789. https://doi.org/10.1016/0025-5408(80)90012-4.

(2) Wang, L.; Chen, B.; Ma, J.; Cui, G.; Chen, L. Reviving Lithium Cobalt Oxide-Based Lithium Secondary Batteries-toward a Higher Energy Density. *Chem. Soc. Rev.* **2018**, *47* (17), 6505–6602. https://doi.org/10.1039/C8CS00322J.

(3) Reimers, J. N.; Dahn, J. R. Electrochemical and in Situ X-Ray Diffraction Studies of Lithium Intercalation in Li_xCoO_2. *J. Electrochem. Soc.* **1992**, *139* (8), 2091–2097.

(4) Ohzuku, T.; Ueda, A. Solid-State Redox Reactions of $LiCoO_2$ (R3m) for 4 Volt Secondary Lithium Cells. *J. Electrochem. Soc.* **1994**, *141* (11), 2972–2977.

(5) Ven, A. V. der; Aydinol, M. K.; Ceder, G. First-Principles Evidence for Stage Ordering in Li_xCoO_2. *J. Electrochem. Soc.* **1998**, *145* (6), 2149. https://doi.org/10.1149/1.1838610.

(6) Van der Ven, A.; Aydinol, M. K.; Ceder, G.; Kresse, G.; Hafner, J. First-Principles Investigation of Phase Stability in $Li_{1-x}CoO_2$. *Phys. Rev. B* **1998**, *58* (6), 2975–2987. https://doi.org/10.1103/PhysRevB.58.2975.

(7) Yano, A.; Shikano, M.; Ueda, A.; Sakaebe, H.; Ogumi, Z. $LiCoO_2$ Degradation Behavior in the High-Voltage Phase Transition Region and Improved Reversibility with Surface Coating. *J. Electrochem. Soc.* **2017**, *164* (1), A6116–A6122.

(8) Yazami, R.; Ozawa, Y.; Gabrisch, H.; Fultz, B. Mechanism of Electrochemical Performance Decay in $LiCoO_2$ Aged at High Voltage. *Electrochimica Acta* **2004**, *50* (2–3), 385–390. https://doi.org/10.1016/j.electacta.2004.03.048.

(9) Xia, H.; Lu, L.; Meng, Y. S.; Ceder, G. Phase Transitions and High-Voltage Electrochemical Behavior of $LiCoO_2$ Thin Films Grown by Pulsed Laser Deposition. *J. Electrochem. Soc.* **2007**, *154* (4), A337. https://doi.org/10.1149/1.2509021.

(10) Takamatsu, D.; Koyama, Y.; Orikasa, Y.; Mori, S.; Nakatsutsumi, T.; Hirano, T.; Tanida, H.; Arai, H.; Uchimoto, Y.; Ogumi, Z. First In Situ Observation of the $LiCoO_2$ Electrode/Electrolyte Interface by Total-Reflection X-Ray Absorption Spectroscopy.

Angew. Chem. Int. Ed. **2012**, *51* (46), 11597–11601. https://doi.org/10.1002/anie.201203910.

(11) Pender, J. P.; Jha, G.; Youn, D. H.; Ziegler, J. M.; Andoni, I.; Choi, E. J.; Heller, A.; Dunn, B. S.; Weiss, P. S.; Penner, R. M.; Mullins, C. B. Electrode Degradation in Lithium-Ion Batteries. *ACS Nano* **2020**, *14* (2), 1243–1295. https://doi.org/10.1021/acsnano.9b04365.

(12) Birkl, C. R.; Roberts, M. R.; McTurk, E.; Bruce, P. G.; Howey, D. A. Degradation Diagnostics for Lithium Ion Cells. *J. Power Sources* **2017**, *341*, 373–386. https://doi.org/10.1016/j.jpowsour.2016.12.011.

(13) Amatucci, G. G.; Tarascon, J. M.; Klein, L. C. Cobalt Dissolution in $LiCoO_2$-Based Non-Aqueous Rechargeable Batteries. *Solid State Ion.* **1996**, *83* (1), 167–173. https://doi.org/10.1016/0167-2738(95)00231-6.

(14) Hu, G.; Cao, J.; Peng, Z.; Cao, Y.; Du, K. Enhanced High-Voltage Properties of $LiCoO_2$ Coated with $Li[Li_{0.2}Mn_{0.6}Ni_{0.2}]O_2$. *Electrochimica Acta* **2014**, *149*, 49–55. https://doi.org/10.1016/j.electacta.2014.10.072.

(15) Gu, R.; Cheng, T.; Ma, Z.; Qian, R.; Lyu, Y.; Nie, A.; Guo, B. Enhanced Cycling Stability of High Voltage $LiCoO_2$ by Surface Phosphorylation. *J. Alloys Compd.* **2019**, *803*, 348–353. https://doi.org/10.1016/j.jallcom.2019.06.253.

(16) Cho, J.; Kim, C.-S.; Yoo, S.-I. Improvement of Structural Stability of $LiCoO_2$ Cathode during Electrochemical Cycling by Sol-Gel Coating of SnO2. *Electrochem. Solid-State Lett.* **2000**, *3* (8), 362–365.

(17) Zhang, J.-N.; Li, Q.; Ouyang, C.; Yu, X.; Ge, M.; Huang, X.; Hu, E.; Ma, C.; Li, S.; Xiao, R.; Yang, W.; Chu, Y.; Liu, Y.; Yu, H.; Yang, X.-Q.; Huang, X.; Chen, L.; Li, H. Trace Doping of Multiple Elements Enables Stable Battery Cycling of $LiCoO_2$ at 4.6 V. *Nat. Energy* **2019**, *4* (7), 594–603. https://doi.org/10.1038/s41560-019-0409-z.

(18) Liu, Q.; Su, X.; Lei, D.; Qin, Y.; Wen, J.; Guo, F.; Wu, Y. A.; Rong, Y.; Kou, R.; Xiao, X.; Aguesse, F.; Bareño, J.; Ren, Y.; Lu, W.; Li, Y. Approaching the Capacity Limit of Lithium Cobalt Oxide in Lithium Ion Batteries via Lanthanum and Aluminium Doping. *Nat. Energy* **2018**, *3* (11), 936–943. https://doi.org/10.1038/s41560-018-0180-6.

(19) zhao, ruirui; Zhang, J.; Lee, G.-H.; Zhang, K.; Lau, V. W.; Lee, J.-J.; Moudrakovski, I.; Yang, Y.-L.; Zhou, F.; Park, M.; Hung, I.-M.; Kang, Y. The Origin of Heavy Elemental Doping to Relieve the Lattice Thermal Vibration of Layered Materials for High Energy Density Li Ion Cathodes. *J. Mater. Chem. A* **2020**. https://doi.org/10.1039/D0TA03979A.

(20) Levasseur, S.; Ménétrier, M.; Delmas, C. Combined Effects of Ni and Li Doping on the Phase Transitions in Li_xCoO_2 Electrochemical and ^7Li Nuclear Magnetic Resonance Studies. *J. Electrochem. Soc.* **2002**, *149* (12), A1533–A1540. https://doi.org/10.1149/1.1516219.

Generalities

Generalities..... 23

1. Lithium ion batteries..... 23

1.1. The working principle of a Li ion battery..... 26

2. $LiCoO_2$ as a positive electrode for Lithium-ion batteries..... 31

2.1. Description of $LiCoO_2$ structure..... 31

2.2. Phases transitions upon lithium deintercalation of $LiCoO_2$..... 32

2.3. Capacity and voltage fading of $LiCoO_2$ occurring during high voltage cycling..... 34

2.3.1. Delithiation induced phase transitions..... 36

2.3.2. Interfacial degradation at electrode/electrolyte surface..... 42

3. Overstoichiometric $LiCoO_2$..... 44

4. Nuclear magnetic resonance..... 47

4.1. Electronic structure..... 48

4.2. Hyperfine interactions..... 50

4.2.1. Fermi Contact interaction..... 51

4.2.2. Knight shift..... 52

4.2.3. Dipolar interaction..... 53

4.2.4. Quadrupolar interaction..... 54

References..... 57

Generalities

1. Lithium ion batteries

Global energy consumption has been growing significantly for recent years. To meet this energy demand, global energy production relies mainly on fossil resources such as coal or oil. Unfortunately, the consumption of these fossil fuels has resulted in increased greenhouse gas emissions which causes global warming. This has led to the realization that society needs to move towards a new way of operating, which is much more economical in its use of non-renewable resources. Therefore, it is essential to find alternative solutions to reduce rapidly CO_2 in atmosphere leading to global warming, while at the same time meeting the needs of daily consumption. In this context, the exploitation of new so-called renewable energies (solar, wind, etc.) is being considered more broadly. These renewable energy sources continued to grow rapidly. Many countries announced their commitment to achieve carbon dioxide emissions to net zero by 2050 with limiting the global temperature rise to 1.5 °C. However, we are long well of what is required to reach net zero emission by 2050. A series of additional measures would be required for such achievement over the next ten years.[1]

Since renewable energy resources are intermittent they should be coupled with an energy storage system. It is therefore necessary to develop new systems capable of reversibly storing the energy produced by these alternative resources for all the mobile devices, including smartphones, laptops and electric cars. One of the possible storage solutions is the use of batteries.

Batteries are electrochemical storage devices allowing to store reversibly energy in the form of chemical energy and use it whenever and wherever it is needed. Nickel-metal hydride (Ni-MH) batteries were the first batteries to be marketed in a hybrid vehicle (Toyota Prius) in late 1997 in Japan. However, as shown in Ragone plot (**Figure 1**), lithium-ion batteries (LiBs) are a system of choice for electric and hybrid vehicle applications. Li-ion technology, whose Nobel Prize in Chemistry was awarded to the three inventors (John Goodenough, Stanley Whittingham and Akira Yoshino) on 9 October 2019, was first commercialized by Sony[2] in 1991, through a battery consisting of a carbon negative electrode, a lithium cobalt oxide ($LiCoO_2$) positive electrode and

an organic liquid electrolyte. This type of battery has a higher operating voltage (~ 3.7 V vs Li^+/Li), as well as a higher gravimetric energy (150 - 250 Wh/kg vs. 50 - 80 Wh/kg for Ni-MH batteries), as shown in the Ragone diagram (**Figure 1**). These batteries have revolutionized electronics. Lithium-ion batteries can store three to four times more energy per unit of mass than conventional batteries, thus ensuring greater autonomy for the general public (computers, mobile phones, etc.).

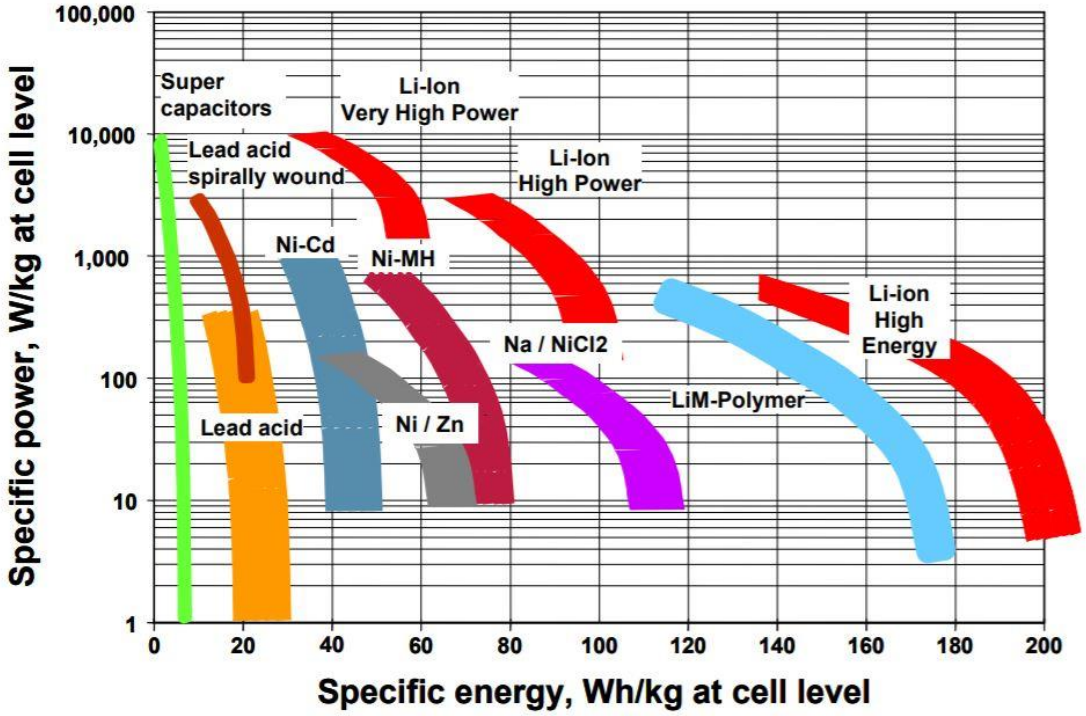

Figure 1. The Ragone plot: Evolution of the specific energy according to the specific power.

With a large number of applications in portable electronics such as mobile phones, laptops and other electronic gadgets and potential applications for automobile purpose, LiBs have gained a lot of attention from researchers worldwide. Described for the first time by Goodenough et al in 1980,[3] $LiCoO_2$ has a layered structure particularly favorable to the insertion and deinsertion of lithium and possesses remarkable electrochemical properties, making it a material of choice. $LiCoO_2$ still holds an absolute advantage over other positive electrode materials and occupies most of the market in the field of portable electronics, because in addition to its ease of preparation it

leads to high potentials between 3 and 4.2 V vs Li^+/Li thanks to the highly oxidizing power of the $Co^{4+/}Co^{3+}$ couple, and it has a theoretical specific capacity as high as 274 mAh/g.

Li deintercalation in $LiCoO_2$ is highly reversible when the cell is cycled up to 4.2 V vs Li^+/Li with a specific capacity of 137 mAh/g vs Li^+/Li. In order to achieve a higher capacity and increase the energy density, cycling voltage above 4.3 V vs Li^+/Li is required. However, working at a high potential leads to a deterioration of the cycling performance,[4] caused by structural instabilities, electrolyte oxidation and Co dissolution.

In order to accommodate the high demand from battery manufacturers all over the world to look for thinner and lighter batteries but with a longer operation time, the battery industry needs higher energy density to extend the service life which means that the $LiCoO_2$ must break through the top limit capacity and cycle several hundred times steadily. A great effort has been made to modify the structural stability of $LiCoO_2$ and the interface stability between $LiCoO_2$ and other inactive components above 4.3 V. Different strategies such as doping with different various metal or coating have significantly improved the performances.

Many compounds are currently being investigated and tested as electrode materials for Li-ion batteries. Although these materials are characterized by X-ray or neutron diffraction, it is necessary to local scale technic in order to improve, among other things, the understanding of their electrochemical behavior: presence of defects, distribution of paramagnetic cations, presence of localized or delocalized electrons, order phenomena...This is why spectroscopic methods for local characterization are useful. Nuclear magnetic resonance (NMR) allows classically (i.e. in diamagnetic materials) to access information on the geometrical environment (of different origin from electron spin). However, almost all active materials for Li-ion batteries are paramagnetic or metallic. It is therefore thanks to the hyperfine interactions (which largely dominate the others and which we will describe in detail below) that local information can be obtained, not only on the local structure but also in the local electronic structure.

As described by Grey et al.[5] NMR tool has been used in the literature for the characterization of different systems used in lithium batteries. It is the lithium nuclei (^7Li and ^6Li) that are typically used as probes because lithium ions are directly involved in the electrochemical process. The

method can thus determine, the new insertion sites during discharge, to follow the oxidation-reduction reactions during battery operation, and finally to know how the local structure evolves during a long cycle.

1.1. The working principle of a Li ion battery

The operation of the cell (**Figure 2**) is based on electrochemical redox reactions that take place at the active materials of the electrodes. In the case of LiBs, operation is also based on a solid-state chemistry reaction, known as an insertion/de-insertion reaction, in which the ions, which have a very small diameter, take place in the host crystal structure of the two electrodes. This intercalation concept was proposed in 1976 by Whittingham for Li//TiS_2 battery.[6] At that time, the use of lithium metal as a negative electrode material made Li-metal batteries inefficient (continuous loss of capacity at the negative electrode with each cycle) and unsafe (formation of dendrites leading to short circuits). In 1980, the concept of a negative electrode of carbon was proposed by R. Yazami et al.[7], they demonstrated a reversible electrochemically intercalating of lithium into graphite using a solid organic electrolyte. Then, Akira Yoshino commissioned the fabrication of a batch of prototype lithium ion cells in 1985 using lithium cobalt oxide ($LiCoO_2$) as a positive electrode and carbonaceous material as negative electrode. In 1991, Sony began mass producing lithium-ion batteries. The innovation and success of the lithium-ion battery is based on the replacement of the lithium metal at the negative electrode with a lithium-carbon intercalation compound, thus eliminating the low efficiency and safety problems inherent in Li-metal batteries. Graphite has, like $LiMO_2$ type materials, a layered character which gives it the ability to reversibly deintercalate and reintercalate lithium ions from its basic structure. On the other hand, it should be noted that carbon remains a negative electrode material of choice because its potential with respect to the Li^+/Li couple is very attractive because it is very low.

A battery is composed of several electrochemical cells that are connected, **Figure 2** shows a schematic illustration of a Li-ion cell and its main components. The two electrodes have an overall potential difference which is a function of the chemical nature of the two electrode materials. Each electrode has a support which serves as a metallic current collector, usually an aluminum collector

for the positive electrode and a copper collector for the negative electrode. The positive electrode ($LiMO_2$, M is a transition metal M=Co in our case) consists of active materials (> 80%), a conductive additive (carbon black) and a polymer binder (PolyVinyliDene Fluoride PVDF). The metal collectors are connected to an external circuit, their role being to ensure the flow of electrons. It should be noted that a separator is placed between the two electrodes in order to avoid an internal short circuit. This is a porous membrane imbibed with a liquid electrolyte allowing both electrical insulation and ionic conduction between the two electrodes. The commonly used electrolyte consists of the $LiPF_6$ salt dissolved in a mixture of ethylene carbonate (EC) and dimethyl carbonate (DMC).

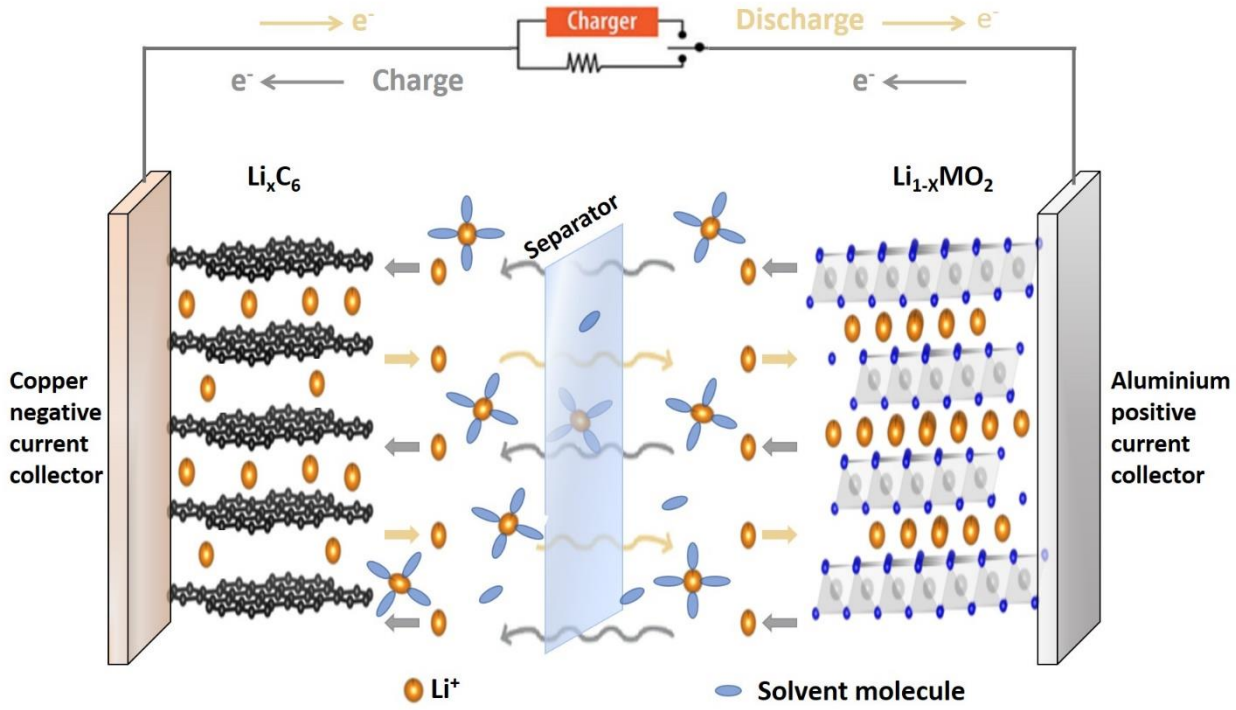

Figure 2. Schematic representation of the working principle of lithium ion batteries with $LiCoO_2$ as a positive electrode and graphite in the negative electrode

During the charge of the cell, the external circuit requires the transfer of a certain number of electrons from the positive electrode to the negative electrode, which induces a redox reaction at both electrodes. At the positive electrode, electron stripping is accompanied by oxidation of the

transition metal and, for charge compensation, deintercalation of Li^+ ions from the host structure according to the following reaction

$$LiCoO_2 \underset{\text{Discharge}}{\overset{\text{Charge}}{\rightleftharpoons}} Li_{1-x}CoO_2 + xLi^+ + xe^- \quad (1)$$

On the other hand, the opposite is observed at the negative electrode, as the arrival of electrons induces the reduction of the carbon host structure as well as the intercalation of Li^+ ions also for the purpose of charge compensation (**Equation 2**).

$$xLi^+ + xe^- + 6\,C \underset{\text{Discharge}}{\overset{\text{Charge}}{\rightleftharpoons}} Li_xC_6 \quad (2)$$

During the discharge, the opposite phenomenon is observed: the transition metal is reduced and the lithium ions are again intercalated in the positive electrode host material. The interest of such system lies in the possibility of storing electrical energy (in chemical form) during charging and in the restitution of this energy during discharge.

It is important to note that in the laboratory batteries, the negative electrode is made of metallic lithium; even if the reversibility of the Li^+/Li couple is poor in terms of long-term cycling, Since the potential of the Li^+/Li couple is constant and equal to - 3.04 V vs. ENH, the cycling curve, i.e. the variation of the potential as a function of the state of charge or discharge, then corresponds almost exclusively to the variation of the potential of the positive electrode.

The performances of a battery are quantified by several characteristic quantities, such as the operating voltage, the capacity, the energy density and the power. These different characteristics depend both on the properties of the materials used (active material), but also on the phenomena at the interfaces between the components of the cell.

The capacity (Q or C), expressed in A.h, is the amount of electric charge that can be stored in the electrode material and then delivered reversibly during cycling. It depends on the active material

used, as well as the mass of the active material contained in the positive electrode. The capacity is given by the formula:

$$Q = I \times t = \frac{F \times \Delta x}{3600 \times Mw} \times m$$

I (A): current flowing through the generator

t (h): current flow time

F (C): number of Faraday (96485 C)

Δx: number of moles of intercalated or deintercalated lithium ions after the time t

m (g): mass of electrochemically active material

M_w ($g.mol^{-1}$): molecular mass of the active material

The capacity can be expressed by volume ($Ah.cm^{-3}$) or per mass (specific capacity $Ah.g^{-1}$). The theoretical specific capacity of an electrode depends on the number of electrons that can be exchanged during the same charge or discharge per mole of active material. This number of exchanged electrons Δx corresponds to the number of Li^+ ions introduced into the host material, in the case of $LiCoO_2$, the maximum theoretical Δx=1. Eventually, the energy density can be an interesting parameter to be considered, is the amount of energy a battery can store per unit of mass or volume. Its value is easily calculated multiplying the working voltage (V_{cell}) with capacity and expressed in Wh/kg or Wh/L. Another interesting parameter is the power density which is the amount of power that the battery can provide on demand. It's can be calculated by dividing energy density by the operating time of the battery and expressed in W/kg or W/L.

The electrochemical tests are characterized by the cycling rate C/n, which means that the maximum theoretical capacity Q_{max} of the battery is obtained when the battery is charged or discharged in n hours. For example, C/20 cycling means that 20 hours are required to deintercalate one mole of lithium. It is important to clearly define Q_{max} to compare the results obtained for different materials because the cycling rate has a strong influence on the performances. It should

also be noted that for commercial batteries Q_{max} is not the maximum theoretical capacity, but the nominal capacity defined by the battery manufacturer for the chosen application.

Furthermore, galvanostatic curve or the variations of the voltage of the battery (E) as a function of the lithium content (x). The potential variations measured on the electrochemical curve are characteristic of the phase transitions that occur at the Li_xMO_2 electrode. Three kinds of behaviors can be observed on the E = f(x) curves, as represented in **Figure 3**.

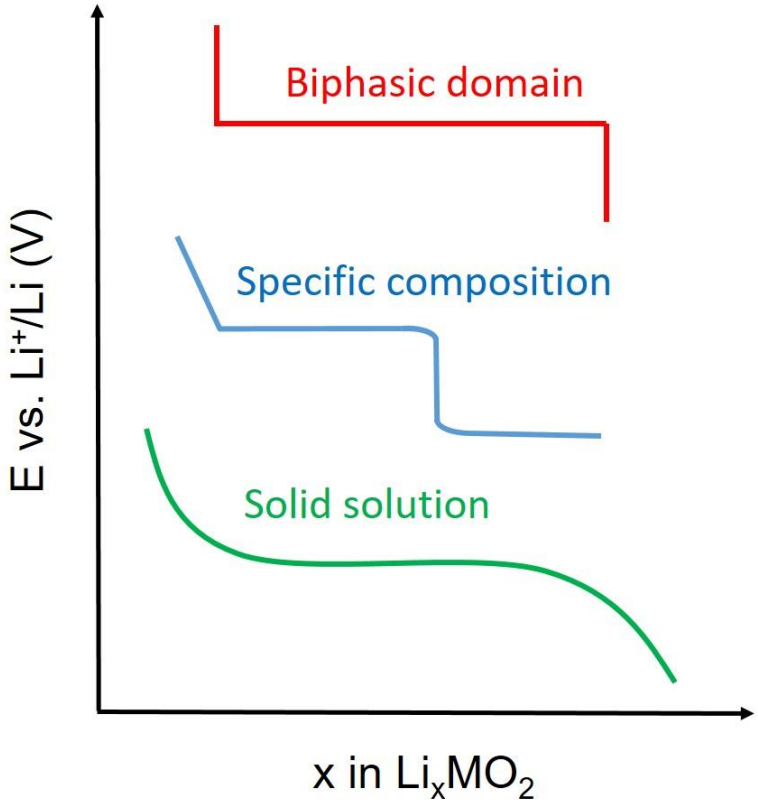

Figure 3. Schematic representation of the possible behaviors observed in a galvanostatic cycling.

These potential variations are related to the structural changes the materials undergo upon cycling. For the solid solution domain, the voltage evolves continuously as a function of x, where the structure of the material remains the same only the lithium amount varies constantly during the lithium deintercalation like in the case of $LiTiS_2$. When the voltage suddenly increases or decreases

and marks a “jump” on the curve, this is characteristic of a specific composition and highlights the existence of a single phase with a well-defined structure. Very often it is a stoichiometric phase or a supercell with ordered cation distribution, the composition domain for the existence of such phases is very narrow. Finally, the potential plateau is characteristic of a two-phase domain meaning there is equilibrium between two phases of different compositions and structures and only the ratio between these two phases evolves along the plateau (Such as the curve of $LiFePO_4$).

2. $LiCoO_2$ as a positive electrode for Lithium-ion batteries

2.1. Description of $LiCoO_2$ structure

$LiCoO_2$ exhibits two different crystal structures depending on both the preparation method and synthesis temperature. Low temperature lithium cobalt oxide (~400 °C, LT- $LiCoO_2$) has a cubic spinel structure with the space group Fd3m,[8] while the phase synthesized at high temperature (>700 °C, HT- $LiCoO_2$) is layered and exhibits an α-$NaFeO_2$ type structure (R-3m space group, a_{hex}=2.815 Å, c_{hex}=14.052 Å).[9] LT- $LiCoO_2$ shows a large hysteresis between the intercalation and de-intercalation of lithium ions,[11] which is due to the mixing of Co^{3+} and Li^+ in the structure, preventing the formation of layered pathways for Li-ion diffusion. HT- $LiCoO_2$ possesses alternating planes of Co^{3+} and Li^+ cations along the [111] direction of the cubic cell due the differences in size between the two cations.

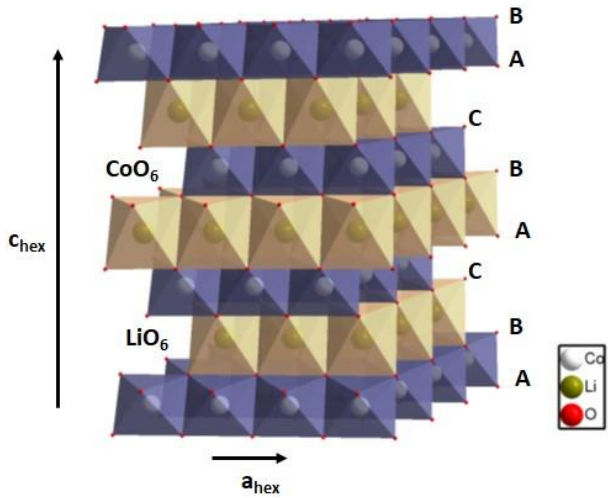

Figure 4. Schematic representation of the structure of O3-$LiCoO_2$

The hexagonal cell is generally used to describe the lamellar oxides, since it makes it possible to visualize the stack more easily, the c_{hex} axis being perpendicular to the (111) planes of the FCC cell and the a_{hex} and b_{hex} axes being parallel to these planes. Cobalt, lithium and oxygen occupied the 3a (0,0,0), 3b (0,0,1/2) and 6c (0,0,z_{ox}) Wyckoff positions respectively.

Figure 4 represents the sequence of octahedra LiO_6 and CoO_6 along the direction c_{hex}. It highlights the two-dimensional character of the structure, which can be described as an alternation between sheets [CoO_2] consisting of CoO_6 octahedra connected by their edges, separated by the interslab space whose interstitial sites are occupied by Li^+ ions. From Delmas et al.[11] nomenclature the structure is named O3-$LiCoO_2$, where O indicate that the lithium is an octahedral site and 3 CoO_2 layers are needed to form the hexagonal unit cell. The O3 stacking corresponds to an AB CA BC AB oxygen stacking. The lithium ions can reversibly deintercalate/intercalate from the van der Waals gap between CoO_2 layers.

2.2. Phases transitions upon lithium deintercalation of $LiCoO_2$

The phase changes upon deintercalation have been extensively studied, as they are believed to influence the reversibility of the intercalation/deintercalation process. An in-depth understanding of structural changes of $LiCoO_2$ during charges-discharges is of significant importance, if one wants to improve the cycling life at high voltage.

As Li is deintercalated from $LiCoO_2$ (**Figure 5**), the material undergoes a series of phase changes. The first transition occurs at a characteristic voltage plateau of ~3.9V versus Li^+/Li ($0.75 \leq x \leq 0.99$ in Li_xCoO_2) that corresponds a two-phase region induced by an insulator–metal transition.[12–14] Indeed, $LiCoO_2$ is a semiconductor with an electronic conductivity lower than 10^{-3} S cm^{-1} at room temperature and an activation energy close to 0.15 Ev,[14] while Li_xCoO_2 at concentrations below $x = 0.75$ is metallic.[15] Both $Li_{0.99}CoO_2$ (this limit value depends on the exact composition of the starting material which can be further discussed[16]) and $Li_{0.75}CoO_2$ phases crystallize in the rhombohedral system with only a small variation in the cell parameter.

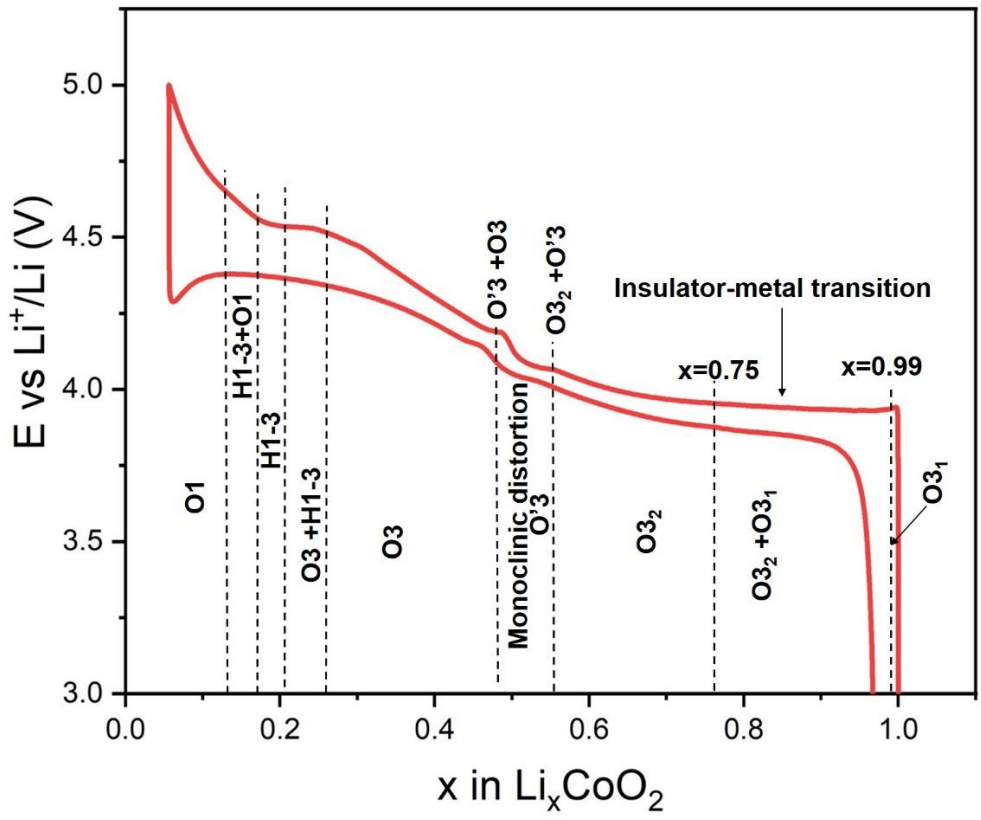

Figure 5. The first charge–discharge curves in the 3–5 V voltage range vs. Li^+/Li of Li_xCoO_2 (C/20 cycling rate).

For further Li deintercalation, the system undergo a transition from rhombohedral to monoclinic structure O'3, typically denoted by the addition of a prime symbol to the structure name,[11] around 0.5 Li. It is attributed to an interslab lithium/vacancy ordering (**Figure 6**) where the in-plane Li and its vacancy positions align with each other in an ordered sequence.[12,13,17] This monoclinic phase is short-lived and transformed again to a rhombohedral O3 phase upon further lithium extraction.

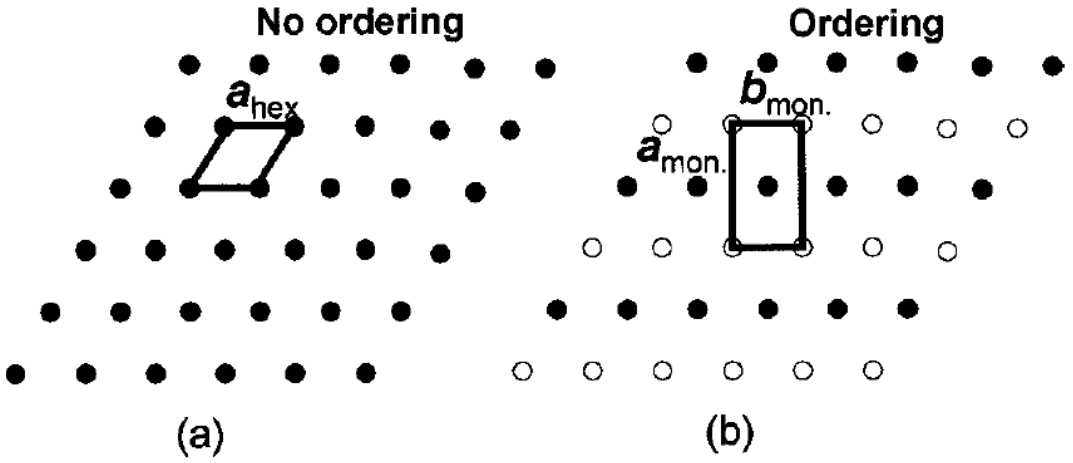

Figure 6. Schematics of (a) lithium ion positions in $LiCoO_2$ or randomly distributed lithium and vacancy positions in Li_xCoO_2 and (b) ordered lithium and vacancy positions in Li_xCoO_2 (x =0.5), where the hexagonal and monoclinic cells are drawn.[18]

At higher voltage, a plateau representing two-phase coexistence separates the O3 solid solution and a hybrid O1/O3 (H1-3) solid solution, which appears as a small step around x = 0.2.[18–20] Further deintercalation results in a two-phase coexistence of O1/O3 and O1.[18,20,21] These high voltage phase transitions will be more detailed in part A.2.3.1.

2.3. Capacity and voltage fading of $LiCoO_2$ occurring during high voltage cycling

When the variations in Li concentration are limited between x=0.4 and 1.0, the intercalation reaction is reversible giving rise to batteries with exemplary cyclability. For using $x \leq 0.4$, in order to achieve more capacity, leads to a significant capacity fade. Research efforts have been done in revealing the degradation mechanisms responsible for the fast performance decay, such as X-ray photoelectron spectroscopy (XPS) analysis, transmission X-ray microscopy analysis on the $LiCoO_2$ bulk grain, in situ diffraction techniques on the phase transition during cycling. However, it is still lacking a systematic and direct comparisons among of various failure mechanisms, leaving confusions as which degradation mechanism is the major contributor to the performance decay and which plays minor roles. Understanding each degradation mechanism and its specific contribution

to the overall performance decay are essential for choosing proper measure to improve battery performance, such as doping, surface coating, and electrolyte additive.

Chemically, high voltage cycling leads to more severe side reactions, thickening the surface phase transformation layer and the electrode/electrolyte interphase layer on particle surface, aggravating dissolution/reduction of transition metal ions and oxygen loss. Mechanically, it leads to severe material cohesion mainly due to the cracking of particles. Thermodynamically, deep delithiation can also trigger the bulk lattice phase transitions, causing irreversible structural changes. Many degradation phenomena have to be considered on component level, such as shown in **Figure 7**.

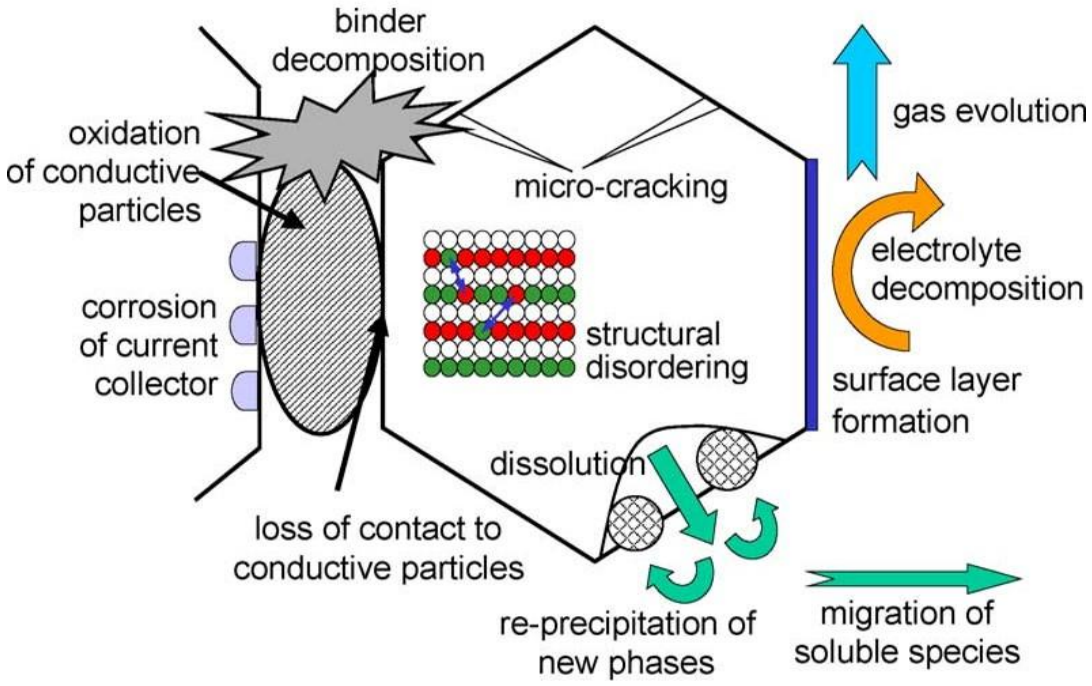

Figure 7. Overview on degradation mechanisms of positive electrode material from Vetter al.[22]

According to Amatucci et al.[23] the fast capacity fade of $LiCoO_2$ electrodes when cycled to 4.4V or 4.5 V vs Li^+/Li is probably due to cobalt dissolution correlated with structural changes. Chen and Dahn,[24] attributed the capacity loss of $LiCoO_2$ electrodes to the impedance growth caused by the formation of a surface layer and not to phase transformations. Such an electronically resistive

surface film may form even quicker when the electrode is cycled to 4.5 V vs Li^+/Li. It seems now generally accepted that below 4.4 or 4.5 V vs Li^+/Li capacity fade is due to impedance growth from side reactions involving $LiPF_6$-based electrolytes and surface species caused by air or moisture exposure. Chen and Dahn[24] indicated that, by creating fresh surfaces, through grinding, very good cycle life could be obtained, and they attributed the beneficial effects of coating to the accompanying removal of surface species.

2.3.1. Delithiation induced phase transitions

The structure and stability of the delithiated phases and phase transitions occurring during charge/discharge have been studied experimentally by ex situ and in situ X-ray diffraction (XRD) and theoretically by first principles calculations, as described below. Ohzuku et al.[13] did an ex situ XRD studies on $LiCoO_2$ electrodes which were charged to different potentials up to 4.8 V. They observed a new phase that formed from the O3 phase when more than 0.75 Li was removed from $LiCoO_2$ (around 4.55 V vs. Li^+/Li). However, even when charged to 4.8 V, the O3 phase did not totally transform to this new phase. In the XRD pattern of the purest new phase they obtained there are still some peaks from the O3 phase, such as the (003) and (104) peaks. However, they indexed all the peaks in this pattern with indices of a monoclinic phase except for the (003) peak from the O3 structure and a peak from polyethylene.

Later on, Amatucci et al. [21] performed an in situ XRD study on a $LiCoO_2$ electrode which was charged to 5.2 V and then discharged to 3 V. They also observed the formation of the new phase when more than 0.75 Li was removed and they followed Ohzuku's indexing of the powder pattern. They observed for the first time that O3-Li_xCoO_2 converted to CoO_2, with an O1 structure, after charging to 5.2 V. Then, Van der Ven and Ceder calculated the phase diagram of Li_xCoO_2 from first principles.[18,25] For $0.0 < x < 0.5$ in Li_xCoO_2 they predicted two phases other than the O3 phase, one is O1 when Li_xCoO_2 is completely deintercalated (i.e., x=0.0), and the other one is a staged-2 compound, named H1-3 by them, that would be the most stable phase in the range $0.12 < x < 0.19$.

From Amatucci et al.[21] the CoO_2 is a hexagonal single-layered phase (O1) believed to be isostructural with CdI_2 and has lattice parameters of a = 2.822 Å and c=4.29 Å with a P3m1 space group (**Figure 8**). The O1 nomenclature was used to reflect the stacking in 'c' direction in this structure with repeating unit of one oxygen-octahedral with an ABAB oxygen stacking. For very low Li content (~i.e., x=0) this structure is observed to be more stable than the O3.[21]

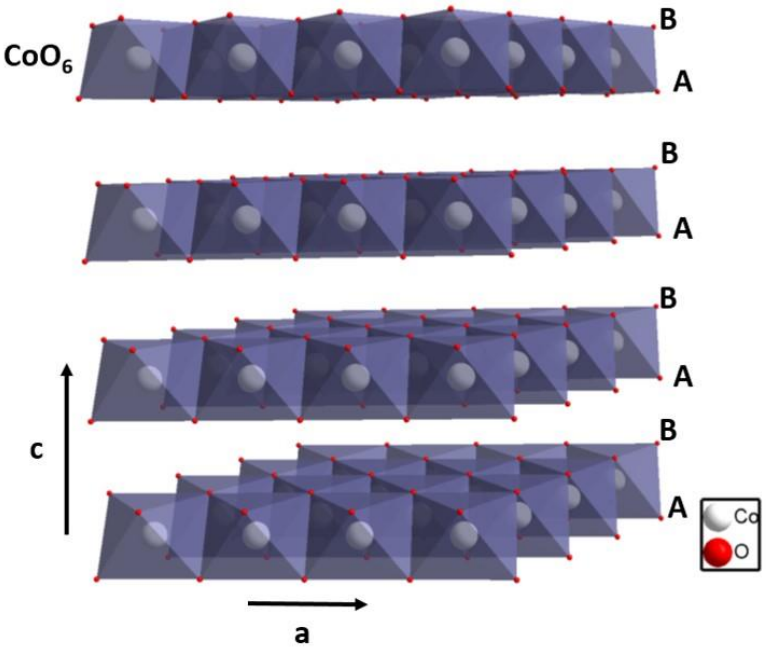

Figure 8. Schematic representation of the O1 phase. Cobalt and lithium occupied the 1a (0,0,0) and 2d (1/3, 2/3, 0.234) Wyckoff positions respectively.

The O3 structure is observed to be stable experimentally for Li concentrations between x =0.3 and 1.0.[10,11,14] Amatucci et al.[21] observed that the O1 host converted immediately back to a three-layer O3 delithiated $LiCoO_2$ type phase on lithium reinsertion. Note that in the O3 host, the oxygen octahedra surrounding Li sites share edges with the octahedra surrounding the Co sites, while in the O1 host, they share faces. Therefore, when ions are present between the metal oxide sheets, the O1 structure is destabilized. The electrostatic repulsion between the Li and Co ions is greater in the latter case.

The preference for O1 upon complete delithiation has been interpreted in the Li_xNiO_2 system in terms of interaction between oxygen p orbitals in the fully deintercalated phases.[26] The CoO_6 octahedra contain σ bonds between the cobalt ion d orbitals and the oxygen p orbitals. For an O3-type structure (AB CA BC packing), the oxygen p orbitals from both sides of the van der Waals gap point toward the same position of the triangular lattice. This means a direct repulsive interaction between the two orbitals through an empty octahedral site of the interslab space which destabilizes the O3 packing for x~0. In contrast, if Li^+ ions are in the O3-type van der Waals gap, there is a gain in energy and a stabilization of the structure. For an O1-type structure (AB packing), the oxygen p orbitals from both sides of the van der Waals gap point toward two different positions of the triangular lattice. These orbitals are not facing each other, a minimization of the interactions in comparison with an O3-type structure is thus observed.

Chen et al.[20] experimentally confirmed the presence of a H1-3 phase in $LiCoO_2$ from ex situ XRD patterns, the H1-3 phase takes the R-3m space group with Li occupying 3a sites, the Co and the two oxygen atoms are in three different 6c sites, with a_{hex} = 2.823 Å and c_{hex} = 27.07 Å. In H1-3, Li ions preferentially occupy octahedral sites that retain O3 stacking, leaving alternating layers having O1 stacking empty. The H1-3 can be also described as stage II which consists of alternating O1 and O3 stacked CoO_2 slabs requiring 6 CoO_2 slabs the unit cell hence an O6[27] structure. In Delmas nomenclature[11] the H1-3 is denoted as O6(O1-O3) with an AB CA CA BC BC AB AB oxygen stacking (**Figure 9**). The best estimated composition of the H1-3 phase is $Li_{0.17}CoO_2$.

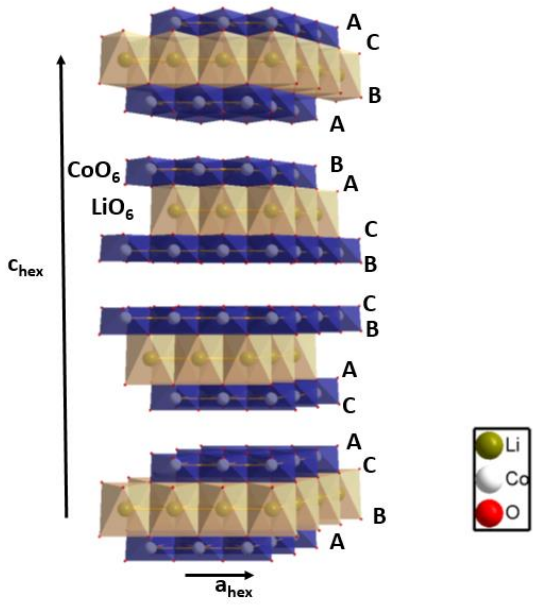

Figure 9. Schematic representation of the H1-3 phase with $a_{hex}=b_{hex}=2.78$ Å and $c_{hex}=25.95$ Å according to Van der Van et. al. [18,28] Cobalt, lithium, oxygen 1 and oxygen 2 occupied the 3a (0,0,0), 6c (0,0,0.425), 6c (0,0,0.277) and 6c (0,0,0.115) Wyckoff positions

In the H1-3 host, oxygen octahedra around the Li sites of every other plane between CoO_2 slabs share edges with the octahedra surrounding Co ions as in O3 leaving alternating layers having O1 stacking empty these octahedra share faces. As, the H1-3 structure can be seen as a hybrid of the O1 and O3 stacking, each CoO_2 slab and one of its nearest neighbor slabs have an O3-type stacking with a Li layer between them. This slab and the other nearest neighbor slab in the opposite direction have an O1-type stacking without Li atoms between them.[18,28]

The O3, O1, and H1-3 host structures are very similar to each other, the only difference between them is in the way in which the CoO_2 slabs are related to each other across the Li planes. Each of these host structures can be derived from the other by a simple gliding of the CoO_2 slabs with respect to each other adjacent to an empty Li plane. These types of glides are likely to have small activation barriers when the Li planes are empty, this means that, if there is a thermodynamic driving force, these glide transformations will likely occur at ambient temperatures. These

transformations of a topotactic nature maintain the alternation of the CoO_2 slabs. In **Figure 10** and **11**, various structure with stacking faults have been represented.

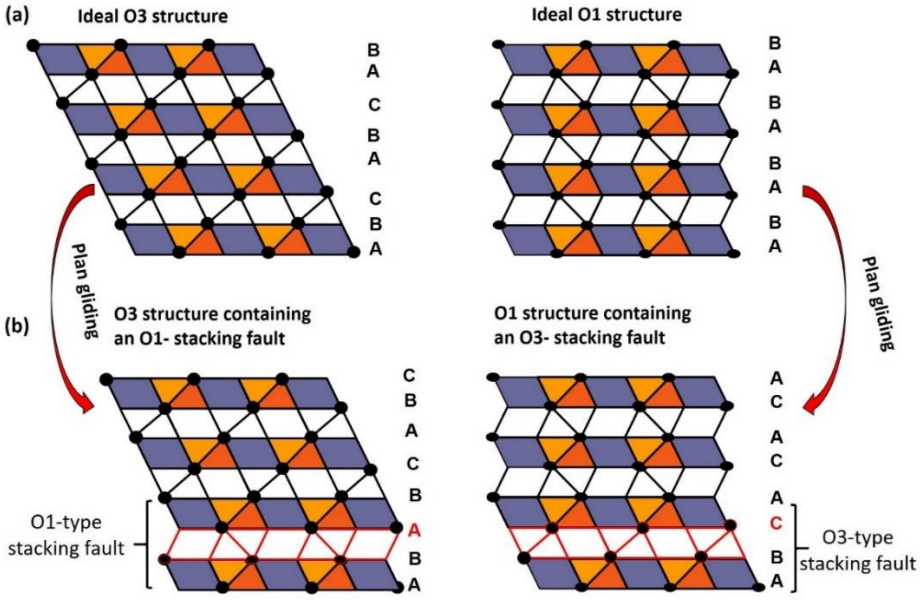

Figure 10. Schematic representation through a section along the (110) plane of (a) the ideal O3 and O1 structures, (b)O3 and O1 structure with an O1 and O3 -type stacking fault respectively after sheets gliding.

The ideal O1 structure can be obtained from O3 by gliding the CoO_2 slabs adjacent to every Li plane in the structure whose corresponding O positions move from an "ABCABC" stacking to an "ABABAB" one with the (2/3, 1/3, 0) and (1/3, 2/3, 0) translation vectors as shown on **Figure 10**. Whereas the O3 host can be transformed to the H1-3 host by gliding the CoO_2 slabs adjacent to every other Li plane (**Figure 11**).

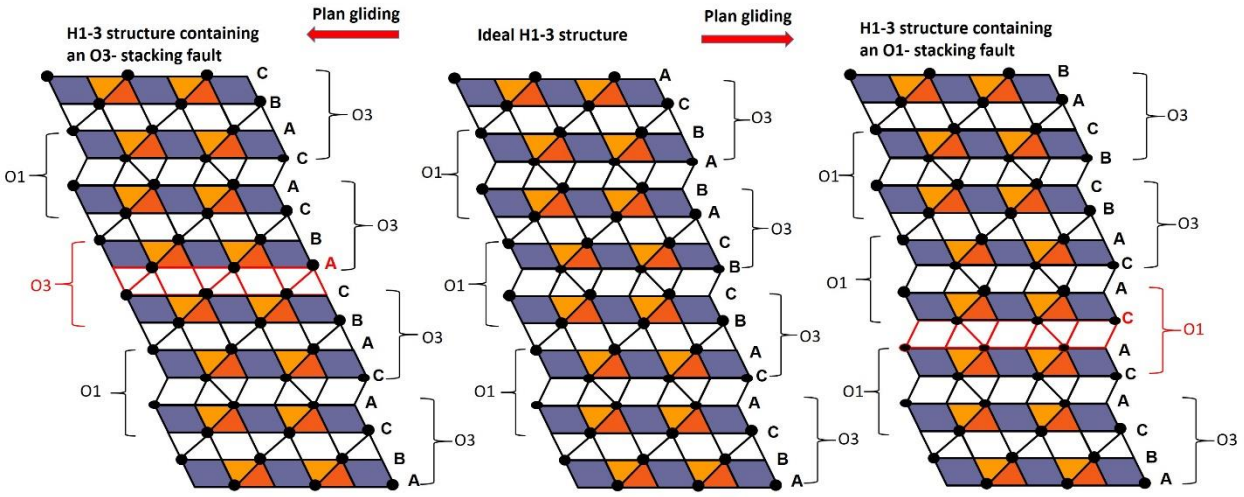

Figure 11. Schematic representation through a section along the (110) plane of the ideal H1-3 structures as opposite to an H1-3 structure with an O1-type stacking fault or O3 -type stacking fault after sheets gliding.

During a phase transition from the O3 phase to the H1-3 phase, the Li atoms in every second interlayer space must be completely removed to create an O1-type stacking for the two CoO_2 slabs next to the Li layer. This shifting occurs for each CoO_2 slab with respect to one of its nearest neighbor slabs.

The phase transitions from O3 to H1-3 occur with a contraction of the c_{hex}. lattice parameter. This generates mechanical strains and micro-cracks between and within the particles. These phase transitions, coupled with the increased mechanical stress, can contribute to the dramatic capacity fading in the deeply charged Li_xCoO_2. Compared to the structural changes below 4.5 V, such as the $O3_1/O3_2$ (insulator-metal transition) phase transition and the order/disorder phase transition, this structural change is much more severe.

Many groups also observed significant amounts of cracking, dislocations, and other extended defects in samples charged to high potential. According to a transmission electron microscope TEM study by Yazami et al.[29], $LiCoO_2$ electrodes cycled to 4.7 V show an irreversible structural phase transition from hexagonal O3 to cubic spinel, accompanying by increased density of dislocations and internal strains. Ex situ transmission electron microscopy (TEM) and electron

diffraction analysis of disassembled positive electrodes after cycling revealed that Li_xCoO_2 particles were strained, fractured, and contained a high density of extended defects, features that were not revealed by X-ray diffraction (XRD) analysis of these positive electrode materials.[30] In particles that are severely strained, electron diffraction reveals two types of cation disorder brought about by electrochemical cycling. One is the Li and Co substitution vacancies on their respective octahedral layers. The second, mainly observed in severely strained and fractured particles, is a partial structural transformation from octahedral cation ordering to spinel ordering with tetrahedral 8a site occupancy.

Xia et al.[31] studied the phase transitions and electrochemical behavior of $LiCoO_2$ thin-film positive electrodes prepared by pulsed laser deposition. They observed from ex-situ XRD, two voltage plateaus at about 4.55 and 4.62 V vs Li^+/Li in the charge discharge curves attributed to the O3 to the H1-3, and the H1-3 to the O1 transitions. The two corresponding peaks observed for the cutoff voltage of 4.7 V, become weak for the charge and convert to one narrow peak for the discharge when raising the voltage to 4.9 V, which indicate by them the irreversibility of these two reactions increases as the cutoff voltage increases. They also showed that lithium diffusion decreases with decreasing Li content for $0.14 < x < 0.4$, This phase transitions occur with a substantial effect on the lattice parameters coupled with the decreasing Li diffusivity, makes Li composition gradients larger, likely leads to large internal strains, and subsequent mechanical degradation of the material.

2.3.2. Interfacial degradation at electrode/electrolyte surface

One of the main obstacles restraining the improvement of lithium-based battery performances is the electrode/electrolyte interface, which is the key to understand battery electrochemistry. The reaction of the electrode material with the electrolyte and other inactive cell components can degrade battery performance. These surface reactions potentially include chemical and electrochemical reactions involving the active material, solvent, salt, binder, and conductive additives. One of the consequences of these surface reactions is the dissolution of transition-metal species that are adverse to the formation of the SEI (Solid Electrolyte Interphase) in the negative

electrode. The other consequence is the formation of a CEI (Cathode Electrolyte Interphase) on the positive electrode, consisting of several compounds including Li_2CO_3, LiF, and alkyl carbonates. This film could contribute to performance degradation if this impedes Li^+ transport, or if continual growth consumes Li.[32]

The electrochemically active $LiCoO_2$ electrolyte interface accounts importantly for the performance degradation under high operation voltage. If the voltage of the positive electrode is too high, the electrolyte will be oxidized, while if the voltage of the negative electrode is too low, the electrolyte will be reduced. In practice, many electrochemical cells (both aqueous and nonaqueous) can safely operate slightly beyond the stability window of the electrolyte if the oxidation/reduction of the electrolyte is self-limiting. This requires that the decomposition products be electronically insulating so that further decomposition does not occur, but ionically conducting so that Li^+ ions can pass through. The decomposition products build up a protective solid electrolyte interphase (SEI) film. This interface is usually further complicated by a passivation layer on the electrode. The SEI formation and growth consume active lithium and electrolyte materials, leading to capacity fading, increasing battery resistance, and poor power density. It allows Li^+ transport and blocks electrons in order to prevent further electrolyte decomposition and ensure continued electrochemical reactions.

These side reactions will first consume large amounts of Li and then change the surface structures of the $LiCoO_2$, hence changing the interfacial Li transport feature and the chemical environment of surface Co ions at the $LiCoO_2$ −electrolyte interface. For instance, Clémençon et al.[33] studied the surface and dimensional changes of individual Li_xCoO_2 crystals during lithium de-intercalation, using ex-situ AFM imaging, they observed the presence of surface Li_2CO_3 impurity particles on stoichiometric $LiCoO_2$ crystals, they were shown to gradually dissolve upon exposure to acid species in the electrolyte. Thus, Park et al.[34] reported that the extraction of Li^+ leads to the formation of surface components including Li_2O and Co_3O_4 via XPS and 2D correlation analysis at the $LiCoO_2$−electrolyte interface. Further, Takamatsu et al.[35] found the different chemical states of Co ions at the material's surface and bulk after the $LiCoO_2$ soaking with electrolyte studied by in situ TRF-XAS, and hence, the irreversible reaction is attributed to the reduction from Co^{3+} to Co^{2+} ions that is in contact with organic electrolyte solutions occurred. The reactions, which are

probably irreversible, are likely to cause capacity fading during subsequent discharge−charge cycling.

Given the inherent structural instability it can be plausibly stabilized by doping with various elements (such as Mn, Ni, Al, and Mg…) and thereby improve electrochemical performance. [36–44] Moreover, the electrochemically active $LiCoO_2$ −electrolyte interface accounts importantly for the performance degradation. Alternative approach consisted of modifying the $LiCoO_2$ surface with coating with inorganics (metal-oxides, phosphates, and fluorides) is usually adopted to suppress the interfacial reactions, which is, of course, at the cost of Li ion diffusion kinetics.[45–48]

3. Overstoichiometric $LiCoO_2$

Electrochemical performances of $LiCoO_2$ based positive electrode in Li-ions batteries are strongly dependent on the synthesis conditions and particularly on the nominal Li/Co ratio of the starting materials. Several studies have been devoted to understand the effect of the non-stoichiometry in $LiCoO_2$. The existence of excess lithium in the overstoichiometric $Li_{1+x}CoO_2$ structure was first presented by Carewska et al.[49] in 1997. While single peak is observed near to 0 ppm for stoichiometric $LiCoO_2$ as Co^{3+} ions are diamagnetic in the low spin state, ^{7}Li MAS NMR spectra exhibit new signals for overstoichiometric $Li_{1+x}CoO_2$ in addition to the one at 0 ppm, suggesting the presence of paramagnetic cobalt ions (**Figure 12**). Several defect models for the lithium over-stoichiometric $LiCoO_2$ have been proposed by other group, with discussing also the electronic state of Co and the nature of charge-compensating defects related with Li excess in $LiCoO_2$. Indeed, Peeters et al.[50] studied in detail the non-stoichiometric $LiCoO_2$ using ^{6,7}Li and ^{59}Co MAS NMR, they provided the presence of paramagnetic cobalt species whose nature reminded unclear for them. First, Imanishi et al.[51] carried out an accurate titration of the cobalt oxidation state in $Li_{1+x}CoO_2$ samples and reported that only Co^{3+} ions are present in the Li overstoichiometric phases. Then, Levasseur et al.[52] studied lithium-overstoichiometric materials, considering several experimental observations (^{7}Li MAS NMR, magnetic data, chemical analyses, etc.) and proposed a structural model in which all the cobalt ions are trivalent and oxygen deficiency in the $Li_{1+x}CoO_2$ structure compensate for lithium excess.

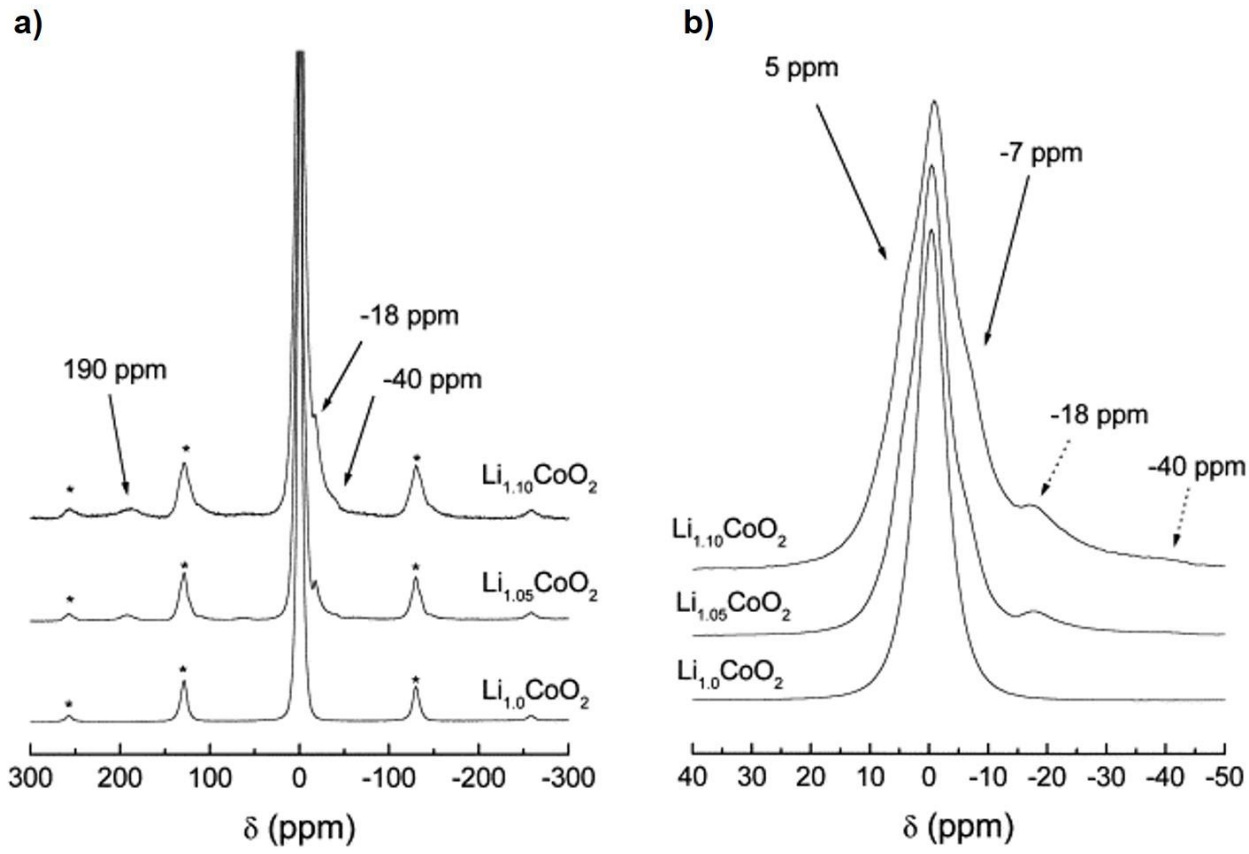

*Figure 12. [7]Li MAS NMR spectra for the various $Li_{x0}CoO_2$ phases with a zoom in the central transition given in b (x_0 =1.0, 1.05 and 1.10; *:spinning sidebands).*[53]

According to these authors, the excess Li replaces some cobalt ions in the CoO_6 slabs, and the charge deficit associated with a Li ion in a Co site is compensated for by an O^{2-} vacancy adopting a hexagonal structure analogue to the stoichiometric $LiCoO_2$. This leads to a formula $[Li]_{interslab}[Co_{1-t}Li_t]_{slab}[O_{2-t}]$ (where t=(x - 1)/(x + 1)). The Li present in the Co layer is surrounded by only 5 oxygen, thus the two neighboring cobalt ions adjacent to the oxygen vacancy are in square-based pyramids involving an intermediate spin configuration (IS) for Co ions (**Figure 13)**.[52]

The presence of single electrons for IS-Co^{3+} will induce a hyperfine interaction with lithium via the oxygen opposite to the vacancy leading to positive or negative shifted additional signals. [7]Li MAS NMR has shown to be a key tool when it comes to discuss the proper Li stoichiometry, as the difference is in the local scale and X-ray diffraction patterns is not able to evidence the

presence of Li in the Co site for overlithiated $LiCoO_2$ samples. Note that the electronic structure of the compound and the hyperfine interaction will be clarified in the following section.

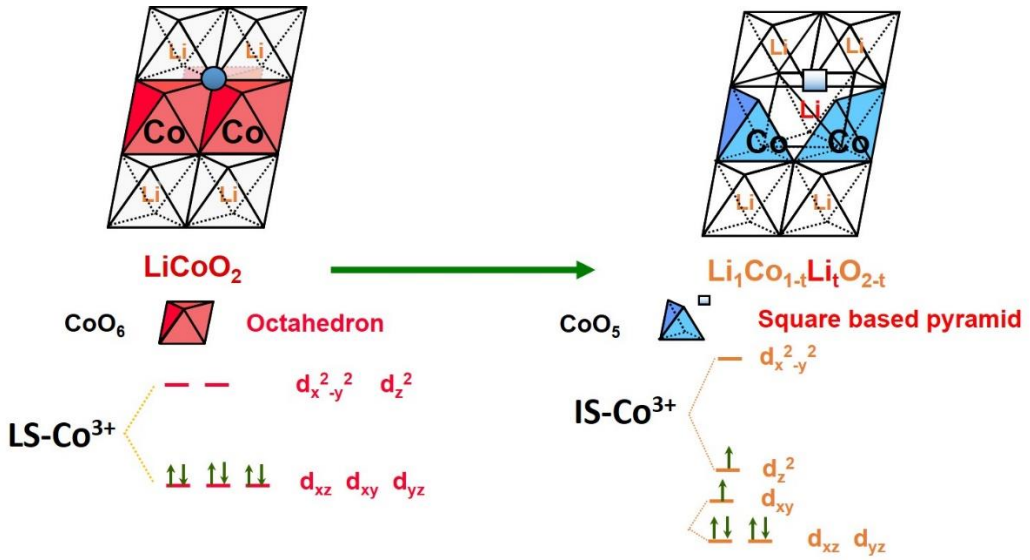

Figure 13. Schematic representation of the structural defect induced by Li substitution and the resulting electronic configuration for the neighboring Co^{3+} ion

This defect related to the lithium non-stoichiometry has been found to influence the electrochemical performances. Indeed, lithium excess is reported to affect the cycle life of Li-ion batteries as the capacity fade increases with increasing nominal Li/Co ratio.[51,54] In addition, stoichiometric and overlithiated $LiCoO_2$ did not feature similar phase transitions within Li-intercalation and de-intercalation during the charge and the discharge of Li_xCoO_2-based electrodes.[54] In **Figure 14**, the first charge curves of Li// Li_xCoO_2 cells with different Li/Co nominal ratio are shown. The stoichiometric $LiCoO_2$, exhibits the particular feature associated with the voltage plateau corresponding to the biphasic domain for $0.75 \leq x \leq 0.93$ and the monoclinic distortion expected at x=0.5.[12,14,17] Whereas, these features have disappeared for the overlithiated samples due to the presence of Li inside the CoO_2 layers which inhibits both the insulator-metal and the monoclinic transition.[54] Despite the fact that the presence of Li in the CoO_2 layer in overlithiated $LiCoO_2$ suppresses some phase transition, the electrochemical performances are not improved by overlithiation.

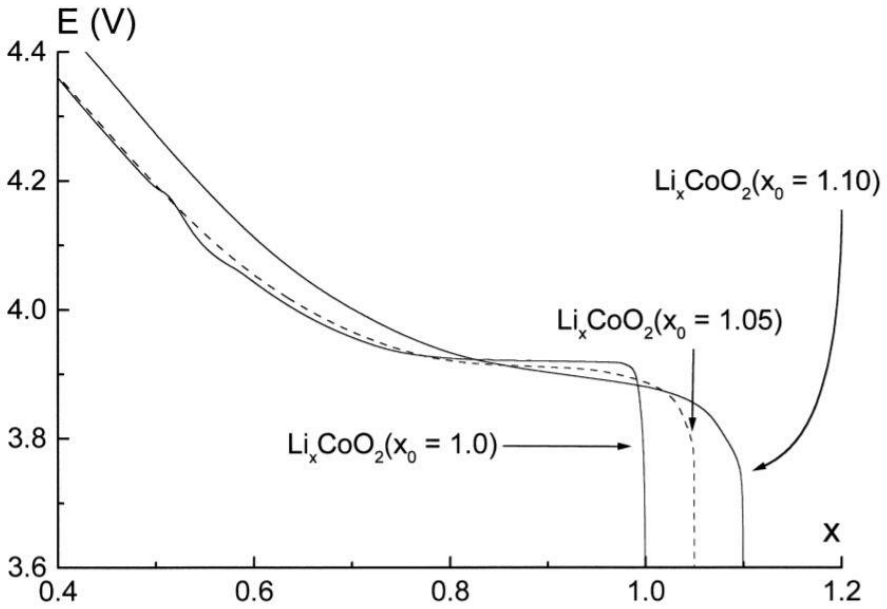

Figure 14.First galvanostatic charge of $LiCoO_2$ synthesized with Li/Co = 1.00, 1.05 or 1.10, from Levasseur et al[54]

Therefore, it is mandatory to control the initial Li/Co stoichiometry. In the following chapter, powders of doped $LiCoO_2$ with well controlled initial Li/M (M=Co, Al or Mg) ratios are synthesized and characterized to further investigate the influence of the initial Li/M ratio on their properties as well as their behavior during charge and discharge process.

4. Nuclear magnetic resonance

Previous studies carried out in the laboratory and by other research groups have shown that solid-state nuclear magnetic resonance (NMR) is a method of choice increasingly used for such local characterization, by exploiting hyperfine magnetic interactions due to the presence of a certain density of localized unpaired electrons (Fermi contact shift) or delocalized electrons (Knight shift) on the probed nucleus. In addition to diffraction and measurements of physical properties (electronic conductivity, magnetism), it is therefore fundamentally important to use NMR to understand the local structure of electrode materials. Additionally, NMR of paramagnetic materials

can provide information of the local electronic structure while analyzing the Fermi contact interaction mechanisms giving rise to a given experimental shift.

4.1. Electronic structure

In lithiated transition metal oxides of the $LiMO_2$ type, lithium is completely ionized, since it gives its electron to the host structure MO_2. The ability of these oxides to exhibit a wide range of lithium concentration is due to the ability of the transition metal to accept different degrees of oxidation. Electronic configurations play a key role in understanding not only the phases studied, but also the NMR signals. **Figure 15** shows the representation of the 3d orbitals of the transition metal M (M=Co in our case). In the absence of a crystal field, which is the case for the free ion, these five 3d orbitals are degenerated. The crystal field produced by octahedral oxygen anion coordination splits the five transition metal d orbitals of the transition metal (each of which can hold two electrons of opposite spin) into two sets of levels labeled e_g and t_{2g} as illustrated in **Figure 15**.

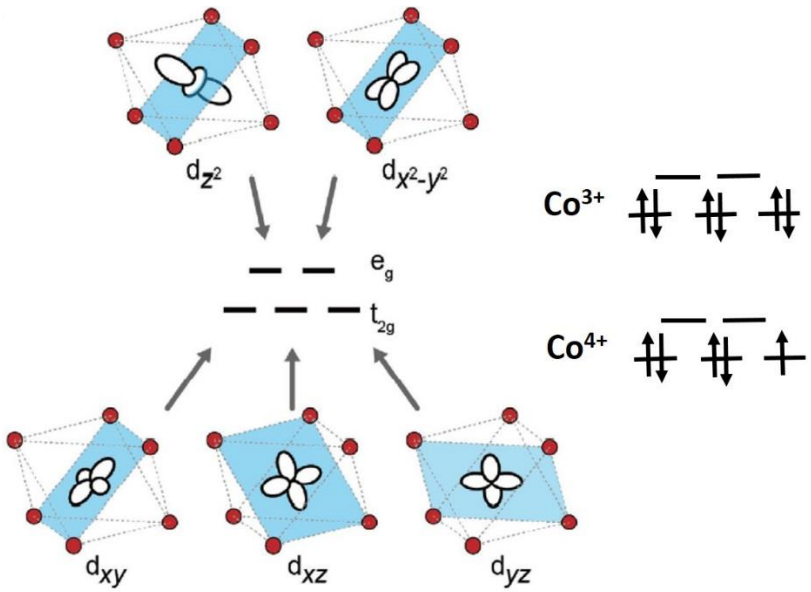

Figure 15. Crystal field spitting of d orbitals in an octahedral environment with the electronic configuration of the Co ions in the octahedral symmetry reproduced from Radin et al.[32]

e_g Orbitals have $d_{x^2-y^2}$ and d_{z^2} symmetries with lobes that point toward the anions, while t_{2g} orbitals, have d_{xy}, d_{yz}, and d_{xz} symmetries, with lobes that point between the oxygen atoms. The e_g levels have a higher energy than the t_{2g} levels due to the increased electrostatic repulsion from the coordinating anions. Note that Co cations in the pristine material have an oxidation state of 3+ and are in low spin state configuration. Under lithium deintercalation the Co^{3+} ($t_{2g}^6e_g^0$) are oxidized to Co^{4+}($t_{2g}^5e_g^0$). The model described above neglects the important role of covalence between transition metal ions and oxygen ions. The model describing this is the Ligand Field Theory presented briefly in **Figure 16**. This covalence is translated into a combination of atomic orbitals to form molecular orbitals.

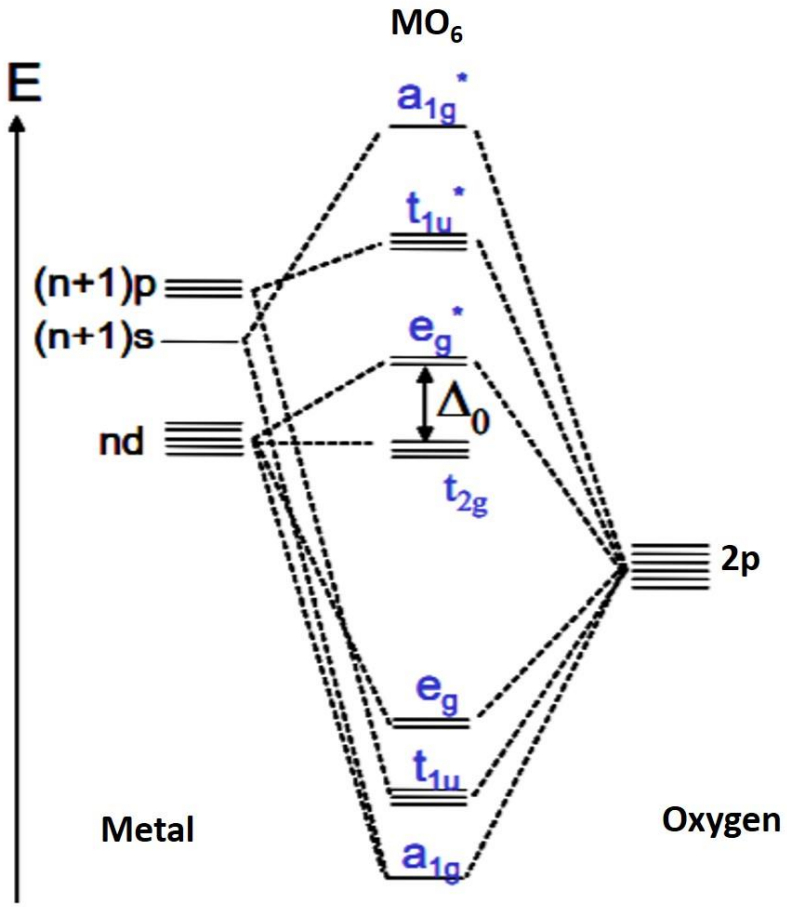

Figure 16. Schematic representation of the band structure expected for oxides with octahedrally coordinated transition-metal cations.

The d_{z^2} and $d_{x^2-y^2}$ orbitals, which point towards the oxygen, combine with the 2p orbitals thereof to form a binding level e_g and an antibonding level e_g*. Since the 2p orbitals of the oxygen are located at lower energy than the 3d orbitals of the transition metal, the e_g level has a strong p-character of oxygen, whereas the antibonding e_g* level has a strong 3d character of the metal. The greater the overlap between the 3d and 2p orbitals, the greater the stabilization of the e_g level and the destabilization of the e_g* level. It should be noted that the level e_g* is often noted e_g while we are talking about levels with a strong 3d character of the metal. The orbitals d_{xy}, d_{yz}, and d_{xz}, do not point toward the 2p orbitals of the oxygen ions. Therefore, they cannot form σ bonds. They are generally considered to be non-bonding levels, called t_{2g} (**Figure 16**). However, these orbitals can give rise to π overlaps with the 2p orbitals of the oxygen atoms. These levels with the main 3d character then become weakly antibonding. The energy difference between the t_{2g} and e_g* levels is called the "gap" and is noted Δ_0. The other levels come from the overlap between the 2p orbitals of the oxygen atoms and the 4s and 4p orbitals of the metal. The bonding combinations of these orbitals have a strong 2p oxygen character. These levels are named t_{1u} and a_{1g} in **Figure 16**.

4.2. Hyperfine interactions

Among the active materials for Li-ion batteries, most of which contain transition metal ions, those that possess transition metal ions with one or more unpaired electrons are called paramagnetic, while those that possess transition metal ions with all their paired electrons are diamagnetic materials. NMR is extremely sensitive to the presence of these unpaired electrons in the environment of the probed nucleus by the interactions called hyperfine. In paramagnetic compounds, the single electrons are localized (implied on the transition metal) whereas in metal compounds, the electrons are delocalized and form a conduction electron cloud; there is then not strictly speaking electron spins, but the appearance of a so-called Pauli susceptibility (Pauli paramagnetism). The presence of a density of such electron spins or conduction electrons will give rise to hyperfine interactions, respectively Fermi contact type or Knight shift. The hyperfine interaction has two contributions: an isotropic one which results the shift and an anisotropic

(dipolar) mainly responsible for the width of the signals. Using magic angle spinning, this dipolar part is partially removed.

Furthermore, the hyperfine interaction has also a dipolar contribution that occur through space. Thus, hyperfine coupling between a nucleus and an unpaired electron results in a shift and broadening of NMR signals. The Hamiltonian of the hyperfine interaction H_{SI} between unpaired electrons, to which corresponds the spin operator $\hat{S}$, and a nucleus, to which corresponds the spin operator $\hat{I}$., can be expressed as follows according to two contributions:

$$H_{IS} = A^i.\hat{I}.\hat{S} + \hat{I}.\tilde{A}_{dip}.\hat{S}$$

Where A^i is the Fermi contact coupling constant, $\hat{I}$ is the spin operator of nucleus, $\hat{S}$ is the spin operator of unpaired electron and $\tilde{A}_{dip}$ is the dipolar tensor of the hyperfine interaction.

4.2.1. Fermi Contact interaction

The Fermi contact interaction is due to the presence of a certain density of single electrons at the site of the NMR probed nucleus. This interaction usually causes large displacements of NMR signals, positive or negative, usually called "Fermi contact shift". The NMR shift signal due to Fermi contact can be expressed as the following:

$$\delta_{iso}^{i} = \frac{A^i}{\hbar} \frac{\chi_M}{\mu_0 \gamma^i g_e \mu_B}$$

χ_M is the magnetic molar susceptibility of the material, ħ is Planck's constant, μ_0 is the magnetic constant, γ^i is the gyromagnetic ratio for the isotope studied by NMR, g_e is the electron factor and μ_B is the Bohr magneton. The hyperfine constant A^i gives the shift signal and depends on the electron spin (i.e., unpaired electron) “density” at the nucleus i $\rho(r = 0)$:

$$A^i = \frac{\mu_0}{3S} \hbar \gamma^i g_e \mu_B \rho^i(0)$$

Where S is the quantum spin number.

$\rho(r = 0)$ depends on the connectivity between the orbitals on the paramagnet and the orbitals on the atom, whose nucleus is probed, it is can expressed by

$$\rho^i(r = 0) = \sum_j(\left|\Psi_j \uparrow (0)\right|^2 - ||\Psi_j \downarrow (0)|^2)$$

With $|\Psi_j\uparrow(0)|^2$ is the probability of presence of positive polarized spin (i.e. with the same polarization as the applied magnetic field) and $|\Psi_j\downarrow(0)|^2$ is the probability of presence of negative polarized spin. The j indicates an "s" type orbital, since according to the symmetry of the atomic orbitals, only the electrons in s orbitals are associated with a finite probability of being found at the nucleus, and only the electron density transferred to the s orbitals needs to be considered.

Based on the previous equation, the Fermi contact shift can be expressed as a function of the magnetic susceptibility of the material and the electron spin density as:

$$\delta_{iso}^i = \frac{1}{3S}\rho^i(0)\chi_M$$

The Fermi contact is generally considered to be additive, indeed, that the shift due to several paramagnetic ions can be considered as the sum of the Fermi contact shift generated by each ion on the probed nucleus. Sometimes the interaction is so strong that the highly shifted signals are no longer observable. Fermi contact shift is temperature dependent as the magnetic susceptibility of a paramagnetic material follows a Curie-Weiss-type law and therefore decreases as the temperature increases. As a result, a decrease in shift in absolute value is expected as temperature increases in the paramagnetic domain.

The magnitude of the Fermi contact shift depends on the transfer of an electron spin density to the site of the probed nucleus, electron density may be transferred either directly from the paramagnet or indirectly via a transferred hyperfine interaction to the s orbitals, and thus, the interaction contains information about the chemical bonding between the paramagnetic element, Li, and the intervening oxygen atoms.

4.2.2. Knight shift

The Knight shift is observed for metallic phases, is analogous to the Fermi-contact shift, except that the shift is a measure of the density of states at the Fermi level. However, for metallic

phases, this density comes from the conduction electrons located at Fermi level in this conduction band and the Pauli paramagnetism they generate. The Knight shift depends on the contribution of the s orbitals of the NMR-active atom (lithium) to the crystal orbitals with energies at or very close to fermi energy the Li 2s partial density of states at the Fermi level $\langle|\Psi_{(r=0)}|^2\rangle$.

$$K = \frac{8\pi}{3}\langle|\Psi_{r=0}|^2\rangle\chi_s^e$$

The Knight shift is directly proportional to the Pauli spin susceptibility χ_s^e of the conduction electrons at the Fermi level. This type of electron-nucleus interaction leads to positive and generally quite strong Knight shifts. However, there can also be a polarization of paired electrons in a full s orbital by Pauli's paramagnetism in an outer (often d) orbital, which implies a negative Knight shift by polarization (often weak) and no signal shift with temperature is therefore not expected for the ideal metal phases.

4.2.3. Dipolar interaction

The other contribution to hyperfine coupling is the dipolar interaction that takes place through space between the electron spin and the probed nuclear spin and varies in $1/r^3$. The importance of this interaction is therefore dependent on the proximity of the single electron to the nucleus being probed. This interaction, like any dipolar interaction, is partially suppressed in rotation at the magic angle spinning (MAS) because of its anisotropy. In the case of a non-spherical distribution of the electron spins around lithium (probed by NMR), it can give rise to an anisotropic line shape. On the other hand, in the case where the g-tensor describing the electron spins is anisotropic, this interaction contains a so-called "pseudocontact" contribution that creates an additional shift.

The observed shift is therefore the sum of the Fermi and pseudocontact shifts. The second contribution is generally much smaller than the first; the Fermi contact term is considered to be predominant in the magnitude of the observed shift for different oxides, and this should also be true for the lithiated lamellar oxides Li_xMO_2.

The recorded signal in rotation at the magic angle spinning (MAS) is then composed of the isotropic signal and its spinning side band whose envelope represents the line shape of the static signal (in the case of relatively low rotation speeds). The anisotropy of the dipolar part of the hyperfine interaction is partly responsible for this line shape. If the rotation speed is insufficient to fully average this very strong interaction, some residual width also remains in the isotropic signal and in each rotation band.

4.2.4. Quadrupolar interaction

Generally, in solid state NMR an atomic nucleus with spin I has its spin energy levels determined by the Zeeman interaction with the external magnetic field B_0. But nuclei with I >1/2, in which the nuclear charge has a non-spherical shape are also characterized by the quadrupole moment *Q* of charges. This charge distribution interacts with the electrostatic electric fields (in fact the electric field gradient EFG) induced on the nucleus by the distribution of electronic charges in the material. Therefore, the nuclear spins are influenced both by the Zeeman and the quadrupolar Hamiltonian H_Q, which can be written as:

$$H_Q = \frac{eQ}{2(2I - I)} I.V.I$$

In this equation, I is the nuclear spin vector, e is the elementary charge, and V is the electric field gradient tensor. The quadrupolar term modifies the NMR spectrum and can be treated as a perturbation if the quadrupole term is small as compared to the Zeeman splitting. Simply put, according to the perturbation theory, the quadrupolar interaction can be divided into two contributions, quadrupolar splitting of the first order $H^{\wedge 1}_Q$ and second order $H^{\wedge 2}_Q$. As the spin of a quadrupole nucleus is larger than I=1/2 a multiple energy levels (2I+1) are developed and therefore multiple transitions are expected. In half-integer spin systems for example an example the ^{7}Li nuclear spin is I=3/2 for ^{7}Li NMR in the layered Li_xCoO_2. There is a -1/2 to 1/2 transition knowns as the central transition and the other transitions (the $-3/2 \leftrightarrow -1/2$ and $1/2 \leftrightarrow 3/2$ transitions) are known as satellite transitions. However, the quadrupolar interaction significantly influences these energy levels (transitions) up to several megahertz in magnitude. Interestingly, the first order

approximation does not affect the central transition, while the second order transition is inversely proportional the Larmor frequency. With increasing field, the second order effect on the central transition decreases. The quadrupolar interaction is typically very small for ^{7}Li but can result in characteristic broadening in static and a series of spinning sidebands in magic angle spinning (MAS) spectra due to the satellite transitions. The contribution from the first-order quadrupolar interaction can be successfully removed by applying fast MAS. However, a part of the second order term of H_Q can't be removed by MAS and broadens the central transition signal. This second-order term involves a small additional contribution to the total shift which varies inversely to B_0^2, with B_0 the strength of the magnetic field. Consequently, high magnetic fields reduce the magnitude of this contribution and therefore, the broadening of the spectral line due to the quadrupolar interaction.

Table 1 shows the quadrupolar nuclei that will be used for our study (^{7}Li, ^{27}Al and ^{59}Co). The highest quadrupole character is detected for ^{27}Al nucleus suggesting that the quadrupolar interactions needed to be taken into account for ^{27}Al MAS NMR as well as the first and second order quadrupolar terms for interpreting the spectra. The quadrupolar character for ^{59}Co is less important than ^{27}Al but it cannot be neglected. As the ^{7}Li quadrupolar moments is too low the quadrupolar contribution can be neglected for this nucleus.

Nucleus	Nuclear spin (I)	Quadrupolar moment (b)
^{7}Li	3/2	-0.04
^{27}Al	5/2	+0.42
^{59}Co	7/2	+0.15

Table 1. Nuclear Quadrupole Moments and spin for ^{7}Li, ^{27}Al and ^{59}Co

The $LiCoO_2$ pristine material is a diamagnetic compound (LS-Co^{3+}) so that no hyperfine interaction is expected for lithium in this material, while when cobalt is oxidized upon lithium deintercalation the electronic properties (Li_xCoO_2 for $x \leq 0.75$ is metallic as described in **part 2.2**) as well as the lithium environments change. Ménétrier et al,[14] attributed the loss of the observably in ^{7}Li MAS NMR when lithium is deintercalated for $0.94 \leq x < 1$ to the localized character of the

Co^{4+} ions, therefore the transferred hyperfine interaction is between the 2s orbital of the alkali ion Li^+ and the t_{2g} orbitals of the Co ions via 2p orbital of the oxygen ion leading to Co-O-Li bond pathway (See **Figure17**). From x=0.94 a second phase appears with a delocalized-electron type behavior, this changes the nature of the hyperfine interaction experienced by lithium from a paramagnetic contact shift type to a Knight shift one due to the participation of its orbitals to the conduction band.

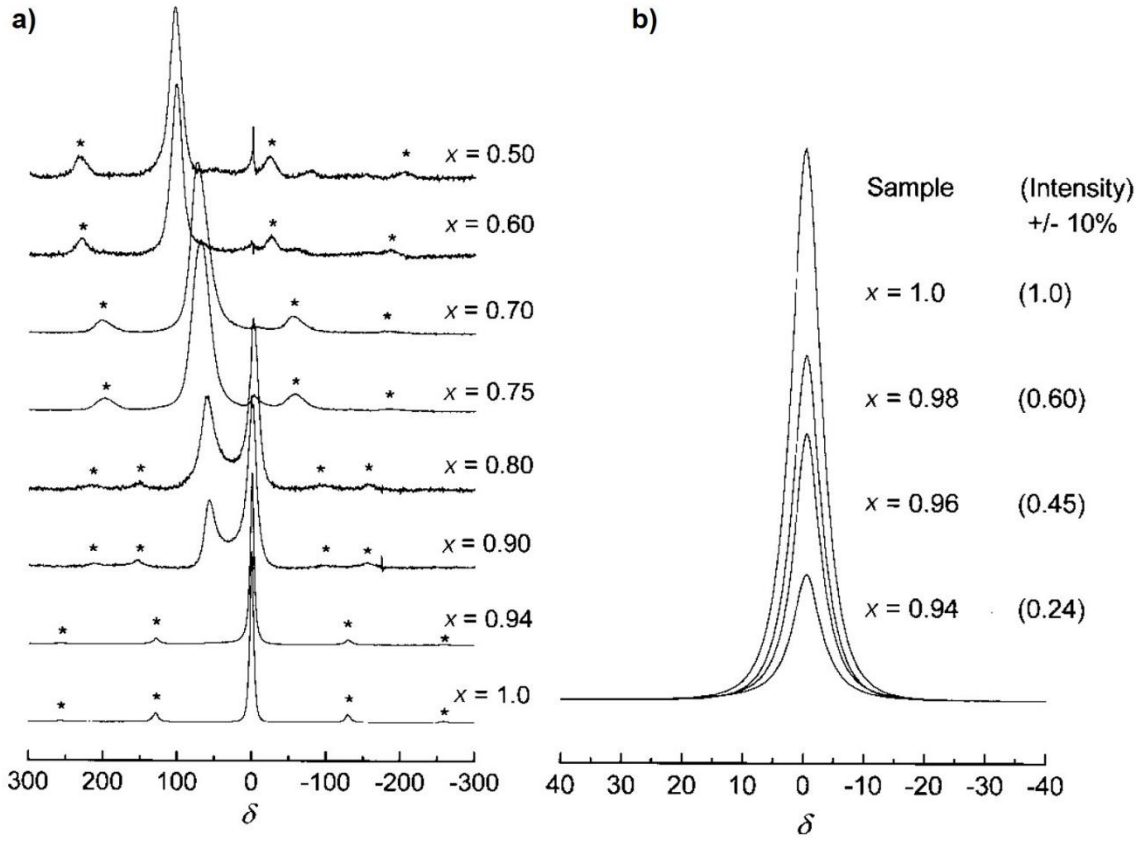

Figure 17. ^{7}Li MAS NMR spectra for the various Li_xCoO_2 deintercalated phases (=spinning sidebands) from Ménétrier et al.[14]*

References

(1) World Energy Outlook 2021 – Analysis https://www.iea.org/reports/world-energy-outlook-2021 (accessed 2022 -02 -06).

(2) Yamahira, T.; Kato, H.; Anzai, M. Nonaqueous Electrolyte Secondary Battery. US5053297A, October 1, 1991.

(3) Mizushima, K.; Jones, P. C.; Wiseman, P. J.; Goodenough, J. B. LixCoO2 (0. *Mater. Res. Bull.* **1980**, *15* (6), 783–789. https://doi.org/10.1016/0025-5408(80)90012-4.

(4) Yano, A.; Shikano, M.; Ueda, A.; Sakaebe, H.; Ogumi, Z. $LiCoO_2$ Degradation Behavior in the High-Voltage Phase Transition Region and Improved Reversibility with Surface Coating. *J. Electrochem. Soc.* **2017**, *164* (1), A6116–A6122.

(5) Grey, C. P.; Dupré, N. NMR Studies of Cathode Materials for Lithium-Ion Rechargeable Batteries. *Chem. Rev.* **2004**, *104* (10), 4493–4512. https://doi.org/10.1021/cr020734p.

(6) Whittingham, M. S. The Role of Ternary Phases in Cathode Reactions. *J. Electrochem. Soc.* **1976**, *123* (3), 315. https://doi.org/10.1149/1.2132817.

(7) Yazami, R.; Touzain, P. A Reversible Graphite-Lithium Negative Electrode for Electrochemical Generators. *J. Power Sources* **1983**, *9* (3), 365–371. https://doi.org/10.1016/0378-7753(83)87040-2.

(8) Li, W.; Reimers, J. N.; Dahn, J. R. Lattice-Gas-Model Approach to Understanding the Structures of Lithium Transition-Metal Oxides $LiMO_2$. *Phys. Rev. B* **1994**, *49* (2), 826.

(9) Antolini, E. $LiCoO_2$: Formation, Structure, Lithium and Oxygen Nonstoichiometry, Electrochemical Behaviour and Transport Properties. *Solid State Ion.* **2004**, *170* (3), 159–171. https://doi.org/10.1016/j.ssi.2004.04.003.

(10) Garcia, B.; Farcy, J.; Pereira-Ramos, J. P.; Baffier, N. Electrochemical Properties of Low Temperature Crystallized $LiCoO_2$. *J. Electrochem. Soc.* **1997**, *144* (4), 1179–1184.

(11) Delmas, C.; Fouassier, C.; Hagenmuller, P. Structural Classification and Properties of the Layered Oxides. *Phys. BC* **1980**, *99* (1), 81–85. https://doi.org/10.1016/0378-4363(80)90214-4.

(12) Reimers, J. N.; Dahn, J. R. Electrochemical and in Situ X-Ray Diffraction Studies of Lithium Intercalation in Li_XCoO_2. *J. Electrochem. Soc.* **1992**, *139* (8), 2091–2097.

(13) Ohzuku, T.; Ueda, A. Solid-State Redox Reactions of $LiCoO_2$ (R3m) for 4 Volt Secondary Lithium Cells. *J. Electrochem. Soc.* **1994**, *141* (11), 2972–2977.

(14) Ménétrier, M.; Saadoune, I.; Levasseur, S.; Delmas, C. The Insulator-Metal Transition upon Lithium Deintercalation from LiCoO2: Electronic Properties and ^{7}Li NMR Study. *J. Mater. Chem.* **1999**, *9* (5), 1135–1140.

(15) Molenda, J.; Stokłosa, A.; Bąk, T. Modification in the Electronic Structure of Cobalt Bronze LixCoO2 and the Resulting Electrochemical Properties. *Solid State Ion.* **1989**, *36* (1), 53–58. https://doi.org/10.1016/0167-2738(89)90058-1.

(16) Ménétrier, M.; Carlier, D.; Blangero, M.; Delmas, C. On "Really" Stoichiometric $LiCoO_2$. *Electrochem. Solid-State Lett.* **2008**, *11* (11), A179. https://doi.org/10.1149/1.2968953.

(17) Shao-Horn, Y.; Levasseur, S.; Weill, F.; Delmas, C. Probing Lithium and Vacancy Ordering in O3 Layered Li_xCoO_2 ($x \approx 0.5$). *J. Electrochem. Soc.* **2003**, *150* (3), A366. https://doi.org/10.1149/1.1553787.

(18) Van der Ven, A.; Aydinol, M. K.; Ceder, G.; Kresse, G.; Hafner, J. First-Principles Investigation of Phase Stability in Li_xCoO_2. *Phys. Rev. B* **1998**, *58* (6), 2975–2987. https://doi.org/10.1103/PhysRevB.58.2975.

(19) Ven, A. V. der; Aydinol, M. K.; Ceder, G. First-Principles Evidence for Stage Ordering in Li X CoO2. *J. Electrochem. Soc.* **1998**, *145* (6), 2149. https://doi.org/10.1149/1.1838610.

(20) Chen, Z.; Lu, Z.; Dahn, J. R. Staging Phase Transitions in Li_xCoO_2. *J. Electrochem. Soc.* **2002**, *149* (12), A1604. https://doi.org/10.1149/1.1519850.

(21) Amatucci, G. G.; Tarascon, J. M.; Klein, L. C. CoO_2, the End Member of the Li_xCoO_2 Solid Solution. *J. Electrochem. Soc.* **1996**, *143* (3), 1114–1123.

(22) Vetter, J.; Novák, P.; Wagner, M. R.; Veit, C.; Möller, K.-C.; Besenhard, J. O.; Winter, M.; Wohlfahrt-Mehrens, M.; Vogler, C.; Hammouche, A. Ageing Mechanisms in Lithium-Ion Batteries. *J. Power Sources* **2005**, *147* (1–2), 269–281. https://doi.org/10.1016/j.jpowsour.2005.01.006.

(23) Amatucci, G. G.; Tarascon, J. M.; Klein, L. C. Cobalt Dissolution in $LiCoO_2$-Based Non-Aqueous Rechargeable Batteries. *Solid State Ion.* **1996**, *83* (1), 167–173. https://doi.org/10.1016/0167-2738(95)00231-6.

(24) Chen, Z.; Dahn, J. R. Methods to Obtain Excellent Capacity Retention in $LiCoO_2$ Cycled to 4.5 V. *Electrochimica Acta* **2004**, *49* (7), 1079–1090. https://doi.org/10.1016/j.electacta.2003.10.019.

(25) Ceder, G.; Van der Ven, A.; Aydinol, M. K. Lithium-Intercalation Oxides for Rechargeable Batteries. *JOM* **1998**, *50* (9), 35–40. https://doi.org/10.1007/s11837-998-0412-5.

(26) Croguennec, L.; Pouillerie, C.; Mansour, A. N.; Delmas, C. Structural Characterisation of the Highly deintercalated $Li_xNi_{1.02}O_2$ Phases (with $X \leq 0.30$). *J. Mater. Chem.* **2001**, *11* (1), 131–141. https://doi.org/10.1039/B003377O.

(27) Delmas, C.; Fouassier, C.; Hagenmuller, P. Structural Classification and Properties of the Layered Oxides. *Phys. BC* **1980**, *99* (1), 81–85. https://doi.org/10.1016/0378-4363(80)90214-4.

(28) Ven, A. V. der; Aydinol, M. K.; Ceder, G. First-Principles Evidence for Stage Ordering in Li X CoO2. *J. Electrochem. Soc.* **1998**, *145* (6), 2149. https://doi.org/10.1149/1.1838610.

(29) Yazami, R.; Ozawa, Y.; Gabrisch, H.; Fultz, B. Mechanism of Electrochemical Performance Decay in $LiCoO_2$ Aged at High Voltage. *Electrochimica Acta* **2004**, *50* (2–3), 385–390. https://doi.org/10.1016/j.electacta.2004.03.048.

(30) Wang, H.; Jang, Y.-I.; Huang, B.; Sadoway, D. R.; Chiang, Y.-M. Electron Microscopic Characterization of Electrochemically Cycled $LiCoO_2$ and $Li(Al,Co)O_2$ Battery Cathodes. *J. Power Sources* **1999**, *81–82*, 594–598. https://doi.org/10.1016/S0378-7753(99)00108-1.

(31) Xia, H.; Lu, L.; Meng, Y. S.; Ceder, G. Phase Transitions and High-Voltage Electrochemical Behavior of $LiCoO_2$ Thin Films Grown by Pulsed Laser Deposition. *J. Electrochem. Soc.* **2007**, *154* (4), A337. https://doi.org/10.1149/1.2509021.

(32) Radin, M. D.; Hy, S.; Sina, M.; Fang, C.; Liu, H.; Vinckeviciute, J.; Zhang, M.; Whittingham, M. S.; Meng, Y. S.; Van der Ven, A. Narrowing the Gap between Theoretical and Practical Capacities in Li-Ion Layered Oxide Cathode Materials. *Adv. Energy Mater.* **2017**, *7* (20), 1602888. https://doi.org/10.1002/aenm.201602888.

(33) Clémençon, A.; Appapillai, A. T.; Kumar, S.; Shao-Horn, Y. Atomic Force Microscopy Studies of Surface and Dimensional Changes in LixCoO2 Crystals during Lithium de-Intercalation. *Electrochimica Acta* **2007**, *52* (13), 4572–4580. https://doi.org/10.1016/j.electacta.2006.12.076.

(34) Park, Y.; Kim, N. H.; Kim, J. Y.; Eom, I.-Y.; Jeong, Y. U.; Kim, M. S.; Lee, S. M.; Choi, H. C.; Jung, Y. M. Surface Characterization of the High Voltage $LiCoO_2$/Li Cell by X-Ray Photoelectron Spectroscopy and 2D Correlation Analysis. *Vib. Spectrosc.* **2010**, *53* (1), 60–63. https://doi.org/10.1016/j.vibspec.2010.01.004.

(35) Takamatsu, D.; Koyama, Y.; Orikasa, Y.; Mori, S.; Nakatsutsumi, T.; Hirano, T.; Tanida, H.; Arai, H.; Uchimoto, Y.; Ogumi, Z. First In Situ Observation of the $LiCoO_2$ Electrode/Electrolyte Interface by Total-Reflection X-Ray Absorption Spectroscopy. *Angew. Chem. Int. Ed.* **2012**, *51* (46), 11597–11601. https://doi.org/10.1002/anie.201203910.

(36) Zhong, Q.; von Sacken, U. Crystal Structures and Electrochemical Properties of $LiAl_yNi_{1-y}O_2$ Solid Solution. *J. Power Sources* **1995**, *54* (2), 221–223. https://doi.org/10.1016/0378-7753(94)02071-A.

(37) zhao, ruirui; Zhang, J.; Lee, G.-H.; Zhang, K.; Lau, V. W.; Lee, J.-J.; Moudrakovski, I.; Yang, Y.-L.; Zhou, F.; Park, M.; Hung, I.-M.; Kang, Y. The Origin of Heavy Elemental Doping to Relieve the Lattice Thermal Vibration of Layered Materials for High Energy Density Li Ion Cathodes. *J. Mater. Chem. A* **2020**. https://doi.org/10.1039/D0TA03979A.

(38) Levasseur, S.; Ménétrier, M.; Delmas, C. Combined Effects of Ni and Li Doping on the Phase Transitions in Li_xCoO_2 Electrochemical and 7 Li Nuclear Magnetic Resonance Studies. *J. Electrochem. Soc.* **2002**, *149* (12), A1533–A1540. https://doi.org/10.1149/1.1516219.

(39) Yoon, W.-S.; Lee, K.-K.; Kim, K.-B. Structural and Electrochemical Properties of $LiAl_YCo_{1-Y}O_2$ Cathode for Li Rechargeable Batteries. *J. Electrochem. Soc.* **2000**, *147* (6), 2023.

(40) Duffiet, M.; Blangero, M.; Cabelguen, P. E.; Song, K. S.; Fauth, F.; Delmas, C.; Carlier, D. Probing Al Distribution in LiCo0.96Al0.04O2 Materials Using ^{7}Li, ^{27}Al, and ^{59}Co MAS

NMR Combined with Synchrotron X-Ray Diffraction. *Inorg. Chem.* **2020**, *59* (5), 2890–2899. https://doi.org/10.1021/acs.inorgchem.9b03260.

(41) Jang, Y.-I.; Huang, B.; Wang, H.; Sadoway, D. R.; Ceder, G.; Chiang, Y.-M.; Liu, H.; Tamura, H. $LiAl_YCo_{1-Y}O_2$ ($R\bar{3}m$) Intercalation Cathode for Rechargeable Lithium Batteries. *J. Electrochem. Soc.* **1999**, *146* (3), 862–868.

(42) Liu, Q.; Su, X.; Lei, D.; Qin, Y.; Wen, J.; Guo, F.; Wu, Y. A.; Rong, Y.; Kou, R.; Xiao, X.; Aguesse, F.; Bareño, J.; Ren, Y.; Lu, W.; Li, Y. Approaching the Capacity Limit of Lithium Cobalt Oxide in Lithium Ion Batteries via Lanthanum and Aluminium Doping. *Nat. Energy* **2018**, *3* (11), 936–943. https://doi.org/10.1038/s41560-018-0180-6.

(43) Zaheena, C. N.; Nithya, C.; Thirunakaran, R.; Sivashanmugam, A.; Gopukumar, S. Microwave Assisted Synthesis and Electrochemical Behaviour of $LiMg_{0.1}Co_{0.9}O_2$ for Lithium Rechargeable Batteries. *Electrochimica Acta* **2009**, *54* (10), 2877–2882. https://doi.org/10.1016/j.electacta.2008.11.009.

(44) Tukamoto, H.; West, A. R. Electronic Conductivity of $LiCoO_2$ and Its Enhancement by Magnesium Doping. *J. Electrochem. Soc.* **1997**, *144* (9), 3164–3168.

(45) Orikasa, Y.; Takamatsu, D.; Yamamoto, K.; Koyama, Y.; Mori, S.; Masese, T.; Mori, T.; Minato, T.; Tanida, H.; Uruga, T.; Ogumi, Z.; Uchimoto, Y. Origin of Surface Coating Effect for MgO on LiCoO2 to Improve the Interfacial Reaction between Electrode and Electrolyte. *Adv. Mater. Interfaces* **2014**, *1* (9). https://doi.org/10.1002/admi.201400195.

(46) Lee, H.; Kim, M. G.; Cho, J. Olivine $LiCoPO_4$ Phase Grown $LiCoO_2$ Cathode Material for High Density Li Batteries. *Electrochem. Commun.* **2007**, *9* (1), 149–154. https://doi.org/10.1016/j.elecom.2006.08.058.

(47) Dai, X.; Wang, L.; Xu, J.; Wang, Y.; Zhou, A.; Li, J. Improved Electrochemical Performance of $LiCoO_2$ Electrodes with ZnO Coating by Radio Frequency Magnetron Sputtering. *ACS Appl. Mater. Interfaces* **2014**, *6* (18), 15853–15859. https://doi.org/10.1021/am503260s.

(48) Chen, Z.; Dahn, J. R. Effect of a ZrO[sub 2] Coating on the Structure and Electrochemistry of Li_xCoO_2 When Cycled to 4.5 V. *Electrochem. Solid-State Lett.* **2002**, *5* (10), A213. https://doi.org/10.1149/1.1503202.

(49) Carewska, M.; Scaccia, S.; Croce, F.; Arumugam, S.; Wang, Y.; Greenbaum, S. Electrical Conductivity and ^{6,7}Li NMR Studies of $Li_{1+y}CoO_2$. *Solid State Ion.* **1997**, *93* (3), 227–237. https://doi.org/10.1016/S0167-2738(96)00545-0.

(50) Peeters, M. P. J.; Van Bommel, M. J.; Neilen-Ten Wolde, P. M. C.; Van Hal, H. A. M.; Keur, W. C.; Kentgens, A. P. M. A ^{6}Li, ^{7}Li and ^{59}Co MAS NMR Study of Rock Salt Type Li_xCoO_2 ($0.48 \leq X \leq 1.05$). *Solid State Ion.* **1998**, *112* (1–2), 41–52. https://doi.org/10.1016/s0167-2738(98)00213-6.

(51) Imanishi, N.; Fujii, M.; Hirano, A.; Takeda, Y.; Inaba, M.; Ogumi, Z. Structure and Electrochemical Behaviors of Li_xCoO_2 (x>1) Treated under High Oxygen Pressure. *Solid State Ion.* **2001**, *140* (1), 45–53. https://doi.org/10.1016/S0167-2738(01)00703-2.

(52) Levasseur, S.; Ménétrier, M.; Shao-Horn, Y.; Gautier, L.; Audemer, A.; Demazeau, G.; Largeteau, A.; Delmas, C. Oxygen Vacancies and Intermediate Spin Trivalent Cobalt Ions in Lithium-Overstoichiometric $LiCoO_2$. *Chem. Mater.* **2003**, *15* (1), 348–354. https://doi.org/10.1021/cm021279g.

(53) Levasseur, S. Evidence for Structural Defects in Non-Stoichiometric HT-$LiCoO_2$: Electrochemical, Electronic Properties and 7Li NMR Studies. *Solid State Ion.* **2000**, *128* (1–4), 11–24. https://doi.org/10.1016/S0167-2738(99)00335-5.

(54) Levasseur, S.; Ménétrier, M.; Suard, E.; Delmas, C. Evidence for Structural Defects in Non-Stoichiometric HT-$LiCoO_2$: Electrochemical, Electronic Properties and ^{7}Li NMR Studies. *Solid State Ion.* **2000**, *128* (1), 11–24. https://doi.org/10.1016/S0167-2738(99)00335-5.

Part A: Understanding the role of Al doping as a function of the ratio Li/M (M=Co+Al) in the improvement of the electrochemical properties

A. Understanding the role of Al doping as a function of the ratio Li/M (M=Co+Al) in the improvement of the electrochemical properties 65

A.1. Introduction 65

A.2. Experimental details and technical background 66

A.3. Study of the 2% Al doped $LiCoO_2$ materials as a function of the Li/M ratio (M=Co+Al)69

A.3.1. Preparation of Al doped $LiCoO_2$ samples from solid state reaction 69

A.3.2. Structural characterization of the starting materials 70

A.3.2.1. Study of the morphology 70

A.3.2.2. Study of the average structure 71

A.3.2.3. Study of the local structure 75

a) ^{7}Li MAS NMR 75

b) ^{27}Al MAS NMR 77

c) ^{59}Co MAS NMR 82

A.3.2.4. Study of magnetic properties 83

A.3.2.5. Discussion 84

A.3.3. Influence of Li/M ratio on the electrochemical performance 85

A.3.4. Conclusion on the 2% Al doped $LiCoO_2$ with various Li/M ratio 88

A.4. Understanding the role of Al doping of $LiCoO_2$ on the mechanisms upon cycling up to 4.8V vs. Li^+/Li 90

A.4.1. Preparation of the 4% Al-doped $LiCoO_2$ 90

A.4.2. Structural properties of pristine st-$LiCoO_2$ and $LiCo_{0.96}Al_{0.04}O_2$ materials 91

A.4.3. Electrochemical properties and general overview 95

A.4.4. Detailed study in the low and high voltage regions 103

A.4.4.1. The $0.73 \leq x < 1$ composition domain (low voltage region). 103

A.4.4.2. The $x \leq 0.5$ composition domain (high voltage region) 105

a) Sample prepared by fixing the Li amount 105

b) Samples prepared with floating voltages 107

c) Structural characterization after cycling at high voltage (3-cycles) 110

A.4.5. Discussion and Conclusion 115

References 117

A. Understanding the role of Al doping as a function of the ratio Li/M (M=Co+Al) in the improvement of the electrochemical properties

A.1. Introduction

As discussed in the bibliographic part of the manuscript, working at high voltage leads to a deterioration of the cycling performance,[1] caused by structural instabilities, electrolyte degradation and Co dissolution.[2–7] More specifically, for charge voltages exceeding 4.5 V vs Li^+/Li, $LiCoO_2$ exhibits detrimental phase transformations: O3 to H1-3 and H1-3 to O1 implying slab glidings.[3,8,9] Consequently, internal strain builds up, leading to crack formation and particle pulverization.[4,10,11] Several strategies were investigated to improve the cycling stability of $LiCoO_2$.[12–14] Among these, metal substitutions of cobalt (Al, Mg, Ti…) have been demonstrated to be a promising and effective method to enhance the electrochemical performances of $LiCoO_2$ at high voltage.[15–19] In 1998, Ceder et al.[20] identified aluminum as a potentially attractive dopant: they observed that substituting Co with Al leads to a higher Li cell average voltage but suffers from a lower capacity at the first charge up 4.4V vs Li^+/Li.[20,21] The similar Al^{3+} and LS-Co^{3+} ionic radii (0.535 Å vs. 0.545 Å) facilitate the substitution while maintaining the layered structure. It has been also reported that the substitution of Co by Al was effective on suppressing cobalt dissolution at 4.5 V versus Li^+/Li.[22] In these previous works, the authors speculate that dopant element is homogeneously distributed and substituted in the Co sites. The effect of aluminum doping with low quantities (such as 2% and 4%) has not been yet much studied especially in the high voltage region. The detection of the dopant for a very low Al content would be difficult due to the low resolution of conventional characterization techniques compared to the case of larger amounts of Al.

The first part will be dedicated to understand the real effect of 2% Al doping with well controlled Li/M(M=Co+Al) stoichiometries. It has been shown from previous studies, that ^{7}Li Magic Angle Spinning Nuclear Magnetic Resonance (MAS NMR) is a key tool to discuss the proper Li/M stoichiometry[23,24] whereas ^{27}Al and ^{59}Co MAS NMR can be used the characterize the Al/Co distribution homogeneity in the slab.[25,26]A conducted study on the effects of 2% Al substitution has been done; therefore, "$Li_xCo_{0.98}Al_{0.02}O_2$" (x=0.98, 1.00 and 1.02) materials were

synthesized and characterized at different scales in order to evidence the homogeneity of aluminum distribution in those materials.

The second part will be devoted to the detailed study of a 4 % Al doped $LiCoO_2$. We choose to study a material with higher quantity of dopant (4% Al) to better visualize the effect of the dopant in the different phenomena at the low and high voltage ranges. Indeed, in a previous PhD, in our group, several 4 % Al-doped $LiCoO_2$ materials with a controlled Li/(Co +Al) stoichiometry were synthesized by various solid state routes.[26,27] The samples were then characterized by ^{7}Li, ^{27}Al ,^{59}Co MAS NMR and synchrotron X-Ray Diffraction (XRD) to discuss their exact Li/M stoichiometry and their homogeneity. The materials were compared with a $LiCo_{0.96}Al_{0.04}O_2$ sample prepared by a co-precipitation route followed by a heat treatment that also exhibits homogeneous Al/Co repartition, but lower particles size. For extensive cycling at high voltage, the sample prepared by the solid-state route showed, however, better stability, since larger particles size minimizes the electrolyte degradation's detrimental effect. Therefore, a sample prepared by a solid state route with homogeneous Al/Co distribution and a Li/M ratio equal to 1.00 has been selected for the present study. First, we report the structural characterizations of the 4% Al-doped $LiCoO_2$ discussing its homogeneity. Then, we aim to understand the role of Al-doping on the low voltage phase transitions and on the high voltage degradation mechanisms involved during cycling, combining techniques with different spatial and sensitivity scales such as XRD, ^{7}Li, ^{59}Co, and ^{27}Al MAS NMR and TEM.

A.2. Experimental details and technical background

Electrodes of undoped and 4% or 2% Al-doped $LiCoO_2$ were prepared by mixing 90% weight of active material, 5% of carbon black, and 5% of polyvinylidene fluoride (PVDF). A slurry was formed by adding N-methyl-pyrrolidone (NMP) and mixed for 1h. The slurry casted onto a 30 µm-thick-aluminum foil, was dried in an oven for 2 hours at T = 80 °C, calendared and punched into discs with an electrode density of 3.062g/cm^3. The electrodes were then dried overnight under vacuum at T = 120 °C and stored in an argon-filled glovebox, where cell assembling was carried out. Electrochemical tests were both carried out in coin cells and Swagelok type cells. Coin cells were used to assess the electrochemical performance of all samples (ie, charge and discharge

capacities, cycle life performance, etc…), while the Swagelok-type design was favored when the cycled samples needed to be recovered for further characterization. The loading of the electrode was also changed for both cell setups. The coin cells were assembled using undoped and Al doped $LiCoO_2$ positive electrodes with a 10 mg/cm^2 active material loading, a disc of Viledon® and Celgard 2400® as separators and a Li metal sheet as negative electrode with 1 M $LiPF_6$ in EC: DEC: DMC as electrolyte. A higher loading of ~ 30 mg/cm^2 was employed to prepare Li de-intercalated $Li_xCo_{0.96}Al_{0.04}O_2$ or Li_xCoO_2 materials in the Swagelok setup to have a sufficient amount of powder for all ex-situ characterizations. One more Viledon separator was added in this case. The materials were recovered in an argon-filled dry box, washed with dimethyl carbonate (DMC) to remove residual electrolyte salt and dried under vacuum. Deintercalated $Li_xCo_{0.96}Al_{0.04}O_2$ and Li_xCoO_2 samples were prepared following two routes: i) by a galvanostatic charge at a C/20 rate applied up to the desired Li content (x) followed by a relaxation step; ii) by a galvanostatic charge at a C/20 rate applied up to the desired voltage followed by a floating step until the current reached ~ 0 mA. This second procedure was used to prepare samples stable at high voltage. All sample powders of the deintercalated compounds were then split in two parts for NMR and XRD characterization.

Powder X-ray diffraction (PXRD) patterns were collected on a PANalitycal X'pert PRO MPD, diffractometer in Bragg-Brentano θ-θ geometry equipped with a Fe filter, a spinner and X'Celerator multi-strip detector using the Co-$K_{\alpha.}$ Radiations. Each pattern was recorded in the (10 - 120°) 2θ range using 0.016° intervals and 15 h total counting time. XRD patterns of the deintercalated materials were collected on a PANalitycal X'pert^3 Powder diffractometer using the Cu-$K_{\alpha.}$ radiations, that allows the study of powder packed in 0.3 mm diameter capillaries.

NMR experiments were performed using a standard Bruker 2.5 mm MAS probe with a 30 kHz typical spinning frequency. ^{7}Li MAS NMR spectra were recorded on a Bruker 300 Advance spectrometer at 116.66 MHz (7.05 T magnet). A Hahn echo sequence [$t_{\pi/2}$-τ1-t_{π}-τ2] synchronized with one period of rotor rotation was used for a 30 kHz spinning frequency. The 90° pulse duration was equal to $t_{\pi/2}$ = 2.0 μs and determined using a LiCl 1 M solution. A recycle time of D_0 = 40s was used for st-$LiCoO_2$ and $LiCo_{0.96}Al_{0.04}O_2$ samples, whereas a shorter D_0 = 4s was enough for all deintercalated samples, to avoid T_1 saturation effects. Single pulse ^{27}Al MAS NMR spectra were

recorded on a Bruker 500 MHz spectrometer at 130.33 MHz (11.7 T magnet). The spectral width was set to 0.5 MHz and the recycle time to D_0 = 5 s, long enough to avoid T_1 saturation effects. As ^{27}Al is a strong quadrupolar nucleus with I = 5/2, a short pulse length of 1.1 μs corresponding to a π/12 pulse determined using an aqueous 1 M $Al(NO_3)_3$ solution was employed. In these conditions, all of the -½ → +½ central transitions are equally excited regardless of the magnitude of the nuclear quadrupole coupling constants and one can extract quantitative data. As all samples contain only 2 or 4% of Al, overnight experiments (10240 scans) were carried out to ensure a good signal/noise ratio.

^{59}Co MAS NMR spectra were recorded on a Bruker 500 MHz spectrometer at 120.35 MHz (11.7 T magnet). The spectral width was set to 0.5 MHz and the recycle time to D_0 = 1 s. A single pulse sequence using a short pulse length of 1.1 μs corresponding to a π/16 pulse was used to extract quantitative data. However, it requires a first-order phasing process with a sin x/x baseline correction due to the dead time of the spectrometer not easily determined due to large overlapping signals. The external reference was a 1M $K_3Co(CN)_6$ aqueous solution.

Electron diffraction patterns as well as images of the samples were obtained using a JEOL 2100 transmission electron microscope working at an accelerating voltage of 200kV. Prior to their introduction in the microscope, samples were de-agglomerated in a mortar with addition of DMC, and a few drops of the resulting suspension were deposited on a copper grid with a formvar carbon film.

The morphology of the samples was analyzed by scanning electron microscopy with a Hitachi S4500 field emission microscope, after metallizing the powders with gold.

The magnetization of each sample was measured using a Quantum Design magnetic property measurement system within a range from 7 to 350 K in zero-field-cooled (ZFC) regimes using an applied field of 1T.

A.3. Study of the 2% Al doped $LiCoO_2$ materials as a function of the Li/M ratio (M=Co+Al)

A.3.1. Preparation of Al doped $LiCoO_2$ samples from solid state reaction

The 2% Al doped $LiCoO_2$ material series was synthesized by a solid state route at the Umicore R & D center. The precursors Li_2CO_3 and Co_3O_4, were initially blended with Al_2O_3 and heat treated at 1050°C for 12h to form the doped $LiCoO_2$ powders with various Li/M ratios (M=Co +Al) and Li/M =0.98, 1.00 or 1.02. Subsequently, grinding and annealing at 800 °C for 5 hours was carried out in order to ensure good homogeneity of the materials (**Figure A.1**), since all synthesis were performed for 10 g at Umicore.

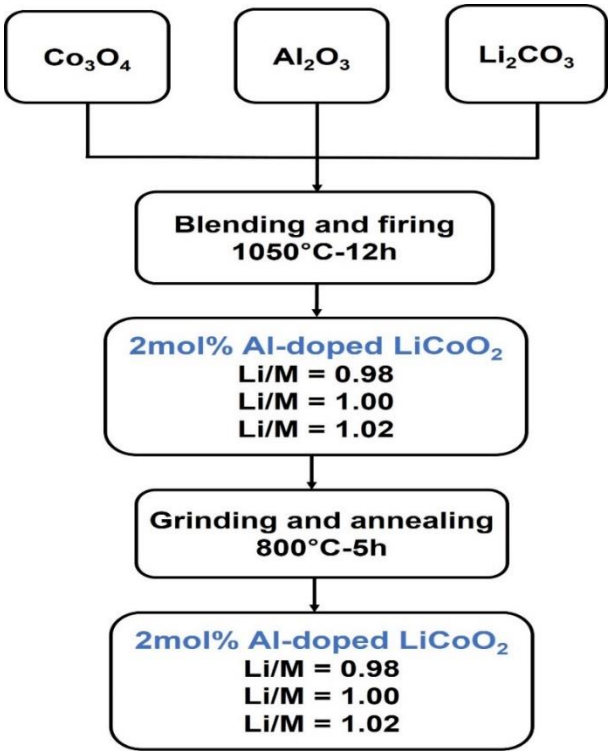

Figure A. 1. Schematic representation of the syntheses of the 2% Al doped $LiCoO_2$ samples with M=(Co+Al).

Additionally, for comparison stoichiometric- $LiCoO_2$ (st-$LiCoO_2$) and overlithiated $Li_{1.02}Co_{0.98}O_{1.98}$ were prepared following the experimental protocol detailed above. The Li_2CO_3 and Co_3O_4 were mixed and heat treated first at 1050°C for 12h then at 800 ° C for 5 hours. In order

to ensure the synthesis of st-$LiCoO_2$, a Li/Co ratio equal to 0.98 was used. In such thermodynamic synthesis conditions, the reaction products are expected to be st-$LiCoO_2$ with traces of Co_3O_4 impurity as will be discussed in the following. To prepare overlithiated $Li_{1.02}Co_{0.98}O_{1.98}$ a Li/Co=1.02 was used. Note that st-$LiCoO_2$ and overlithiated $Li_{1.02}Co_{0.98}O_{1.98}$ will be used as reference materials for all the manuscript.

Chemical analyzes by ICP-AES (Inductively Coupled Plasma - atomic emission spectroscopy) allowed to determine the final $(Li / Co)_{exp}$ and $(Li/(Co+Al))_{exp}$ ratios of the materials (**Table A.1)**. Experimental values are in good agreements with theoretical ones. However, one sample with $(Li/M)_{th} = 1.02$ shows a slight deviation to the theoretical value with $(Li/M)_{exp} \approx 1.01$.

Target formula	**Li/Co**		**Li/M (M=Co+Al)**	
	Target	**Experimental (ICP)**	**Target**	**Experimental (ICP)**
"$Li_{0.98}Co_{0.98}Al_{0.02}O_2$"	1.00	0.99	0.98	0.97
"$Li_{1.00}Co_{0.98}Al_{0.02}O_2$"	1.02	1.01	1.00	0.99
"$Li_{1.02}Co_{0.98}Al_{0.02}O_2$"	1.04	1.03	1.02	1.01
"$Li_{0.98}CoO_2$"	0.98	0.97	-	-
"$Li_{1.02}CoO_2$"	1.02	1.02	-	-

Table A. 1. ICP results for the prepared samples.

Additional characterization of the starting materials, such as synchrotron XRD, (^{7}Li, ^{59}Co, ^{27}Al) MAS NMR and magnetic properties are though required to draw proper conclusions about the exact chemical and structural nature of the phases, whose results will be shown later.

A.3.2. Structural characterization of the starting materials

A.3.2.1. Study of the morphology

Information regarding the morphology and the average size of the particles can be gathered from scanning electron microscopy (SEM) shown in **Figure A.2** for Al doped $LiCoO_2$ samples with various Li/M ratio. SEM micrographs have shown that all powders show a spherical-shaped particles and smother surface of the prepared particles with the highest Li/M.

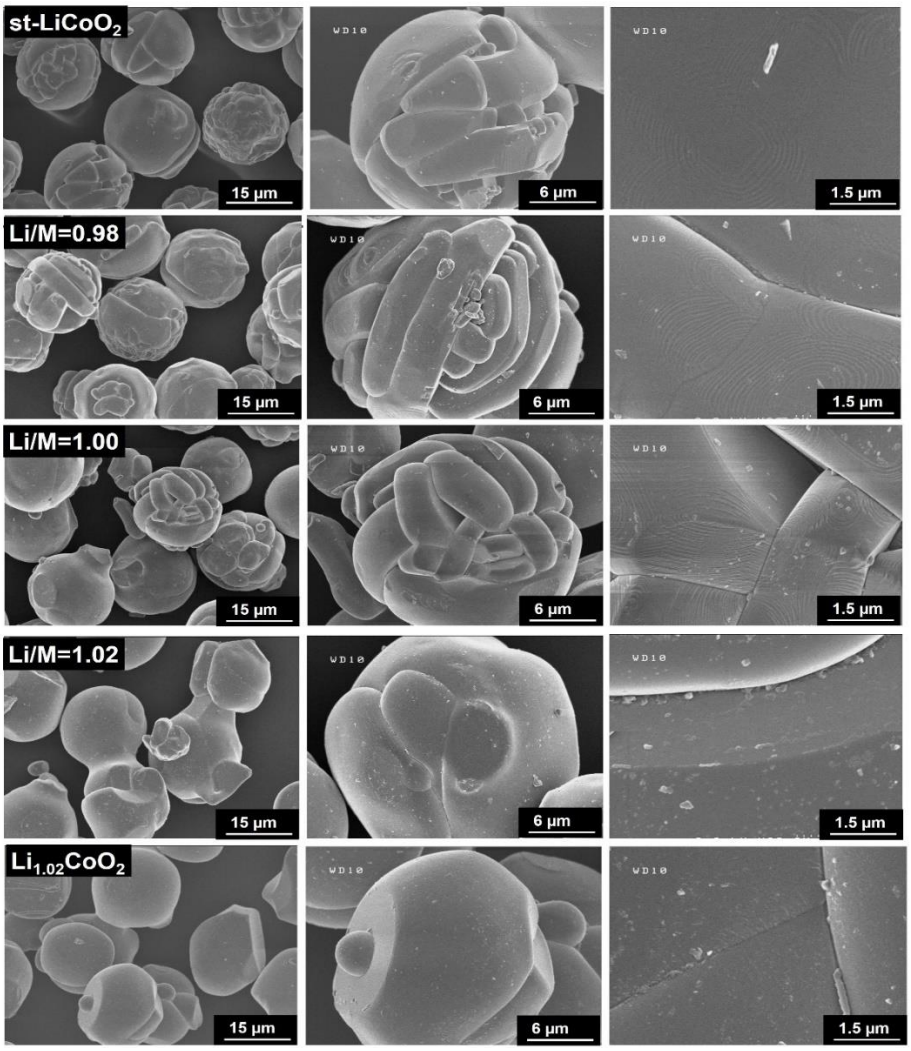

Figure A. 2. SEM micrographs of 2% Al doped $LiCoO_2$ samples with various Li/M ratio (M =Co+Al), compared to st-$LiCoO_2$.

The average particle size exhibited by all samples increases with the initial (Li/M) ratio, ranging from ~ 13 µm for Li/M=0.98 to ~ 15 - 25 µm Li/M=1.02 which was expected because of the flux role played by melted Li_2CO_3 during the heat treatment as in the case of st-$LiCoO_2$.[28–30]

A.3.2.2. Study of the average structure

Synchrotron X-ray diffraction (SXRD) patterns of st-$LiCoO_2$ and 2% Al doped $LiCoO_2$ with different Li/M ratio are presented in **Figure A.3**. All powders are well crystallized layered

phases, showing thin diffraction peaks indexed in the *R-3m* space group of the O3 stacking of $LiCoO_2$.

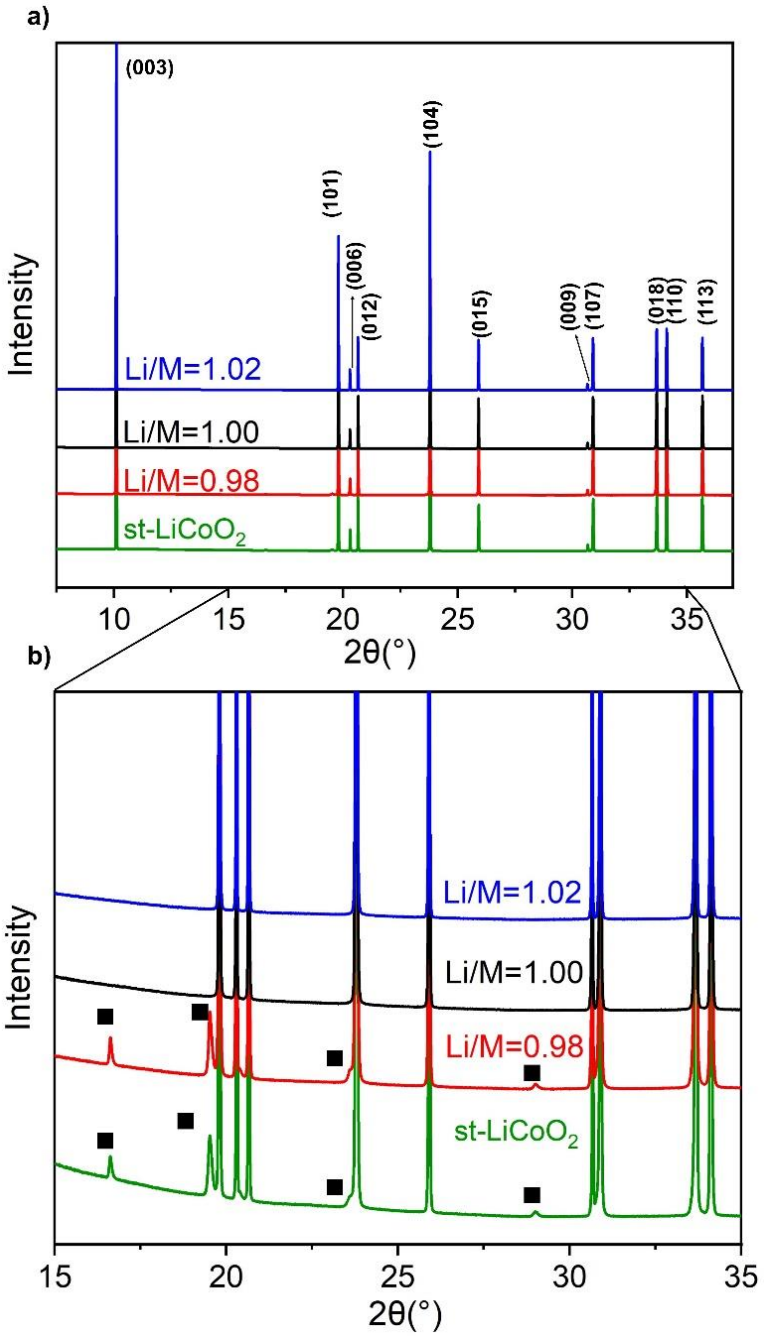

*Figure A. 3. S-X-ray powder diffraction patterns for 2% Al doped $LiCoO_2$ compared with st-$LiCoO_2$). A zoom in the b) 15° to 35° region (*All the patterns were collected with λ = 0.826 Å, ■: Co_3O_4)

Pure phases are obtained for Li/M ≥ 1.00, whereas additional weak peaks have been detected for Li/M =0.98 similar to st-$LiCoO_2$ arising from remaining traces of spinel (Fd3m space group) cobalt-based oxide precursors, as expected from the use of the Li/(Co+Al) = 0.98 ratio in the precursors mixture. The three Al-doped phases consist therefore in:

Li/M=0.98 → $LiCo_{0.98}Al_{0.02}O_2$ +Co_3O_4 (two phases)

Li/M=1.00 → $LiCo_{0.98}Al_{0.02}O_2$ (pure phase)

Li/M=1.02 → $Li_{1.02}Co_{0.98}Al_{0.02}O_2$ (pure phase)

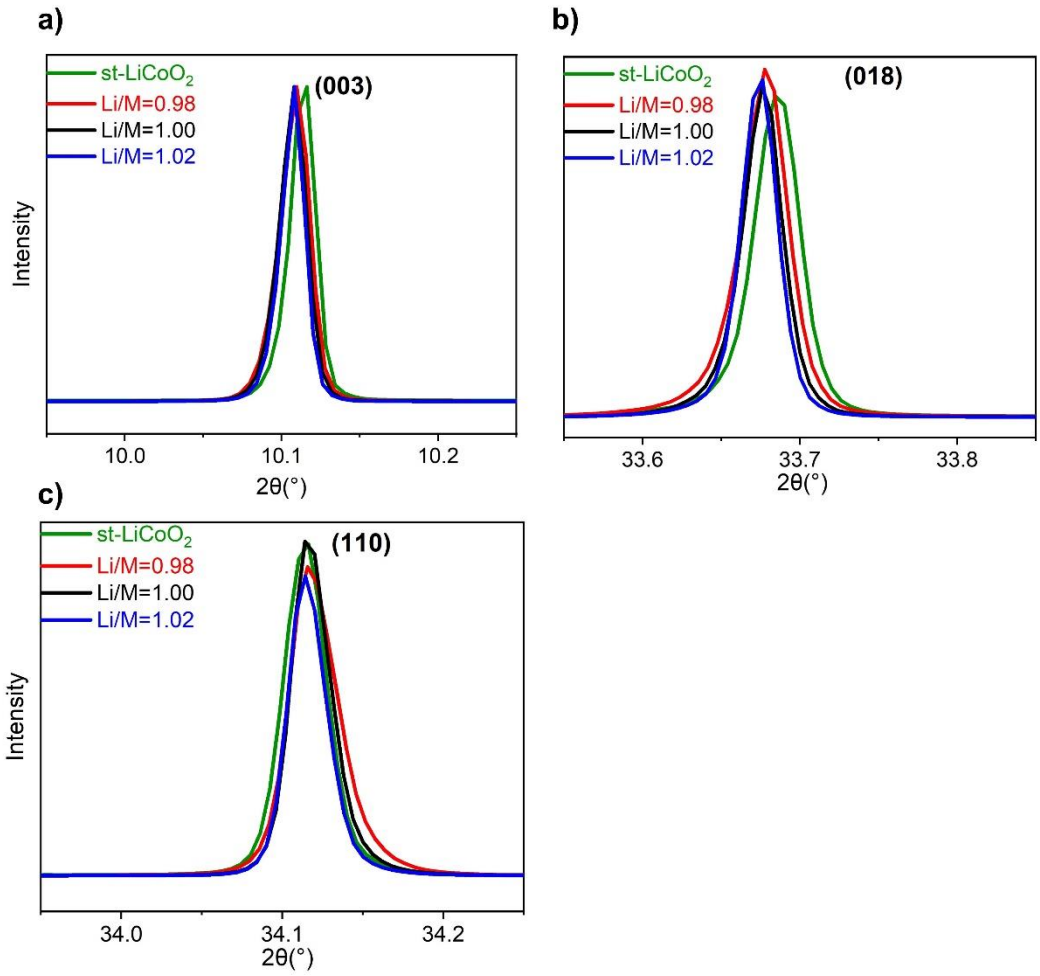

*Figure A. 4. Zoom on the a) (003), b) (018) and c) (110) diffraction peaks from the synchrotron X-ray diffraction patterns (*All the patterns were collected with λ = 0.826 Å).

Compared to st-$LiCoO_2$, Al doped materials exhibit (003) and (108) diffraction peaks shifted toward lower angles and the (110) peak is almost not shifted (**Figure A.4**) what indicates a $c_{hex.}$ increases and a rather similar $a_{hex.}$ lattice. The lattice constants deduced from Le bail refinement on the SXRD data are shown in **Table A.2**. Clearly, substitution of Al for Co leads to a longer $c_{hex.}$ which is consistent with previous studies.[21,26,31,32] The refined $a_{hex.}$ are, however, rather similar here, in agreement with very similar ionic radius size for Al^{3+} and LS-Co^{3+}: $r_{Al^{3+}} = 0.535$ Å, $r_{Co^{3+}} = 0.545$ Å. The $c_{hex.}$ lattice parameter related to the interlayer distance, increases more significantly. The refined cell parameters for Co_3O_4 as impurity for st-$LiCoO_2$ and the doped material with Li/M=0.98 are rather similar to the one reported in literature (a=8.084 Å).[33]

Samples	**a_{hex} (Å)**	**c_{hex} (Å)**	**c/a**
st-$LiCoO_2$ + Co_3O_4	2.8158 (9)	14.0532 (8)	4.99
	8.0702 (8)	-	-
Li/M = 0.98: Al-doped phase + Co_3O_4	2.8153 (1)	14.0595 (1)	4.99
	8.0750 (8)	-	-
Li/M = 1.00 : Al-doped phase	2.8154 (1)	14.0593 (1)	4.99
Li/M = 1.02 : Al-doped phase	2.8156 (1)	14.0610 (6)	4.99

Table A. 2. Hexagonal lattice parameters deduced from synchrotron X-ray refinement of various Al doped $LiCoO_2$ materials.

It has been demonstrated in a previous PhD study, that SXRD is a powerful technique to discuss the homogeneity of the Al doping. Indeed, if an Al gradient composition exist in the sample, it leads to a distribution of cell parameters resulting in some asymmetric broadening. This was especially observed for the (018) and (110) peaks.[26] Among the various Al-doped material, the one prepared with Li/M =0.98 exhibits some asymmetry toward smaller angles for the (018) peak, and toward higher angles for the (110) one (**Figure A.4**). This suggests that this compound exhibits an inhomogeneous distribution of Al with domains containing more than 2% of Al and domains containing less than 2% with a composition gradient. The other doped samples exhibit symmetrical

diffraction lines indicating a good homogeneity of Al/Co cation repartition. Note that, the diffraction lines of our samples were even thinner than the ones of the standards used for calibration using the MYTHEN detector, what prevent the possibility of performing Rietveld refinements.

A.3.2.3. Study of the local structure

a) ^{7}Li MAS NMR

As mentioned in the introduction, ^{7}Li and ^{27}Al MAS NMR are key tools to probe respectively the Li/M stoichiometry, and the homogeneity of the materials. **Figure A.5** shows ^{7}Li MAS NMR spectra for the 2% Al doped $LiCoO_2$ samples prepared with various Li/M ratios, compared to stoichiometric and overlithiated $Li_{1.02}Co_{0.98}O_{1.98}$. The samples with Li/M ≤ 1.00 present a single signal near to 0 ppm like st-$LiCoO_2$. This is a typical signature for the stoichiometry as it has been already reported;[34] which can be explained by the fact that all cobalt ions are in low spin state (LS-Co^{3+}: $t_{eg}^{6}e_{g}^{0}$), leading to a Li signal characteristic for a diamagnetic environment. The Li^{+} ions are therefore surrounded by 6 M^{3+} as first cationic neighbor (90° Li-O-M) and 6 M^{3+} as second cationic neighbor (180° Li-O-M). A distribution of Al^{3+} and Co^{3+} around Li is expected and lead to a small broadening of the signal compared to st-$LiCoO_2$.

The sample prepared with Li/M = 1.02, exhibits a large number of additional signals located at 1063, 176, 7.70, 3.78, -5.28, -10.04, and -14.60 ppm really similar to the signals observed for overlithiated $[Li]_{interslab}[Co_{0.98}Li_{0.02}]_{slab}O_{1.98}$ (**Figure A.5**). In fact, paramagnetic intermediate spin state (IS-Co^{3+} $d_{xz}^{2}\,d_{xy}^{2}\,d_{yz}^{1}\,d_{z2}^{1}\,d_{x2-y2}^{0}$) cobalt ions are formed due to Li in Co layer with the presence of the oxygen vacancy.[24,35] Hyperfine interactions are therefore expected with all adjacent Li nuclei as 1st/2nd neighbors. The complete attribution of signals could not be realized. We, however, believe that the signal with the larger shift located at 1063 ppm (**Figure A.5.c**), is attributed to Li located in the transition metal layer. Indeed, this Li would undergo a strong Fermi contact interaction with two IS-Co^{3+} ions (**Figure A.6.b**) due to the unpaired electron in the t_{2g} type orbital, pointing in the direction of the former O-O edge between LiO_6 and CoO_6, not present anymore due to the O vacancy. All other signals are assigned to Li located in the interslab space with various environments versus IS-Co^{3+} and O-vacancy. The intensity of the Fermi-contact shifted signals is directly linked to the amount of Li excess found inside the CoO_2 layers.

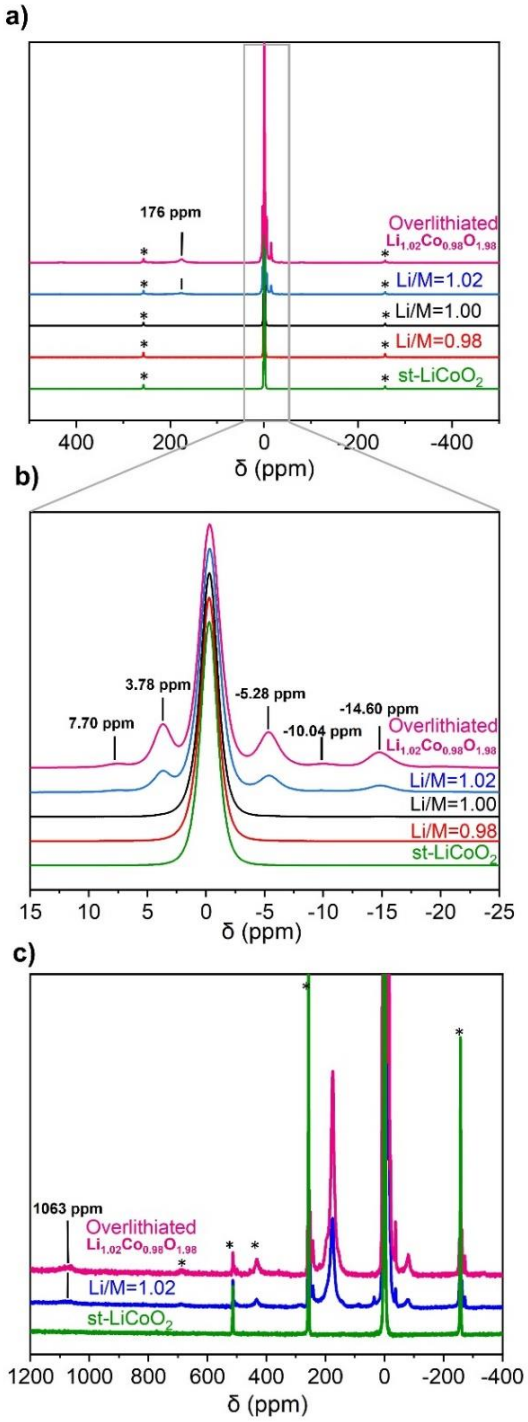

*Figure A. 5. (a) ^{7}Li MAS NMR spectra of 2% Al doped $LiCoO_2$ samples with various Li/M stoichiometries (M=Co+Al) compared with stoichiometric and overlithiated $Li_{1.02}Co_{0.98}O_{1.98}$ (Hahn echo, B_0 = 7.05T *: spinning sidebands), (b) zoom in the region (-25 ppm ≤ δ ≤ 15 ppm) and (c) Li/M=1.02 compared with overlithiated $Li_{1.02}Co_{0.98}O_{1.98}$.*

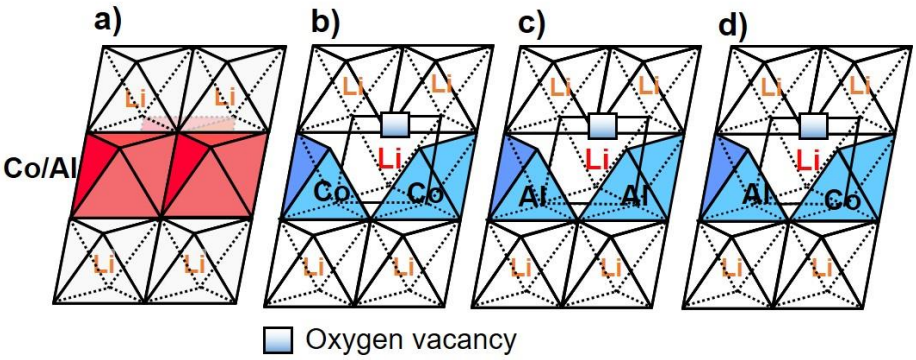

Figure A. 6. a) Schematic representation of partial Li environment for Li/M =1.00. Additional Li environments for Li/M >1.00 in b, c and d. (M=Co+Al)

As discussed above, the additional signals for Al doped sample (Li/M=1.02) are similar to those shown for the overlithiated $Li_{1.02}Co_{0.98}O_{1.98}$ but exhibit weaker intensity. This can reflect either a lower amount of Li in the TM layer or a strong preference for two Al to be located near to the O vacancy forming thus two adjacent AlO_5 environments (**Figure A.6.c**). In that case, no paramagnetic interactions are expected for the adjacent Li, that should contribute to the intensity of the signal around 0 ppm. The formation of one CoO_5 and one AlO_5 around the O vacancy is rather unlikely (**Figure A.6.d**), as one would have expected Li environments different than in overlithiated $Li_{1.02}Co_{0.98}O_{1.98}$ because of the interaction with a single IS-Co^{3+} instead of two and therefore different shifted signals.

b) ^{27}Al MAS NMR

^{27}Al MAS NMR was used to probe the Al environments at a local scale. As discussed in previous work, different signals are observed corresponding to different Al environments, denoted as Al-(Al_nCo_{6-n}), for Al surrounded by n Al^{3+} and (6-n) Co^{3+}.[25,26] From Gaudin's study on $Li(Co_{1-y}Al_y)O_2$ samples (See **Figure A.7**), the signal with the higher chemical shift located at ~62 ppm corresponds to Al surrounded by 6 Co in the slab (denoted as Al-(Al_0Co_6)). The set of other signals located at ~ 55, ~ 48, ~ 40, ~ 33, ~ 26, ~ 18 ppm correspond to Al surrounded by n Al^{3+} and (6-n) Co^{3+} with n varying respectively from 0 to 6.

A zoom around the central transition of the ^{27}Al MAS NMR spectra is plotted in **Figure A.8.**

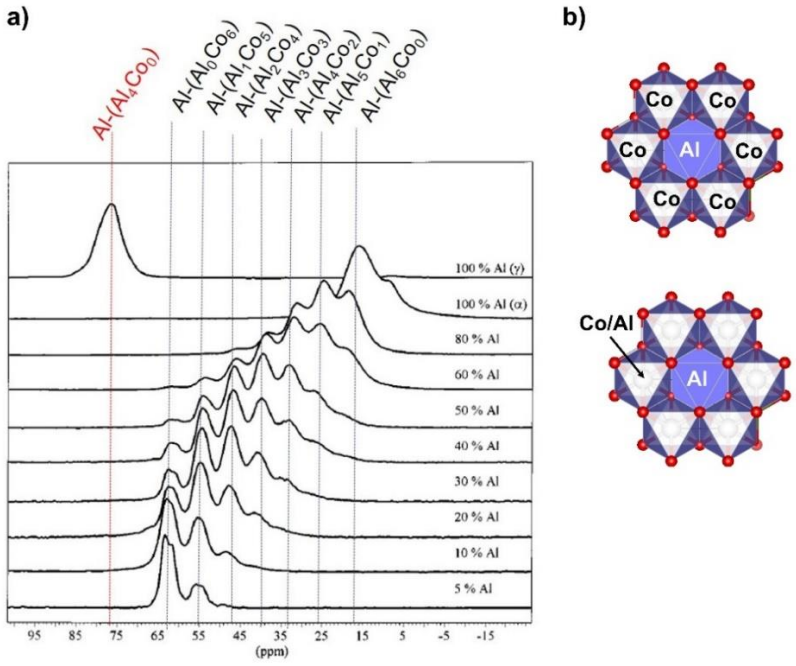

Figure A. 7. [27]*Al NMR spectra reported by Gaudin et al.*[25] *with b) a schematic representation of Al environments*

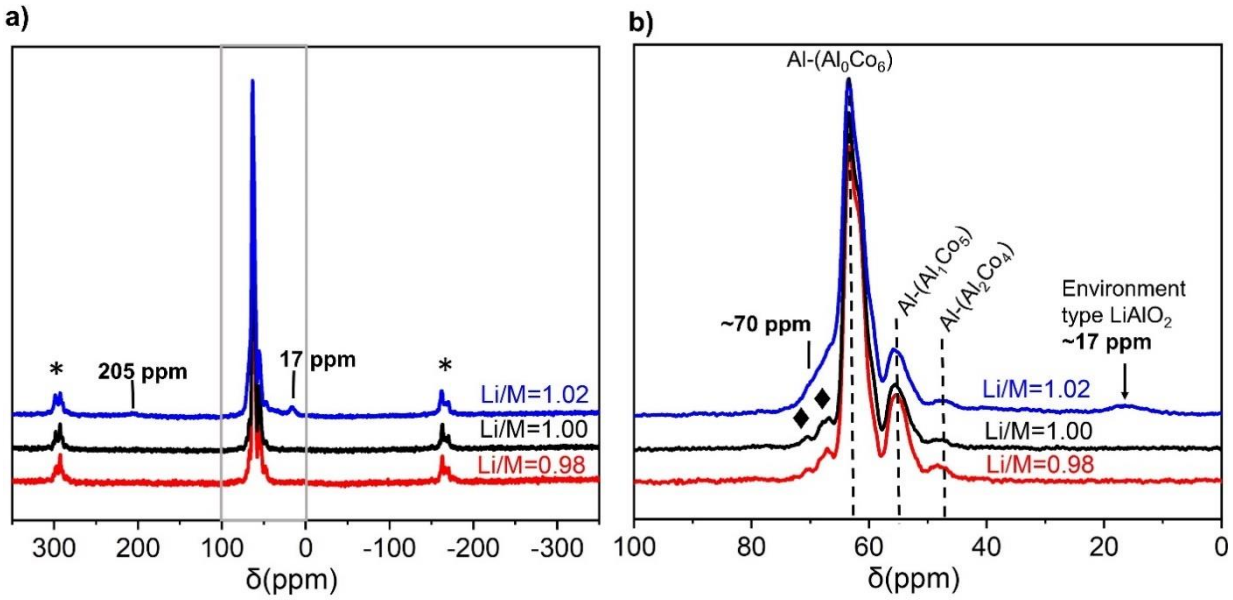

Figure A. 8. (a) [27]Al and MAS NMR spectra of 2% Al doped $LiCoO_2$ samples with various Li/M ratio *(M=Co+Al)*. A zoom in the central transitions is given in (b) (*: spinning sidebands, ♦: satellite transitions at 69 and 73 ppm)

The Li/M=0.98 and Li/M=1.00 samples present similar Al spectra: a main signal with the larger chemical shift located at ~62 ppm is attributed to the Al with 6 Co^{3+} as first cationic neighbors in the TM layer. This signal exhibits a clear second order quadrupolar line shape. Small signals located around 69 and 73 ppm are assigned to the satellite (±1/2; ±3/2) and (±3/2; ±5/2) transitions expected for this main signal. In addition, two other signals are observed at 56 and 48 ppm corresponding respectively to Al-(Al_1Co_5) and Al-(Al_2Co_4) environments. The Li/M=0.98 and Li/M=1.00 samples do not exhibit other Al environments that would be Al-richer (**See Figure A.7**) since they are not expect for a low Al doping amount and a good Al repartition.

The sample prepared with lithium excess (Li/M=1.02) clearly shows new additional signals located at ~ 17 ppm, ~ 70 ppm and ~ 205 ppm. The discussion of the origin of these signals can be given as the following:

- As outside of the standard chemical shift window for Al nuclei, the broad shifted signal located at ~ 205 ppm can be assigned to Al in the vicinity of paramagnetic IS-Co^{3+} that therefore undergoes a hyperfine interaction. A positive shift can be expected for the 90° $Co^{3+(IS)}$-O-Al interaction trough a delocalization mechanism by hybridization between the t_{2g} orbital of Co^{IS} carrying a spin pointing toward the middle of the O-O common edge and the 3s orbital of Al^{3+} (**Figure A.9.a**). Note that we discarded the possible environment of Al in square-based pyramid next to IS-Co^{3+} as described in **Figure A.6.a** based on ^{7}Li MAS NMR.
- The signal located around 70 ppm that overlap the satellite transitions of the main signals, is then assigned to Al^{3+} ions in AlO_5 diamagnetic environments located nearby the O-vacancy and therefore surrounded in the slab by 4 LS-Co^{3+}, 1 Al^{3+} and 1 Li^+(**Figure A.6.c**). Indeed, chemical shift range around 70 ppm is reported in literature for AlO_5 environment **(Figure A.9.b)**.[36]
- Finally, the signal located at ~ 17 ppm correspond to Al surrounded by 6 Al in the slab as in layered α-$LiAlO_2$ (**Figure A.9.b**).[37] Such local environment is not expected from the statistical homogeneous repartition of Co and Al in the slab. Synchrotron XRD study, however indicated a good Al/Co repartition since no peak asymmetry was observed for this phase. Note that no crystalline secondary

α-$LiAlO_2$ was neither detected by XRD. We therefore believe that those Al-rich environments are not present inside the Al-doped material, but probably on the surface as an amorphous or nano-sized phase.

The Al-doped Li/M = 1.02 compound would therefore consist in a rather homogenously Al-doped material (although two Al seems to segregate around the O vacancies and the Li present in the slab) and amorphous or nano-sized α-$LiAlO_2$ type domain that could be located at the surface of the particles. Further investigation of the material surface will be required to better understand those observations, but regarding the low amount of the Al-rich environments, this may be challenging.

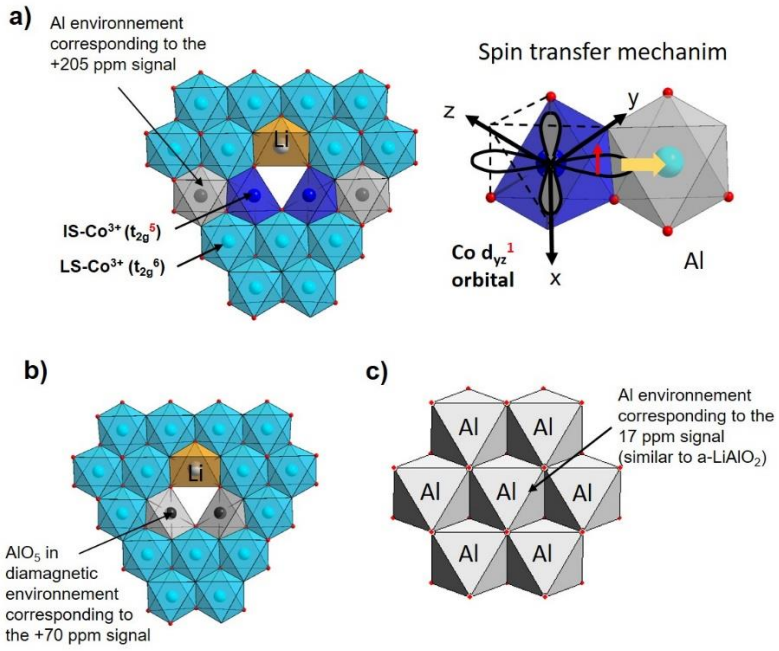

Figure A. 9. Schematic representation of Al environments for the Li/M =1.02 sample (M=Co+Al).

One can compute the probability P(y, 6-n) of each Al-(Al_nCo_{6-n}) environment assuming a statistical distribution of Al and Co, for a $LiCo_{0.98}Al_{0.02}O_2$ composition (y = 0.02) using the following binomial law:

$$P(y, 6-n) = C_6^{6-n} y^n (1-y)^{6-n}$$

For example, in the case of n=0 the probability to find Al surrounded by Al_0Co_6 atoms as second neighbours expected at 62 ppm for y = 0.02 composition is 0.88.

The resulting theoretical intensity distribution is schematically depicted by the orange rectangles. For such a low Al-doping amount, negligible signal intensity is indeed expected for Al-(Al_3Co_3) environments and for Al-richer ones (n > 3). Although, the relative intensities observed for all doped sample slightly deviate from the theoretical ones (**Figure A.10**), the Li/M=1.00 sample appears to be the most homogeneous one. The sample prepared with Li/M=0.98, exhibits larger relative intensity than expected for Al-(Al_1Co_5) and Al-(Al_2Co_4) environments indicated a less homogeneous sample, in agreement with our conclusions from synchrotron XRD (this sample exhibited some asymmetrical broadening due to Al composition gradient). Finally, the Li/M=1.02 sample consist in a rather homogenously Al-doped material with some additional α-$LiAlO_2$ domains discussed above.

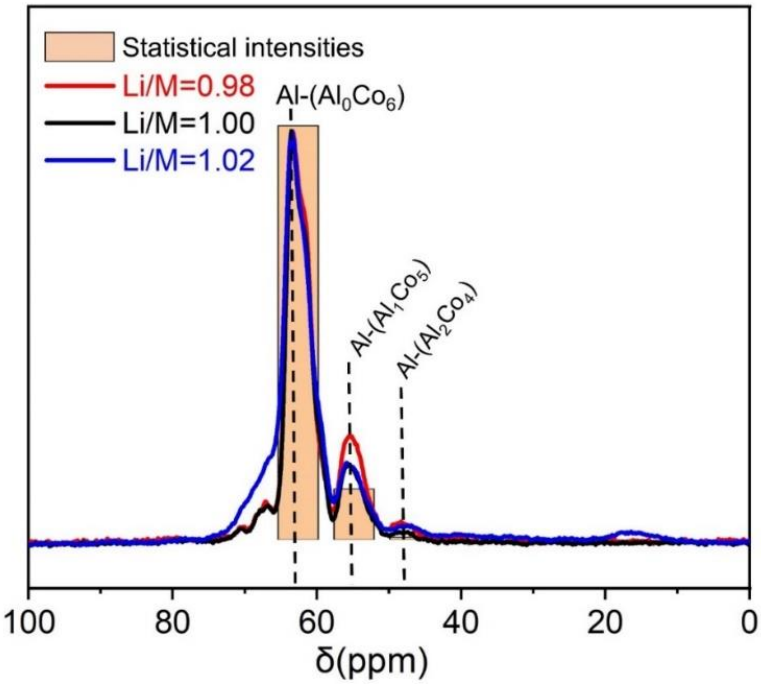

Figure A. 10. ^{27}Al MAS NMR spectra recorded at 130.33 MHz using a 30 kHz spinning frequency of the 2% Al doped $LiCoO_2$ *samples in comparison with the theoretical intensity distribution of the different Al environments versus Co, expected for a 2% Al-doped sample.*

c) ^{59}Co MAS NMR

^{59}Co MAS NMR was used in addition to ^{27}Al MAS NMR to characterize the Co local environments in the materials. **Figure A.11** displays a zoom in the central transition of ^{59}Co MAS NMR for the different 2% Al doped $LiCoO_2$ material in comparison with the st-$LiCoO_2$. The latter exhibits a single signal located at 14137 ppm as expected for LS-Co^{3+} surrounded by 6 LS-Co^{3+} in the slab in agreement with literature[38]. Despite broader signals observed for ^{59}Co MAS NMR, compared to ^{27}Al MAS NMR, distinct signals can be resolved for the Al doped material. The most intense one located at 14132 ppm is assigned to LS-Co^{3+} ions surrounded by six other LS-Co^{3+}, denoted as Co-(Co_6Al_0). The other signals located at 14105 ppm, 14077 ppm and 14047 ppm are assigned to Co surrounded by n Al^{3+} and (6-n) Co^{3+} in the slab with n varying respectively from 1 to 3, denoted as Co-($Co_{6-n}Al_n$).[26] Comparison with statistical intensities was less straightforward due to the strong overlap of those broad signals, but no Al-rich environments (n = 4, 5 and 6) were detected.

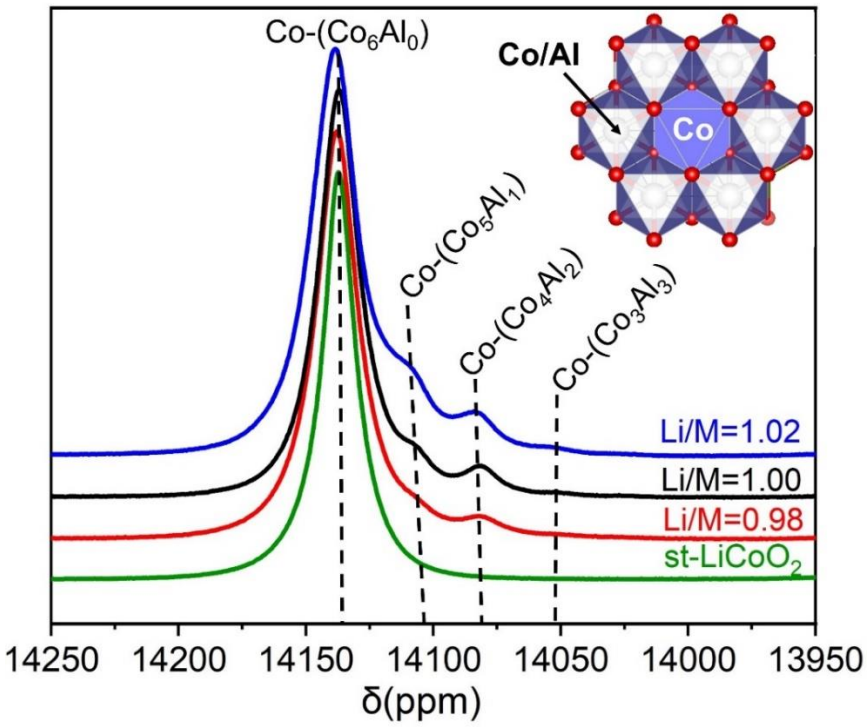

Figure A. 11.^{59}Co MAS NMR spectra of 2% Al doped $LiCoO_2$ samples with various Li/M ratio.

Since the ^{59}Co NMR chemical shift range is very large, the shift position is very sensitive to the local environments (distances, angles). Therefore, as an inhomogeneous Al-doping in $LiCoO_2$ generates a larger distribution of distances and angles around Co, it leads to signals broadening. The most homogenous material of the series from ^{59}Co MAS NMR is therefore the one with Li/M =1.00 confirming thus the results from ^{27}Al MAS NMR.

A.3.2.4. Study of magnetic properties

The molar magnetic susceptibility data of measurement for 2% Al $LiCoO_2$ doped samples are plotted as a function of temperature in **Figure A.12**.

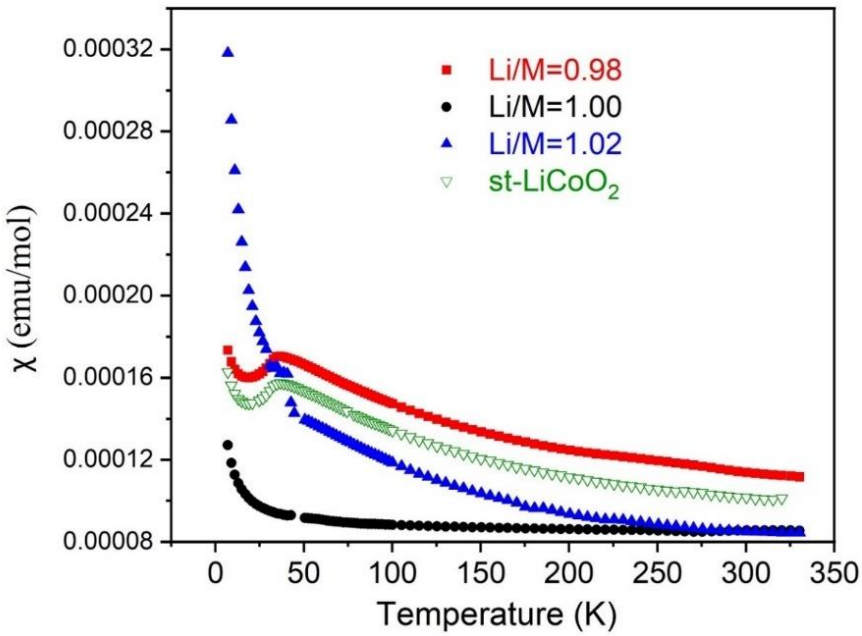

Figure A. 12. Thermal evolution of the molar magnetic susceptibility for 2% Al doped $LiCoO_2$.

For st-$LiCoO_2$, one expect the magnetic susceptibility (χ) to be almost temperature (T) independent and result from the Van Vleck-type paramagnetism associated with diamagnetic LS-Co^{3+} ions in the structure[39,40]. However, here since the st-$LiCoO_2$ was prepared with a Li/Co ratio equal to 0.98, residual Co_3O_4 is present and leads to a temperature dependence with a bump observed at 35 K , due to the antiferromagnetic transition of the Co_3O_4 phase study.[40] The Al doped $LiCoO_2$ (Li/M=0.98) and st-$LiCoO_2$ (Li/Co=0.98) exhibit similar curves, which clearly confirms our previous conclusion regarding this sample that consists in a mixture of $LiCo_{0.98}Al_{0.02}O_2$ and

Co_3O_4. The Al doped sample (Li/M=1.00) sample clearly shows a temperature independent magnetic susceptibility from 50 K in agreement with the present of diamagnetic LS-Co^{3+} ($t_{2g}^6e_g^0$) in that sample. On the contrary, the overlithiated material (Li/M=1.02) exhibits a typical Curie-Weiss behavior for the magnetic susceptibility for T >100 K, in good agreement with the presence of IS-Co^{3+} ions as discussed from ^{7}Li MAS NMR results. Only for those two samples, we were able to fit satisfactorily the curves using the Curie Weiss law: ($\chi = \chi_0 + C/(T-\theta)$). The Curie constant value fitted for the Li/M = 1.02 sample is much lower than the one expected if one considers that all Li in the TM layer are located next to two IS-Co^{3+} (C_{th} = 0.04 emu.K.mol^{-1} in that case). This indicates that Li in the TM layer is also located next to some diamagnetic AlO_5 pyramids in agreement with our NMR study.

Li/M	χ_0 (emu.mol^{-1}) × 10^{-5}	C (emu.K.mol^{-1})
1.00	8.36 (1)	0.001 (2)
1.02	6.55 (1)	0.006 (1)

Table A. 3. The calculated diamagnetic susceptibility χ_0 and the Curie constant C from the fitting of the $\chi=f(T)$ curve in the 100-300K temperature range.

A.3.2.5. Discussion

The combination of SXRD, ^{7}Li, ^{27}Al and ^{59}Co MAS NMR and magnetic measurements leads to the following conclusions:

- The sample prepared with Li/M = 0.98 is biphasic: it consists in a non-homogeneously Al-doped material with a mean Al content slightly higher than 2% ($LiCo_{0.98-\varepsilon}Al_{0.02+\varepsilon}O_2$) and Co_3O_4.
- The sample prepared with Li/M=1.00 is the most homogeneous Al-doped material of the series corresponding to a single $LiCo_{0.98}Al_{0.02}O_2$ phase with only LS-Co^{3+} ions.

- The sample prepared with Li/M=1.02 consists in a $Li_{\sim 1.02}[Co_{\sim 0.98}Al_{\sim 0.02}]_{\sim 0.98}O_{\sim 1.98}$ phase with an ε amount of α-$LiAlO_2$ type domains that are believed to be located at the surface of the particles, that lowered slightly the amount of excess of Li and Al in the doped material. The $Li_{\sim 1.02}[Co_{\sim 0.98}Al_{\sim 0.02}]_{\sim 0.98}O_{\sim 1.98}$ material exhibits a rather homogeneous repartition of Al, although around the Li excess ions in the TM plane, its seems more favorable to have either two IS-Co^{3+} ions or two Al^{3+} ions in square-based pyramids (and not one IS-Co^{3+} and one Al^{3+}).

A.3.3. Influence of Li/M ratio on the electrochemical performance

The first cycle for Li//$Li_xCo_{0.98}Al_{0.02}O_2$ cells of the various 2% Al doped materials (Li/M=0.98, 1.00 and 1.02) is plotted in **Figure A.13**. All curves are plotted as a function of both Li content in the phase (x in $Li_xCo_{0.98}Al_{0.02}O_2$) and the capacity in mAh/g. The molar mass used to calculate the capacity is therefore different depending on the initial Li/M ratio. As previously reported, the galvanostatic charge curve obtained for the Li_xCoO_2 material shows several phase transitions: the potential plateau at 3.93 V corresponding to the two-phase domain for $0.75 \leq x \leq 0.94$ due to an insulator-metal transition, the monoclinic distortion for x = 0.5 resulting from a Li / vacancy ordering in the interslab and then the formation of the H1-3 phase around x ~0.17 revealed by a clear change of slope.[9,41–43] A different behavior is observed in the case of the phases doped with aluminum even with very low quantity (2%). The trace of the monoclinic distortion for x = 0.5 disappeared for Li/M≥1.00. This can be explained by the presence of Al^{3+} in substitution of some Co^{3+} which prevent the Li/vacancy ordering. It was also the case for the overlithiated $LiCoO_2$, even a very little excess of Li found in the Co layers hinders the Li-vacancy ordering at x = 0.5.[24]

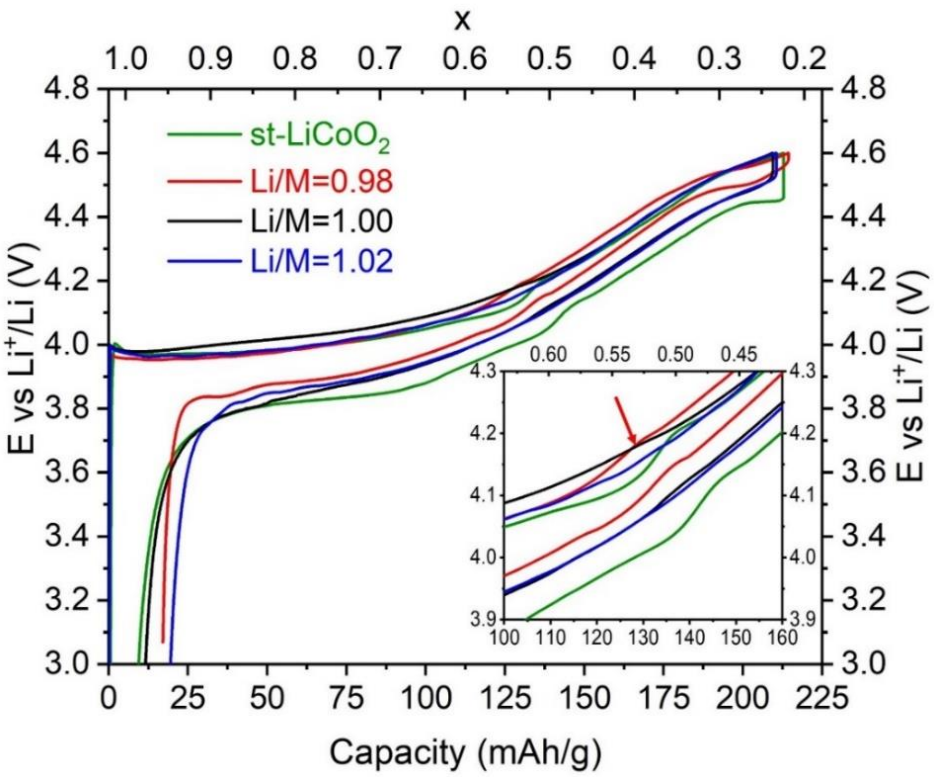

Figure A.13. First cycle for 2% Al doped $LiCoO_2$ at C/20 as positive electrode in $Li//Li_xCo_{0.98}Al_{0.02}O_2$ compared to those of st-$LiCoO_2$. A zoom on the monoclinic transition is given in insert.

The absence of a phase transition further confirms that Al is successfully introduced into the lattice, suppressing the phase transitions. Whereas, for the doped material with Li/M=0.98, the monoclinic transition is still observed as shown by the small change of slope in the near x= 0.5 region. This is a further evidence of an inhomogeneous Al-doping leading to the coexistence of un-doped and Al doped domains in agreement with our previous conclusion from SXRD and MAS NMR. Consequently, it is true that greater amount of Al doping influence the electrochemical performances, it seems that even percentages as small as 2% of Al also have a measurable effect on electrochemical properties.

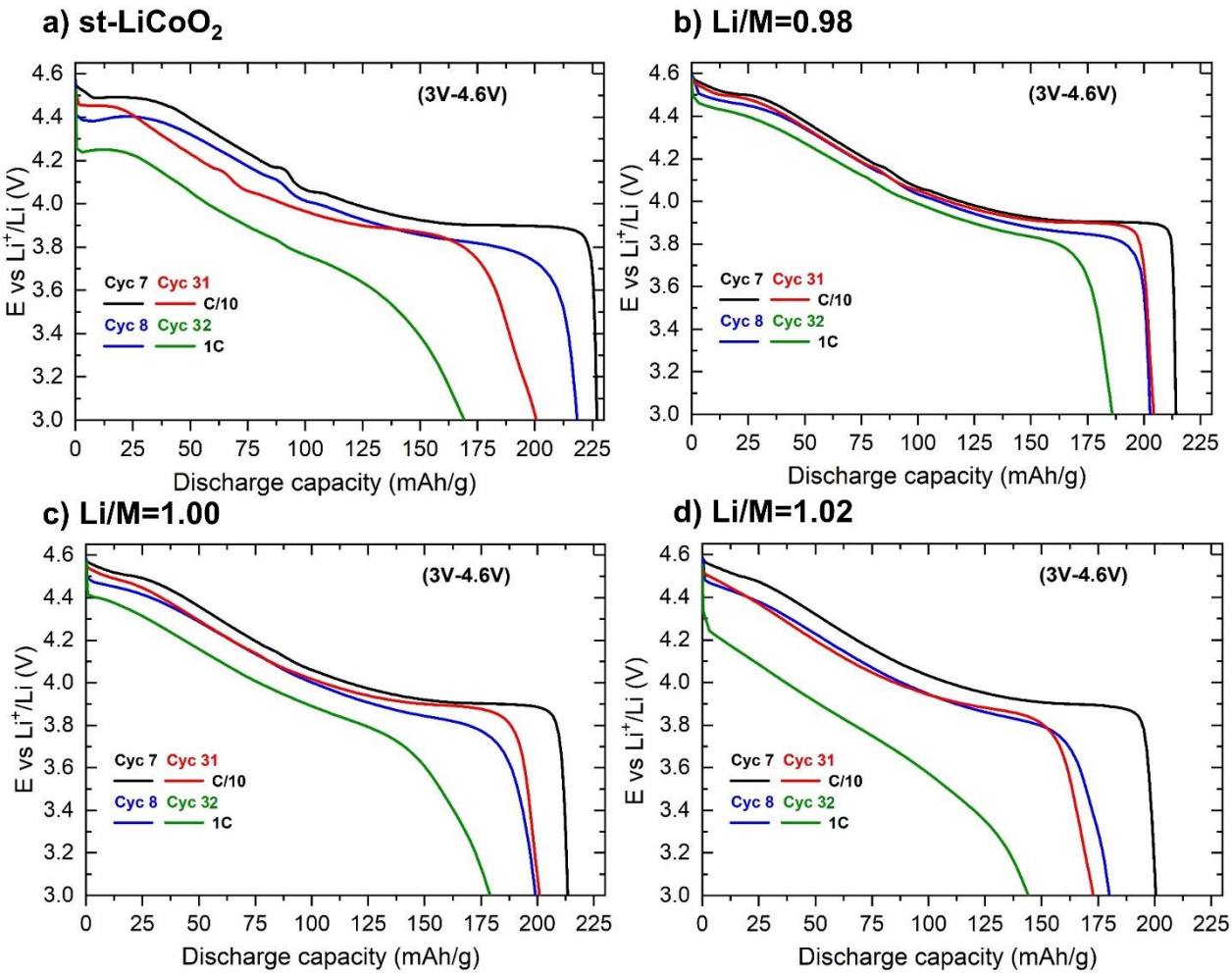

Figure A.14. Discharge profiles (3V-4.6V) of Li//$Li_xCo_{0.98}Al_{0.02}O_2$ cells observed for the 7, 8, 31 and 32th cycles using C/10 and 1C rates compared to st-$LiCoO_2$.

Extended electrochemical tests were further performed in the 3-4.6V range. **Figure A.14** shows the discharge capacity profiles of st-$LiCoO_2$ compared to 2% Al doped materials with various Li/M ratios at 1C and C/10 cycling rate. The 7th discharge capacity of st-$LiCoO_2$ is 227 $mAhg^{-1}$, which is higher than Al doped samples showing 213 $mAhg^{-1}$ and 200 $mAhg^{-1}$ for Li/M ≤ 1.00 and Li/M=1.02 respectively with C/10 cycling rate. However, the discharge capacity is improved by Al doping with Li/M≤ 1.00. In **Figure A.15**, the discharge capacity is plotted as a function of the number of cycles. The materials were cycled with a cutoff voltage of 4.5V for the first six cycles using different C rates. Then, from cycle number 7 a cutoff voltage of 4.6V has been

used with 1C or C/10 cycling rate. Good cyclability appears for Al doped sample with Li/M ≤ 1.00. In agreement with literature, Al doping improves the capacity retention upon cycling.

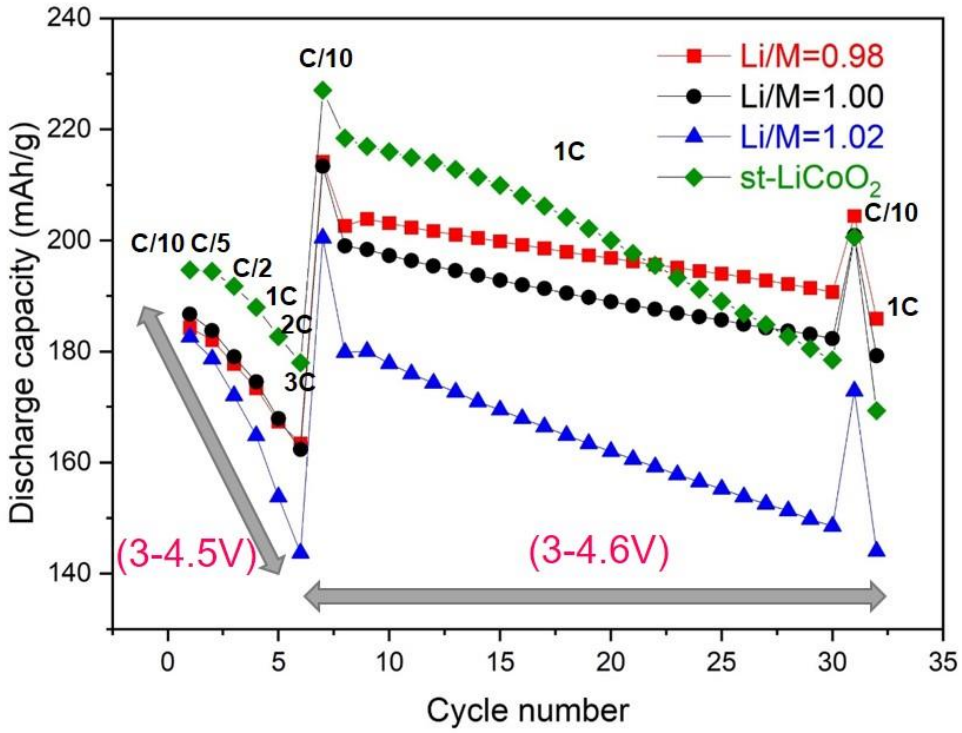

Figure A. 15. Cycling performances of st-$LiCoO_2$ compared to Al doped $LiCoO_2$ with various Li/M ratios using different C rates.

A.3.4. Conclusion on the 2% Al doped $LiCoO_2$ with various Li/M ratio

In this first chapter of **Part A**, series of 2% Al doped $LiCoO_2$ materials has been synthesized with different Li/M ratio (0.98, 1.00 and 1.02) from solid state reaction of (Co_3O_4, Al_2O_3) and Li_2CO_3. The understanding of the Al distribution within these Al doped $LiCoO_2$ powders has been succeeded through the combined use of synchrotron XRD with ^{27}Al and ^{59}Co MAS NMR. Moreover, ^{7}Li MAS NMR has shown to be a key technic when it comes to discussing the proper Li stoichiometry, and also the presence of Li excess within the structure to form overlithiated phases can only be certified through their NMR spectra, as the difference is in the local scale and cannot be detected either from XRD. The synthesized materials consist of:

- **For Li/M=0.98: $LiCo_{0.98-\varepsilon}Al_{0.02+\varepsilon}O_2$** and **$Co_3O_4$.**

- **For Li/M=1.00:** Single **$LiCo_{0.98}Al_{0.02}O_2$** phase presenting the most homogeneous Al distribution**.**
- For **Li/M=1.02: $Li_{\sim 1.02}[Co_{\sim 0.98}Al_{\sim 0.02}]_{\sim 0.98}O_{\sim 1.98}$** with a rather homogeneous Al-doping and presence of Li excess in the (Co, Al) slab preferentially surrounded by two IS-Co^{3+} or two Al^{3+} in square pyramids, and ε amount of α-$LiAlO_2$ type domains that are believed to be located at the surface of the particles.

Electrochemical tests clearly evidence that the initial Li/M ratio influences the electrochemical properties even with the same amount of aluminum, and it has been shown from these results that the possible contribution of Li excess leads to the increase of capacity losses. However, good capacity retentions were obtained for samples with Li/M $\leq$1.00 up to 4.6V.

A.4. Understanding the role of Al doping of $LiCoO_2$ on the mechanisms upon cycling up to 4.8V vs. Li^+/Li

In order to study the role of the Al doping on the mechanisms upon cycling, we selected a material with a larger quantity of dopant: 4% Al, although still reasonable from application point of view. This sample was prepared during the PhD of Marie Duffiet in our group among several 4 % Al-doped $LiCoO_2$ materials with a controlled Li/(Co +Al) stoichiometry.[26,27] A specific solid state synthesis route, described below, allows to get a sample as homogenously doped as the one obtained by a coprecipitation route followed by a heat treatment.

A.4.1. Preparation of the 4% Al-doped $LiCoO_2$

The 4% Al-doped $LiCoO_2$ sample was synthesized in Umicore R&D center by a solid state route from a mixture of Al_2O_3, Co_3O_4 and Li_2CO_3.[26]

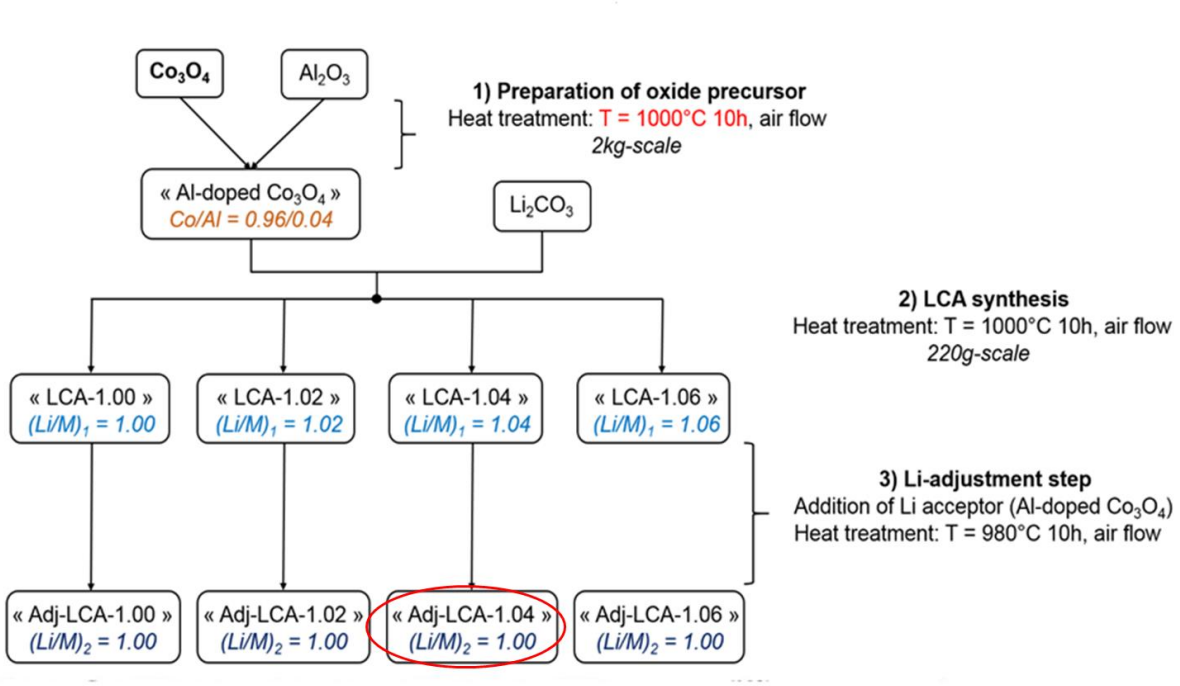

Figure A. 16. Schematic representation of synthetic routes for 4 % Al doped $LiCoO_2$ from Duffiet's PhD.[27]

The synthesis has been made in 3 steps: in the first step, Co_3O_4 and Al_2O_3 were grinded and heat-treated under air at T = 1000 ° C for 10h in the ratio Co / Al = 0.96 / 0.04 to form the Al-doped Co_3O_4 precursor. The precursor is mixed in a second step with Li_2CO_3, in various ratios (Li/ Co + Al) = 1.00, 1.02, 1.04, 1.06 and then the powers were thermally treated under air at T =1000 ° C for 10h. The last step consists to readjust the quantity of lithium on the materials by adding the doped Co_3O_4 precursor to the four powders thermally for 10 hours at 980 ° C to reach the ratio (Li / M = 1.00). (See **Figure A.16**). Among all those samples prepared, we selected the most homogeneous one based on SXRD and NMR characterization for further study: adj-LCA-1.04.

Final $(Li/Co)_{exp.}$ and $(Li/(Al+Co))_{exp.}$ ratios obtained by Induced Coupled Plasma (ICP) for $LiCo_{0.96}Al_{0.04}O_2$ materials are gathered in **Table A.4**. The results show that the experimental values are in good agreements with the theoretical ones.

Target formula	**Li/Co**		**Li/M (M=Co+Al)**	
	Target	**Experimental**	**Target**	**Experimental**
"$Li_{1.00}Co_{0.96}Al_{0.04}O_2$"	1.04	1.04	1.00	1.00

Table A. 4. ICP analysis of the 4% Al doped $LiCoO_2$ sample studied here.

A.4.2. Structural properties of pristine st-$LiCoO_2$ and $LiCo_{0.96}Al_{0.04}O_2$ materials

X-ray diffraction patterns of pristine st-$LiCoO_2$ and 4% Al-doped $LiCoO_2$ (**$LiCo_{0.96}Al_{0.04}O_2$**) samples are plotted in **Figure A.17**. The two materials exhibit similar line-width and are very well crystallized. All diffraction lines can be indexed in the rhombohedral R-3m space group of the O3 stacking, which can be described using an hexagonal cell. Lebail refinement was performed using a pseudo-Voigt type profile function, which allows a good fit of the peaks line shape. Therefore no asymmetry is seen in the XRD patterns suggesting a homogeneous Al doping,[26] as shown on **Figure A.17**. As Co is partially substituted with Al, the $a_{hex.}$ lattice parameter reflecting the M-M bond length slightly decreases from 2.816 (1) Å to 2.814 (1) (even though the difference is very

weak it goes with the tendency expected from ionic radii : $r_{Al^{3+}}$= 0.535 Å, $r_{Co^{3+}}$= 0.545 Å). The $c_{hex.}$ lattice parameter related to the interlayer distance, increases more significantly from 14.052 (1) Å to 14.062 (1) Å in agreement with the literature[21] as already observed for 2% Al doped materials.

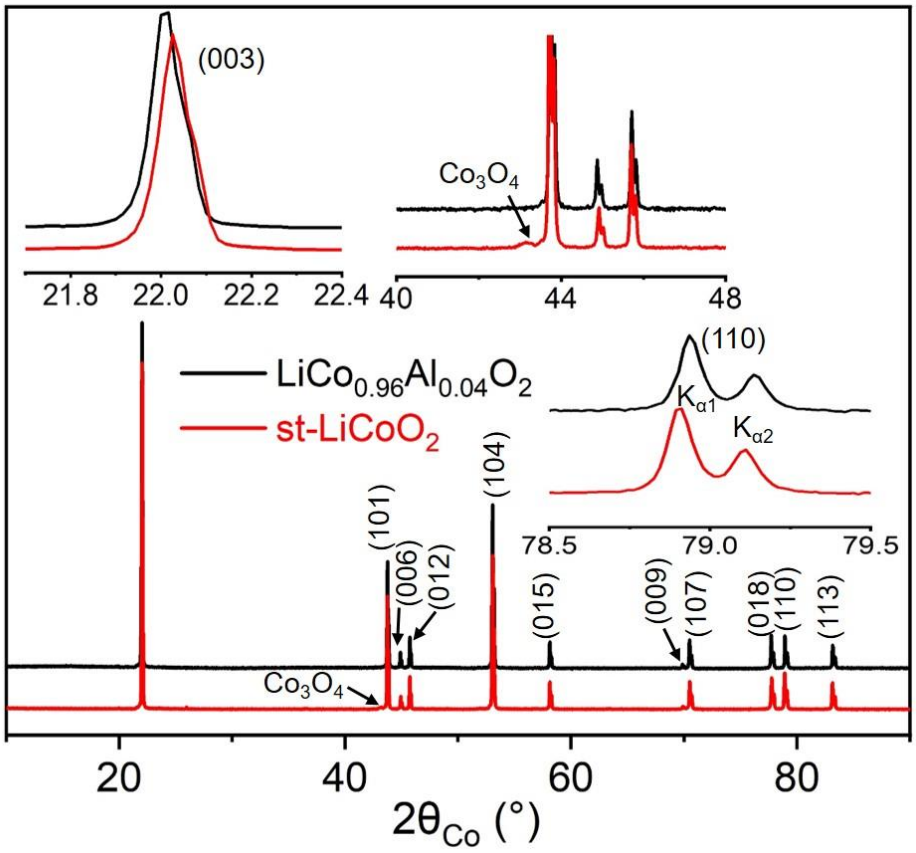

Figure A. 17. X-ray diffraction patterns $LiCo_{0.96}Al_{0.04}O_2$ compared to st-$LiCoO_2$. Insert: zoom of the (003) and (110) peaks.

$LiCo_{0.96}Al_{0.04}O_2$ and st-$LiCoO_2$ materials exhibit both a single ^{7}Li MAS NMR signal very close to 0 ppm (**Figure A.18**) that indicates that no paramagnetic ions are present in the Li environment,[34] in good agreement with the target formulas. Indeed, for Li/M = 1.00, only diamagnetic LS-Co^{3+} ions with the $t_{2g}^6e_g^0$ electronic configuration are expected in the layered phase. Note that the signal of $LiCo_{0.96}Al_{0.04}O_2$ is slightly broader than the one of st-$LiCoO_2$, as several Li environments versus Co/Al are expected in that material. However, the resolution of the ^{7}Li MAS NMR experiment is too low to distinguish clearly the different contributions.

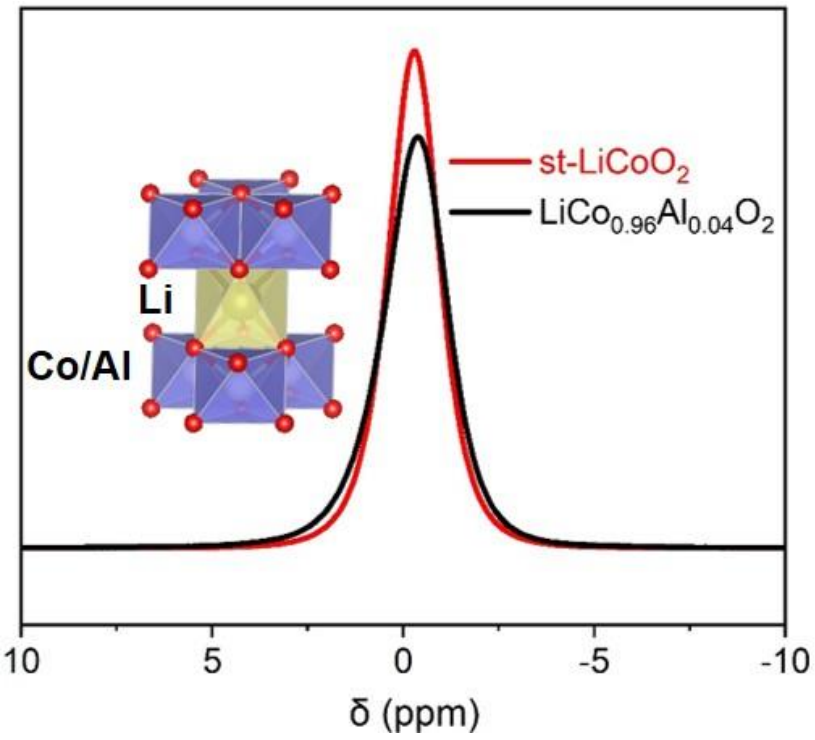

Figure A. 18. ^{7}Li MAS NMR of the $LiCo_{0.96}Al_{0.04}O_2$ compared to st-$LiCoO_2$.

^{27}Al and ^{59}Co MAS NMR were additionally used to characterize the Al/Co local environments (**Figure A.19**). In **Figure A.19.a**, a zoom in the central transition of the ^{27}Al MAS NMR spectra of $LiCo_{0.96}Al_{0.04}O_2$ is shown. As discussed in previous works,[25,26] a set of signals is observed, each corresponding to a different Al environment denoted as Al-(Al_nCo_{6-n}) for Al surrounded by n Al^{3+} and (6-n) Co^{3+}. The signal with the higher chemical shift located at ~62 ppm corresponds to Al surrounded by 6 Co in the slab (denoted as Al-(Al_0Co_6)). This signal exhibits a clear second order quadrupolar line shape. Small signals located around 69 and 73 ppm are assigned to the satellite (±1/2; ±3/2) and (±3/2; ±5/2) transitions expected for this main signal. The other signals located at 55 ppm, 48 ppm, and 40 ppm correspond to Al surrounded by n Al^{3+} and (6-n) Co^{3+} with n varying respectively from 1 to 3, respectively. Signals for Al in a Al-rich environment as Al-(Al_4Co_2), Al-(Al_5Co_1), and Al-(Al_6Co_0) expected at lower ppm values [32] were not detected for our sample due to the very low intensity expected for those environments for a good homogeneity of Al distribution. Indeed, the relative intensities observed in our sample are really close from the one expected for a statistical repartition of Co and Al in the slab.

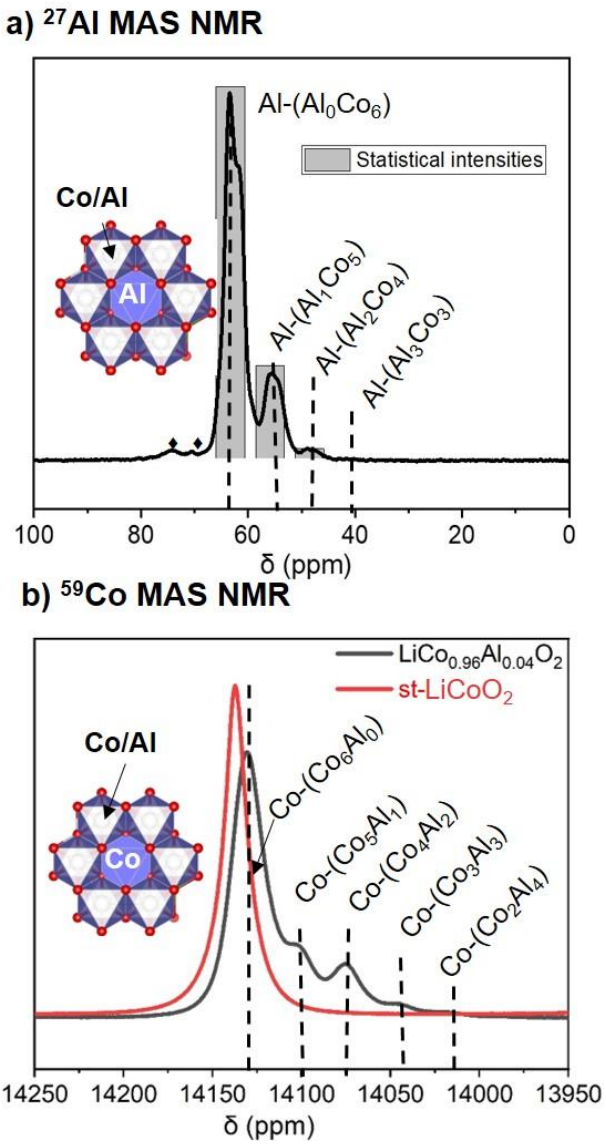

Figure A. 19. a) ^{27}Al and b) ^{59}Co MAS NMR of the $LiCo_{0.96}Al_{0.04}O_2$ compared to st-$LiCoO_2$ (♦: satellite transitions).

^{59}Co MAS NMR spectra of $LiCo_{0.96}Al_{0.04}O_2$ and st-$LiCoO_2$ materials are displayed in **Figure A.19.b**. St-$LiCoO_2$ exhibits a single signal located at 14137 ppm as expected for LS-Co^{3+} surrounded by 6 LS-Co^{3+} in the slab, in agreement with literature[38]. Despite broader signals observed for ^{59}Co MAS NMR, compared to ^{27}Al MAS NMR, distinct signals can be resolved for $LiCo_{0.96}Al_{0.04}O_2$. The most intense one located at 14132 ppm is assigned to LS-Co^{3+} ions

surrounded by six other LS-Co^{3+}, denoted as Co-(Co_6Al_0). The other signals located at 14105 ppm, 14077 ppm, 14047 ppm, and 14021 ppm are assigned to Co surrounded by n Al^{3+} and (6-n) Co^{3+} in the slab with n varying respectively from 1 to 4, denoted as Co-($Co_{6-n}Al_n$).[26] Comparison with statistical intensities was less straightforward due to the strong overlap of those broad signals, but no Al-rich environments (n = 5 and n = 6) were detected.

The combined characterization of the $LiCo_{0.96}Al_{0.04}O_2$ sample by XRD and ^{7}Li, ^{27}Al and ^{59}Co MAS NMR indicate that the sample is diamagnetic, therefore with no Li excess, and that the Al repartition in the Co layer is homogeneous.

A.4.3. Electrochemical properties and general overview

$LiCo_{0.96}Al_{0.04}O_2$ and st-$LiCoO_2$ were used as positive electrode in Li cells that were cycled at C/20 rate. A cutoff voltage of 5V has been used in order to visualize all the phase transition. The resulting cycling curves clearly show that the substitution of Co by a small amount of Al (4%) has a profound effect on the electrochemical behavior (**Figure A.20**).

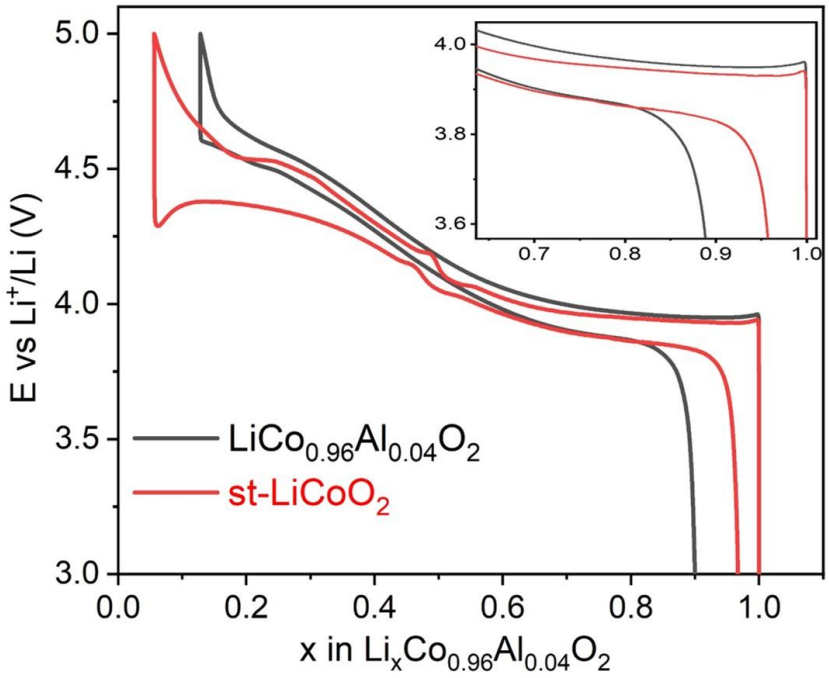

Figure A. 20. The first charge–discharge curves in the 3–5 V voltage range vs. Li^+/Li of $Li_xCo_{0.96}Al_{0.04}O_2$ and Li_xCoO_2 samples (C/20 cycling rate).

When st-$LiCoO_2$ is delithiated, several phase transitions occur as discussed in the introduction. During the 1st cycle curve of $LiCo_{0.96}Al_{0.04}O_2$ at C/20, a voltage plateau is observed in the low voltage region, but seems less extended that the one related to the Mott insulator-metal transition[44] observed for st-$LiCoO_2$(**Figure A.20**). The cycling curve of $LiCo_{0.96}Al_{0.04}O_2$ also does not feature the monoclinic transition around x = 0.5[41,42,45] nor the O3/H1-3 voltage plateau on charge. Another striking difference between the two cycling curves is the large polarization observed at the beginning of the discharge for st-$LiCoO_2$, not present for the doped material. Overall, the Al-doped sample shows a larger irreversible capacity than st-$LiCoO_2$ as previously discussed in the literature.[31,33,35,36]

The suppression of Li/vacancy ordering for x = 0.5, as Co^{3+} is partially substituted by Al^{3+} suggests that the driving force and ΔG formation energy for Li-ordering is rather modest and easily perturbed by minor doping entropy increase. The absence of this phase transition further confirms that Al is successfully homogeneously introduced into the $LiCoO_2$ lattice.

If charged up to 4.5V vs Li^+/Li, the capacity difference between the two materials is rather weak (198 mAh/g for st-$LiCoO_2$ versus 196 mAh/g for $LiCo_{0.96}Al_{0.04}O_2$), but when charged up to 5V, the Al-doped phase shows a much lower capacity (247 mAh/g) than the undoped one (258 mAh/g) since less Li is deintercalated at 5V from the latter (**Figure A.20**).

Extended electrochemical tests were further performed. **Figure A.21** shows the discharge capacity profiles and the cycling performances of st-$LiCoO_2$ and $LiCo_{0.96}Al_{0.04}O_2$ samples at different cycling rate. Indeed, as Al-doping act as top of charge limiter,[20] when cycling up to 4.6V at C/10, the Li concentration reached in the two materials significantly differs: $Li_{0.15}CoO_2$ and $Li_{0.22}Co_{0.96}Al_{0.04}O_2$. Thus, the 8th discharge displayed on **Figure A.21.c** performed at 1C leads to very different 220 and 180 $mAhg^{-1}$ capacities for st-$LiCoO_2$ and $LiCo_{0.96}Al_{0.04}O_2$ respectively. However, the capacity retention is better for the Al-doped compound, as the time spent at high state of charge and the unit cell volume contraction is less for $LiCo_{0.96}Al_{0.04}O_2$ compared to st-$LiCoO_2$. A strict comparison of cycle life for a same state of charge would require $LiCo_{0.96}Al_{0.04}O_2$ to be cycled at a higher voltage.

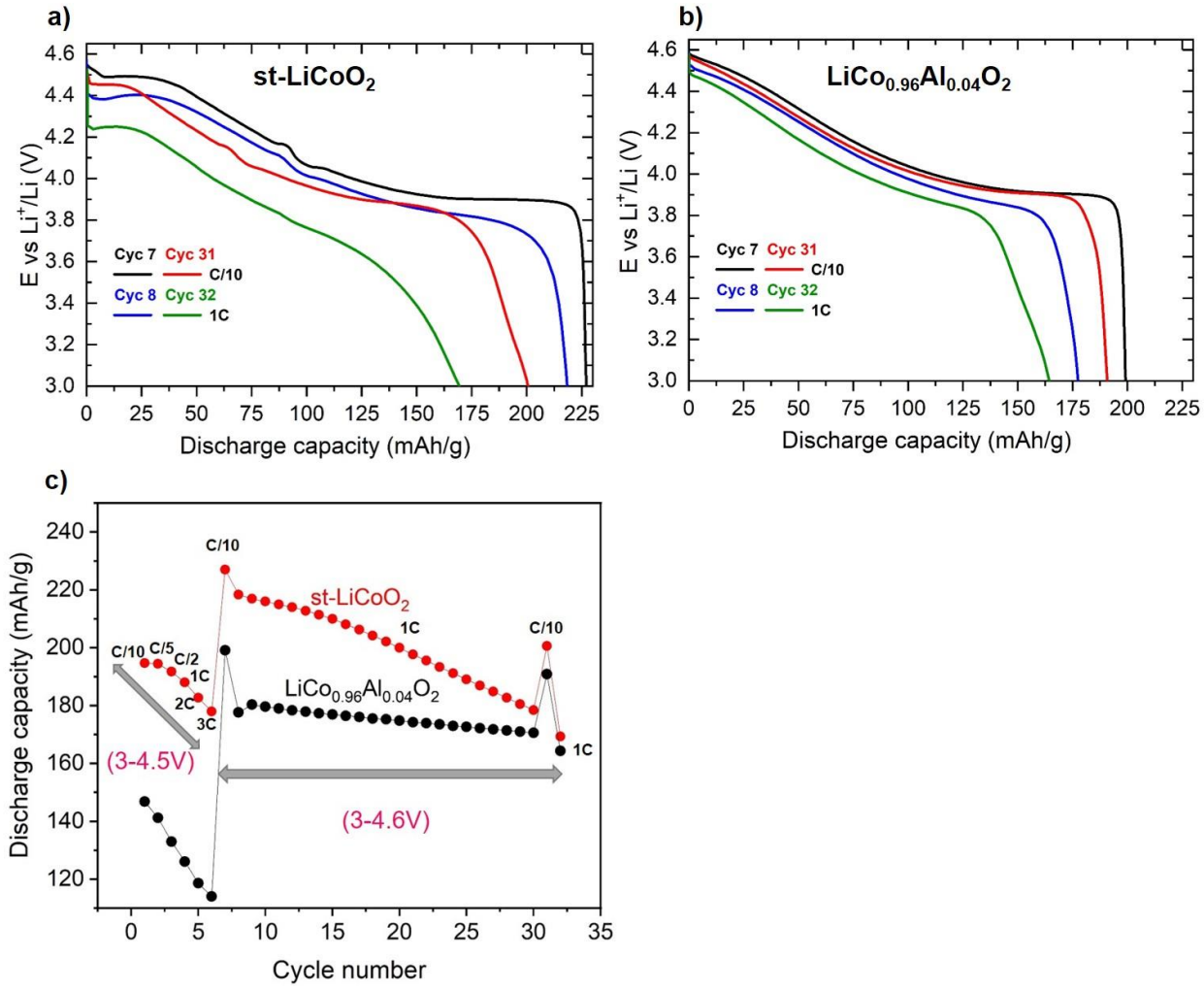

Figure A. 21. Discharge profiles (3V-4.6V) of Li//$LiMO_2$ (M=Co, Al) cells observed for the 7, 8, 31 and 32th cycles of a) st-$LiCoO_2$ and b) $LiCo_{0.96}Al_{0.04}O_2$. c) The discharge capacity versus cycle number of st-$LiCoO_2$ and $LiCo_{0.96}Al_{0.04}O_2$ using different C rates.

In order to have a general overview of the mechanisms involved during charging, XRD and NMR study were performed on deintercalated samples prepared using a galvanostatic charge (C/20 rate) applied up to the desired Li content (x) followed by a relaxation step (See **Figure A.22).**

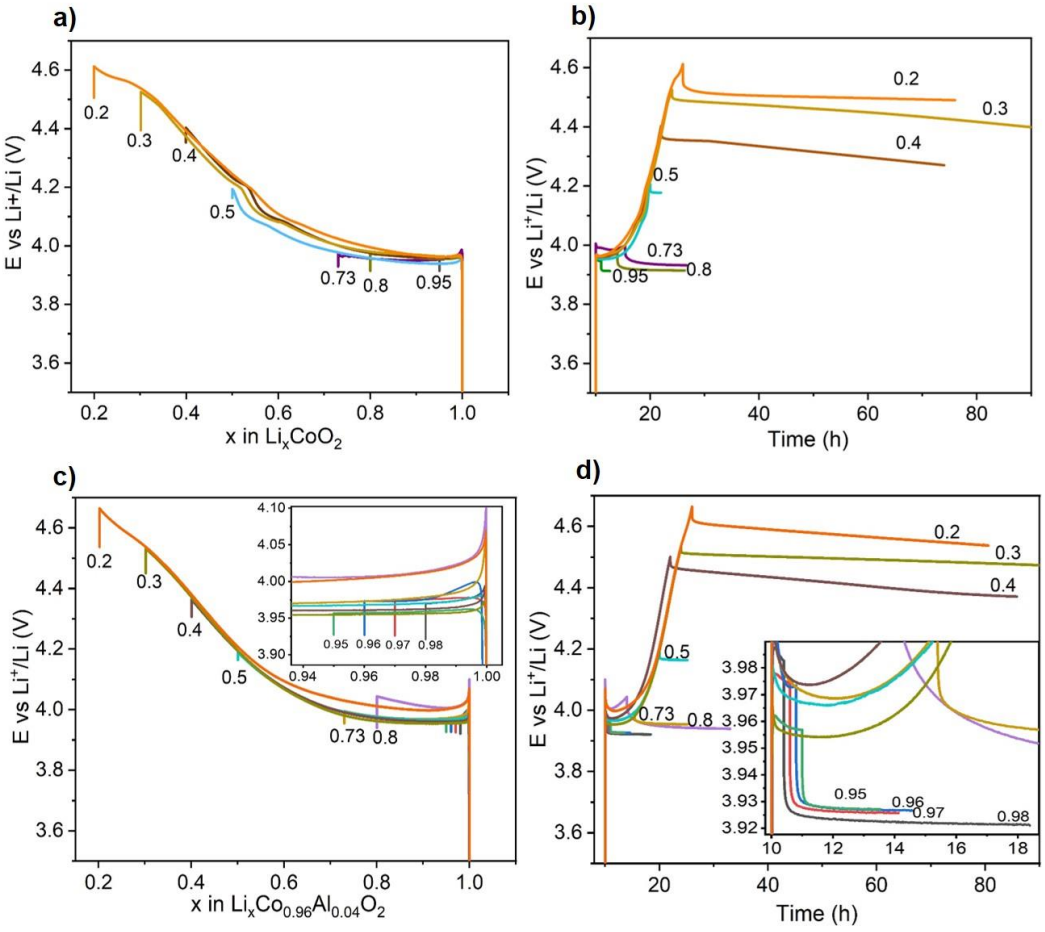

Figure A. 22. Galvanostatic charge of Li/ Li_xMO_2 cells used to prepare the various a, b) Li_xCoO_2 and c, d) $Li_xCo_{0.96}Al_{0.04}O_2$ phases (C/20 rate).

XRD patterns of the electrochemically deintercalated Li_xCoO_2 and $Li_xCo_{0.96}Al_{0.04}O_2$ samples were recorded in order to follow the structural changes during deintercalation (**Figure A.23 and A.24**). Special attention was given to the (003) diffraction peak evolution that allows to directly follow the changes in the interslab distance, related to the lithium amount and stacking modifications (**Figure A.23.b and A.24.b**). In the two systems, upon deintercalation this peak shifts towards lower angles up to x=0.5, and then shifts back to higher angles for lower Li amount. This denotes an expansion of the structure along the $c_{hex.}$ followed by a contraction (**Table A.5**) which is consistent with the literature[42] and commonly observed during the Li de-intercalation of layered Li_xMO_2 materials.[9] Indeed, the electrostatic repulsion between adjacent CoO_2 layers

increases when Li ions are initially removed from the structure, resulting in an increase in the $c_{hex.}$ lattice parameter. When the Li content is reduced below x =0.5, the average charge on the oxygen ions decreases (covalence of the Co-O bonds increases) and the electrostatic repulsion between the oxygen ions is lowered resulting in a contraction of the host along the c axis[9].

The individual XRD patterns will be discussed below.

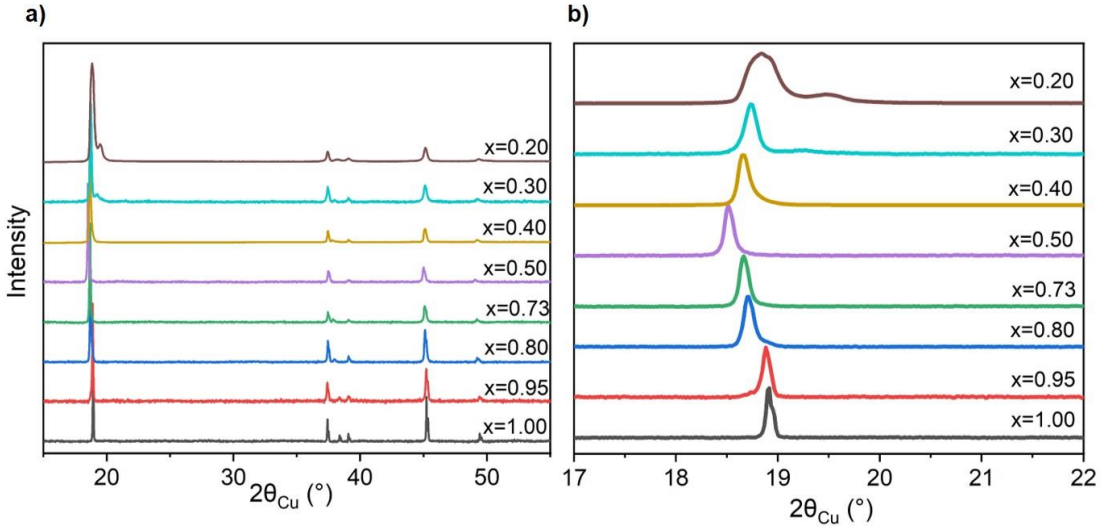

Figure A. 23. X-ray diffractogramms of the electrochemically deintercalated $Li_xCo_{0.96}Al_{0.04}O_2$ materials with b) the detail in the (00l) line.

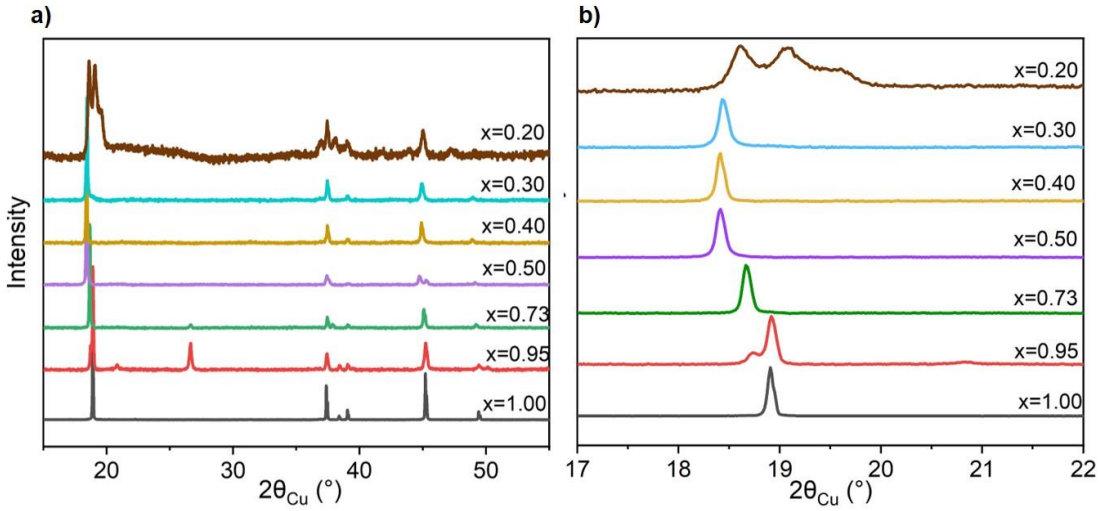

Figure A. 24. X-ray diffractogramms of the electrochemically deintercalated Li_xCoO_2 materials with b) the detail in the (00l) line.

Compound	Space-group	Phase	a (Å)	c (Å)
$LiCo_{0.96}Al_{0.04}O_2$	R-3m	$O3_1$	2.814 (1)	14.062 (1)
$Li_{0.98}Co_{0.96}Al_{0.04}O_2$	R-3m	$O3_1$	2.813 (1)	14.063 (2)
$Li_{0.97}Co_{0.96}Al_{0.04}O_2$	R-3m	$O3_1$	2.813 (1)	14.063 (4)
$Li_{0.95}Co_{0.96}Al_{0.04}O_2$	R-3m	$O3_1$	2.813 (1)	14.064 (2)
	R-3m	$O3_2$	2.809 (1)	14.171 (2)
$Li_{0.80}Co_{0.96}Al_{0.04}O_2$	R-3m	$O3_1$	2.796 (1)	14.086 (2)
	R-3m	$O3_2$	2.810 (1)	14.211 (2)
$Li_{0.73}Co_{0.96}Al_{0.04}O_2$	R-3m	$O3_2$	2.809 (1)	14.239 (6)
$Li_{0.50}Co_{0.96}Al_{0.04}O_2$	R-3m	O3	2.807 (1)	14.355 (7)
$Li_{0.40}Co_{0.96}Al_{0.04}O_2$	R-3m	O3	2.812 (1)	14.247 (4)
$Li_{0.30}Co_{0.96}Al_{0.04}O_2$	R-3m	O3	2.817 (1)	14.214 (4)
	R-3m	H1-3	2.807 (1)	27.740 (2)
$Li_{0.20}Co_{0.96}Al_{0.04}O_2$	R-3m	O3	2.835 (1)	13.899 (4)
	R-3m	H1-3	2.784 (1)	27.340 (2)

Table A. 5. Refined unit cell parameters for $Li_xCo_{0.96}Al_{0.04}O_2$ from the XRD data.

As for st-$LiCoO_2$, when Li ions are initially removed from the structure, the electrostatic repulsion between adjacent CoO_2 layers increases resulting in an increase in the $c_{hex.}$ lattice parameter. Then, when the Li content is reduced below $x = 0.5$, the average charge on the oxygen ions decreases (covalence of the Co-O bonds increases) and the electrostatic repulsion between the oxygen ions is lowered resulting in a contraction of the host along the c axis.[9] This is a very common phenomenon found for layered Li_xMO_2 materials.

While Li is in diamagnetic environments for the two pristine $LiCo_{0.96}Al_{0.04}O_2$ and st-$LiCoO_2$ samples, giving rise to signals close to 0 ppm, hyperfine interactions due to the formation of

paramagnetic LS-Co^{4+} ($t_{2g}^5e_g^0$) ions are expected for the deintercalated samples. **Figure A.25** shows the evolution of the ^{7}Li MAS NMR spectra of the Li_xCoO_2 and $Li_xCo_{0.96}Al_{0.04}O_2$ series.

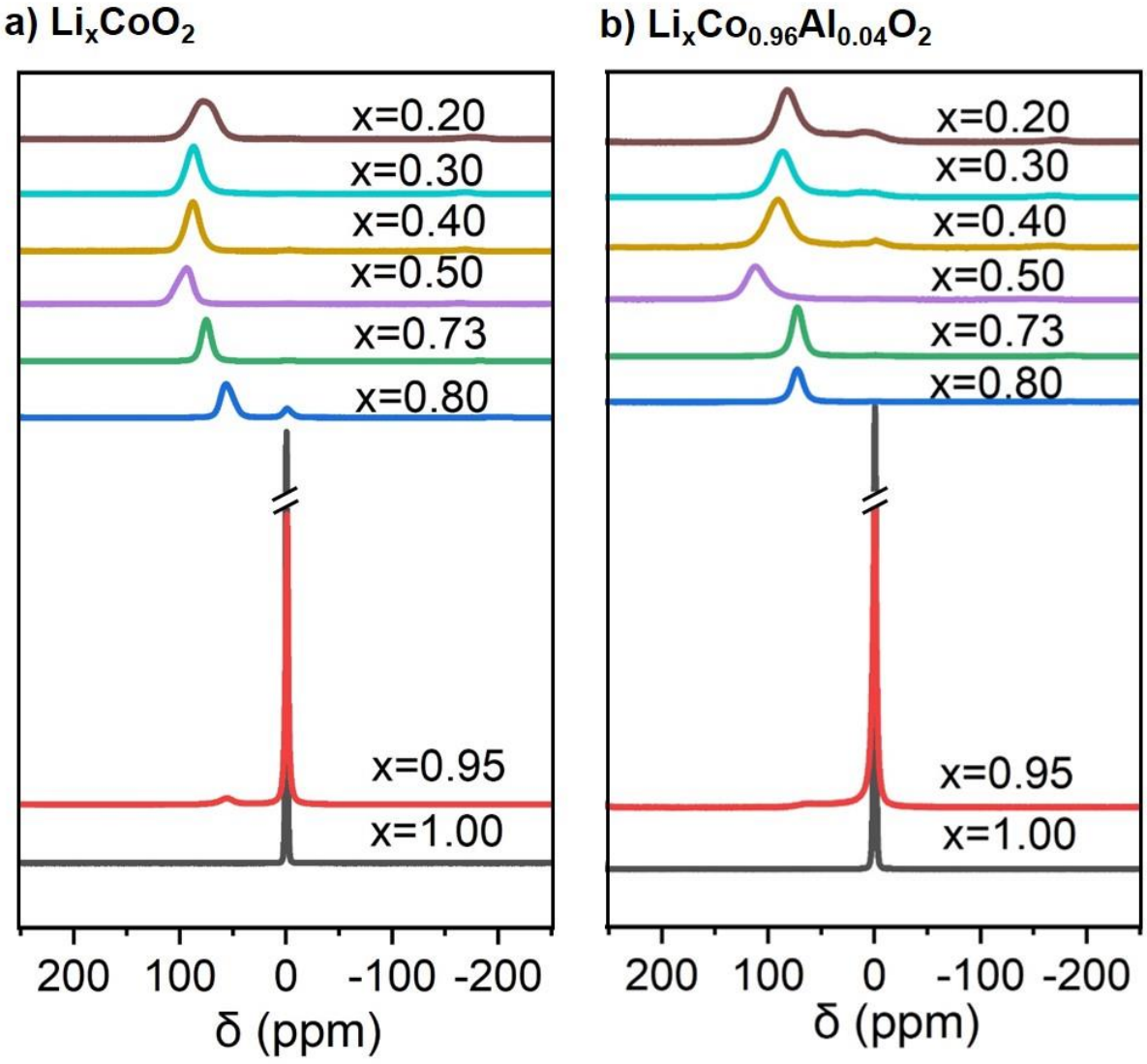

Figure A. 25. Ex-situ ^{7}Li MAS NMR spectra for a) Li_xCoO_2 and b) $Li_xCo_{0.96}Al_{0.04}O_2$ (rotor-synchronized Hahn echo sequence, ν_R = 30 kHz). Arbitrary intensities are used here to better visualize the shifts.

The results observed for Li_xCoO_2 samples are in good agreement with the literature:[44,46] i) as x decreases at the early stage of the charge, the intensity of the 0 ppm signal decreases, due to a strong hyperfine interaction between the single electron of the formed LS-Co^{4+} ($t_{2g}^5e_g^0$) ions and

adjacent Li nuclei. Ménétrier et al.[44] interpreted this intensity decrease by the localized character of the single electron of Co^{4+}, found in one of the t_{2g} orbitals pointing directly towards adjacent lithium 2s orbital through the common edge of the CoO_6 and LiO_6 octahedra. Instead of leading to a new signal, this interaction is so strong that it leads to a loss of signal; ii) upon further lithium removal, a very weak new signal starts to appear at 61 ppm and increases in intensity at the expense of the 0 ppm signal. This signal is shifted to higher ppm values until x=0.5. Ménétrier et al.[44] attributed this new signal to a Knight interaction due to the participation of the 2s orbital of lithium at the Fermi level, in good agreement with the metallic character of Li_xCoO_2 phases for $x < 0.74$.[44] NMR is thus sensitive to the change in nature of the hyperfine interaction from localized electronic spins (Fermi contact) to delocalized ones (Knight shift). For $x < 0.5$, the Knight shifted signal is displaced back towards lower ppm values as also observed by Shimoda et al. [47] The global evolution of the Li signal position versus x results from an interplay between the change in the local electronic structure (number of formal Co^{4+} ions and localized versus delocalized electron spin character) and the change of local geometric structure (overall Li-O-Co distances or angles evolution).

The overall evolution of the XRD patterns (**Figure A.23**) and ^{7}Li MAS NMR spectra (**Figure A.25**) of the $Li_xCo_{0.96}Al_{0.04}O_2$ series is rather similar to the one of Li_xCoO_2. But, some differences were observed in the low and high voltage regions that will be discussed in detail. To highlight these differences, first, in the low voltage region further Li contents were prepared in the $0.73 \leq x < 1$ composition range. Then, in the high voltage region, in order to discuss the effect of the state of charge (Li content) as well as the cutoff voltage, samples have been prepared following two routes as described in the experimental section: i) using a galvanostatic charge applied up to the desired Li content (x) followed by a relaxation step (**Figure A.22**) ii) using a galvanostatic charge applied up to the desired voltage followed by a floating step until the current reached ~ 0 mA (more details will be given in the following). The first route allows comparing samples prepared at the same state of charge, but prepared at different voltages that might induce different electrolyte degradation and the second route allows comparing phases at equilibrium for a given

voltage but with different Li content. In addition, this second route leads to more aged samples since they spend more time at high voltage during the floating step.

A.4.4. Detailed study in the low and high voltage regions

A.4.4.1. The $0.73 \leq x < 1$ composition domain (low voltage region).

Several $Li_xCo_{0.96}Al_{0.04}O_2$ materials were prepared in the $0.73 \leq x < 1.00$ composition range to determine if – similarly to Li_xCoO_2[44] - a two phase domain associated to the insulator-metal transition exists. Their XRD patterns are given in **Figure A.26**. The patterns of the x = 1.00, 0.98 and 0.97 phases can be indexed using a single phase crystallizing in the R-3m space group of the O3 stacking, named here $O3_1$. The pattern of the x = 0.73 phase can also be indexed using a single phase crystallizing in the R-3m space group of the O3 stacking, named here $O3_2$. However, for x=0.95 and x=0.80, the two O3 phases co-exist: the (003) peak of the $O3_1$ phase, located at 2θ=18.91°, disappears as x decreases while the (003) peak of the $O3_2$ phase, located at lower angle appears (2θ = 18.73°, see **Figure A.26.b**) appears. This indicates the existence of a biphasic domain in a much narrower composition range compared to st-$LiCoO_2$ ($0.73 \leq x \leq 0.99$).[34] One can make the hypothesis that the $O3_1$- $O3_2$ transition is also due to an insulator-metal transition.

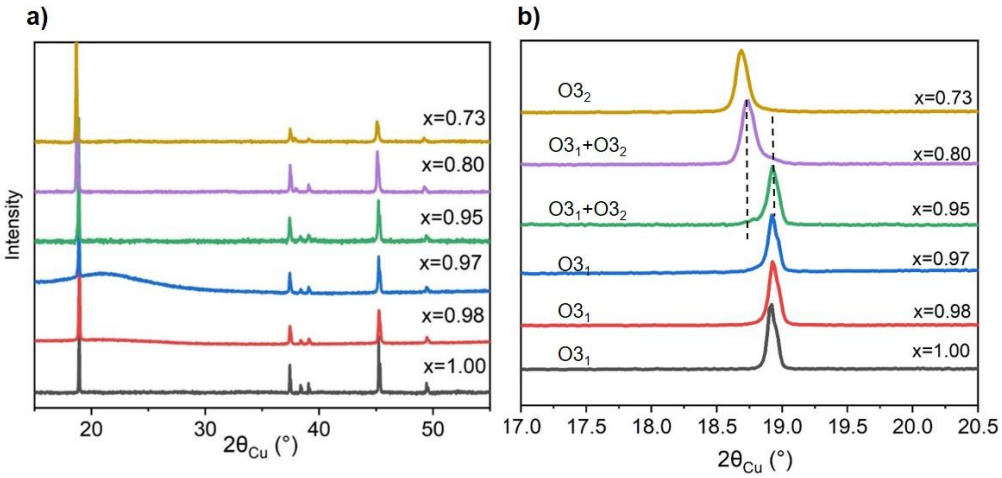

Figure A. 26. a) X-ray diffraction patterns of the electrochemically deintercalated $Li_xCo_{0.96}Al_{0.04}O_2$ materials prepared with targeted Li compositions by controlling the Li content, in the low potential region V< 4V vs Li^+/Li with b) the detail in the (003) line.

^{7}Li MAS NMR confirms that the system behaves locally as two phase domain as shown in **Figure A.27.a**: for x=0.98, the signal close to 0 ppm decreases in intensity with x in $Li_xCo_{0.96}Al_{0.04}O_2$ and the Knight-shifted signal starts to appear at 61 ppm indicating an insulator to metal transition. While the biphasic domain appears at early stage in ^{7}Li MAS NMR (x=0.98), it was only detected from x=0.95 in the XRD data (See **Figure A.26**). ^{7}Li MAS NMR is indeed very sensitive to the local scale while XRD technique requires a significant particle size for the interference phenomenon.

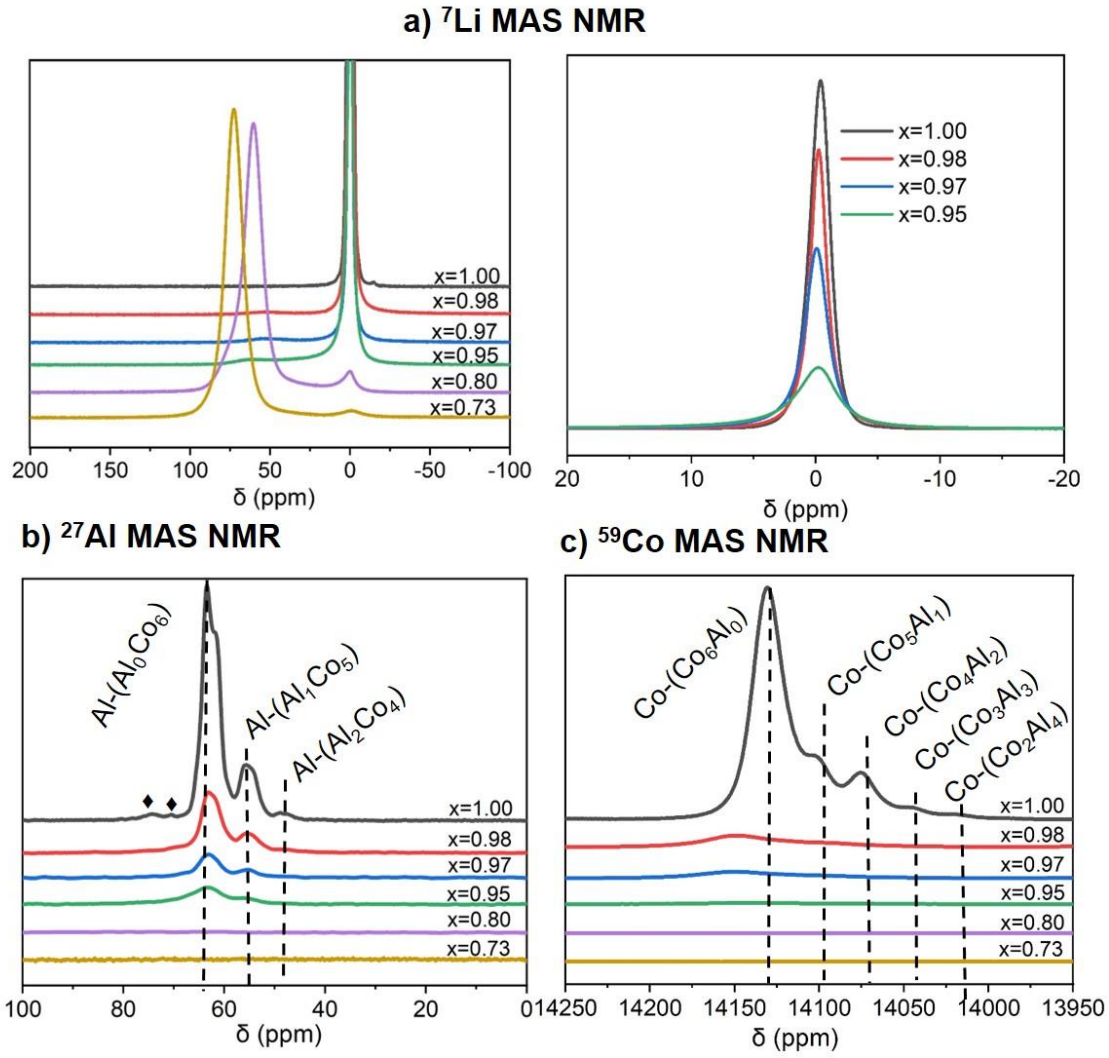

Figure A. 27. Ex-situ a) ^{7}Li b) ^{27}Al and c) ^{59}Co MAS NMR of the deintercalated $Li_xCo_{0.96}Al_{0.04}O_2$ by controlling the Li content in the low voltage region (♦: satellite transitions).

^{27}Al and ^{59}Co MAS NMR were also performed to confirm findings from the ^{7}Li MAS NMR study (**Figure A.27.b** and **A.27.c**). From the ^{27}Al and ^{59}Co MAS NMR study, the intensity of all different signals corresponding to Al/Co environments decrease constantly at an early delithiation stage and vanish for x = 0.80 and x = 0.95, respectively for ^{27}Al and ^{59}Co NMR. These signal losses could come from a strong Fermi contact interaction (localized state) and a stronger contribution of the s orbitals of Al and Co at the Fermi level compared to Li (delocalized state). For those nuclei, either a very broad signal not detected in our conditions or a very fast relaxation beyond the NMR timescale are to be expected.

A.4.4.2. The $x \leq 0.5$ composition domain (high voltage region)

a) Sample prepared by fixing the Li amount

The XRD patterns of the x=0.5 and x=0.4 samples of the $Li_xCo_{0.96}Al_{0.04}O_2$ system can be indexed using a single O3 type phase (**Figure A.23**). However, for x=0.3, the co-existence of two (00l) lines indicates the presence of two phases that can be both indexed using the R-3m space, what suggests the presence of O3 and H1-3 phases. However, the diffraction line located around $2\theta = 19.2°$ and other extra lines are broad and weak. Those two phases are still present for x = 0.2, but, for this composition, the XRD pattern shows even broader peaks, which could be explained by the existence of stacking faults within the layered oxide.[48] However, in the case of st-$LiCoO_2$ (**Figure A.24**), a pure O3 phase is observed for x = 0.3 and three phases coexist for x=0.2: O3, H1-3 and another phase with an intermediate interslab space that can results from an intergrowth of O3 and H1-3 stacking. Note that such in intermediate phase was not observed during operando measurements and might be formed only during the relaxation step.[29] In the two systems, no signature of the formation of the O1 phase (P3m1 space group with a_{hex} = 2.822 Å and c_{hex} = 4.29 Å) phase has been observed for compounds prepared up to x = 0.2.

Figure A.28.a and **28.b** shows the ^{7}Li NMR spectra of the deintercalated samples from st-$LiCoO_2$ and from $LiCo_{0.96}Al_{0.04}O_2$. The spectra of the $Li_{0.5}CoO_2$ and $Li_{0.5}Co_{0.96}Al_{0.04}O_2$ phases are rather similar with a Knight shifted signal located at 94 ppm and 112 ppm respectively. For lower Li content, however, the spectra differ significantly.

In the Li_xCoO_2 system, the signal shifts to lower ppm values with a strong decrease in intensity and a small broadening of the signal for x=0.2 (**Figure A.28.a**).[46] This signal is assigned to Li in the O3-type environment, expected to be similar in the H1-3 stacking locally if we assume that a negligible amount of Li is present in the O1 interslab space. The broad signal for x = 0.2 may be due to the co-existence of 3 phases for this materials as seen by XRD, that probably exhibit slightly different compositions leading to different shifted signals. No rapid exchange is therefore observed at the NMR timescale between those domains.

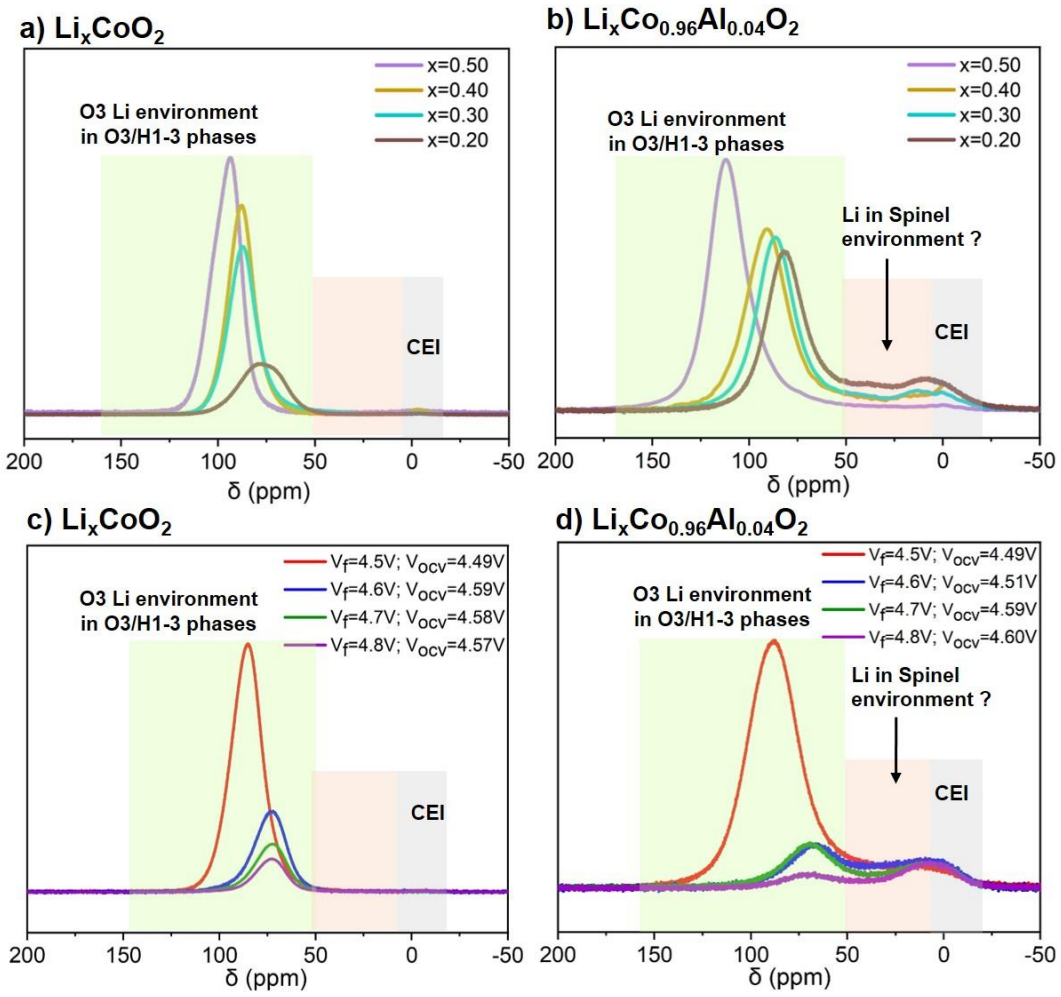

Figure A. 28. Comparison of ^{7}Li MAS NMR for highly deintercalated phases of a) Li_xCoO_2 and b) $Li_xCo_{0.96}Al_{0.04}O_2$ with fixed Li contents of c) Li_xCoO_2 and d) $Li_xCo_{0.96}Al_{0.04}O_2$ with fixed floating voltages. The ex-situ NMR spectra intensities were normalized with respect to the number of mass of the electrode powder filled in the rotor and number of scans.

In the $Li_xCo_{0.96}Al_{0.04}O_2$ system, the main signal assigned to Li in O3 and H1-3 phases shifts also to lower ppm values, and for $x < 0.3$, new contributions appear in the [-20;50] ppm range with significant intensity (**Figure 28.b**). Signals located in 10-50 ppm could be attributed to Li in spinel-type environment as a first approximation according to Godillot et al. [49], this point will be discussed in detail below. Additionally, signals located around 0 ppm can be assigned to diamagnetic lithium environments from the CEI (Cathode Electrolyte Interphase). Note that the signal intensity of the $Li_{0.2}Co_{0.96}Al_{0.04}O_2$ is larger than expected from the composition, indicating the participation of the electrolyte decomposition parasitic reaction in agreement with the presence of significant signals of Li in the CEI.

b) Samples prepared with floating voltages

With the aim to prepare highly deintercalated, more homogeneous and aged samples, an additional floating step after the charge has been used: cells were galvanostatically charged up to a given potential (4.5V, 4.6V, 4.7V and 4.8V) at C/20, followed by a floating step until the current reached ~ 0 mA (**Figure A.29**). The Li content of those materials is difficult to estimate due to the parasitic reaction of the electrolyte degradation, but are respectively lower than 0.32, 0.17, 0.10, 0.09 for st-$LiCoO_2$ (**Figure A.29.a**) and 0.32, 0.24, 0.18, 0.15 for $LiCo_{0.96}Al_{0.04}O_2$ (**Figure A.29.b**). The last two compositions exhibit therefore lower Li contents than samples of the previous section. One can observe that for floating voltages $V_f \geq 4.6$ V, the cell voltage dropped significantly (V_{OCV} as opposed to V_f) when the cell was disconnected. Indeed, the highest reached V_{ocv} is only 4.6V, which remains higher than the voltage observed for the materials prepared without floating (**Figure A.22**).

A really similar behavior was observed for the Li_xCoO_2 samples prepared in the same way, but the 4.6V voltage remains stable after disconnecting the cell ($V_{OCV} \approx V_f$), whereas the voltage drops to 4.51V for the Al doped compound.

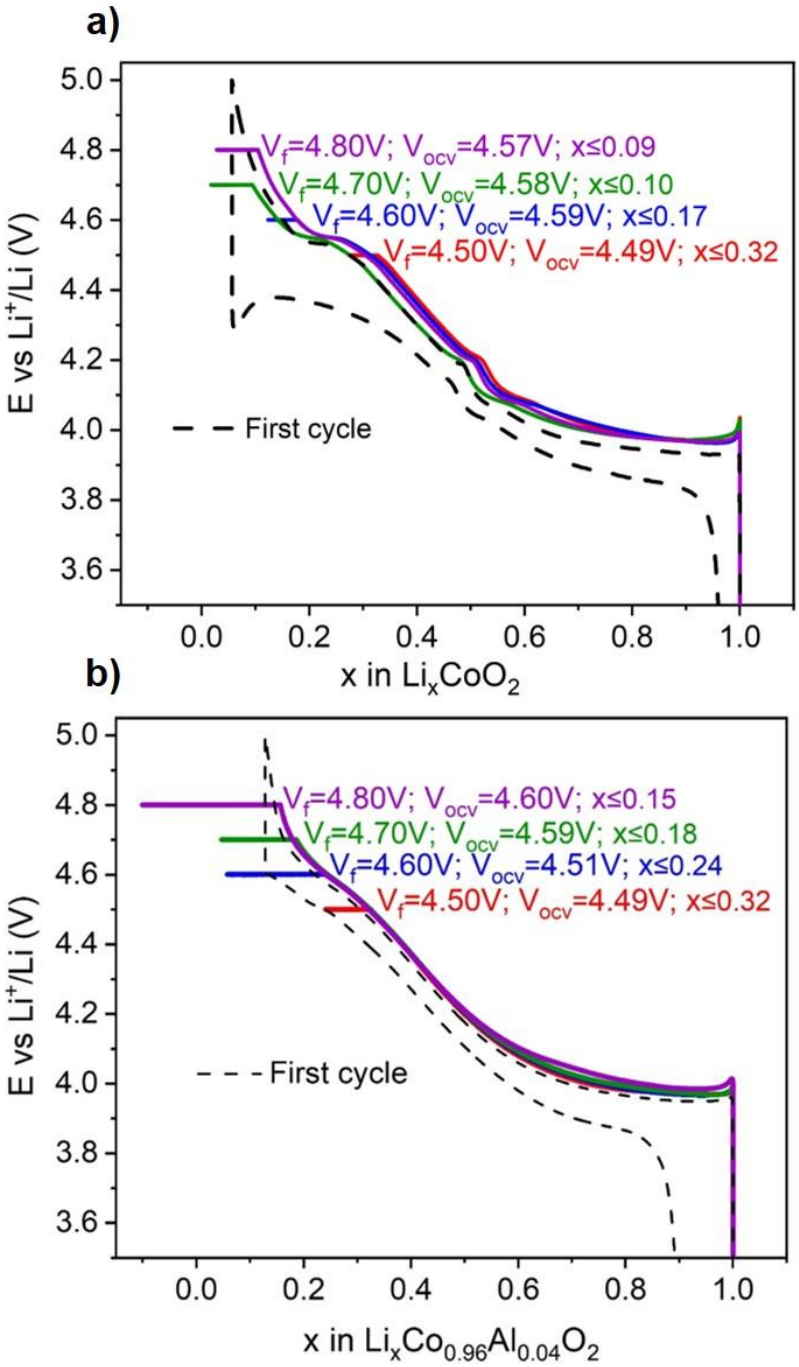

Figure A. 29. Galvanostatic charge of Li//$LiCo_{0.96}Al_{0.04}O_2$ cells stopped at different voltage from 4.5V to 4.8 V compared to a first cycle curve ($V_f=V_{floating}$ and V_{ocv} corresponds to the voltage measured before disassembling the cell).

The different materials were then characterized by XRD (**Figures A.30**) and ^{7}Li MAS NMR (**Figure A.28.c and d).** All diffraction peaks for materials prepared at V_f =4.5 V can be indexed based on the O3 structure with rather similar Li content ($Li_{0.24}Co_{0.96}Al_{0.04}O_2$ and $Li_{0.27}CoO_2$ if one neglects the electrolyte degradation at this voltage). For the materials prepared at V_f =4.6V, two peaks are observed for Li_xCoO_2 at 2θ=19.76° and 2θ=20.34°, which correspond respectively to the $(006)_{H1\text{-}3}$ and $(00\ell)_{int}$ diffraction lines of the H1-3 and intermediate phase between H1-3 and O1 type structures as detected also by operando XRD.[29] Only the $(006)_{H1\text{-}3}$ diffraction line is observed in the case of the Al-doped sample at the same V_f =4.6V. At 4.7V, three very broad contributions are observed for Li_xCoO_2 assigned to the $(006)_{H1\text{-}3}$, $(00\ell)_{int}$ and $(001)_{O1}$ diffraction lines, indicating structures with a high density of stacking faults, resulting in overall structural disorder. In the case of the Al doped compounds, the $(006)_{H1\text{-}3}$ peak remains narrow and the $(001)_{O1}$ diffraction line appears at 2θ=20.92° for $V_f \geq$ 4.7V. Finally, Li_xCoO_2 prepared at 4.8V also exhibits broad diffraction line assigned to a defected H1-3 phase with $x \leq 0.09$ and $Li_xCo_{0.96}Al_{0.04}O_2$ exhibits broad diffraction lines assigned to H1-3 and O1 phases with an overall Li content $x \leq 0.15$.

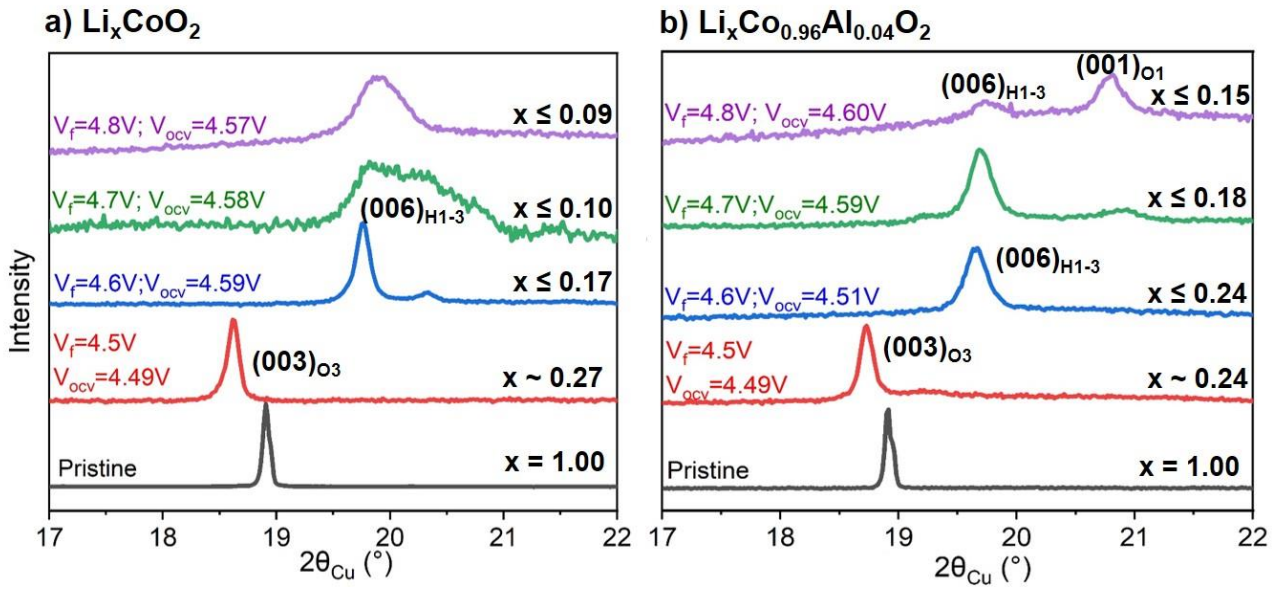

Figure A. 30. Detail in the (00l) line from XRD for a) Li_xCoO_2 and b) $Li_xCo_{0.96}Al_{0.04}O_2$ (V_f=$V_{floating}$ and V_{ocv} corresponds to the voltage measured before disassembling the cell).

From ^{7}Li MAS NMR (**Figure A.28.c and d**), spectra of the materials prepared at V_f=4.5V are very similar to the ones of, respectively, $Li_{0.3}CoO_2$ and $Li_{0.3}(Co_{0.96}Al_{0.04})O_2$ phases, with a single Knight shifted signal located around ~75 ppm. For the three samples prepared at larger floating voltages $V_f \geq 4.6V$, the line shape of the ^{7}Li signal of Li_xCoO_2 samples remains almost unchanged (**Figure A.28.c**). Several contributions are observed for $Li_xCo_{0.96}Al_{0.04}O_2$ samples (**Figure A.28.d**) as already discussed above, but in different relative amounts. The intensity of the signal located in the [~50-130] ppm of Li in the O3 and H1-3 phases strongly decreases while the intensity of signals corresponding to Li in (supposedly) spinel type environment at [10-50] ppm and to Li in the CEI around 0 ppm remain essentially the same.

The ^{7}Li MAS NMR results suggest that the CEI formed at high voltage could be either very thin or unstable for st-$LiCoO_2$, and may be dissolved by the electrolyte solvent after the cell disconnection or by the electrode washing step using DMC prior to our measurements. Additionally, no signal associated to a lithiated spinel phase was detected in this case. As opposed to st-$LiCoO_2$, new local Li environments potentially assigned to both a disordered (as not seen by XRD) spinel-like lithiated phase and a stable CEI were observed for $Li_xCo_{0.96}Al_{0.04}O_2$. These features could explain the higher stability upon cycling of the Al-doped samples and their highest irreversible capacity during the first cycle.

c) Structural characterization after cycling at high voltage (3-cycles)

To further understand the performance of $LiCo_{0.96}Al_{0.04}O_2$ at high voltage, this material was charged-discharged 3 times between 3V and 4.8V with a C/20 rate then recovered at the end of discharge after a floating at 3V (**Figure A.31.a**). The sample was then characterized by XRD, MAS NMR and TEM. XRD and NMR data of this new sample was compared to the data collected for the pristine phase and a $Li_{0.98}Co_{0.96}Al_{0.04}O_2$ prepared by galvanostatic charge, as the phase at this composition is found to have cell parameters very close to the ones of the material recovered after 3 cycles (**Table A.6**). From the electrochemical curve (**Figure A.31.a)**, a x=0.95 value was predicted, but, the cell undergoes some electrolyte decomposition at high voltage that shifted slightly the cycling curves on the left.

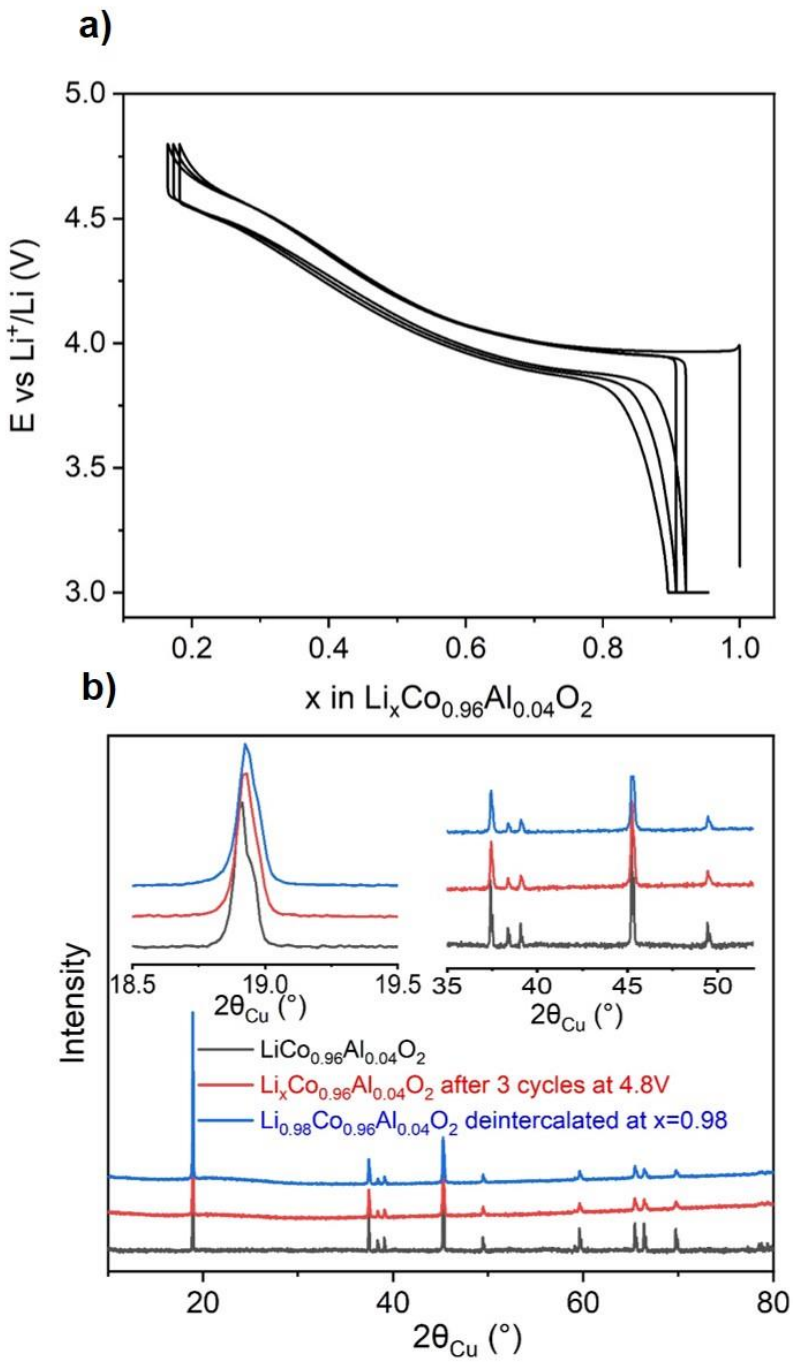

Figure A. 31. a) 3 cycles of galvanostatic charge / discharge (3V-4.8V) of an Li // $Li_xCo_{0.96}Al_{0.04}O_2$ and stopped in potential at 3V cell with a rate of C/20. b) X-ray diffractogramme of $Li_xCo_{0.96}Al_{0.04}O_2$ cycled compared to the pristine and the deintercalated $Li_{0.98}Co_{0.96}Al_{0.04}O_2$.

Compound	Space-group	Phase	**a (Å)**	**c (Å)**
$LiCo_{0.96}Al_{0.04}O_2$	R-3m	$O3_1$	2.814 (1)	14.062 (1)
$Li_{0.98}Co_{0.96}Al_{0.04}O_2$	R-3m	$O3_1$	2.813 (1)	14.063 (2)
$Li_xCo_{0.96}Al_{0.04}O_2$ after 3 cycles at 4.8V	R-3m	$O3_1$	2.813 (1)	14.064 (3)

Table A. 6. Refined unit cell parameters for $Li_xCo_{0.96}Al_{0.04}O_2$ cycled 3 times between (3V-4.8V) and stopped in potential at 3V compared to the pristine and the deintercalated $Li_{0.98}Co_{0.96}Al_{0.04}O_2$ from the XRD data.

In **Figure A.32.a**, a strong signal located near 0 ppm assigned to Li in the O3 phase surrounded by diamagnetic LS-Co^{3+} ions is clearly observed for the $Li_xCo_{0.96}Al_{0.04}O_2$ sample recovered after 3 cycles up to 4.8V, similarly to the x = 1 and x = 0.98 samples. Additional new signals located at 12 ppm, 25 ppm and 43 ppm can also be observed. Signals in this range have already been observed for highly deintercalated materials and were attributed to Li in spinel-like environment as a first approximation. According to Godillot et al.[49] the 12 ppm and 24 ppm signals may be assigned to Li in the 8a tetrahedral sites of the spinel structure, that may differ from their Co/Al local environments here and the 43 ppm signal is assigned to Li in the 16c octahedral sites. Note that Co_3O_4-type phase was not detected by XRD indicating that the spinel-type environments are either located in a very disordered phase or only at a very local scale (**Figure A.31.b**). ^{59}Co and ^{27}Al MAS NMR is not really informative regarding the spinel formation since a loss of signals for those phases is expected : in Co_3O_4, an electronic delocalization occurs on Co ions leading to a very strong hyperfine interaction with ^{59}Co nuclei that directly carries the electronic spins; in $CoAl_2O_4$, the hyperfine interaction between the Co^{2+} ions and the ^{27}Al nuclei is also very strong and the absence of signal for Al was already reported[50] and was also confirmed by our group while heat treating Co_3O_4 with Al_2O_3 at 1000 °C.[25] Indeed, the ^{59}Co and ^{27}Al MAS NMR spectra of the $Li_xCo_{0.96}Al_{0.04}O_2$ sample recovered after 3 cycles up to 4.8V are really similar to the ones of the x= 0.98 sample, so no major structural modification occurs within the O3 phase (**Figure A.32.b and c**).

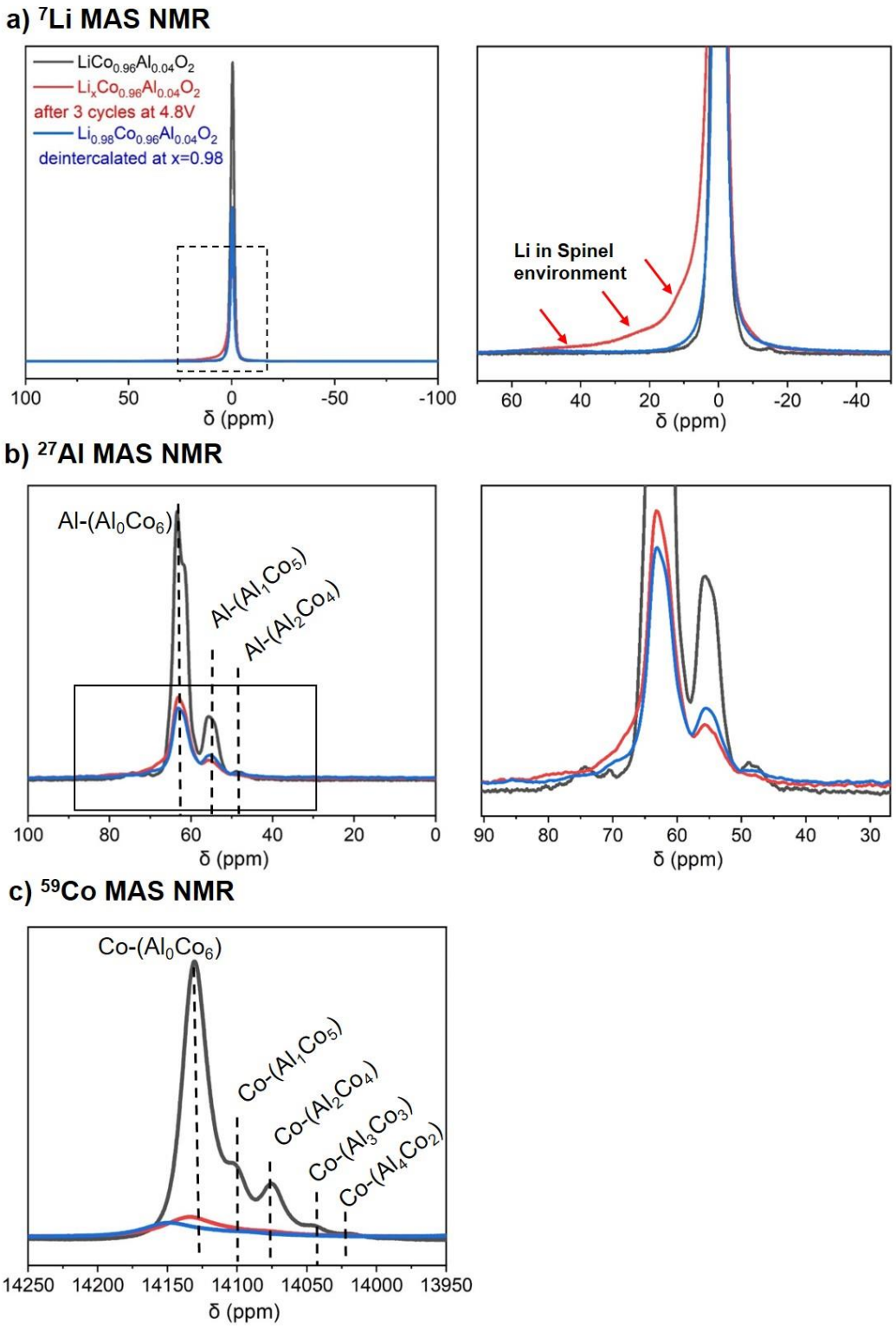

Figure A. 32. a)[7]Li, [27]Al and c) [59]Co MAS NMR of $Li_xCo_{0.96}Al_{0.04}O_2$.

TEM was used to confirm the hypothesis of the existence of a spinel phase in the cycled $Li_xCo_{0.96}Al_{0.04}O_2$ material and to spatially localize it. **Figure A.33.a**, shows a nano-beam electron diffraction pattern obtained from the center of one crystal of the cycled $Li_xCo_{0.96}Al_{0.04}O_2$ material (**Figure A.33.c**). This diffraction pattern corresponds to the [211] zone axis of the $LiCo_{0.96}Al_{0.04}O_2$ phase using the hexagonal axis system (R-3m space group). When the nano-beam is displaced from the center to the edge of the crystal (**Figure A.33.f**), another pattern is obtained (**Figure A.33.d**).

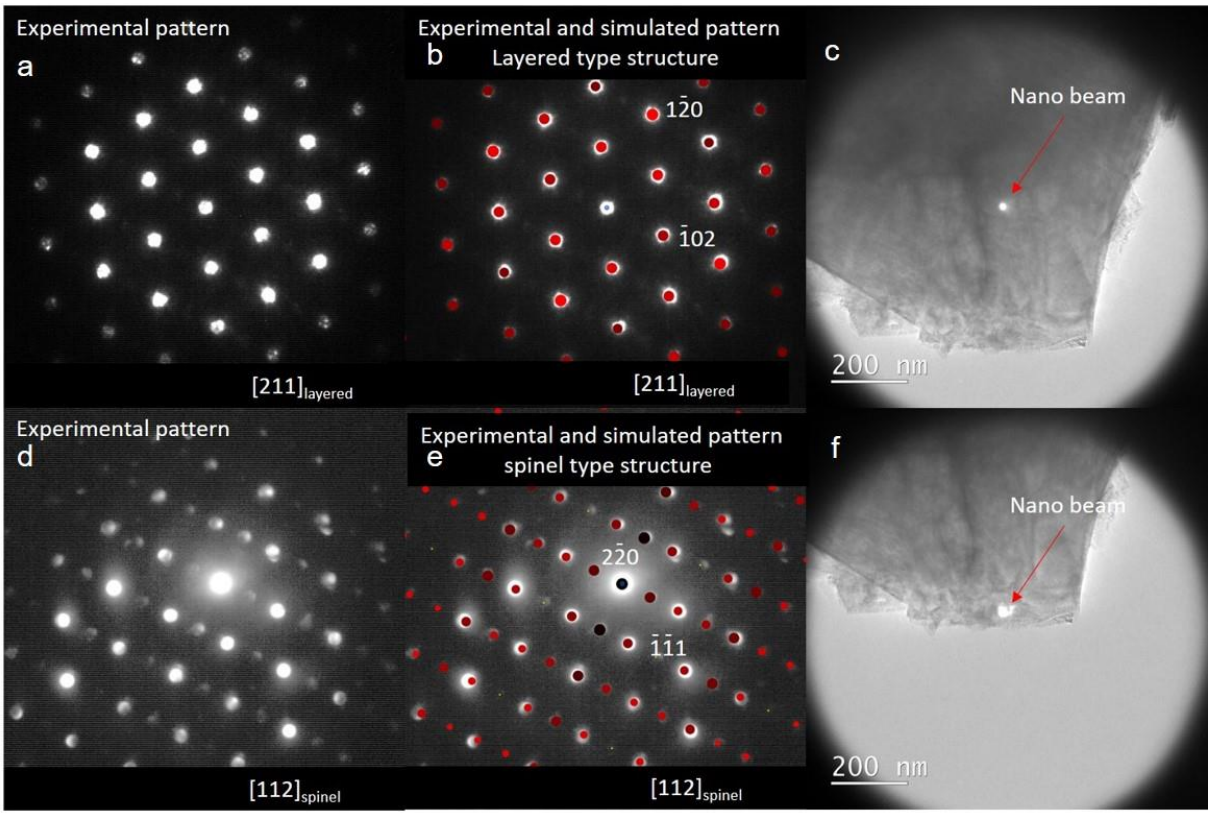

Figure A. 33. Nanobeam electron diffraction on the cycled $Li_xCo_{0.96}Al_{0.04}O_2$.a) experimental diffraction pattern related to the center of the particle indexed with the $Li_xCo_{0.96}Al_{0.04}O_2$ structure, b) comparison of experimental and simulated pattern c) location of the beam corresponding to pattern a, d) experimental diffraction pattern related to the edge of the particle indexed with a spinel type structure, e) comparison of experimental and simulated pattern and f) location of the beam corresponding to pattern d.

The presence of a spinel type phase has to be considered to explain it. Indeed, all the reflections of this pattern can be indexed by considering the [112] spinel zone axis as demonstrated by the superposition of the experimental pattern with the [112] spinel zone axis simulated pattern (**Figure A.33.e**). Nevertheless, note that some reflections have much higher intensities than others. These intense reflections seem to match those observed in the center of the crystal and indeed, some interplanar distances are identical in both structures as for instance $d_{1\text{-}20lay}$ and $d_{4\text{-}40spi}$ or $d_{\text{-}204lay}$ and $d_{\text{-}1\text{-}11spi}$. The pattern obtained on the edge of the crystal must then be considered as the superposition of patterns belonging to both lamellar and spinel structures. This finding is thus in line with our ^{7}Li MAS NMR study indicating the presence of spinel-like environments for Li and additionally reveals that those domains are present at the surface of the particles only.

A.4.5. Discussion and Conclusion

$LiCo_{0.96}Al_{0.04}O_2$ was synthesized by a specific solid state route. ^{27}Al MAS NMR and XRD studies revealed that the Al-doping in this material is homogeneous while ^{7}Li MAS NMR indicates that its stoichiometry (Li/M=1.00) is ideal. Our electrochemical cycling study in Li cells reveals that even a low substituted amount of Co with Al (4%) has a profound effect on the electrochemical performance and yields a better cycling stability in the 3-4.6 V voltage range. XRD and ^{7}Li MAS NMR studies revealed that up to 4.5 V vs Li^+/Li, the overall structural evolution of the $LiCo_{0.96}Al_{0.04}O_2$ and st-$LiCoO_2$ phases is similar, although i) the insulator-metal transition does not occur in the same composition range and ii) the monoclinic distortion at x = 0.5 is hindered by Al doping. At higher voltages (> 4.6 V vs. Li^+/Li), noticeable structural differences have been evidenced in the deintercalated $Li_xCo_{0.96}Al_{0.04}O_2$ and Li_xCoO_2 materials and may be responsible for the enhanced cycling stability of Al-doped $LiCoO_2$. The XRD study shows that the deintercalated phases prepared for $x < 0.2$ from st-$LiCoO_2$, either by fixing the Li content or by a floating method, present the co-existence of several phases (O3, H1-3, O1 and phases with intermediate interslab space) with stacking faults. Whereas, deintercalated samples prepared from $LiCo_{0.96}Al_{0.04}O_2$ are more crystalline, and the formation of phases with intermediate interslab space is not observed. In addition, at 4.6V, the O1 phase is not observed for the Al-doped sample.

More interestingly, ^{7}Li MAS NMR reveals very different Li local environments in the high voltage phases. Unlike Li_xCoO_2, for Al-doped phases, signals assigned to Li in spinel-like

environments and in a diamagnetic CEI layer are observed in addition to the signal corresponding to Li in the interslab space of the O3 /H1-3 structures. Those observations do not depend on the materials preparation (by fixing the Li content or the floating voltage). The spinel phase is still detected after a few cycles in discharged $LiCo_{0.96}Al_{0.04}O_2$ phase is and the TEM study revealed that it is located at the surface of the particles. Since only signals of Li in the interslab space of the O3 or H1-3 structure were observed for Li_xCoO_2, we believe that the CEI formed on that material has a different nature and is unstable (either dissolved after the cell disconnection or by the electrode washing step prior to the measurements).[51] The different reactivity of the surface of $LiCoO_2$ and Al-doped $LiCoO_2$ has already been reported in literature: the basic character of the $LiCo_{1-x}Al_xO_2$ surface makes these materials less reactive than $LiCoO_2$ toward acidic species (such as HF) that are present in $LiPF_6$-based electrolytes.[52] The strong polarization observed at the beginning of the discharge from 5V in the st-$LiCoO_2$ system might therefore result from i) the high resistivity character of that CEI at high voltage that may dissolve then while discharging as unstable; ii) the formation of the H1-3 or O1 phase at the particles surface with a low interslab space that may also prevent a good Li^+ ions diffusivity back to the particles.

Based on our study, we believe that Al-doping improves the cycling performance of $LiCoO_2$ up to 4.6V, mainly by modifying the particles surface evolution upon cycling at high voltages. Even during the first charge, it leads to the formation of a surface reconstruction with the formation of a lithiated spinel-type phase that should have a good ionic conductivity. In the case if $LiCoO_2$, the formation of a spinel phase has been also reported,[53] is either not lithiated as not detected by ^{7}Li MAS NMR or formed only upon extended cycling. The lithiated spinel phase formed on the Al-doped compound, may then react differently with the electrolyte to form a stable CEI layer, which composition is different from the one formed on Li_xCoO_2. The formation of the Li-containing spinel phase and a stable CEI at the surface of the particles probably also explains the strong reduction of Co dissolution observed at high voltage as reported by Myung et al.[22]

References

(1) Yano, A.; Shikano, M.; Ueda, A.; Sakaebe, H.; Ogumi, Z. $LiCoO_2$ Degradation Behavior in the High-Voltage Phase Transition Region and Improved Reversibility with Surface Coating. *J. Electrochem. Soc.* **2017**, *164* (1), A6116–A6122.

(2) Yazami, R.; Ozawa, Y.; Gabrisch, H.; Fultz, B. Mechanism of Electrochemical Performance Decay in $LiCoO_2$ Aged at High Voltage. *Electrochimica Acta* **2004**, *50* (2–3), 385–390. https://doi.org/10.1016/j.electacta.2004.03.048.

(3) Xia, H.; Lu, L.; Meng, Y. S.; Ceder, G. Phase Transitions and High-Voltage Electrochemical Behavior of $LiCoO_2$ Thin Films Grown by Pulsed Laser Deposition. *J. Electrochem. Soc.* **2007**, *154* (4), A337. https://doi.org/10.1149/1.2509021.

(4) Takamatsu, D.; Koyama, Y.; Orikasa, Y.; Mori, S.; Nakatsutsumi, T.; Hirano, T.; Tanida, H.; Arai, H.; Uchimoto, Y.; Ogumi, Z. First In Situ Observation of the $LiCoO_2$ Electrode/Electrolyte Interface by Total-Reflection X-Ray Absorption Spectroscopy. *Angew. Chem. Int. Ed.* **2012**, *51* (46), 11597–11601. https://doi.org/10.1002/anie.201203910.

(5) Pender, J. P.; Jha, G.; Youn, D. H.; Ziegler, J. M.; Andoni, I.; Choi, E. J.; Heller, A.; Dunn, B. S.; Weiss, P. S.; Penner, R. M.; Mullins, C. B. Electrode Degradation in Lithium-Ion Batteries. *ACS Nano* **2020**, *14* (2), 1243–1295. https://doi.org/10.1021/acsnano.9b04365.

(6) Birkl, C. R.; Roberts, M. R.; McTurk, E.; Bruce, P. G.; Howey, D. A. Degradation Diagnostics for Lithium Ion Cells. *J. Power Sources* **2017**, *341*, 373–386. https://doi.org/10.1016/j.jpowsour.2016.12.011.

(7) Amatucci, G. G.; Tarascon, J. M.; Klein, L. C. Cobalt Dissolution in $LiCoO_2$-Based Non-Aqueous Rechargeable Batteries. *Solid State Ion.* **1996**, *83* (1), 167–173. https://doi.org/10.1016/0167-2738(95)00231-6.

(8) Chen, Z.; Dahn, J. R. Methods to Obtain Excellent Capacity Retention in $LiCoO_2$ Cycled to 4.5 V. *Electrochimica Acta* **2004**, *49* (7), 1079–1090. https://doi.org/10.1016/j.electacta.2003.10.019.

(9) Van der Ven, A.; Aydinol, M. K.; Ceder, G.; Kresse, G.; Hafner, J. First-Principles Investigation of Phase Stability in Li_xCoO_2. *Phys. Rev. B* **1998**, *58* (6), 2975–2987. https://doi.org/10.1103/PhysRevB.58.2975.

(10) Jiang, Y.; Yan, P.; Yu, M.; Li, J.; Jiao, H.; Zhou, B.; Sui, M. Atomistic Mechanism of Cracking Degradation at Twin Boundary of LiCoO2. *Nano Energy* **2020**, *78*, 105364. https://doi.org/10.1016/j.nanoen.2020.105364.

(11) Jiang, Y.; Qin, C.; Yan, P.; Sui, M. Origins of Capacity and Voltage Fading of $LiCoO_2$ upon High Voltage Cycling. *J. Mater. Chem. A* **2019**, *7* (36), 20824–20831. https://doi.org/10.1039/C9TA06579B.

(12) Hu, G.; Cao, J.; Peng, Z.; Cao, Y.; Du, K. Enhanced High-Voltage Properties of $LiCoO_2$ Coated with $Li[Li_{0.2}Mn_{0.6}Ni_{0.2}]O_2$. *Electrochimica Acta* **2014**, *149*, 49–55. https://doi.org/10.1016/j.electacta.2014.10.072.

(13) Gu, R.; Cheng, T.; Ma, Z.; Qian, R.; Lyu, Y.; Nie, A.; Guo, B. Enhanced Cycling Stability of High Voltage $LiCoO_2$ by Surface Phosphorylation. *J. Alloys Compd.* **2019**, *803*, 348–353. https://doi.org/10.1016/j.jallcom.2019.06.253.

(14) Cho, J.; Kim, C.-S.; Yoo, S.-I. Improvement of Structural Stability of LiCoO2 Cathode during Electrochemical Cycling by Sol-Gel Coating of SnO2. *Electrochem. Solid-State Lett.* **2000**, *3* (8), 362–365.

(15) Zhang, J.-N.; Li, Q.; Ouyang, C.; Yu, X.; Ge, M.; Huang, X.; Hu, E.; Ma, C.; Li, S.; Xiao, R.; Yang, W.; Chu, Y.; Liu, Y.; Yu, H.; Yang, X.-Q.; Huang, X.; Chen, L.; Li, H. Trace Doping of Multiple Elements Enables Stable Battery Cycling of $LiCoO_2$ at 4.6 V. *Nat. Energy* **2019**, *4* (7), 594–603. https://doi.org/10.1038/s41560-019-0409-z.

(16) Wang, L.; Chen, B.; Ma, J.; Cui, G.; Chen, L. Reviving Lithium Cobalt Oxide-Based Lithium Secondary Batteries-toward a Higher Energy Density. *Chem. Soc. Rev.* **2018**, *47* (17), 6505–6602. https://doi.org/10.1039/C8CS00322J.

(17) Liu, Q.; Su, X.; Lei, D.; Qin, Y.; Wen, J.; Guo, F.; Wu, Y. A.; Rong, Y.; Kou, R.; Xiao, X.; Aguesse, F.; Bareño, J.; Ren, Y.; Lu, W.; Li, Y. Approaching the Capacity Limit of Lithium Cobalt Oxide in Lithium Ion Batteries via Lanthanum and Aluminium Doping. *Nat. Energy* **2018**, *3* (11), 936–943. https://doi.org/10.1038/s41560-018-0180-6.

(18) zhao, ruirui; Zhang, J.; Lee, G.-H.; Zhang, K.; Lau, V. W.; Lee, J.-J.; Moudrakovski, I.; Yang, Y.-L.; Zhou, F.; Park, M.; Hung, I.-M.; Kang, Y. The Origin of Heavy Elemental Doping to Relieve the Lattice Thermal Vibration of Layered Materials for High Energy Density Li Ion Cathodes. *J. Mater. Chem. A* **2020**. https://doi.org/10.1039/D0TA03979A.

(19) Levasseur, S.; Ménétrier, M.; Delmas, C. Combined Effects of Ni and Li Doping on the Phase Transitions in Li_xCoO_2 Electrochemical and ^{7}Li Nuclear Magnetic Resonance Studies. *J. Electrochem. Soc.* **2002**, *149* (12), A1533–A1540. https://doi.org/10.1149/1.1516219.

(20) Ceder, G.; Chiang, Y.-M.; Sadoway, D. R.; Aydinol, M. K.; Jang, Y.-I.; Huang, B. Identification of Cathode Materials for Lithium Batteries Guided by First-Principles Calculations. *Nature* **1998**, *392* (6677), 694.

(21) Jang, Y.-I.; Huang, B.; Wang, H.; Sadoway, D. R.; Ceder, G.; Chiang, Y.-M.; Liu, H.; Tamura, H. $LiAl_YCo_{1-Y}O_2$ ($R\bar{3}m$) Intercalation Cathode for Rechargeable Lithium Batteries. *J. Electrochem. Soc.* **1999**, *146* (3), 862–868.

(22) Myung, S.-T.; Kumagai, N.; Komaba, S.; Chung, H.-T. Effects of Al Doping on the Microstructure of $LiCoO_2$ Cathode Materials. *Solid State Ion.* **2001**, *139* (1), 47–56. https://doi.org/10.1016/S0167-2738(00)00828-6.

(23) Levasseur, S. Evidence for Structural Defects in Non-Stoichiometric HT-$LiCoO_2$: Electrochemical, Electronic Properties and ^{7}Li NMR Studies. *Solid State Ion.* **2000**, *128* (1–4), 11–24. https://doi.org/10.1016/S0167-2738(99)00335-5.

(24) Levasseur, S.; Ménétrier, M.; Shao-Horn, Y.; Gautier, L.; Audemer, A.; Demazeau, G.; Largeteau, A.; Delmas, C. Oxygen Vacancies and Intermediate Spin Trivalent Cobalt Ions in Lithium-Overstoichiometric $LiCoO_2$. *Chem. Mater.* **2003**, *15* (1), 348–354. https://doi.org/10.1021/cm021279g.

(25) Gaudin, E.; Taulelle, F.; Stoyanova, R.; Zhecheva, E.; Alcántara, R.; Lavela, P.; Tirado, J. L. Cobalt(III) Effect on ^{27} Al NMR Chemical Shifts in $LiAl_xCo_{1-x}O_2$. *J. Phys. Chem. B* **2001**, *105* (34), 8081–8087. https://doi.org/10.1021/jp0105948.

(26) Duffiet, M.; Blangero, M.; Cabelguen, P. E.; Song, K. S.; Fauth, F.; Delmas, C.; Carlier, D. Probing Al Distribution in $LiCo_{0.96}Al_{0.04}O_2$ Materials Using ^{7}Li, ^{27}Al, and ^{59}Co MAS NMR

Combined with Synchrotron X-Ray Diffraction. *Inorg. Chem.* **2020**, *59* (5), 2890–2899. https://doi.org/10.1021/acs.inorgchem.9b03260.

(27) Duffiet, M. Investigation of Structural Failure Mechanisms of $LiCoO_2$ at High Voltage and Material Optimization through Aluminum Doping. PhD Thesis, Université de Bordeaux, 2019.

(28) Lundblad, A.; Bergman, B. Synthesis of $LiCoO_2$ Starting from Carbonate Precursors II. Influence of Calcination Conditions and Leaching. *Solid State Ion.* **1997**, *96* (3), 183–193. https://doi.org/10.1016/S0167-2738(97)00017-9.

(29) Duffiet, M.; Blangero, M.; Cabelguen, P.-E.; Delmas, C.; Carlier, D. Influence of the Initial Li/Co Ratio in $LiCoO_2$ on the High-Voltage Phase-Transitions Mechanisms. *J. Phys. Chem. Lett.* **2018**, *9* (18), 5334–5338. https://doi.org/10.1021/acs.jpclett.8b02252.

(30) Levasseur, S.; Ménétrier, M.; Delmas, C. Combined Effects of Ni and Li Doping on the Phase Transitions in Li_xCoO_2 Electrochemical and 7 Li Nuclear Magnetic Resonance Studies. *J. Electrochem. Soc.* **2002**, *149* (12), A1533–A1540. https://doi.org/10.1149/1.1516219.

(31) Yoon, W.-S.; Lee, K.-K.; Kim, K.-B. Structural and Electrochemical Properties of LiAl Y Co1- Y O 2 Cathode for Li Rechargeable Batteries. *J. Electrochem. Soc.* **2000**, *147* (6), 2023.

(32) Xie, M.; Hu, T.; Yang, L.; Zhou, Y. Synthesis of High-Voltage (4.7 V) $LiCoO_2$ Cathode Materials with Al Doping and Conformal Al $_2O_3$ Coating by Atomic Layer Deposition. *RSC Adv.* **2016**, *6* (68), 63250–63255. https://doi.org/10.1039/C6RA10531A.

(33) Kuboon, S.; Hu, Y. H. Study of NiO−CoO and Co_3O_4−Ni_3O_4 Solid Solutions in Multiphase Ni−Co−O Systems. *Ind. Eng. Chem. Res.* **2011**, *50* (4), 2015–2020. https://doi.org/10.1021/ie101249r.

(34) Ménétrier, M.; Carlier, D.; Blangero, M.; Delmas, C. On "Really" Stoichiometric $LiCoO_2$. *Electrochem. Solid-State Lett.* **2008**, *11* (11), A179. https://doi.org/10.1149/1.2968953.

(35) Carlier, D.; Cheng, J.-H.; Pan, C.-J.; Ménétrier, M.; Delmas, C.; Hwang, B.-J. DFT+U Calculations and XAS Study: Further Confirmation of the Presence of CoO_5 Square-Based Pyramids with IS-Co^{3+} in Li-Overstoichiometric $LiCoO_2$. *J. Phys. Chem. C* **2013**, *117* (50), 26493–26500. https://doi.org/10.1021/jp409850q.

(36) Faenza, N. V.; Pereira, N.; Halat, D. M.; Vinckeviciute, J.; Bruce, L.; Radin, M. D.; Mukherjee, P.; Badway, F.; Halajko, A.; Cosandey, F.; Grey, C. P.; Van der Ven, A.; Amatucci, G. G. Phase Evolution and Degradation Modes of $R\bar{3}M$ $Li_X Ni_{1-Y-Z} Co_Y Al_Z O_2$ Electrodes Cycled Near Complete Delithiation. *Chem. Mater.* **2018**, *30* (21), 7545–7574. https://doi.org/10.1021/acs.chemmater.8b02720.

(37) Alcántara, R.; Lavela, P.; Relaño, P. L.; Tirado, J. L.; Zhecheva, E.; Stoyanova, R. X-Ray Diffraction, EPR, and 6Li and 27Al MAS NMR Study of $LiAlO_2$−$LiCoO_2$ Solid Solutions. *Inorg. Chem.* **1998**, *37* (2), 264–269. https://doi.org/10.1021/ic9707220.

(38) Siegel, R.; Hirschinger, J.; Carlier, D.; Matar, S.; Ménétrier, M.; Delmas, C. 59Co and ^{6,7}Li MAS NMR in Polytypes O2 and O3 of $LiCoO_2$. *J. Phys. Chem. B* **2001**, *105* (19), 4166–4174. https://doi.org/10.1021/jp003832s.

(39) Kikkawa, S.; Miyazaki, S.; Koizumi, M. Deintercalated $NaCoO_2$ and $LiCoO_2$. *J. Solid State Chem.* **1986**, *62* (1), 35–39. https://doi.org/10.1016/0022-4596(86)90213-6.

(40) Artemenko, A.; Ménétrier, M.; Pollet, M.; Delmas, C. Reinvestigation of the Magnetic Behavior of O3–$LiCoO_2$. *J. Appl. Phys.* **2009**, *106* (6), 64914. https://doi.org/10.1063/1.3226700.

(41) Shao-Horn, Y.; Levasseur, S.; Weill, F.; Delmas, C. Probing Lithium and Vacancy Ordering in O3 Layered Li_xCoO_2 (x≈0.5). *J. Electrochem. Soc.* **2003**, *150* (3), A366. https://doi.org/10.1149/1.1553787.

(42) Reimers, J. N.; Dahn, J. R. Electrochemical and in Situ X-Ray Diffraction Studies of Lithium Intercalation in Li_xCoO_2. *J. Electrochem. Soc.* **1992**, *139* (8), 2091–2097.

(43) Carlier, D.; Van der Ven, A.; Delmas, C.; Ceder, G. First-Principles Investigation of Phase Stability in the O2-LiCoO $_2$ System. *Chem. Mater.* **2003**, *15* (13), 2651–2660. https://doi.org/10.1021/cm030002t.

(44) Ménétrier, M.; Saadoune, I.; Levasseur, S.; Delmas, C. The Insulator-Metal Transition upon Lithium Deintercalation from LiCoO2: Electronic Properties and 7Li NMR Study. *J. Mater. Chem.* **1999**, *9* (5), 1135–1140.

(45) Ohzuku, T.; Ueda, A. Solid-State Redox Reactions of LiCoO2 (R3m) for 4 Volt Secondary Lithium Cells. *J. Electrochem. Soc.* **1994**, *141* (11), 2972–2977.

(46) Geng, F.; Shen, M.; Hu, B.; Liu, Y.; Zeng, L.; Hu, B. Monitoring the Evolution of Local Oxygen Environments during LiCoO $_2$ Charging *via Ex Situ* ^{17} O NMR. *Chem. Commun.* **2019**, *55* (52), 7550–7553. https://doi.org/10.1039/C9CC03304A.

(47) Shimoda, K.; Murakami, M.; Takamatsu, D.; Arai, H.; Uchimoto, Y.; Ogumi, Z. In Situ NMR Observation of the Lithium Extraction/insertion from LiCoO2 Cathode. *Electrochimica Acta* **2013**, *108*, 343–349. https://doi.org/10.1016/j.electacta.2013.06.120.

(48) Casas-Cabanas, M.; Rodríguez-Carvajal, J.; Canales-Vázquez, J.; Laligant, Y.; Lacorre, P.; Palacín, M. R. Microstructural Characterisation of Battery Materials Using Powder Diffraction Data: DIFFaX, FAULTS and SH-FullProf Approaches. *J. Power Sources* **2007**, *174* (2), 414–420. https://doi.org/10.1016/j.jpowsour.2007.06.216.

(49) Godillot, G.; Huo, H.; Ménétrier, M.; Bourgeois, L.; Guerlou-Demourgues, L.; Delmas, C. Promising Nanometric Spinel Cobalt Oxides for Electrochemical Energy Storage: Investigation of Li and H Environments by NMR. *J. Phys. Chem. C* **2012**, *116* (50), 26598–26607. https://doi.org/10.1021/jp307458z.

(50) Gaudon, M.; Apheceixborde, A.; Ménétrier, M.; Le Nestour, A.; Demourgues, A. Synthesis Temperature Effect on the Structural Features and Optical Absorption of $Zn_{1-x}Co_xAl_2O_4$ Oxides. *Inorg. Chem.* **2009**, *48* (19), 9085–9091. https://doi.org/10.1021/ic900482v.

(51) Zhang, J.-N.; Li, Q.; Wang, Y.; Zheng, J.; Yu, X.; Li, H. Dynamic Evolution of Cathode Electrolyte Interphase (CEI) on High Voltage $LiCoO_2$ Cathode and Its Interaction with Li Anode. *Energy Storage Mater.* **2018**, *14*, 1–7. https://doi.org/10.1016/j.ensm.2018.02.016.

(52) Dahéron, L.; Dedryvère, R.; Martinez, H.; Flahaut, D.; Ménétrier, M.; Delmas, C.; Gonbeau, D. Possible Explanation for the Efficiency of Al-Based Coatings on $LiCoO_2$: Surface Properties of $LiCo_{1-x}Al_xO_2$ Solid Solution. *Chem. Mater.* **2009**, *21* (23), 5607–5616. https://doi.org/10.1021/cm901972e.

(53) Wang, H.; Jang, Y.-I.; Huang, B.; Sadoway, D. R.; Chiang, Y.-M. Electron Microscopic Characterization of Electrochemically Cycled $LiCoO_2$ and $Li(Al,Co)O_2$ Battery Cathodes. *J. Power Sources* **1999**, *81–82*, 594–598. https://doi.org/10.1016/S0378-7753(99)00108-1.

Part B: Comparison of the dopant role in the different Mg doped $LiCoO_2$ material as a function of the ratio Li/M (M=Co+Mg)

B. Comparison of the dopant role in the different Mg doped $LiCoO_2$ material as a function of the ratio Li/M (M=Co+Mg) 125

B.1. General introduction 125

B.2. Structural characterization of the starting materials 126

B.2.1. Introduction 126

B.2.2. Syntheses of Mg doped $LiCoO_2$ 127

B.2.3. Study of the morphology 128

B.2.4. Study of the average structure by XRD 129

B.2.5. Study of the local structure by ^{7}Li and ^{59}Co MAS NMR 133

B.2.6. Study of magnetic properties 138

B.2.7. General discussion 140

B.2.8. Conclusion on chapter B.2 145

B.3. Evaluation of the electrochemical performances for the 2%Mg doped materials 147

B.3.1. Cycling experiments with various upper cutoff voltages 148

B.3.2. GITT in the low voltage region 151

B.4. Study of the mechanisms occurring during Li deintercalation for the 2% Mg doped $LiCoO_2$ samples with $Li/M \geq 0.98$ up to 4.8 V vs Li^+/Li 155

B.4.1. Study of the average structure by XRD 157

B.4.2. Study of the local structure by ^{7}Li MAS NMR 159

B.4.3. Structural characterization after cycling at high voltage for Li/M=0.98 162

B.5. Conclusion for chapter B.3 and B.4 166

References 167

B. Comparison of the dopant role in the different Mg doped $LiCoO_2$ material as a function of the ratio Li/M (M=Co+Mg)

B.1. General introduction

The effect of Aluminum as a dopant was investigated in the previous chapter, it is important to study the impact of other element such as Magnesium. Tukamoto et al.[1] first reported that Mg substitution improves the cycling performances which was also confirmed by other groups.[2–5] The thermal stability of the positive electrode materials increases also when doping $LiCoO_2$ with Mg: Yin et al.[6] reported that the exothermic peak (the main peak indicating the amount of O_2 evolution) was shifted to a higher temperature of about 90°C in Mg-doped $LiCoO_2$ as compared to $LiCoO_2$.

This part is devoted to the understanding the effect of Mg doping on samples with well controlled Li/M (M=Co+Mg) stoichiometries. It is composed of three chapters:

- In the first chapter, a study on the effects of 2% Mg substitution will be done, therefore materials with various Li/M stoichiometries (Li/M=0.96, 0.98 and 1.00) are synthesized and characterized at the local and average scale in order to evidence the homogeneity of the magnesium distribution in the samples with different Li/M ratio. In this study, Li/M ratio was limited to 1.00 in order to, in theory, avoid the presence of extra Li in the slabs.
- In the second chapter, we will study the role of Mg as a dopant on the electrochemical performance for the various samples.
- Finally, in the last chapter, we aim to understand the role of Mg-doping on the mechanisms involved during cycling at high voltages, combining XRD and ^{7}Li MAS NMR to probe different scales.

B.2. Structural characterization of the starting materials

B.2.1. Introduction

According to the ionic radius of Mg^{2+} ions (0.72 Å) compared to Li^{+} (0.76 Å) and Co^{3+} (0.545 Å), several structural hypotheses have been made in literature.

- If Mg^{2+} substitutes Co^{3+} leading to the $[Li]_{interslab}[Co_{1-y}Mg_y]_{slab}O_2$ theoretical formula, it should lead to the formation of Co^{4+} ions for charge compensation or eventually to IS-Co^{3+} if oxygen vacancy are formed as it was shown by Levasseur et al.[2] Tukamoto et al.[1] studied the effect of varying the Mg dopant concentration in $LiCoO_2$. They found that the partial substitution of Co by Mg increases the electronic conductivity by over two orders of magnitude. This results were further confirmed by Levasseur et al[7], in our lab, who carried out a study combining Mg doping and Li overstoichiometry. They synthesized several $Li_{x0}Co_{1-y}Mg_yO_2$ materials (where x_0 is the Li/(Co+ Mg) ratio, x_0= 0.98, 1.0, and 1.10) using solid state reaction. From ^{7}Li MAS NMR results, they observed additional signals located at 55, 325 and -30 ppm with two shoulders on the central line at 8 and -9 ppm. The great similarity that exists between the ^{7}Li NMR spectra of the overlithiated $Li_{x0}CoO_2$ and Mg doped $LiCoO_2$ phases leads them to believe that a structural defect leading to the presence of IS-Co^{3+} ions associated with oxygen vacancy also exists in the Mg doped phases; they attribute then the signal at 325 ppm to the presence of Li^{+} ions first neighbors of $Co^{3+(IS)}$ ions (interaction at 90°), the signal at -30 ppm coming from lithium ions having Co^{3+IS} ions second neighbors (interaction at 180°). The shoulders at 8 and -9 ppm result from Li^{+} ions near the oxygen deficiency and the signal at 55 ppm to a Knight-shift-type interaction, resulting from the presence of itinerant electron holes which induce metallic behavior in the sample, at least at the local scale.
- If the Mg^{2+} ions substitute both Li^{+} and Co^{3+} ions leading to the $[Li_{1-y/2}Mg_{y/2}]_{interslab}[Co_{1-y/2}Mg_{y/2}]_{slab}O_2$ theoretical formula, then Co remains 3+ and no oxygen vacancy is required for charge compensation. Pouillerie et al.[3], reported that in the Mg doped $LiNiO_2$ system, some Mg exist in the lithium layer. However, Dahn et al.[8], investigated the structure of $LiCoO_2$ with various Mg doping amounts using Rietveld refinement and found that none of the Mg was in the lithium layer. More recently, Kong et al.[9] studied the effect of Mg

substitution at Li and Co sites in $LiCoO_2$ and showed that this substitution enhance the capacity retention.

During the finalization of this manuscript, Huang et al.[10] reported in literature the effect of Mg substitution at the Li site by synthetizing a "$Li_{0.9}Mg_{0.05}CoO_2$" sample using solid state reaction with 3% excess of Li_2CO_3. Note that, although not mentioned, MgO impurity can be seen in their XRD pattern. The exact stoichiometry of the phase is not reported or discussed in that paper. Mg substitution for Li^+ in the lithium layer should lead to the formation of Co^{2+} ions: $[Li_{1-y}Mg_y]_{interslab}[Co^{III}_{1-y}Co_y^{II}]_{slab}O_2$. That was indeed observed in this study by XAS, but assigned Li-Mg mixing at the surface of the material. Finally, it is concluded that Mg^{2+} was successful introduced into the Li site acting as pillar to prevent slab gliding upon cycling. This effect, together with surface Li-Mg mixing are believed to be beneficial to the improvement of electrochemical performance.

Previous studies and this very recent one, reveals that a precise control of Li/M ratio is crucial for the electrochemical properties. The effect of Mg substitution, should be correlated with the overall stoichiometry of the sample, since the Li/Co ratio can also be larger than 1.00 in $LiCoO_2$. In this part, we will focus on 2% magnesium doped materials prepared using a solid state route at Umicore R&D using several Li/M ratios close to 1.00. Our efforts were dedicated to accurately characterize the structure of those materials using SXRD and ^7Li, ^{59}Co MAS NMR and magnetic measurements as complementary tools.

B.2.2. Syntheses of Mg doped $LiCoO_2$

The 2% Mg doped $LiCoO_2$ phases have been synthesized by a solid state route following the same steps as in section **A.3.1**. The precursors Li_2CO_3 and Co_3O_4, were initially blended with MgO and heat treated at 1050°C for 12h to form the doped $LiCoO_2$ powders with various Li/M ratios (M=Mg +Co =0.96, 0.98 and 1.00). Subsequently, grinding and annealing at 800 °C for 5 hours was carried out in order to ensure good homogeneity of the materials, since all synthesis were performed for 10g at Umicore.

All characterizations were performed under the same experimental conditions than in **part A** section **A.2**. Chemical analyzes by ICP-AES (Inductively Coupled Plasma - atomic emission spectroscopy) allowed to determine the final $(Li / Co)_{exp}$ and $(Li/(Mg+Co))_{exp}$ ratios for

2% Mg doped $LiCoO_2$ materials and are gathered in **Table B.1**. Experimental values are in good agreements with the theoretical ones.

Target formula	**Li/Co**		**Li/M (M=Co+Mg)**	
	Target	**Experimental**	**Target**	**Experimental**
"$Li_{0.96}Co_{0.98}Mg_{0.02}O_2$"	0.98	0.97	0.96	0.95
"$Li_{0.98}Co_{0.98}Mg_{0.02}O_2$"	1.00	0.99	0.98	0.97
"$Li_{1.00}Co_{0.98}Mg_{0.02}O_2$"	1.02	1.01	1.00	0.99

Table B. 1. ICP results for the 2% Mg doped $LiCoO_2$ powders

As in the previous chapter, an overlithiated lithium cobalt oxide ($Li_{1.02}Co_{0.98}O_{1.98}$) and a stoichiometric one (st-$LiCoO_2$) prepared respectively using Li/Co = 1.02 and 0.98 were used as reference materials for comparison.

B.2.3. Study of the morphology

The scanning electron microscopy images (**Figure. B.1**) show a larger primary particles size around ~20 μm and smoother surface when the Li/M ratio increases. The sample with Li/M=0.98 and Li/M=1.00 features a clearly identified population of particles with an average diameter around ~35μm and ~50 μm respectively. The particle size increases with the nominal Li/M ratio due to the role of the flux played by Li_2CO_3 at high temperature. Note that the sample with Li/M=0.96 has some smaller particles on the surface which are not observed for the other materials. Those particles may result from impurities as discussed further.

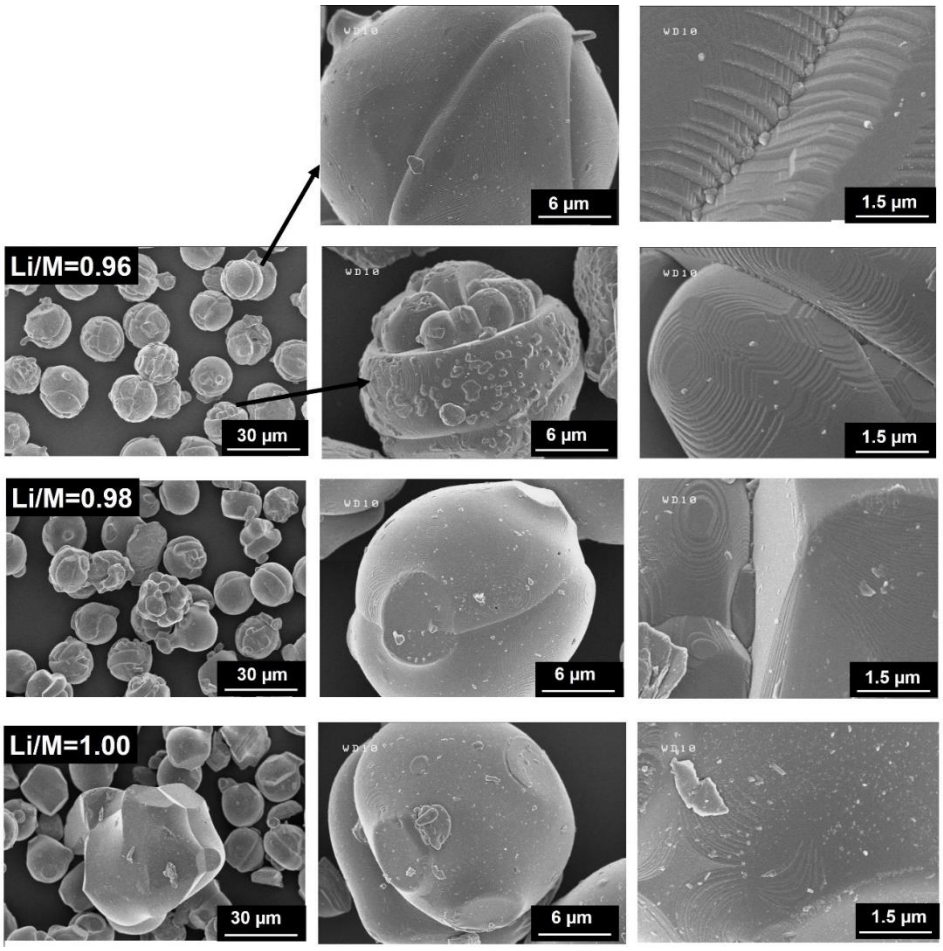

Figure B. 1. SEM micrographs of 2% Mg doped $LiCoO_2$ samples with various Li/M ratios with M= Co+Mg.

B.2.4. Study of the average structure by XRD

Typical powder X-ray diffraction patterns of Mg doped $LiCoO_2$ are presented in **Figure B.2** in comparison with st-$LiCoO_2$. The well-resolved $K_{\alpha 1}$ and $K_{\alpha 2}$ lines indicate the good crystallinity of the samples. All XRD patterns exhibits the diffraction lines expected for the layered O3 structure indexed in the R-3m space group, which indicate that the rhombohedral structure is well maintained throughout the materials series. No clear change of cell parameters or intensity ratios can be observed depending on the (Li/M) ratios using laboratory XRD as the instrumental resolution may be insufficient. Therefore, diffraction patterns were recorded at ALBA synchrotron in collaboration with François Fauth. Synchrotron XRD patterns are plotted in the **Figure B.3**.

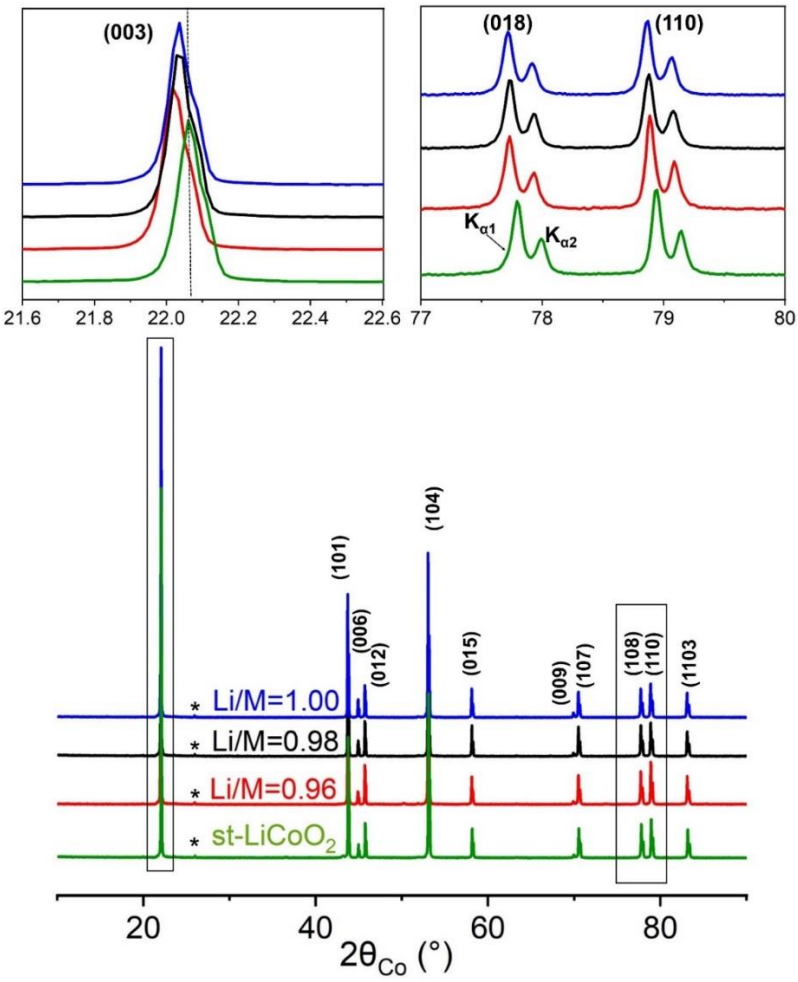

Figure B. 2. X-ray powder diffraction patterns for 2% Mg doped $LiCoO_2$ compared with stoichiometric $LiCoO_2$ (= sample holder).*

The diffraction lines are really narrow thus confirming the good crystallinity of the samples. The diffraction lines of our samples were even narrower than the ones of the standards used for calibration due to the technical limitations regarding the MYTHEN detector used which make Rietveld refinements very difficult to be performed. In fact, higher resolution is needed for such refinements, and since the samples were measured in the beam time of a PhD student from our group the detector couldn't be changed. Nevertheless, the angular resolution as well as the low level of noise, allow us a better characterization of our samples. The material with Li/M=1.00 is

pure, whereas both Li/M=0.96 and Li/M=0.98 samples present additional peaks at 2θ=22.56° and 2θ=32.17°. These peaks correspond to the to the (200) and (220) peaks arising from remaining traces of rocksalt (Fm-3m space group) magnesium oxide precursor. Those peaks were more intense in the case of Li/M=0.96 than for Li/M=0.98, furthermore, laboratory XRD was not sufficient to detect them for Li/M=0.98 sample. Note that the presence of Co_3O_4 as impurity in $LiCoO_2$ is in good agreement with the Li/Co=0.98 ratio used for the synthesis in order to ensure the preparation of st-$LiCoO_2$ as already discussed in the first part.

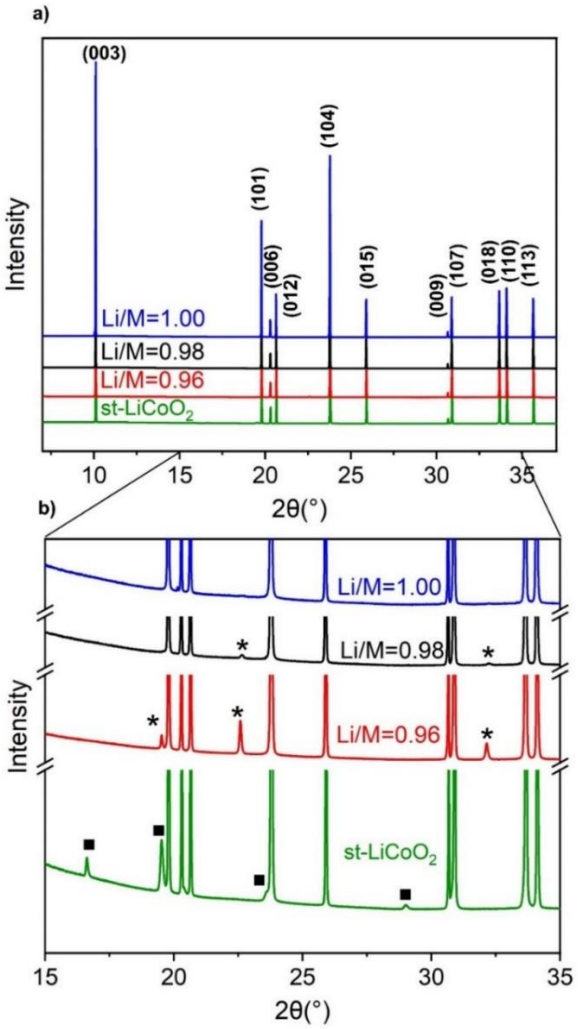

Figure B. 3.a) Synchrotron X-ray powder diffraction patterns for 2% Mg doped $LiCoO_2$ compared with stoichiometric $LiCoO_2$. All the patterns were collected with λ = 0.8260 Å. *A zoom in the b) 15° to 35° region is given (■: Co_3O_4; *: MgO).*

It has been demonstrated that the synchrotron-based X-ray characterization is a powerful tool for characterizing the homogeneity of the doping.[11] As shown from the diffraction peaks in the **Figure B.4,** no pronounced asymmetry has been observed acting, therefore, as a first evidence of the good homogeneity of Mg distribution in the O3 phases.

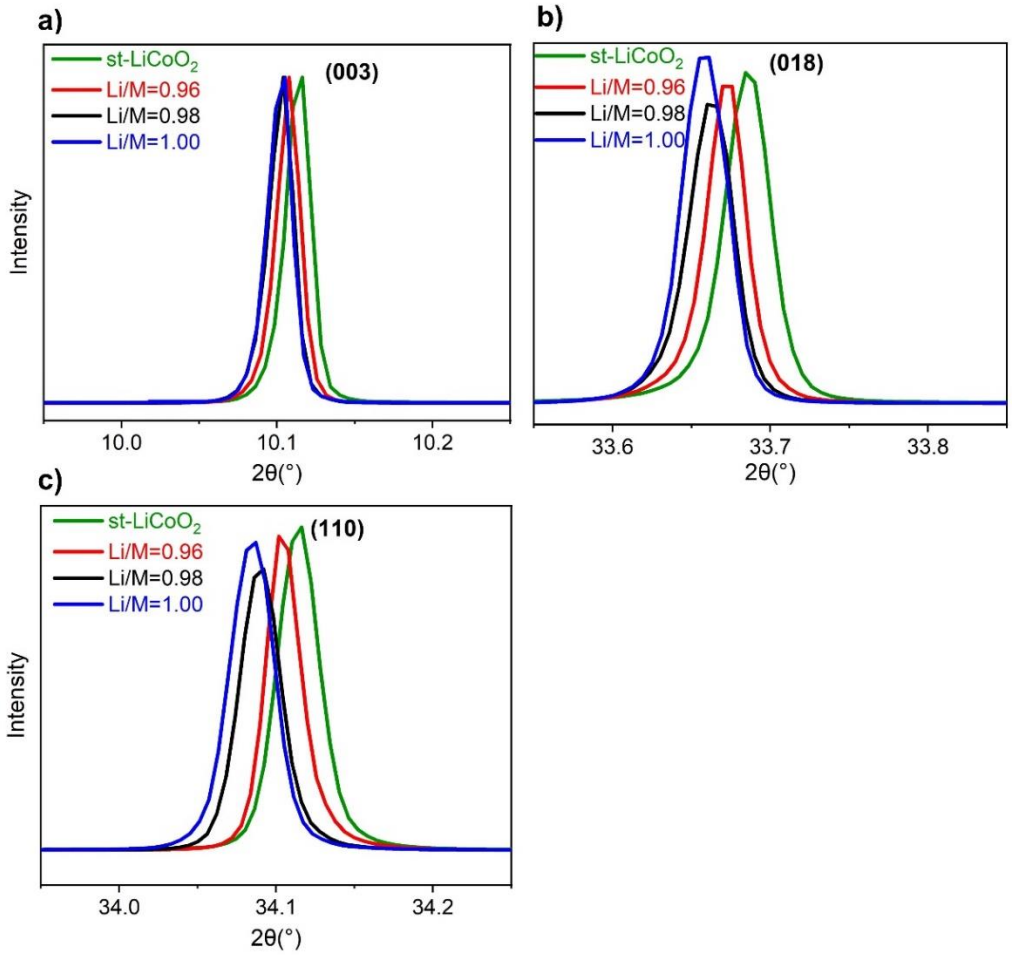

*Figure B. 4. Zoom on the (003), (018) and (110) diffraction peaks from the synchrotron X-ray diffraction patterns (*All the patterns were collected with λ = 0.8260 Å).

Compared to st-$LiCoO_2$, Mg doping leads to the shift of the (003) and (110) diffraction peaks toward lower angles (See **Figure B.4**) which are mainly characteristics of the $c_{hex.}$ and $a_{hex.}$ increase respectively. The structural parameters deduced from Le Bail refinement of the SXRD of the Li/M doped phase given in **Table B.2**, in comparison with the non-doped material.

Samples	Target formula	Impurity	a (Å)	c (Å)	c/a
st-$LiCoO_2$	"$Li_{0.98}CoO_2$"	Co_3O_4	2.8158 (1)	14.0532 (1)	4.99
			8.0702 (8)	-	-
0.96	"$Li_{0.96}Co_{0.98}Mg_{0.02}O_2$"	MgO	2.8164 (1)	14.0596 (1)	4.99
			4.2178 (8)	-	-
0.98	"$Li_{0.98}Co_{0.98}Mg_{0.02}O_2$"	MgO	2.8173 (1)	14.0606 (1)	4.99
			4.2056 (1)	-	-
1.00	"$Li_{1.00}Co_{0.98}Mg_{0.02}O_2$"	-	2.8177 (1)	14.0619 (1)	4.99

Table B. 2. Hexagonal lattice parameters deduced from synchrotron X-ray refinement of various Mg doped $LiCoO_2$ materials and identified impurities, in comparison with the st-$LiCoO_2$ sample.

The a_{hex} and c_{hex} cell parameters are slightly larger than those of st-$LiCoO_2$, what can come from the larger size of the Mg^{2+} ion compared to the Co^{3+} ion ($r_{Mg^{2+}}$= 0.72Å, $r_{Co^{3+}}$= 0.545 Å) which would indicate that Mg is not uniquely located on the Li site. The refined cell parameter for Co_3O_4 and MgO (Co_3O_4: a=8.080 Å and MgO: a=4.213 Å)[12,13] were rather similar to those extracted from literature which confirm the existence of these phases as impurities. Nevertheless, one cannot exclude the presence of a small amount of Co in the MgO phase.

B.2.5. Study of the local structure by ^{7}Li and ^{59}Co MAS NMR

^{7}Li MAS NMR spectra for the various 2% Mg doped materials compared to st-$LiCoO_2$ and overlithiated-$Li_{1.02}Co_{0.98}O_{1.98}$ is shown in **Figure B.5.a**. st-$LiCoO_2$ presents a single signal near to 0 ppm, characteristic of a stoichiometric sample Li/Co = 1.00, as has been already discussed in previous chapter. This material exhibits a single Li site surrounded by cobalt ions in low spin state (LS-Co^{3+}) with a diamagnetic electronic configuration ($t_{2g}^{6}e^{0}_{g}$), so no Fermi contact interaction occurs. **Figure B.6** shows the ^{7}Li MAS NMR spectra of Li/M=1.00 doped material compared with the overlithiated $Li_{1.02}Co_{0.98}O_{1.98}$ (Li/Co=1.02).

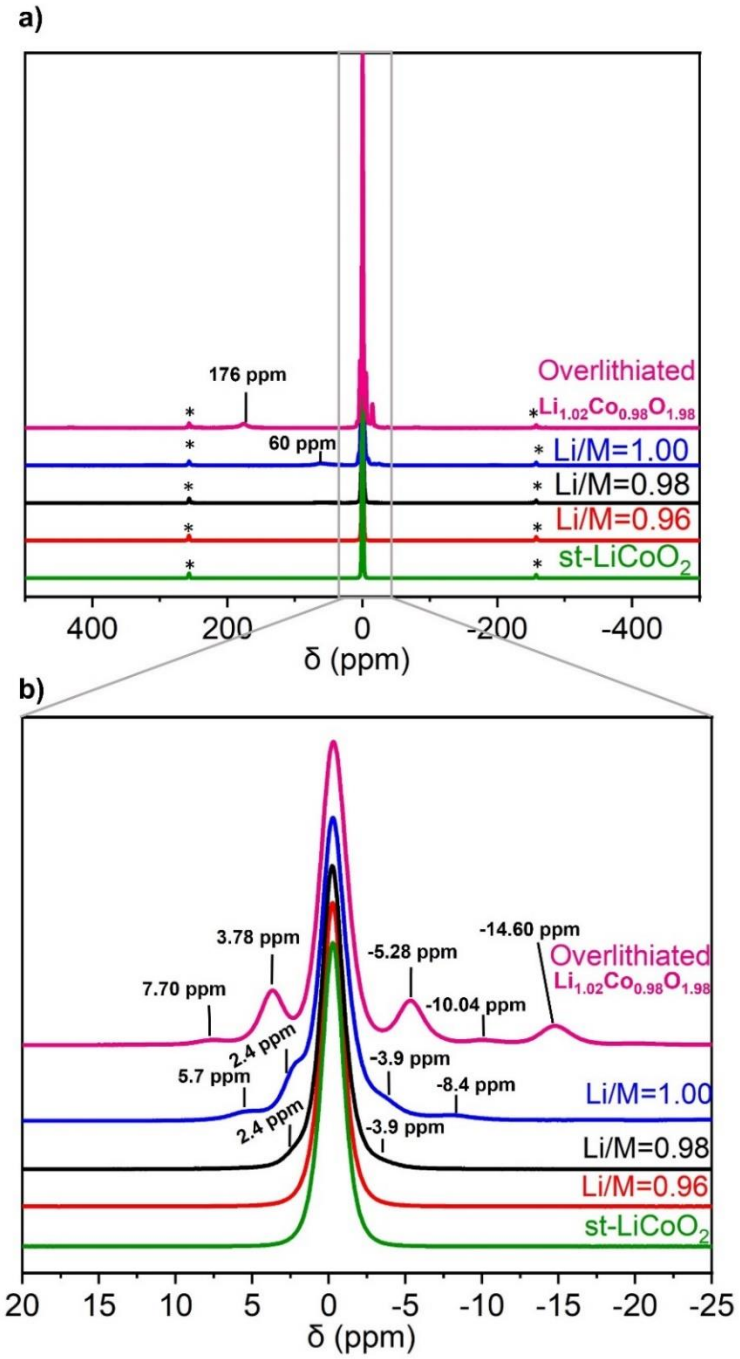

*Figure B. 5.(a) ^{7}Li MAS NMR spectra of 2% Mg doped $LiCoO_2$ samples with various Li/M stoichiometries (rotor-synchronized Hahn echo sequence, ν_R=30kHz, B_0 =7.05T *: spinning sidebands) compared to st-$LiCoO_2$ (prepared with Li/Co = 0.98) and overlithiated $Li_{1.02}Co_{0.98}O_{1.98}$ and (b) zoom in the region (-25 ppm ≤ δ ≤ 20 ppm).*

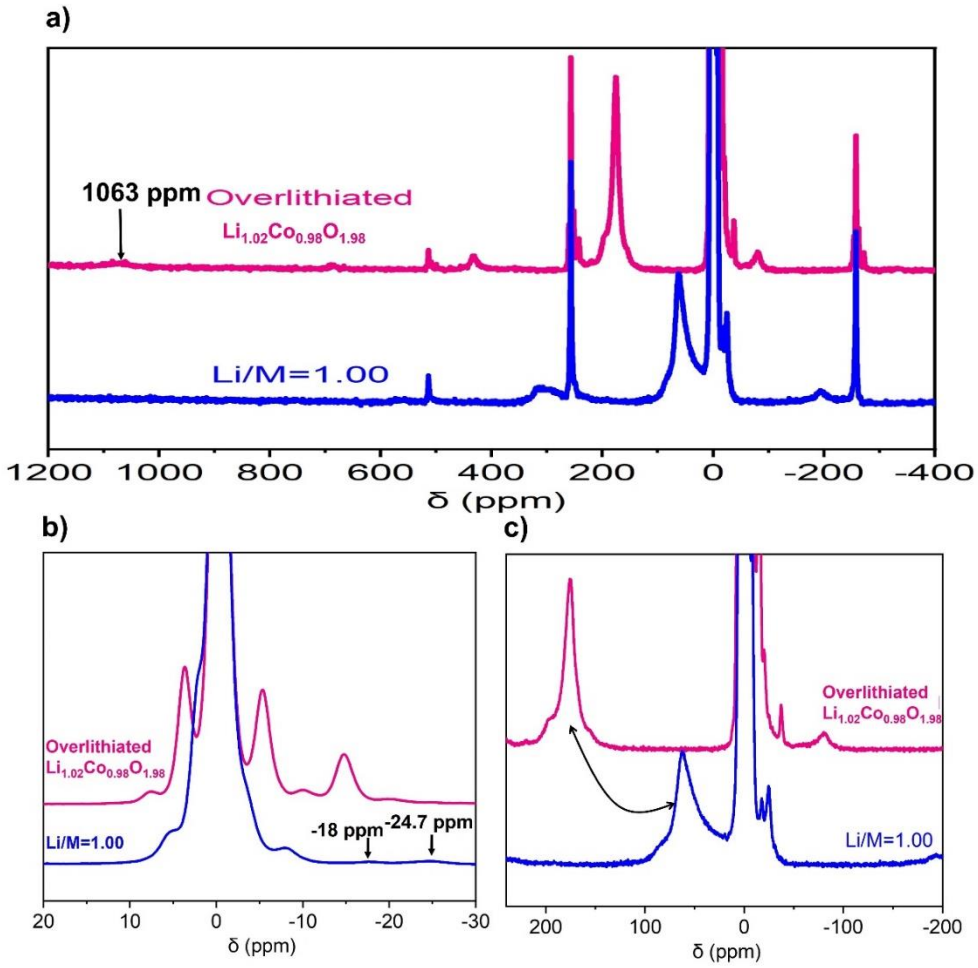

*Figure B. 6. (a) ^{7}Li MAS NMR spectra of $LiCo_{0.98}Mg_{0.02}O_2$ compared with the overlithiated $Li_{1.02}Co_{0.98}O_{1.98}$ sample (Hahn echo, B_0 = 7.05T *: spinning sidebands), with a zoom in (b) 20 ppm ≤ δ ≤ -30 ppm (c) and -200 ppm ≤ δ ≤ 200 ppm region.*

The overlithiated $[Li]_{interslab}[Co_{0.98}Li_{0.02}]_{slab}O_{1.98}$ in **Figure.B.6** exhibits a large number of additional signals located at 1063, 176, 7.70, 3.78, -5.28, -10.04, and -14.60 ppm. In this sample, paramagnetic intermediate spin state cobalt ions (IS-Co^{3+} d_{xz}^2 d_{xy}^2 d_{yz}^1 d_{z2}^1 d_{x2-y2}^0) are formed due to the presence of Li in the Co layer associated to an oxygen vacancy.[14] Hyperfine interactions are therefore expected between those unpaired electrons and nuclei of adjacent Li ions as 1st/2nd neighbors. The complete attribution of signals depending on the local environment could not be realized regarding the large number of different possible configurations. We, however, believe that the signal with the larger shift located at 1063 ppm, is assigned to Li located in the transition metal

layer. Indeed, this Li would undergo a strong Fermi contact interaction with two IS-Co^{3+} ions due to the unpaired electron in the t_{2g} type orbital, pointing in the direction of the former O-O edge between LiO_6 and CoO_6, not present anymore due to the O vacancy. All other signals are assigned to Li located in the interslab space with various environments versus IS-Co^{3+} and the position of the O-vacancy. [14]

The NMR spectra of the Mg doped materials with various Li/M shows that:

- The sample with Li/M=0.96 exhibits a narrow signal near 0 ppm similar to st-$LiCoO_2$, meaning that Li environments remain mostly unchanged by Mg doping. As no broadening of the signal has been detected, this tends to show that no or a very small amount of Mg in incorporated in the structure.
- For the sample with Li/M=0.98, in addition to the signal at 0 ppm, small tiny extra signals are observed at 2.4, -3.9 and 60 ppm (**Figure.B.5.b**). One can consider that this material is diamagnetic as a first approximation with negligible amount of paramagnetic ions leading to those Fermi contact shifted signals.
- For the Li/M=1.00 doped phase, the NMR spectrum shows, in addition to the diamagnetic signal at 0 ppm, several new signals at 289, 60, 5.7, 2.4, -3.9, -8.4, -18 and -24.7 ppm. These features clearly evidence that the material is paramagnetic. It should be noted that some of these shifted signals are different from those observed in Li/M=0.98 sample. They are also different from those observed in overlithiated $LiCoO_2$.[14] The signal located at ~1063 ppm is not observed for the Li/M=1.00 doped phase, meaning that no Li is present in the slab close to two IS-Co^{3+}.

As discussed in the introduction, Levasseur et al.[7] reported in their study three extra signals at 325, 55, and -27 ppm in addition to two shoulders on the central line at -9 and 8 ppm in the Mg doped $LiCoO_2$ materials studied. The spectra were interpreted by the presence of localized electrons due to paramagnetic $Co^{3+(IS)}$ ions in square based pyramid with oxygen vacancy and itinerant ones which induce metallic behavior in the sample, at least at the local scale. The local environment is depicted in **Figure B.7**. The difference observed in the chemical shift values for the $Li_{x0}Co_{1-y}Mg_yO_2$ phases and our system is probably due to different stoichiometry and

also to different recording conditions that affect the resolution and sample temperature. According to the strong difference with the ^{7}Li NMR spectra of the overlithiated phase, we however, believe, that the local electronic configuration in the Mg doped sample with Li/M = 1.00 is different. All observed signals could result from the formation of Co^{4+} ions, although a complete signal assignment could not be proposed here. The presence of Co^{4+} ions in the Mg doped sample with Li/M = 1.00 would explain the strong increase of conductivity observed for such materials in literature.[1]

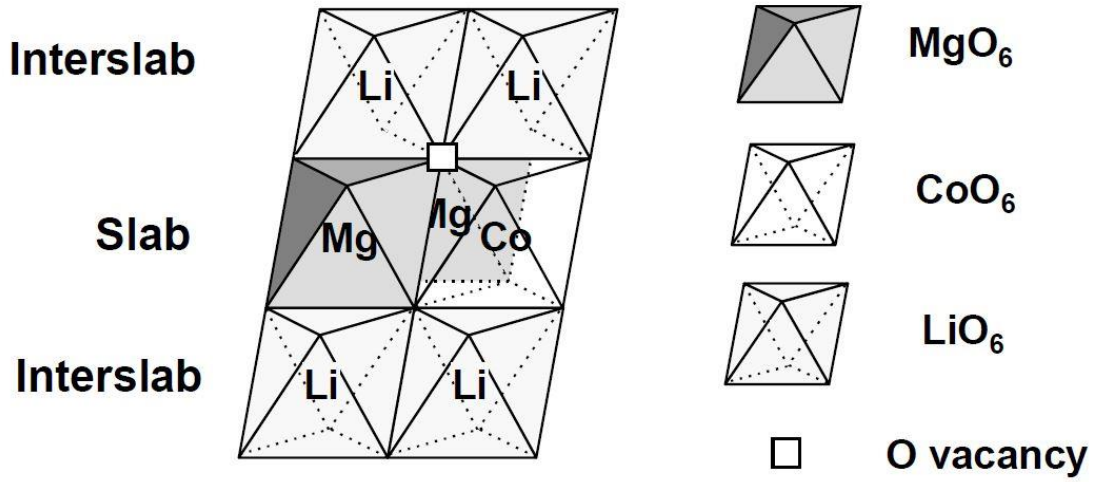

Figure B. 7. schematic representation of the local configuration of the structural defect revealed in the $Li_{x0}Co_{1-y}Mg_yO_2$ phases from Levasseur Phd. [15]

^{59}Co MAS NMR of the 2% Mg doped materials with different Li/M ratio are displayed in **Figure B.8**, we observe for the Li/M=0.96 sample, one signal with a chemical shift around 14135 ppm, which is very close to the one for st-$LiCoO_2$ (14137 ppm). This signal is however slightly larger than the one of st-$LiCoO_2$, may be due to the presence of some slightly different Co environments (tiny distribution). In the spectra of the Li/M=0.98, and Li/M=1.00 samples, the main signal is much broader with some asymmetry and is shifted to larger ppm values. In addition, other signals are observed in the right part of the spectrum (at 14083 ppm for Li/M =0.98 and 14093 ppm / 1428 ppm for Li/M = 1.00). Note that extra signals were observed for both overlithiated $Li_{1.02}Co_{0.98}O_{1.98}$ and Al doped $LiCoO_2$,[11] so that their origin cannot simply been related either to a

Fermi contact interaction with adjacent paramagnetic Co ions or to shielding interaction of LS-Co^{3+} ions in different diamagnetic environments.

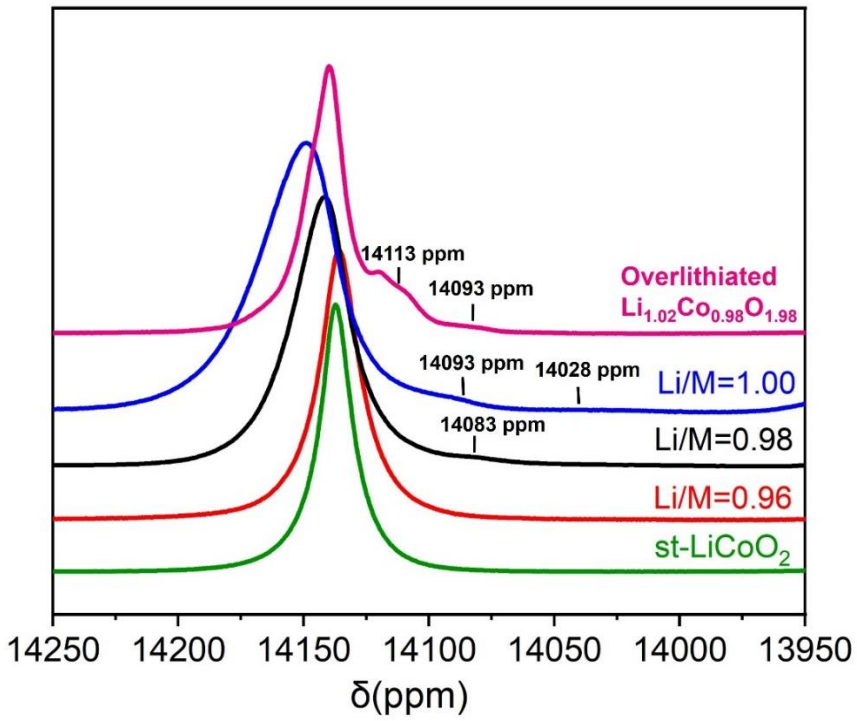

Figure B. 8.[59]Co MAS NMR spectra of 2% Mg doped $LiCoO_2$ samples with various Li/M stoichiometry compared to stoichiometric and overlithiated $Li_{1.02}Co_{0.98}O_{1.98}$

B.2.6. Study of magnetic properties

The magnetic measurements were done in order to find out if there are paramagnetic species in the materials. The molar magnetic susceptibility data of measurement for Mg doped samples are plotted as a function of temperature in **Figure B.9**. Using magnetic measurement, we are trying to characterize very small amount of paramagnetic ions and regarding this we find out a lack of precision of these results. But still, some trends were observed.

For st-$LiCoO_2$ (with some Co_3O_4) and Li/M=0.96 samples, the magnetic susceptibility (χ) is almost temperature (T) independent which is attributed to Van Vleck-type paramagnetism associated with diamagnetic Co^{3+} ions in the structure, in good agreement with previous study.[16,17] This is consistent with the NMR study where we showed that both st-$LiCoO_2$ and the Li/M=0.96

materials does not show ^{7}Li Fermi contact shifted signals as Co^{3+} are in a low spin state with S=0 ($t_{2g}^{6}e_{g}^{0}$).

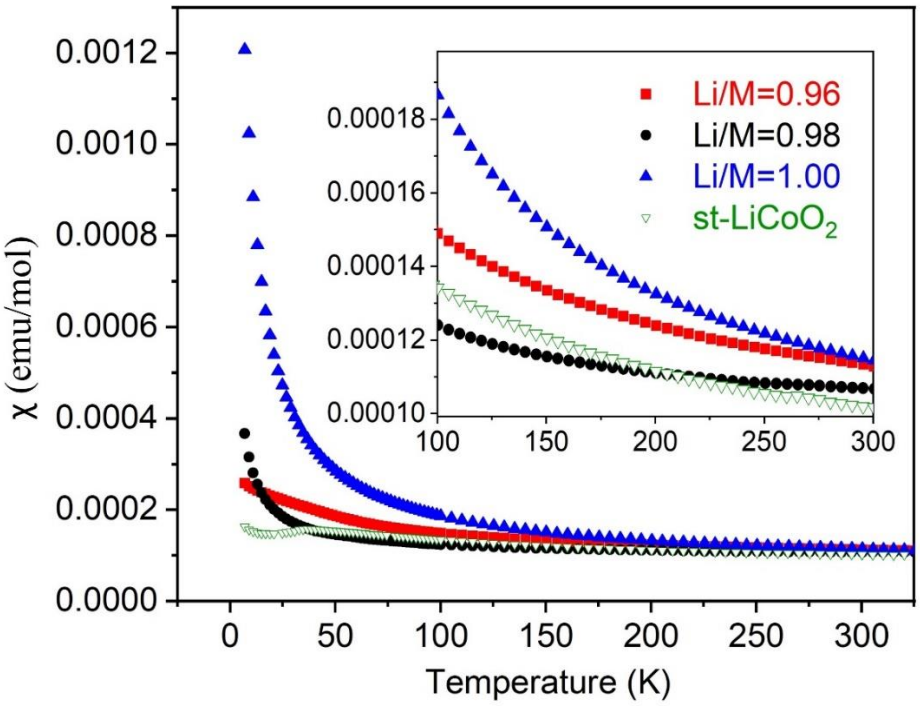

Figure B. 9. Thermal evolution of the (a) molar magnetic susceptibility. Insert: Zoom in the (100-300K) region.

In addition a bump is observed for st-$LiCoO_2$ around 35K, it has been attributed in previous study[17] to the antiferromagnetic transition of the Co_3O_4 phase with T_N =35K since the SXRD shows the existence of cobalt oxide impurity phase in st-$LiCoO_2$.

The magnetic susceptibility of the Li/M=0.98 sample also presents a very weak temperature dependence, although more paramagnetic than the Li/M = 0.96 one. This is in agreement with our ^{7}Li MAS NMR study showing very weak Fermi contact shifted signals. Among the series, the Li/M =1.00 sample is clearly the one showing the strongest temperature dependency of the magnetic susceptibility. This curve could be fitted in the 100K-350K region using the Curie-Weiss law: ($\chi = \chi_0 + C/(T-\theta)$). The Curie constant value fitted for the Li/M = 1.00 sample C_{exp} = 0.011 emu.K.mol^{-1} is slightly higher than the one expected if one considers that all Mg in the TM layer lead to the formation of LS-Co^{4+} (C_{th} = 0.0075 emu.K.mol^{-1}). One cannot discard the

hypothesis of the formation of IS-Co^{3+} located next to two Mg in the slab (C_{th} = 0.01 emu.K.mol^{-1} in that case). However, based on ^{7}Li MAS NMR study (NMR shifts were different to those observed in the literature in case of IS-Co^{3+} ions, our results are closer to hypothesis of the formation of Co^{4+} ions than IS-Co^{3+} ions.

B.2.7. General discussion

Based our SXRD, ^{7}Li and ^{59}Co MAS NMR and magnetic properties studies, we concluded that:

- The sample prepared with Li/M = 0.96 consists of a two phases mixture: ε-Mg doped $LiCoO_2$ and MgO.
- The sample prepared with Li/M=0.98 is a Mg doped $LiCoO_2$ with mainly LS-Co^{3+} ions and traces of MgO impurity.
- The sample prepared with Li/M=1.00 is a single Mg doped phase with paramagnetic ions. The following formula will be considered, assuming that magnesium substitute the Co site: $[Li_{1.00}]_{Li}$ $[Co^{3+}_{0.96}$ $Co^{4+}_{0.02}$ $Mg_{0.02}]_{Co}O_2$.

Considering the large size of the Mg^{2+} ion (in octahedral site: $r_{Mg^{2+}}$= 0.72Å, $r_{Co^{3+}}$= 0.545 Å), several hypotheses regarding the location of magnesium in the structure as well as the Li/M ratio can be considered.

B.2.7.1. Li/M=0.96

For the **Li/M=0.96** sample**,** we concluded that it consists in an ε-Mg doped $LiCoO_2$ diamagnetic phase with some MgO as impurity. If the Mg has entered into the structure, this can be only explained by the fact that Mg^{2+} ions are located in the interslab space and accompanied with the formation of a Li vacancy. This will therefore lead to the following formula with Li deficiency: $[Li_{0.98}\square_{\varepsilon}Mg_{\varepsilon}]_{interslab}Co_{1.00}O_2$ + (0.02- ε) MgO

An intermediate situation with a doping amount of Mg located in the Li site lower than 1% and the formation of the Mg-richer rock salt phase can also be an option.

In the first case, the substitution of Li^{+} by Mg^{2+} in the interslab space with the formation of a Li vacancy would be driving by the stabilization of LS-Co^{3+} in our synthesis conditions. (Mg^{2+}+ □)

thus would replace two Li^+ ions in the interslab space and avoid the formation of paramagnetic Co^{2+} ions, not seen here. Therefore, some MgO would be remaining as we are not strictly in the correct stoichiometry ratio to form a $Li_{1-2y}Mg_yCoO_2$ compound. Considering this hypothesis, the two end members of this solid solution series would be $LiCoO_2$ and $Mg_{0.5}CoO_2$ ($MgCo_2O_4$). The latter exhibiting a spinel structure, one can expect a limited solid solution. In order to check this hypothesis several materials $Li_{1-2y}Mg_yCoO_2$ with various Mg amount have been prepared following this scheme: $2Li^+$ replaced by $1Mg^{2+}$ + 1 vacancy from $LiCoO_2$. To do so, in our laboratory, Co_3O_4, MgO and Li_2CO_3 precursors were mixed using an agate grinder in different proportions of Mg (y = 0.02, 0.04 and 0.10) in the glove box. After homogenizing the mixture, the samples have been heat treated first to 600°C for 12h under air flow followed by a step of grinding then to 1050°C for 12h under argon.

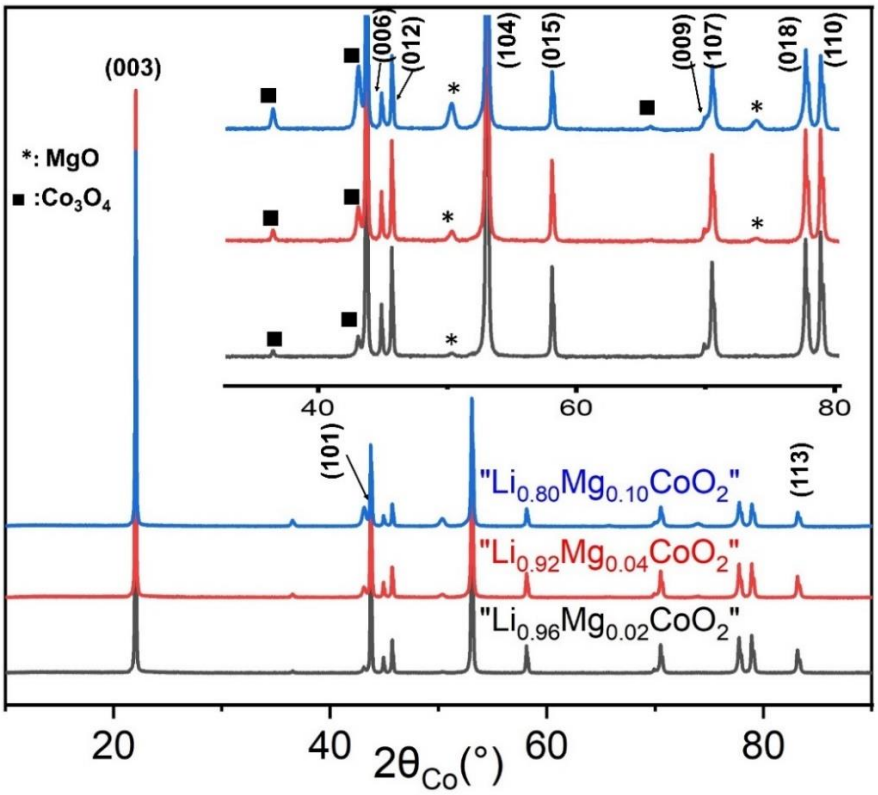

Figure B. 10. X-ray powder diffraction patterns for "$Li_{1-2y}Mg_yCoO_2$" with y= 0.02, 0.04 and 0.10. The study carried out from the X-ray diffraction is recorded under the following conditions: 10-120 ° 2θ, with a step of 0.02 °.

The materials have been then studied by XRD and the resulting patterns are plotted in **Figure B.10**. The major peaks of the diffractogramms can be indexed using the R-3m space group of $LiCoO_2$, but all patterns show the presence of traces of magnesium and cobalt oxide (MgO and Co_3O_4). The peaks related to these impurities become more intense with increasing y. The refined cell parameters for MgO and Co_3O_4 as impurities are really close from those extracted from literature (MgO: a=4.213 Å and Co_3O_4: a=8.080 Å).[12,13]

y	Li/M	Target formula	Impurity	a (Å)	c (Å)	Space group
0.00	-	"$Li_{0.98}CoO_2$"		2.8158 (1)	14.0532 (1)	R-3m
			Co_3O_4	8.0702 (8)	-	Fd-3m
0.02	0.94	"$Li_{0.96}Mg_{0.02}CoO_2$"		2.8154 (1)	14.056 (7)	R-3m
			MgO	4.219 (1)	-	Fm-3m
			Co_3O_4	8.075(3)	-	Fd-3m
0.04	0.88	"$Li_{0.92}Mg_{0.04}CoO_2$"		2.8154 (1)	14.055 (1)	R-3m
			MgO	4.208 (1)	-	Fm-3m
			Co_3O_4	8.081 (1)	-	Fd-3m
0.10	0.73	"$Li_{0.80}Mg_{0.10}CoO_2$"		2.8149(2)	14.052 (6)	R-3m
			MgO	4.210 (1)	-	Fm-3m
			Co_3O_4	8.080 (1)	-	Fd-3m

Table B. 3. Hexagonal lattice parameters deduced from X-ray refinement of $Li_{1-2y}Mg_yCoO_2$ with y= 0.02, 0.04 and 0.10

The cell parameters from Le bail refinement are presented in **Table B.3**, the results show that the cell parameters of the prepared materials are rather the same that those of st-$LiCoO_2$. This result invalidates our hypothesis of Mg substitution mechanisms ($2Li^+$ replaced by $1Mg^{2+}$ + 1 vacancy from $LiCoO_2$). Indeed, if it was the case we could find similar cell parameters for

Li/M=0.96 prepared by Umicore and the material with y=0.2. Our observation can easily be explained if we take into account the following equivalence:

"$Li_{1-2y}Mg_yCoO_2$" = (1-2y) $LiCoO_2$ + y MgO + 2y/3 Co_3O_4

Since the preparation of a $[Li_{0.98}\square_{0.01}Mg_{0.01}]_{interslab}\,Co_{1.00}O_2$ sample was not verified in our conditions, we rather believe that using Li/M = 0.96, we form an ε-Mg doped $LiCoO_2$ and MgO rocksalt phase containing some Co ions.

B.2.7.2. Li/M=0.98

For the Li/M = 0.98 phase, we concluded that it consists in an Mg doped $LiCoO_2$ with mainly LS-Co^{3+} ions and traces of MgO impurity. From NMR the presence of a low amount of paramagnetic ions so that the sample can be considered as diamagnetic to a first approximation. Since the ionic size of Mg^{2+} (0.72 Å) is close to that of Li^+, it can be expected that Mg will preferably substitute for Li in $LiCoO_2$, but the corresponding formula would exhibit a significant amount of paramagnetic Co^{4+} ions if we consider the relative Li/M and Li/Co ratios used: $[Li_{0.98}Mg_{0.02}]_{interslab}[Co^{III}_{0.94}Co^{IV}_{0.04}\square_{0.02}]_{slab}\,O_2$. Regarding the large amount of paramagnetic Co^{IV} ions formed, this hypothesis can be discarded. Similarly, if Mg substitutes Co in the slab: $[Li_{0.98}\square_{0.02}]_{interslab}\,[Co^{III}_{0.94}\,Co^{IV}_{0.04}Mg_{0.02}]_{slab}O_2$, a significant amount of Co^{4+} is expected. Finally, considering that the phase is diamagnetic to a first approximation, we can suggest that for a 2% Mg doped material and Li/M = 0.98, we replace ($1Li^+$ + $1Co^{3+}$) by 2 Mg^{2+} in the lattice thus forming: $[Li_{0.99}Mg_{0.01}]_{interslab}[Co^{III}_{0.99}Mg_{0.01}]_{slab}O_2$. The general formula would be then: $[Li_{1-y/2}Mg_{y/2}]_{Interslab}[Co^{3+}_{1-y/2}Mg_{y/2}]_{slab}O_2$ with no vacancies in the slab and interslab and stabilization of LS-Co^{3+}. Several syntheses with a larger amount of Mg were prepared with relative stoichiometry following the scheme: ($1Li^+$ + 1 Co^{3+}) replaced by 2 Mg^{2+}. The syntheses were made following the same experimental setup explained in **section B.2.7.1**. The XRD patterns of the prepared materials based on the following formula $[Li_{1-y/2}\,Mg_{y/2}]_{Interslab}\,[Co^{3+}_{1-y/2}\,Mg_{y/2}]_{slab}\,O_2$ with y= 0.02, 0.04 and 0.10 are plotted in **Figure B.11**.

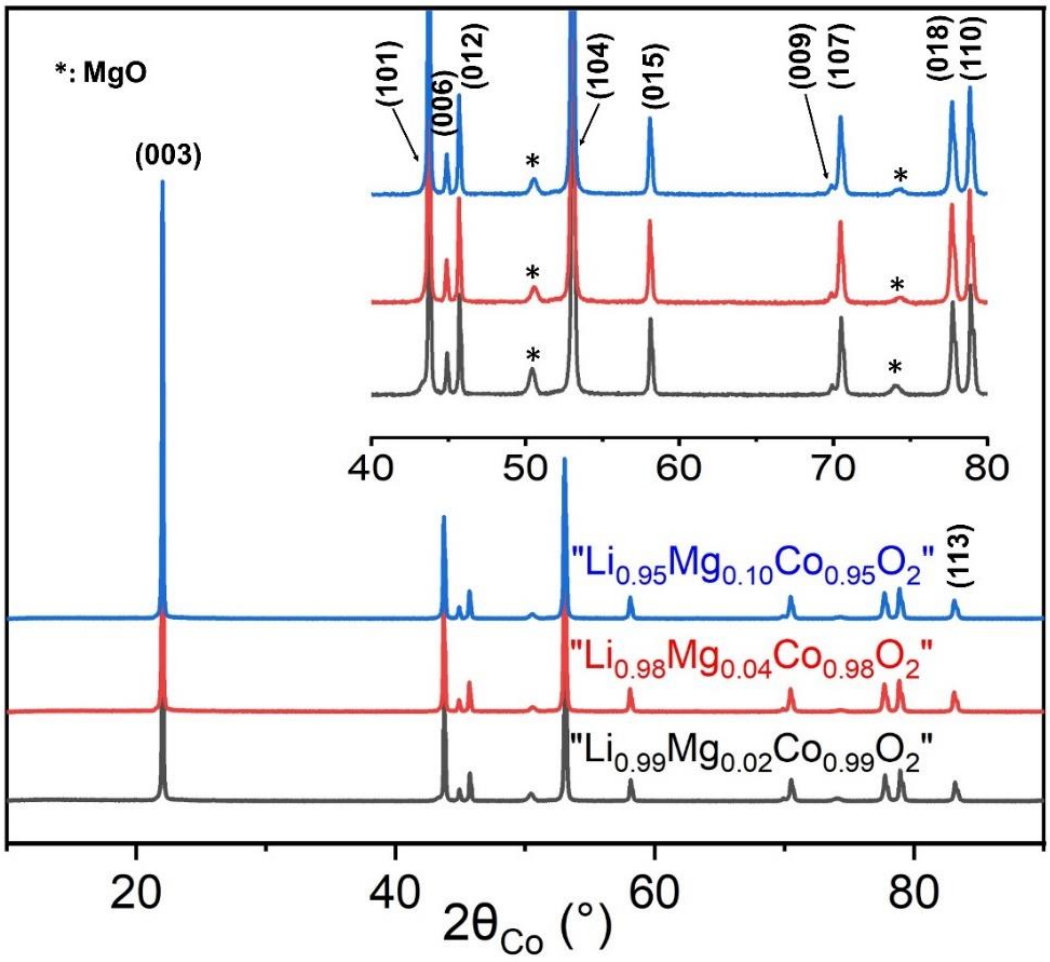

Figure B. 11. X-ray powder diffraction patterns for $Li_{1-y2}Mg_yCo_{1-y/2}MgO_2$ with y= 0.02, 0.04 and 0.10

All the diffraction patterns are characteristic of the high temperature layered $LiCoO_2$. Additional peaks were observed for all the synthesized materials arising from magnesium oxide precursor whose intensity remains almost unchanged when increasing y. The refined cell parameters from Le bail refinement are presented in **Table B.4**, an increase in the c_{hex} parameter is observed with increasing the amount of Mg. The change in the cell parameters show that the doping has been succeed, but the amount of Mg as dopant is lower than the targeted composition. The refined cell parameters for MgO as impurity are really close from those extracted from literature (MgO: a=4.213 Å).[12]

y	Li/M	Target formula	Impurity	a (Å)	c (Å)	Space group
0.00	-	"$Li_{0.98}CoO_2$"	Co_3O_4	2.8158 (1)	14.053 (1)	R-3m
				8.0702 (8)	-	Fd-3m
0.02	0.98	"$Li_{0.99}Mg_{0.02}Co_{0.99}O_2$"	MgO	2.8155 (1)	14.051 (1)	R-3m
				4.200 (1)	-	Fm-3m
0.04	0.96	"$Li_{0.98}Mg_{0.04}Co_{0.98}O_2$"	MgO	2.8157 (1)	14.057 (1)	R-3m
				2.207 (1)	-	Fm-3m
0.10	0.90	"$Li_{0.95}Mg_{0.10}Co_{0.95}O_2$"	MgO	2.8169 (1)	14.065 (6)	R-3m
				2.191 (1)	-	Fm-3m

Table B. 4. Hexagonal lattice parameters deduced from X-ray refinement of various Mg doped $LiCoO_2$ materials

The results of this hypothesis let us to think that were not far from the real formula of Li/M=0.98. However, the difference with the Li/M = 0.98 that we previously studied may be explained by the MgO precursor used in our lab that may be less reactive than the Mg precursors used at Umicore research center.

B.2.8. Conclusion on chapter B.2

In this part, 2% Mg doped $LiCoO_2$ materials prepared by solid state reaction with different Li/M ratios have been studied. Our study makes it possible to separate the relative effects of doping with Li and different stoichiometries in lithium based on the combination of characterization techniques such as ICP, SXRD, SEM, magnetic measurement and ^{7}Li, ^{59}Co MAS NMR. ^{7}Li MAS NMR has shown to be key when it comes to discussing the proper Li stoichiometries as no difference is observed in the SXRD patterns of the series of 2% Mg doped $LiCoO_2$.

Indeed, the material with Li/M=0.96 clearly evidence to an ε-Mg doped $LiCoO_2$ and MgO rocksalt phase containing some Co ions. The Li/M=0.98 is a Mg doped $LiCoO_2$ with mainly

LS-Co^{3+} ions and traces of MgO with a coexistence of Mg in the Li and in the Co layers: **$[Li_{0.99}Mg_{0.01}]_{Li}$ $[Co^{III}_{0.99}$ $Mg_{0.01}]_{Co}O_2$.** Finally, the Li/M=1.00 sample is a single Mg doped phase whose formula can be written as the following **$[Li_{1.00}]_{Li}[Co^{3+}_{0.96}$ $Co^{4+}_{0.02}$ $Mg_{0.02}]_{Co}O_2$.**

The effect of the initial Li/M ratio on the electrochemical properties will be helpful for better comprehension of these material series. A proper investigation of the phase transition mechanisms depending on the initial Li/M ratio will therefore be carried out in the following (**chapter B.3 and B.4)**.

B.3. Evaluation of the electrochemical performances for the 2%Mg doped materials

Zhu et al.[18] showed that Mg doping in $LiCo_{0.97}Mg_{0.03}O_2$ pronouncedly improved the cycling performance although it slightly decreased the initial discharge. They found that some phase transitions still continue to occur. It has been reported that during charge/discharge process, the Mg^{2+} dopant ions move to the electrode surface and form a solid solution which can act as a coating layer and prevent the dissolution of Co^{4+} ions into the electrolyte.[19,20] Thus, this solid solution acts as the buffer to phase transition and the structure becomes very stable.

Interestingly, on Ni-based positive electrode materials, Delmas et al.[3,21] proposed that the structural stability could be significantly improved when the dopant ions with a similar ionic radius to Li^+ (0.76 Å) were substituted into the Li sites. In fact, when Mg^{2+} ions substitute the Li sites in $LiNi_{0.86}Co_{0.09}Mg_{0.05}O_2$, cycling stability was enhanced by 70% after 200 cycles between 3.4 and 4.3 V at 60 °C. The Mg^{2+} ions in the interslab space should screen the $O^{2-}O^{2-}$ repulsions in the beginning of the charge and act as pillars at the end of the deintercalation process, thus preventing the interslab collapse. This pillaring effect was also observed later from other group in Mg doped $LiCoO_2$ materials.[9,22]

Evidencing the effect of Mg doping for a very low Mg (2%) content in $LiCoO_2$ is more challenging than in the case of larger amounts of Mg. One could guess that the effects reported for Mg doping regarding its electrochemical properties, are strongly dependent on the distribution of Mg within $LiCoO_2$ linked to the Li/M ratio. The following aims to study Mg doped materials with various Li/M ratio as a positive electrode for Li-ion batteries. Therefore, because all performances change should be rooted in the material structure and the lithium insertion–deinsertion processes, an ex situ X-ray diffraction and ^7Li MAS NMR characterizations were conducted on de-intercalated phases in order to study in more detail the structural and electronic changes occurring during cycling.

B.3.1. Cycling experiments with various upper cutoff voltages

The dependence of cyclability on cutoff voltage was examined. The charge discharge curves of Mg doped materials with various Li/M stoichiometries compared to st-$LiCoO_2$ are presented in **Figure B.12**, the four profiles on this figure correspond to the first cycle curves for different cutting voltages values of 4.5V, 4.6V, 4.7V and 4.8 V.

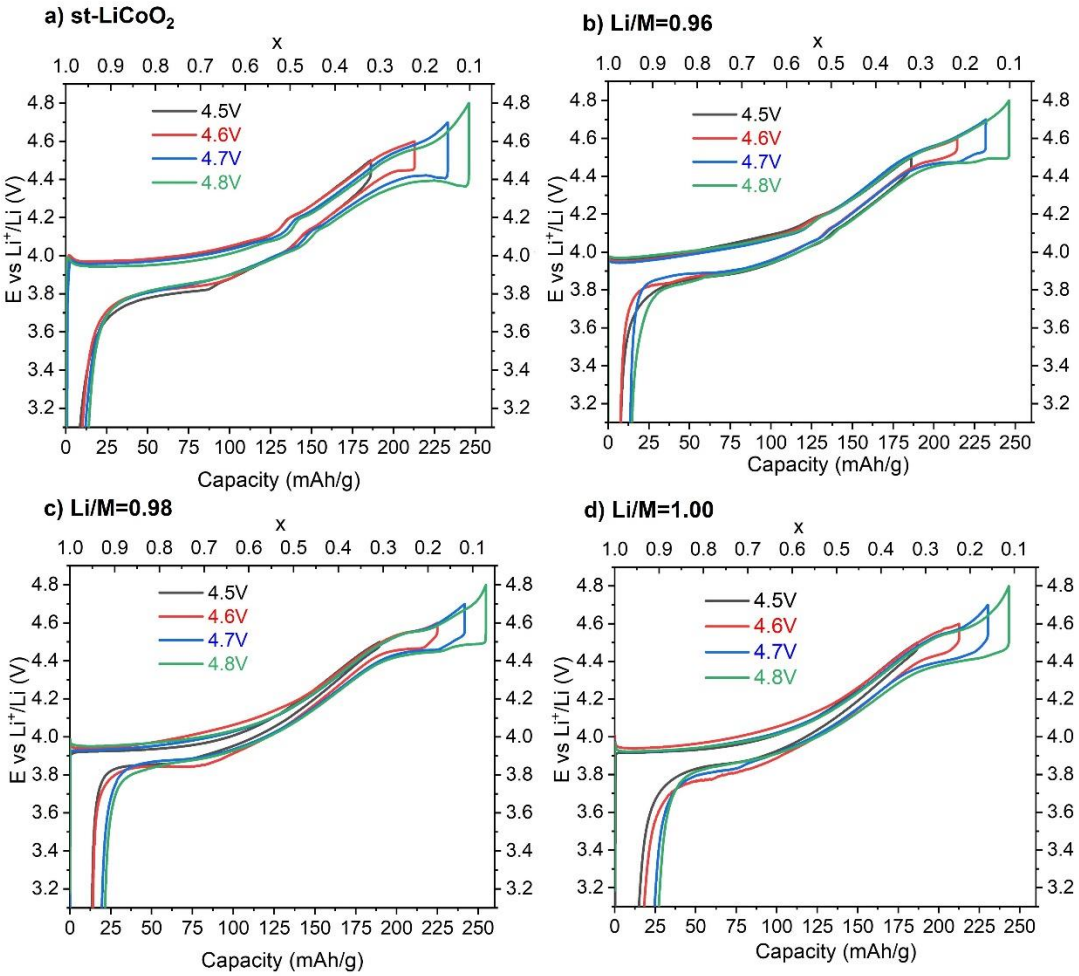

Figure B. 12. First cycle recorded at C/20 and up to various cutoff voltage for a) st-$LiCoO_2$ compared to Mg doped $LiCoO_2$ with b) Li/M=0.96, c) Li/M=0.98 and d) Li/M=1.00.

All curves are plotted as a function of Li content and the specific capacity in mAh/g. The molar masses used for specific capacity were calculated depending on the initial Li/M ratio for each material, whereas the initial value for x was fixed to 1.00 for all materials. When Li is

deintercalated, the charge capacity, as expected, is higher when increasing the cutoff voltage. While the irreversible capacity for st-$LiCoO_2$ is similar regardless the cutoff voltage, it is increasing for cycling from 4.7V for all Mg doped materials. st-$LiCoO_2$ shows a large polarization at high voltage that is reduced for the three Mg-doped samples.

The cycling behavior of the **Li/M = 0.96** phase is very close to that of st-$LiCoO_2$ but with a larger polarization during the first charge that prevent the observation of the voltage plateau at the beginning of the charge. The monoclinic distortion at x = 0.5, can, however still been seen. Overall, even if some feature of st-$LiCoO_2$ are observed, the cycling curve of the Li/M=0.96 sample is quite different indicating that some (ε amount) Mg ions may have been incorporated into $LiCoO_2$ and that the presence of MgO at the surface of the particle influences the polarization of the cell and possible side reactions at high voltage.

The two other **Li/M =0.98 and 1.00** samples present almost similar electrochemical behavior: the structural transformation related to Li/□ vacancy ordering at x=0.5 transition is suppressed. This shows that the presence of the Mg^{2+} impedes the Li/□ ordering.

The material with Li/M=1.00 shows the highest irreversible capacity losses. The origin of irreversible capacity may come from some structural changes. In this context, further study of the different phases transition occurring during Li-deintercalation will be given in the following part for all the doped material with various Li/M ratio.

Extended electrochemical tests were further performed in the 3-4.6V range. **Figure B.13** shows the discharge capacity profiles of st-$LiCoO_2$ and Mg doped samples at 1C and C/10 cycling rate. The 7^{th} discharge capacity of st-$LiCoO_2$ is 227 $mAhg^{-1}$, which is higher than Mg doped samples showing 216 $mAhg^{-1}$, 210 $mAhg^{-1}$ for Li/M ≤ 0.98 and Li/M=1.00 with C/10 cycling rate. However, the discharge capacity is improved by Mg doping with Li/M≤ 0.98.

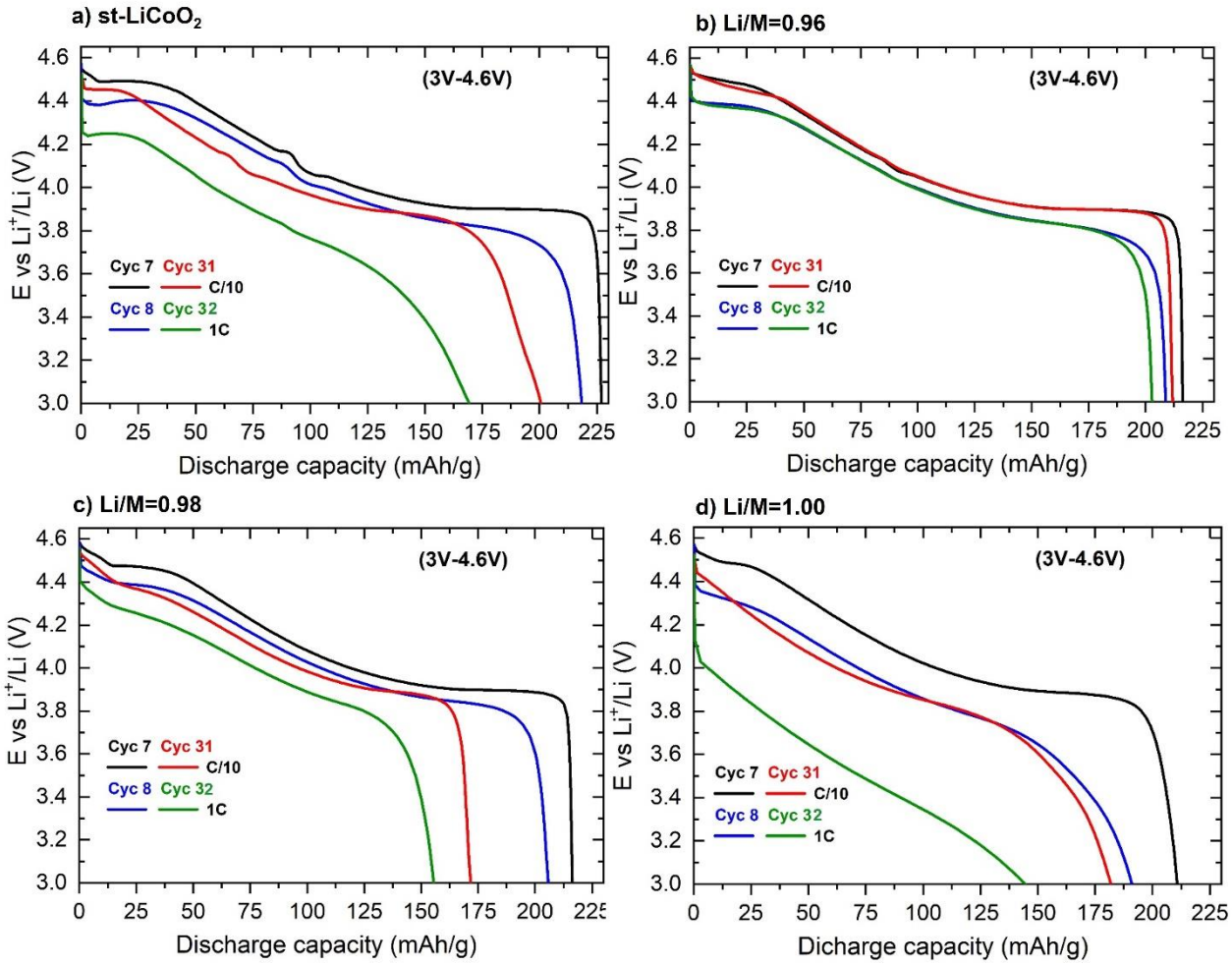

Figure B. 13. Discharge profiles (3V-4.6V) of Li//$LiMO_2$ cells observed for the 7, 8, 31 and 32th cycles of a) st-$LiCoO_2$ compared to Mg doped $LiCoO_2$ with various Li/M ratios using C/10 and 1C rates.

In **Figure B.14**, the discharge capacity is plotted as a function of the number of cycles operated with a cutoff voltage of 4.6V. Excellent cyclability appears for Mg doped sample with Li/M=0.96. Note that the latter has been shown to be ε-Mg doped $LiCoO_2$ with MgO (possibly containing some Co ions) at the surface of the particles that can either prevent the surface of the material from degradation at high voltage or modify the nature of the CEI as discussed in **part A** for Al-doped materials.

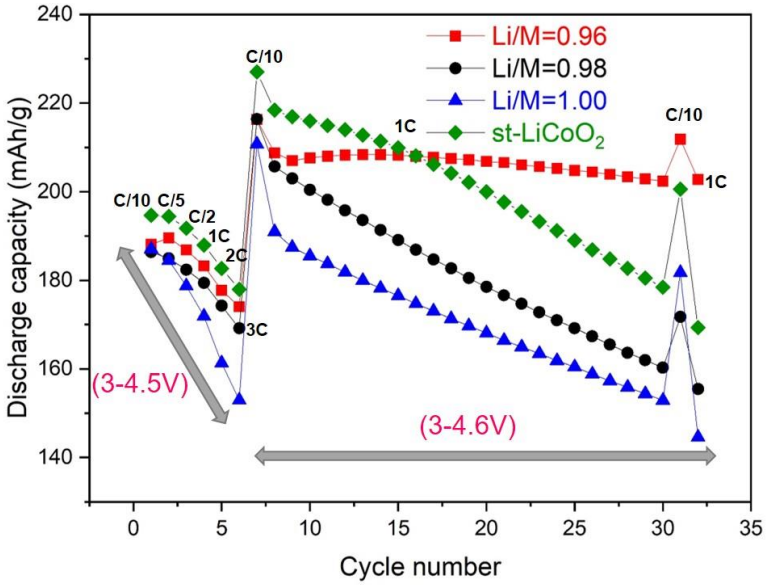

Figure B. 14. Cycling performances of st-$LiCoO_2$ compared to Mg doped $LiCoO_2$ with various Li/M ratios using different C rates.

B.3.2. GITT in the low voltage region

During $LiCoO_2$ delithiation, several phase transitions occur as discussed in the first chapter. We showed above that some of these features disappear when doping with Mg and the behavior of the curves change with the Li/M ratio. The main difference in electrochemical curves concerns the beginning of the deintercalation (insulator-metal transition) at low voltage and the end of the deintercalation at high voltage (structural transitions). Therefore, in parallel with continuous galvanostatic tests, a galvanostatic intermittent titration (GITT) analysis was performed in the low voltage region for Mg doped and st-$LiCoO_2$ (**Figure B.15**). In this technique, a constant current is applied to the cell in order to de-insert Li ions for a determined period of time, followed by an open-circuit voltage (OCV) period, in which the battery relaxes and reaches a steady-state potential. To do so, a coin cell is charged at repetitively at very low rate (C/100) for 1h followed by 4h relaxation periods. Charge and rest from curves until 3.95V are plotted in order to visual well the insulator-metal transition for the various materials.

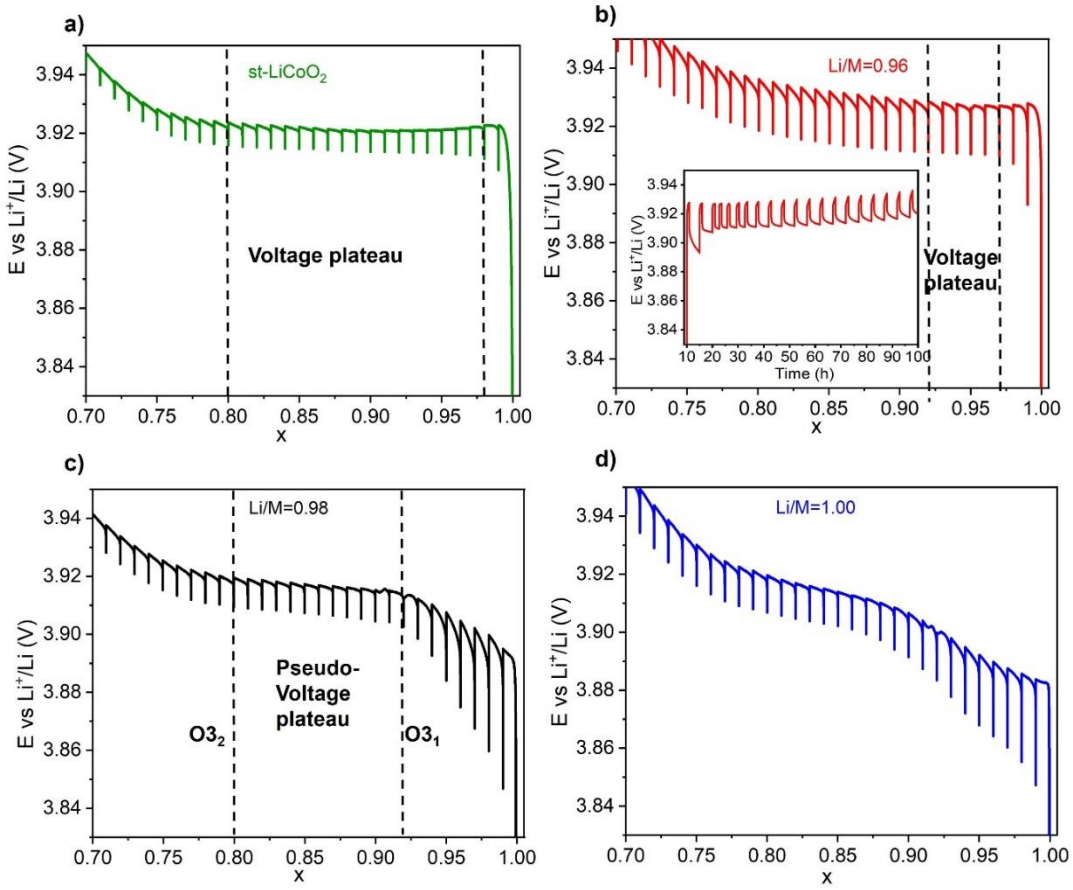

Figure B. 15. First GITT charge of a Li standard a) st-$LiCoO_2$ compared to Mg doped $LiCoO_2$ with b) Li/M=0.96, insert the corresponding curve as a function of time c) Li/M=0.98 and d) Li/M=1.00 cells 300 h (1h charge using C/100 rate and 4h relaxation.

GITT results (**Figure B.15**) show clear difference in the equilibrium potentials between doped and undoped materials. Indeed, the two phase domain starts very early for st-$LiCoO_2$ (at the second deintercalation step) from x=0.98 to x=0.8, whereas, it is shorter for the Li/M=0.96 doped material ($0.92 \leq x \leq 0.97$). The sample with Li/M =0.98 presents a pseudo-voltage plateau in the composition domain $0.85 \leq x \leq 0.97$. Whereas, for Li/M =1.00 doped material, the voltage plateau is not observed anymore as in the case of overlithiated $Li_{1+x0}CoO_2$.[24]

Unfortunately, those GITT experiments could not be realized at high voltage region since the electrolyte degradation becomes huge and prevent satisfactory relaxation of the voltage. Therefore, we analyzed the electrochemical profiles during the first cycle up to 4.8V

(**Figure B.16.a).** A zoom in the high voltage window and the associated $d(Q-Q_0)/dV$ curves are shown in **Figure B.16.b**. The monoclinic transition is visualized in the derivative curve with the emergence of two peaks at E~ 4.08V and E~ 3.18V respectively corresponding $O3_2 \rightarrow O'3$ and $O'3 \rightarrow O3$ transition for st-$LiCoO_2$ and Li/M=0.96 materials.

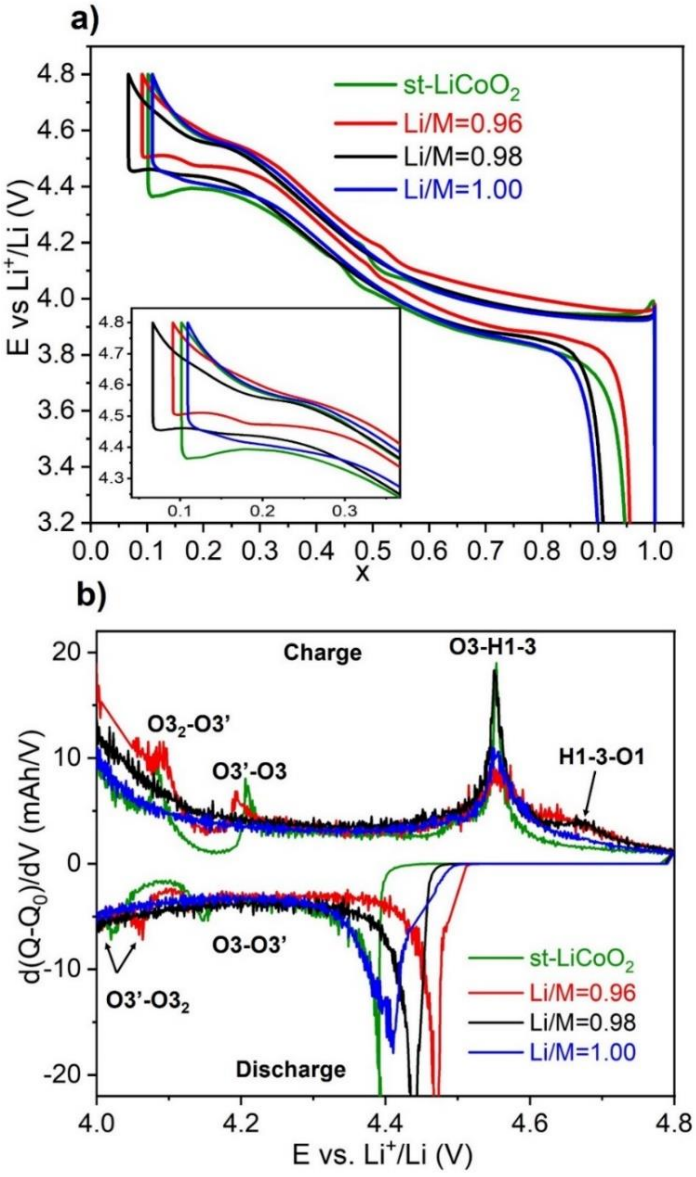

Figure B. 16.(a) First cycle for st-$LiCoO_2$ compared to Mg doped $LiCoO_2$ with various Li/M ratios at C/20 up to 4.8 V. Insert: Zoom on the high voltage electrochemical window of the curves plotted. (b) Corresponding $d(Q-Q_0)/dV$ curves for 4-4.8V window.

Another important consideration to be made regards the phase transition at high voltage for Mg doped materials. The influence of the initial Li/M on these phases transition namely O3‑H1-3 and H1-3‑O1 transitions has never been discussed in our knowledge. The peak observed at ~ 4.55V, in charge, for st-$LiCoO_2$ denotes the O3→H1-3 transition. This transition was also observed for all Mg doped sample, whereas the sample samples with Li/M ≥ 0.98 present less defined peaks compared to the others. The H1-3→ O1 transition seems to appear at 4.64 V, such feature is considerably harder to distinguish in the derivative curves during the charge due to the broadening of the peak. Note that this peak is absent of the derivative curve during the discharge because of the substantial polarization reported at high voltage.

These results clearly confirm that the material with Li/M=0.96 is ε-Mg doped $LiCoO_2$ with MgO, while the samples with Li/M ≥ 0.98 are Mg doped which is consistent with the study on **chapter B.2**.

B.4. Study of the mechanisms occurring during Li deintercalation for the 2% Mg doped $LiCoO_2$ samples with Li/M ≥ 0.98 up to 4.8 V vs Li^+/Li

In order to better understand the role of Mg-doping on the mechanisms involved during cycling, several phases from the material with Li/M=0.98 and 1.00 were prepared by electrochemical deintercalation (**Figure B.17**) and studied by ^{7}Li MAS NMR and by XRD. These two materials were chosen as we showed the successful substitution of Mg for both Li/M=0.98 and 1.00. For this study, swagelok cells featuring thick film electrodes prepared following the same experimental protocol in **part A**, the typical active material loading was ~ 30-40 mg as a positive electrode, Li as negative electrode and $LiPF_6$ in EC: DMC as electrolyte. Cells were galvanostatically charged up to a given potential (4.5V, 4.6V, 4.7V and 4.8V) at C/20, followed by a floating step until the current reached ~ 0 mA as illustrated in **Figure B.17**. The materials were recovered in an argon-filled dry box, washed in dimethyl carbonate (DMC) to remove residual electrolyte salt and dried under vacuum.

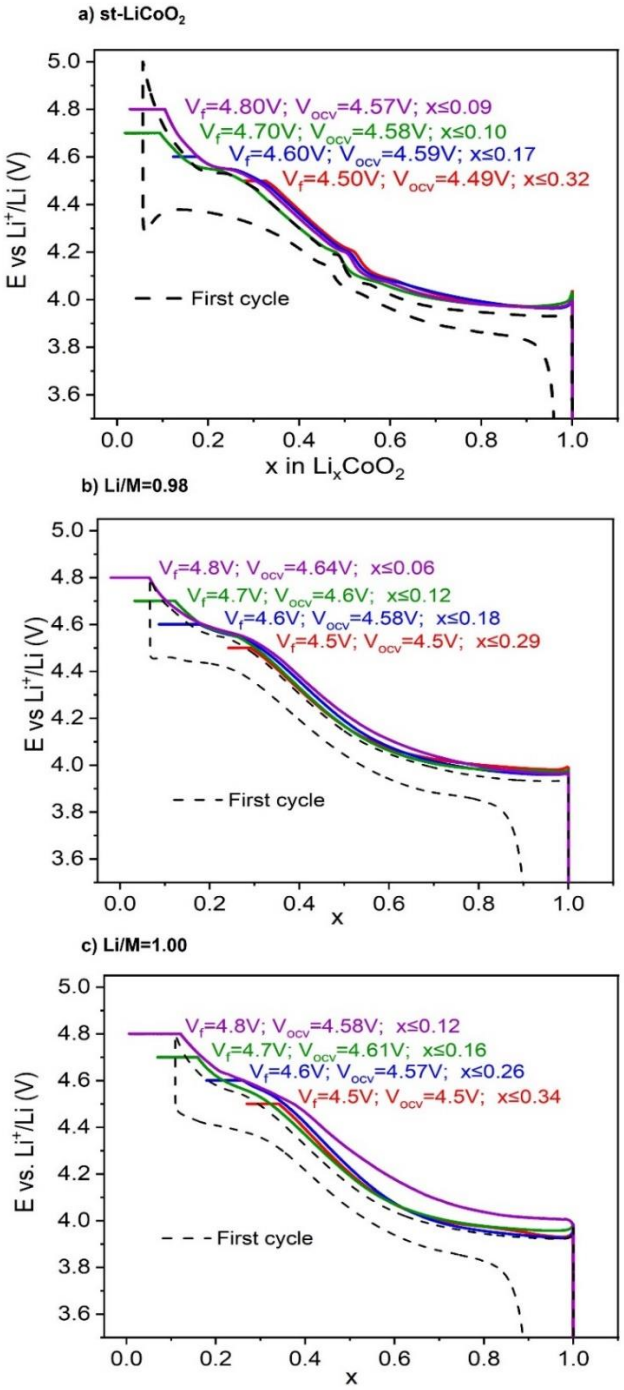

Figure B. 17. Galvanostatic charge of a) st-$LiCoO_2$, b) Li/ Li/M=0.98 and c) Li/ Li/M=1.00 cells stopped at different voltage from 4.5 to 4.8 V compared to the first charge-discharge curve (V_{ocv} corresponds to the voltage measured at the end of relaxation before disassembling the cell and $V_f=V_{floating}$).

The Li content of the materials prepared with different cutoff voltages (4.5V, 4.6V, 4.7V and 4.8V) is difficult to estimate due to the parasitic reaction of the electrolyte degradation (**Table B.5**). One can observe that for the floating voltages V_f > 4.6 V, the potential drops significantly, when the cell was disconnected so that the highest V_{ocv} reached is only 4.6V.

	4.5V	**4.6V**	**4.7V**	**4.8V**
Li content for st-$LiCoO_2$	0.32	≤ 0.17	≤ 0.10	≤ 0.09
Li content for Li/M=0.98	0.29	≤ 0.18	≤ 0.12	≤ 0.06
Li content for Li/M=1.00	0.34	≤ 0.26	≤ 0.16	≤ 0.12

Table B. 5. The Li contents of the materials prepared with different cutoff voltages

The sample powders were transferred to rotors and capillaries for NMR and XRD characterization respectively. Note that for a given composition two characterizations were performed on the same sample.

B.4.1. Study of the average structure by XRD

To follow the structural evolution upon charge, XRD patterns of 2% Mg doped phases (Li/M=0.98 and 1.00) were collected with copper radiation using 0.3mm glass capillaries (**Figure B.18**). Special attention was given to the (00l) diffraction peak evolution, that allows to directly follow the changes in the interslab distance which is characteristic of the metal and lithium layer stacking modifications (see **Figure B.18.b and c)**.

- All diffraction peaks for the materials prepared at V_f =4.5 V can be indexed based on the O3 structure with rather similar Li content (x=0.27 for st-$LiCoO_2$, x~ 0.24 for Li/M=0.98 and x~ 0.26 for Li/M=1.00 if one neglects the electrolyte degradation at this voltage). This peak is shifted to low angle values for both samples meaning that the $c_{hex.}$ parameter increased compared to the pristine materials.

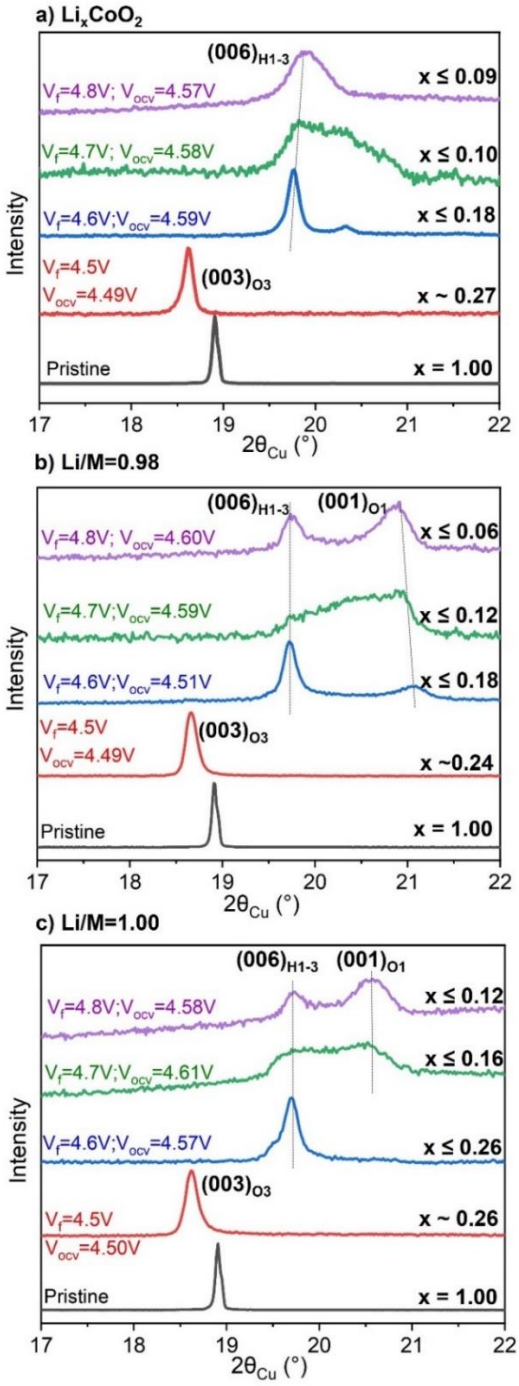

Figure B. 18. Detail in the (00l) line from XRD for a) st-$LiCoO_2$, b) Li/M=0.98 and c) Li/M=1.00) (V_{ocv} corresponds to the voltage measured at the end of relaxation before disassembling the cell and V_f=$V_{floating}$).

- For the materials prepared at V_f =4.6V, two peaks are observed for Li_xCoO_2 at 2θ=19.76° and 2θ=20.34°, which correspond respectively to the $(006)_{H1-3}$ and $(00\ell)_{int}$ diffraction lines of the H1-3 and intermediate phase between H1-3 and O1 type structures as detected also by operando XRD.[24] For the doped samples with Li/M≥0.98, the $(003)_{O3}$ peak disappear and new peaks appears at higher angle values, with an interslab distance d= 4.55 Å at 2θ~19.71° corresponding to the $(006)_{H1-3}$ diffraction line of the H1-3-type structure (**Figure B.18.b**). Indeed, the associated average interlayer distance d(006) for non-doped $LiCoO_2$ is 4.51 Å, meaning that the corresponding c_{hex} parameter is approximately 27.06 Å.[25] The H1-3 phase is also formed during Li^+ de-intercalation and exhibits a higher interlayer distance d(006) = 4.55 Å for the two Mg-doped samples instead of 4.51 Å for Li_xCoO_2. The Mg doped sample with Li/M=0.98 exhibit a second phase with d=4.22 Å which can be assigned to the (001) diffraction line of the O1 structure.
- For the materials prepared at $V_{floating}$=4.7V, a gradual broadening and asymmetry encompassing of the $(006)_{H1-3}$ and $(001)_{O1}$ diffraction were observed for the samples. In any case, from their peak broadening, those structures may contain a high number of stacking faults resulting in overall structural disorder.
- For the materials prepared at $V_{floating}$=4.8V, Li_xCoO_2 prepared also exhibits broad diffraction line assigned to a defected H1-3 phase and Mg doped phases exhibit broad diffraction lines assigned to H1-3 and O1 phases.

B.4.2. Study of the local structure by ^{7}Li MAS NMR

^{7}Li MAS NMR spectroscopy measurements were performed for Li/M=0.98 and 1.00 phases and are shown in **Figure B.19**. As already discussed in **chapter B.1** in the NMR section **B.2.5**, the pristine Li/M=0.98 sample has a main signal centered on 0 ppm and a weak peak at 60 ppm. Whereas, the pristine Li/M= 1.00 sample shows paramagnetic additional signals.

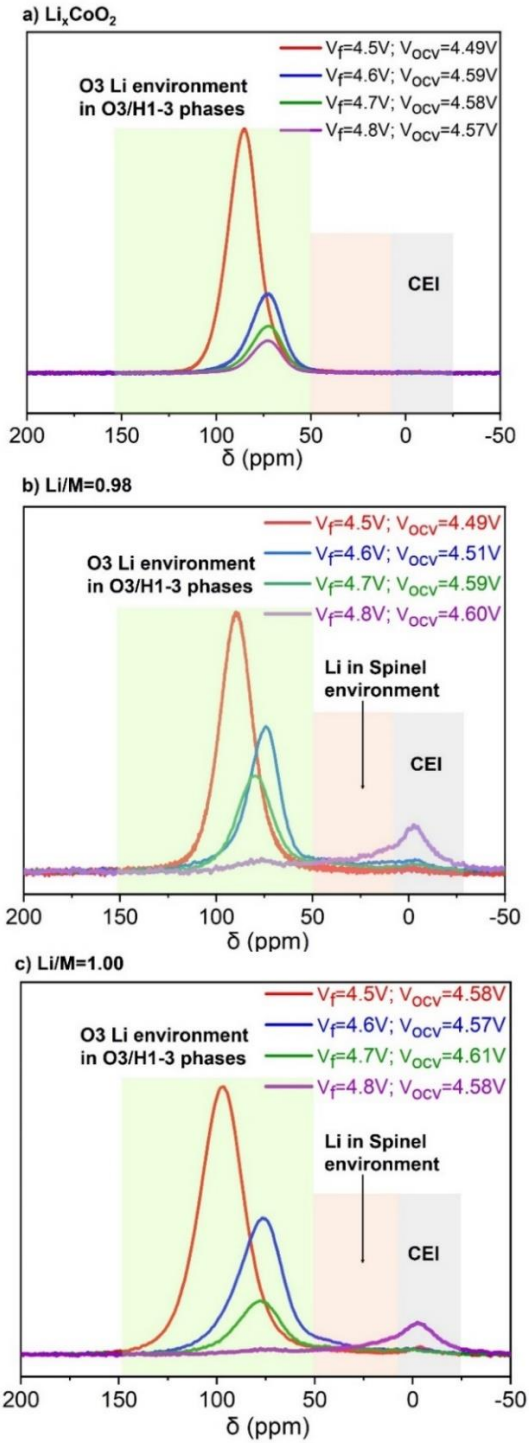

Figure B. 19. Ex-situ ^{7}Li MAS NMR spectra for 2% Mg doped $LiCoO_2$ materials (Hahn echo, B_0 = 7.05T, V_{ocv} corresponds to the voltage measured at the end of relaxation before disassembling the cell and V_f=$V_{floating}$).

The study of Li_xCoO_2 at high and low voltage from ^{7}Li MAS NMR has been done in **part A**. The two main conculsions for x ≤0.5 were (**Figure B.19.a**):

- The intensity of the Knight-Shifted signal in the 50-130 ppm range decrease and shifted to small ppm value upon deintercalation. This signal is assigned to Li in the O3-type environment, expected to be similar in the H1-3 stacking locally if we assume that a negligible amount of Li is present in the O1 interslab space.
- The CEI formed at high voltage could be either very thin or unstable and may be dissolved by the electrolyte solvent after the cell disconnection or by the electrode washing step using DMC prior to our measurements. Additionally, no signal associated to a lithiated spinel phase was detected in this case.

From ^{7}Li MAS NMR (**Figure B.19**) spectra, Li/M=0.98 and 1.00 deintercalated phases showed similar behavior as 4% Al doped $LiCoO_2$ at high voltage (**Figure A.28**).

- For the doped materials prepared at V_f=4.5V, a single Knight shifted signal located around ~80 ppm and 100 ppm is observed for Li/M=0.98 and Li/M=1.00 respectively.
- For the three samples prepared at larger floating voltages $V_f \geq 4.6V$, the intensity of the signal located in the [~50-130] ppm of Li in the O3 and H1-3 phases strongly decreases and shifts to lower ppm values. The line shape of the ^{7}Li signal of Li_xCoO_2 samples remains almost unchanged (**Figure B.19.a**). Whereas, new contributions appear in the [-20;50] ppm range with significant intensity for Li/M ≥0.98 samples. Signals located in 10-50 ppm could be attributed to Li in spinel-type environment according to Godillot et al. [26] As we also observed for the Al-doped sample and confirmed by TEM experiments in **part A.4.4.2.c**. Additionally, signals located around 0 ppm can be assigned to diamagnetic lithium environments from the CEI (Cathode Electrolyte Interface).
- For the doped materials at $V_{floating}$ = 4.8V, the intensity of the signal at 0 ppm increases.

Interestingly, increasing the Li/M ratio leads to broader signals with Li in O3 environnements (**Figure B.19.c**).

B.4.3. Structural characterization after cycling at high voltage for Li/M=0.98

As the doped Li/M=0.98 material showed better electrochemical performances than the doped Li/M=1.00, we decided to further understand the cycling performance of Li/M=0.98 at high voltage. This material was galvanostatically charged to 4.6V followed by a floating step for 48h then discharged to 3V with a C/20 rate and recovered after a floating at 3V (**Figure B.20**). Another material was prepared using the same condition but without floating at 4.6V (1 cycle charged-discharged between 3V and 4.6V with a C/20 rate then recovered after a floating at 3V) in order to investigate the effect of the floating at high voltage.

From the electrochemical curve (**Figure B.20**), the x=0.81 value was predicted to be achieved after the floating back to 3V, so a sample with x=0.81 was prepared using a galvanostatic charge followed by a relaxation step. But, the cell undergoes some electrolyte decomposition at high voltage that shifted slightly the cycling curves on the left. Therefore, another x=0.90 sample was also prepared for comparison. The sample was then studied by XRD and ^{7}Li MAS NMR and compared with all the prepared phases.

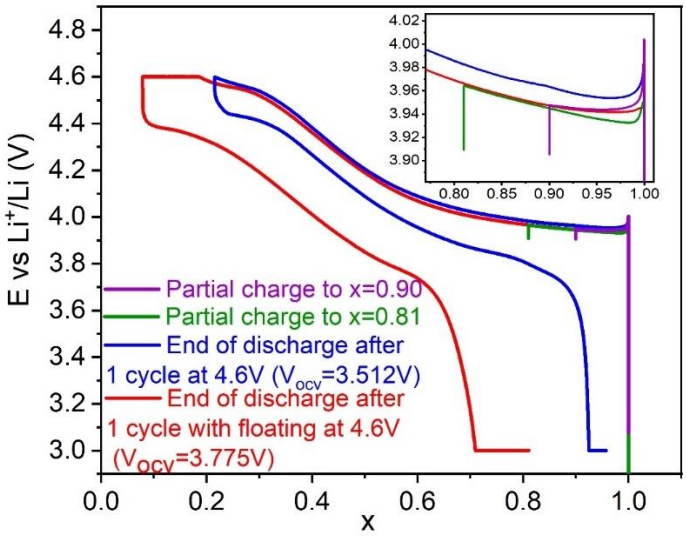

Figure B. 20.One cycle of galvanostatic charge / discharge (3V-4.6V) of an Li // Li/M=0.98 and stopped in potential at 3V cell with a rate of C/20.

The XRD patterns of the cycled materials recovered at the end of discharge, in comparison with the pristine one and the deintercalated phases at x=0.81 and x=0.9 are shown in **Figure B.21**. We can notice that the diffraction lines appear to be slightly broader on the XRD patterns of the material recovered after floating at high voltage. The (003) peak of the pristine Li/M=0.98 phase, located at 2θ=18.91° is slightly shifted to lower angle values for x=0.90 showing an increase of c_{hex} parameter (**Table B.6**). Another new peak appears at lower angle (2θ = 18.63°, see **Figure B.21.b**) for x=0.81. One can attribute the transition to the insulator-metal transition ($O3_1$-$O3_2$).

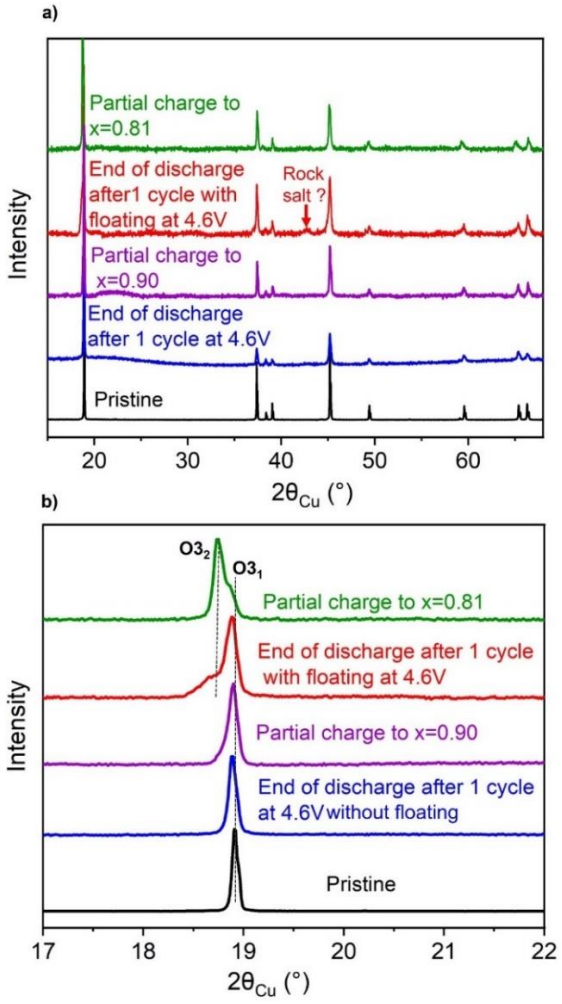

Figure B. 21. X-ray diffractogramms of the electrochemically deintercalated Li/M=0.98 materials with b) the detail in the (003) line.

For the two phases charged at 4.6V we observed that:

- The material recovered at end of discharge without floating at 4.6V presents a single O3 phase.
- The material recovered at end of discharge with floating shows a biphasic domain attributed to $O3_1$-$O3_2$ transition. Also, additional peak located at $2\theta = 42.70°$ was observed for this sample which may be attributed to the presence of a rocksalt phase (MgO or MgO phase containing some Co).

For all cycled materials, the main structural parameters are reported in **Table B.6**, in comparison with those of the pristine phase.

Sample	Space-group	Phase	**a (Å)**	**c (Å)**
pristine	R-3m	O3	2.8173 (1)	14.0606 (1)
Partial charge to x=0.90	R-3m	$O3_1$	2.8147 (1)	14.0978 (2)
Partial charge to x=0.81	R-3m	$O3_1$	2.7746 (1)	14.0830 (1)
		$O3_2$	2.8109 (1)	14.1615 (1)
End of discharge after 1 cycle at 4.6V	R-3m	$O3_1$	2.8174 (1)	14.0790 (2)
End of discharge after 1 cycle at with floating at 4.6V	R-3m	$O3_1$	2.8174 (1)	14.1121 (1)
		$O3_2$	2.7333 (1)	14.3117 (1)

Table B. 6. Refined unit cell parameters from the XRD data

^{7}Li NMR MAS spectra for the materials cycled up to 4.6V recovered at 3V are compared to the ones of the pristine material and to the x=0.81 and x=0.9 ones is shown in **Figure B.22**.

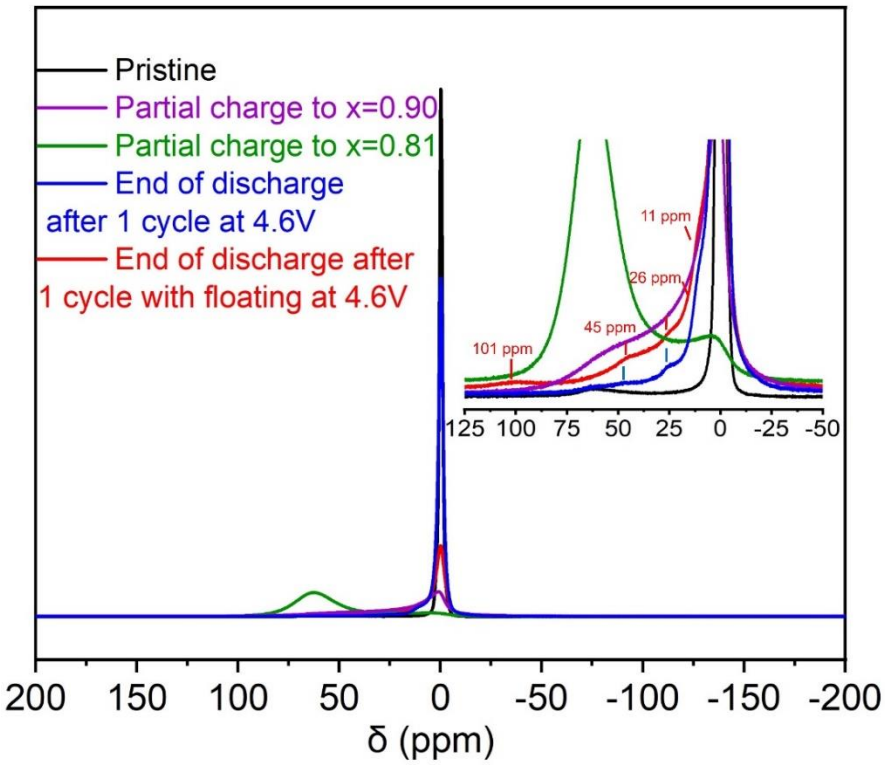

Figure B. 22. ^{7}Li MAS NMR of the electrochemically deintercalated Li/M=0.98 materials.

All the samples exhibit the same signal at ~0 ppm, however, the magnitude of this signal changes for the cycled material.

- The electrochemically deintercalated material with x=0.90 shows a broadening of the main signal at 0 ppm with the appearance of small signal around ~60 ppm.
- The electrochemically deintercalated material with x=0.81 presents a broad and intense signal located at 60 ppm. This signal is attributed to the Knight shift signal as an electronic delocalization is expected.
- The materials recovered at the end of discharge without floating present new additional signals located at 11 ppm, 26 ppm and 45 ppm. The signal at 11 ppm may come from Co^{4+} localized or locally delocalized around Mg. According to Godillot et al.[26] the 26 ppm signals may be assigned to Li in the 8a tetrahedral sites of the spinel structure, that may differ from their Co/Mg local environments here and the 45 ppm signal is assigned to Li in the 16c octahedral sites.

- The material prepared using a floating at 4.6V exhibits slightly similar spectra than the material prepared at x=0.9 with less intense signal. In addition, a new signal appears at 101 ppm, which may come from the Li in O3 and O1 oxygen stacking which was not fully reintercalated to the structure.

B.5. Conclusion for chapter B.3 and B.4

Series of 2% Mg doped $LiCoO_2$ with well controlled Li/M ratio were studied from electrochemical tests. It has been confirmed that even with same quantity of doping, the Li/M ratio influences the electrochemical properties. The material with Li/M=1.00 shows the highest polarization and irreversible capacity losses; this effect was already observed for the non-doped material with larger initial Li/Co in previous study.[27] We showed also that the initial Li/M ratio impacts the structural changes associated to Li de-intercalation (voltage plateau, O3-H1-3 transition). Whereas, no Beneficial role of Mg-doping on capacity retention has been observed except for the material prepared with Li/M=0.96 which contain MgO on the surface.

A proper investigation of the phase transition mechanisms at high voltage depending on the initial Li/M has been be carried out. Based on ^{7}Li MAS NMR for electrochemically deintercalated Li/M $\geq$ 0.98 materials, it was clearly observed the appearance of a new broad signals for the doped material at high voltage. Signals assigned to Li in spinel-like environments and in the diamagnetic CEI layer are observed in addition to the one of Li in the interslab space of the O3 or H1-3 structure. The comparison of the Li/M=0.98 and Li/M=1.00 materials clearly evidence the role of Li/M ratio upon cycling.

The fact of holding the voltage at high voltage showed a pronounced behavior for Li/M=0.98. After cycling, the spinel-like environments are maintained as we demonstrated in part A. All these features can play a favorable role in the electrochemical behavior at high voltage. Further work will be required to confirm it. Also, the study of the electrochemically deintercalated Li/M = 0.96 material which could not be done in the context of this thesis, would be interesting to understand the role of MgO at the surface of the particles on the formation of the SEI.

References

(1) Tukamoto, H.; West, A. R. Electronic Conductivity of $LiCoO_2$ and Its Enhancement by Magnesium Doping. *J. Electrochem. Soc.* **1997**, *144* (9), 3164–3168.

(2) Levasseur, S.; Ménétrier, M.; Delmas, C. On the $Li_xCo_{1-y}Mg_yO_2$ System upon Deintercalation: Electrochemical, Electronic Properties and ^{7}Li MAS NMR Studies. *J. Power Sources* **2002**, *112* (2), 419–427. https://doi.org/10.1016/S0378-7753(02)00456-1.

(3) Pouillerie, C.; Croguennec, L.; Biensan, P.; Willmann, P.; Delmas, C. Synthesis and Characterization of New $LiNi_{1-Y}Mg_YO_2$ Positive Electrode Materials for Lithium-Ion Batteries. *J. Electrochem. Soc.* **2000**, *147* (6), 2061.

(4) Kim, H.-J.; Jeong, Y. U.; Lee, J.-H.; Kim, J.-J. Crystal Structures, Electrical Conductivities and Electrochemical Properties of $LiCo_{1-x}Mg_xO_2$ ($0 \leq x \leq 0.11$). *J. Power Sources* **2006**, *159* (1), 233–236. https://doi.org/10.1016/j.jpowsour.2006.04.030.

(5) Mladenov, M.; Stoyanova, R.; Zhecheva, E.; Vassilev, S. Effect of Mg Doping and MgO-Surface Modification on the Cycling Stability of $LiCoO_2$ Electrodes. *Electrochem. Commun.* **2001**, *3* (8), 410–416. https://doi.org/10.1016/S1388-2481(01)00192-8.

(6) Yin, R.-Z.; Kim, Y.-S.; Shin, S.-J.; Jung, I.; Kim, J.-S.; Jeong, S.-K. In Situ XRD Investigation and Thermal Properties of Mg Doped $LiCoO_2$ for Lithium Ion Batteries. *J. Electrochem. Soc.* **2012**, *159* (3), A253–A258.

(7) Levasseur, S.; Ménétrier, M.; Delmas, C. On the Dual Effect of Mg Doping in $LiCoO_2$ and $Li_{1+\delta}CoO_2$: Structural, Electronic Properties, and ^{7}Li MAS NMR Studies. *Chem. Mater.* **2002**, *14* (8), 3584–3590. https://doi.org/10.1021/cm021107j.

(8) Luo, W.; Li, X.; Dahn, J. R. Synthesis and Characterization of Mg Substituted $LiCoO_2$. *J. Electrochem. Soc.* **2010**, *157* (7), A782. https://doi.org/10.1149/1.3424909.

(9) Kong, W.; Zhou, D.; Ning, D.; Yang, W.; Wong, D.; Zhang, J.; Li, Q.; Yang, J.; Schulz, C.; Liu, X. Unraveling the Distinct Roles of Mg Occupation on Li or Co Sites on High-Voltage $LiCoO_2$. *J. Electrochem. Soc.* **2021**, *168* (3), 30528. https://doi.org/10.1149/1945-7111/abebf7.

(10) Mg-Pillared $LiCoO_2$: Towards Stable Cycling at 4.6 V. https://doi.org/10.1002/anie.202014226.

(11) Duffiet, M.; Blangero, M.; Cabelguen, P. E.; Song, K. S.; Fauth, F.; Delmas, C.; Carlier, D. Probing Al Distribution in $LiCo_{0.96}Al_{0.04}O_2$ Materials Using ^{7}Li, ^{27}Al, and ^{59}Co MAS NMR Combined with Synchrotron X-Ray Diffraction. *Inorg. Chem.* **2020**, *59* (5), 2890–2899. https://doi.org/10.1021/acs.inorgchem.9b03260.

(12) Tsirelson, V. G.; Avilov, A. S.; Abramov, Y. A.; Belokoneva, E. L.; Kitaneh, R.; Feil, D. X-Ray and Electron Diffraction Study of MgO. *Acta Crystallogr. Sect. B* **1998**, *54* (1), 8–17. https://doi.org/10.1107/S0108768197008963.

(13) Kuboon, S.; Hu, Y. H. Study of NiO−CoO and Co_3O_4 −Ni_3O_4 Solid Solutions in Multiphase Ni−Co−O Systems. *Ind. Eng. Chem. Res.* **2011**, *50* (4), 2015–2020. https://doi.org/10.1021/ie101249r.

(14) Levasseur, S.; Ménétrier, M.; Shao-Horn, Y.; Gautier, L.; Audemer, A.; Demazeau, G.; Largeteau, A.; Delmas, C. Oxygen Vacancies and Intermediate Spin Trivalent Cobalt Ions in Lithium-Overstoichiometric $LiCoO_2$. *Chem. Mater.* **2003**, *15* (1), 348–354. https://doi.org/10.1021/cm021279g.

(15) Levasseur, S. Contribution À L'étude Des Phases Li_x(Co, M) O_2 En Tant Que Matériaux D'électrode Positive Des Batteries Li-Ion. Effets Combinés de La Surstoechiométrie En Lithium et de La Substitution (M= Ni, Mg). PhD Thesis, Université Sciences et Technologies-Bordeaux I, 2001.

(16) Kikkawa, S.; Miyazaki, S.; Koizumi, M. Deintercalated $NaCoO_2$ and $LiCoO_2$. *J. Solid State Chem.* **1986**, *62* (1), 35–39. https://doi.org/10.1016/0022-4596(86)90213-6.

(17) Artemenko, A.; Ménétrier, M.; Pollet, M.; Delmas, C. Reinvestigation of the Magnetic Behavior of O3–$LiCoO_2$. *J. Appl. Phys.* **2009**, *106* (6), 64914. https://doi.org/10.1063/1.3226700.

(18) Zhu, X.; Shang, K.; Jiang, X.; Ai, X.; Yang, H.; Cao, Y. Enhanced Electrochemical Performance of Mg-Doped $LiCoO_2$ Synthesized by a Polymer-Pyrolysis Method. *Ceram. Int.* **2014**, *40* (7, Part B), 11245–11249. https://doi.org/10.1016/j.ceramint.2014.03.170.

(19) Zaheena, C. N.; Nithya, C.; Thirunakaran, R.; Sivashanmugam, A.; Gopukumar, S. Microwave Assisted Synthesis and Electrochemical Behaviour of $LiMg_{0.1}Co_{0.9}O_2$ for

Lithium Rechargeable Batteries. *Electrochimica Acta* **2009**, *54* (10), 2877–2882. https://doi.org/10.1016/j.electacta.2008.11.009.

(20) Kim, H.-S.; Ko, T.-K.; Na, B.-K.; Cho, W. I.; Chao, B. W. Electrochemical Properties of $LiM_xCo_{1-x}O_2$ [M = Mg, Zr] Prepared by Sol–gel Process. *J. Power Sources* **2004**, *138* (1), 232–239. https://doi.org/10.1016/j.jpowsour.2004.06.024.

(21) Pouillerie, C.; Croguennec, L.; Delmas, C. The $Li_xNi_{1-y}Mg_yO_2$ (y=0.05, 0.10) System: Structural Modifications Observed upon Cycling. *Solid State Ion.* **2000**, *132* (1), 15–29. https://doi.org/10.1016/S0167-2738(00)00699-8.

(22) Huang, Y.; Zhu, Y.; Fu, H.; Ou, M.; Hu, C.; Yu, S.; Hu, Z.; Chen, C.-T.; Jiang, G.; Gu, H.; Lin, H.; Luo, W.; Huang, Y. Mg-Pillared $LiCoO_2$: Towards Stable Cycling at 4.6 V. *Angew. Chem. Int. Ed. n/a* (n/a). https://doi.org/https://doi.org/10.1002/anie.202014226.

(23) Levasseur, S. Evidence for Structural Defects in Non-Stoichiometric HT-$LiCoO_2$: Electrochemical, Electronic Properties and ^{7}Li NMR Studies. *Solid State Ion.* **2000**, *128* (1–4), 11–24. https://doi.org/10.1016/S0167-2738(99)00335-5.

(24) Duffiet, M.; Blangero, M.; Cabelguen, P.-E.; Delmas, C.; Carlier, D. Influence of the Initial Li/Co Ratio in $LiCoO_2$ on the High-Voltage Phase-Transitions Mechanisms. *J. Phys. Chem. Lett.* **2018**, *9* (18), 5334–5338. https://doi.org/10.1021/acs.jpclett.8b02252.

(25) Ceder, G.; Van der Ven, A.; Aydinol, M. K. Lithium-Intercalation Oxides for Rechargeable Batteries. *JOM* **1998**, *50* (9), 35–40. https://doi.org/10.1007/s11837-998-0412-5.

(26) Godillot, G.; Huo, H.; Ménétrier, M.; Bourgeois, L.; Guerlou-Demourgues, L.; Delmas, C. Promising Nanometric Spinel Cobalt Oxides for Electrochemical Energy Storage: Investigation of Li and H Environments by NMR. *J. Phys. Chem. C* **2012**, *116* (50), 26598–26607. https://doi.org/10.1021/jp307458z.

(27) Duffiet, M. Investigation of Structural Failure Mechanisms of $LiCoO_2$ at High Voltage and Material Optimization through Aluminum Doping. PhD Thesis, Université de Bordeaux, 2019.

General conclusion

In this PhD work, several Al and Mg doped $LiCoO_2$ materials were studied in the purpose of understanding the role of the doping on the electrochemical properties and on the mechanisms involved upon cycling at high voltages.

In this first chapter of Part A, series of 2% Al doped $LiCoO_2$ materials has been synthesized with different Li/M (M= Co+Al) ratio (0.98, 1.00 and 1.02) from solid state reaction. The characterization of the Al distribution within those phases has been performed through the combined use of synchrotron XRD with ^{27}Al and ^{59}Co MAS NMR. Moreover, ^{7}Li MAS NMR has shown to be a key technique when it comes to discuss the Li stoichiometry. Indeed, the presence of Li excess within the structure to form overlithiated phases can only be certified through their NMR spectra, as not detected by XRD. Electrochemical tests clearly evidence that the initial Li/M ratio influences the electrochemical properties even for a same amount of aluminum. Finally, rather good capacity retentions were obtained for samples with Li/M $\leq$1.00 up to 4.6V.

The second part was dedicated to the detailed study of an homogenously doped $LiCo_{0.96}Al_{0.04}O_2$ material with Li/M = 1.00. Our electrochemical cycling study in Li cells reveals that even a low substituted amount of Co with Al (4%) has a profound effect on the electrochemical performance and yields a better cycling stability in the 3-4.6 V voltage range. Based on the study of the deintercalated $Li_xCo_{0.96}Al_{0.04}O_2$ in comparison with Li_xCoO_2, we believe that Al-doping improves the cycling performance of $LiCoO_2$ up to 4.6V, mainly by modifying the particles surface evolution upon cycling at high voltages. Even during the first charge, it leads to the formation of a surface reconstruction with the formation of a lithiated spinel-type phase that should have a good ionic conductivity. In the case of $LiCoO_2$, the formation of a spinel phase is either not lithiated as not detected by ^{7}Li MAS NMR or formed only upon extended cycling. The lithiated spinel phase formed on the Al-doped compound, may then react differently with the electrolyte to form a stable CEI layer, whose composition is different from the one formed on Li_xCoO_2. The formation of the

Li-containing spinel phase and a stable CEI at the surface of the particles probably also explains the strong reduction of Co dissolution observed at high voltage.

In part B, the 2% Mg doped $LiCoO_2$ materials prepared by solid state reaction with different Li/M (M = Co+Mg) ratios (M=0.96, 0.98 and 1.00) have been studied. Our study allowed to discuss the position of Mg^{2+} ions depending on the overall stoichiometry. The material with Li/M=0.96 clearly evidence to an ε-Mg doped $LiCoO_2$ and MgO rocksalt phase. The Li/M=0.98 phase is a Mg doped $LiCoO_2$ with LS-Co^{3+} ions and a coexistence of Mg in the Li and in the Co layers ($[Li_{0.99}Mg_{0.01}]_{Li}$ $[Co^{III}_{0.99}$ $Mg_{0.01}]_{Co}O_2$). Finally, the Li/M=1.00 sample is a single Mg doped phase whose formula can be written as the following $[Li_{1.00}]_{Li}[Co^{3+}_{0.96}$ $Co^{4+}_{0.02}$ $Mg_{0.02}]_{Co}O_2$.

The electrochemical study carried out on the Mg doped phases with various Li/M ratio presented in a second part. Excellent cyclability was observed for the material with Li/M=0.96. The latter has been shown to be ε-Mg doped $LiCoO_2$ with MgO (containing some Co ions). The presence of MgO at the surface of the particles can either prevent the surface of the material from degradation at high voltage or modify the nature of the CEI as discussed in **part A** for Al-doped materials. Moreover, the study of the deintercalated phases for Li/M≥0.98 has shown a similar behavior to that of the $Li_xCo_{0.96}Al_{0.04}O_2$ phases at high voltage.

Through these results, we contributed to a better fundamental knowledge of Mg or Al doped $LiCoO_2$ with various Li/M ratio. Further work would now require to establish i) the origin and the exact nature of the structural defect highlighted in the various Mg doped systems that we have studied, ii) the study of deintercalated Mg doped material with Li/M=0.96 in order to understand the good capacity retention shown by this material and iii) the effect of Mg and Al co-doped $LiCoO_2$ on the electrochemical properties. A preliminary study of the starting materials for the Al and Mg co-doped system has already been carried out. The continuation of this work will therefore reside in the detailed study of the effect of the homogeneity of doping and Li stoichiometry in the Mg and Al co-doped $LiCoO_2$ on their electrochemical properties.